Doctoral Thesis

University of Natural Resources and Life Sciences, Vienna

Fluidized bed heat transfer and solids mixing in view of a post-combustion carbon capture process

Dipl.-Ing. Gerhard Hofer

Supervisor:
Univ.Prof. Dipl.-Ing. Dr.techn. Tobias Pröll

December 13, 2018

Affidavit

I declare in lieu of oath, that I wrote this thesis and performed the associated research myself, using only the literature cited in this manuscript.

Acknowledgements

Thank you, Tobias! From every point of view I want to thank my doctorate supervisor, who always supported me and brought substantial light into my life.
I want to thank my colleagues from university for the innumerable enjoyments we were able to share and for the friendship. Special thanks go to Florian Zerobin, who always possesses the feeling for the moment and an incredible calmness.
I wish to mention Florian Pröll, who not just helped with the design of electrical circuitry, but showed me a great deal what life is about. Thank you!
I gratefully acknowledge the support by the institute of sanitary engineering and water pollution control (SIG) for providing the lab facilities. Special thanks go to Friedrich Kropitz for his unhesitating support.
I want to thank the reviewers for their critical and productive feedback, which certainly helped to enrich the articles and make them intelligible.
None of this would have been possible without the unconditional support of my parents Gerhard and Rosemarie. Thank you for your love!
I wish to thank my grandparents Michael and Margarete for their support. Unfortunately, Michael died in early 2018. He was an inspiring example for many.
A tremendously huge amount of appreciation goes to my friend and love Raphaela. I could have done *this* without her. Nevertheless, the time would not have been as fulfilling as it was, still is and is going to be. The life she is sharing and the love she is giving cannot be paid with any good on earth, except maybe my limitless love for her.

Abstract

Controlling CO_2 emissions from large point sources may help to save the environment and the human race. Therefore, temperature swing adsorption is proposed as promising alternative to liquid amine gas treating for capturing CO_2 at its very formation, e.g. power plants. In order to overcome the limitations of the leading technology, temperature swing adsorption by nature offers solid sorbents possibly preventing the valuable amine reagents from evaporation. Furthermore, it is assumed that the solids-based process is more energy efficient because of the higher CO_2 bonding capacity.
To carry out temperature swing adsorption in the most efficient way, heat transfer between the particles and the solids-immersed heat exchangers must be well studied in terms of the design of the in-bed heat exchangers to be implemented. In addition, mass transfer rates are to be sufficient for removing CO_2 efficiently from flue gases varying in the composition. Thus, this thesis is concerned with both the in-bed, i.e. wall-to-bed heat transfer and particle mixing characteristics of bubbling fluidized beds considering particles classified as Geldart group *B*.
Models available for the prediction of tube bundle heat transfer rates are rare and justify the effort of utilizing cold flow models for the investigation of fluidized bed phenomena just as the wall-to-bed heat transfer. Having erected a capable cold flow model for measuring in-bed heat transfer coefficients it seemed logically to extend its capabilities for the measurement of particle residence time distributions in cross-flow bubbling fluidized beds, such as the ones proposed for the temperature swing adsorption process. Therefore, a measurement system based on inductive tracer detection was built and put into operation.
With regard to the wall-to-bed heat transfer it was shown that the prediction of heat transfer coefficients strongly depends on the mathematical model used for heat transfer estimations and that heat transfer coefficients vary strongly, although considering particles merely in the Geldart group *B* range. Thus, heat transfer coefficients can be as high as $\approx 600\,\mathrm{W\,m^{-2}\,K^{-1}}$ for powders of 130µm in mean diameter. However, particles of ≈700µm in mean diameter show a maximum heat transfer coefficient of just above $200\,\mathrm{W\,m^{-2}\,K^{-1}}$. The models used for the calculation of heat transfer coefficients fairly predict the experimental data.
In view of particle mixing processes it was shown that the inductive measurement system is suitable to obtain particle residence time distributions in bubbling fluidized beds with continuous solids exchange. Although bubbling fluidized bed reactors are known to exhibit mixing characteristics similar to (continuous) stirred tank reactors, it was shown that the behavior tends towards the characteristics of a plug flow reactor with axial dispersion for fluidization numbers around five. Whereas the behavior clearly stems from the formation of dead spaces and short circuit flows in the stated fluidization regime, no mixing deficits were observed for higher fluidization numbers.
Supplementary experiments are planned to investigate the influence of particle cross-flow on the wall-to-bed heat transfer as well as to examine the influence of tube bundles on the solids residence time distribution and mixing characteristics.

Kurzfassung

CO_2-Emissionen gefährden die Gesundheit des Menschen und seiner Umwelt. Die einhergehende Erderwärmung könnte mittels einem auf der Temperaturwechseladsorption basierenden Prozess abgeschwächt werden. Zur Zeit bildet die Aminwäsche den Stand der Technik hinsichtlich der CO_2-Abscheidung aus Rauchgasen. Es wird angenommen, dass das auf Feststoffen basierende Konkurrenzverfahren aufgrund der höheren Bindungskapazität von CO_2 an die reaktive Oberfläche der aminfunktionalisierten Teilchen energieeffizienter ist und außerdem Einsparungen der Betriebsmittel erzielt werden können.
Um das Adsorptionsverfahren möglichst effizient durchzuführen, muss die Wärmeübertragung zwischen den als Wirbelschicht ausgeführten Reaktorstufen und den darin eingetauchten Wärmetauschern optimiert werden. Darüber hinaus müssen die Stoffübergangsraten ausreichend hoch sein, um CO_2 effizient aus Rauchgasen unterschiedlicher Zusammensetzung zu entfernen. Deshalb beschäftigt sich diese Dissertation sowohl mit der Wärmeübertragung in blasenbildenden Wirbelschichten, als auch mit den damit einhergehenden Partikelmischvorgängen.
In der Literatur gibt es eine beschränkte Anzahl mathematischer Modelle, die für die Berechnung von Wärmeübergangskoeffizienten in Wirbelschichten zur Verfügung stehen. Deshalb wurde im Zuge dieser Arbeit ein Wirbelschicht-Kaltmodell zur Messung von Wärmeübergangskoeffizienten aufgebaut. Außerdem wurde es für die Messung von Partikelverweilzeitverteilungen in Wirbelschichten mit kontinuierlichem Feststoffaustausch ausgestattet. Ein Messsystem, basierend auf der induktiven Tracerdetektion, wurde entworfen und aufgebaut.
In Bezug auf die Wärmeübertragung zwischen Wirbelschichten und Rohrbündeln wurde gezeigt, dass die Abschätzung von Wärmeübergangskoeffizienten stark von den verfügbaren mathematischen Modellen abhängt und dass die Wärmeübergangskoeffizienten stark in ihrer Quantität variieren. Beispielsweise können Wärmeübergangskoeffizienten für Partikel mit einem mittleren Korndurchmesser von 130µm im Bereich von $600\,\mathrm{W\,m^{-2}\,K^{-1}}$ liegen, wohingegen Partikel mit einem mittleren Korndurchmesser von 700µm nurmehr einen maximalen Wärmeübergangskoeffizienten von knapp über $200\,\mathrm{W\,m^{-2}\,K^{-1}}$ aufweisen. Die für die Berechnung von Wärmeübergangskoeffizienten verwendeten Modelle sind dabei mehr oder weniger in der Lage, die experimentell bestimmten Werte vorherzusagen.
Im Hinblick auf Partikelmischprozesse wurde gezeigt, dass das induktive Messprinzip zur Untersuchung von Partikelmischvorgängen in blasenbildenden Wirbelschichten geeignet ist. Für Fluidisierungszahlen um fünf wurde gezeigt, dass die Mischcharakteristika von blasenbildenden Wirbelschichten den von (kontinuierlich betriebenen) Rührkesseln ähneln, sie allerdings von jenen eines Pfropfenstromreaktors mit axialer Dispersion beeinflusst sind. Während das beschriebene Verhalten eindeutig auf die Bildung von Totzonen und Kurzschlussströmungen im angegebenen Fluidisierungsbereich zurückzuführen ist, wurden bei höheren Fluidisierungszahlen keine Mischungsdefizite beobachtet.
Es sind ergänzende Versuche geplant, um den Einfluss der Partikelquerströmung auf den Wärmeübergang sowie den Einfluss von eingetauchten Rohrbündeln auf die Feststoffverweilzeitverteilung und -mischcharakteristik zu untersuchen.

List of publications

Included in the thesis

[1] G. Hofer, J. Fuchs, G. Schöny, and T. Pröll, "Heat transfer challenge and design evaluation for a multi-stage temperature swing adsorption process," *Powder Technology*, vol. 316, pp. 512–518, July 2017

[2] G. Hofer, G. Schöny, J. Fuchs, and T. Pröll, "Investigating wall-to-bed heat transfer in view of a continuous temperature swing adsorption process," *Fuel Processing Technology*, vol. 169, pp. 157–169, Jan. 2018

[3] G. Hofer, G. Schöny, and T. Pröll, "Acting on hydrodynamics to improve the local bed-to-wall heat transfer in bubbling fluidized beds," *Chemical Engineering Research and Design*, vol. 134, pp. 309–318, June 2018

[4] G. Hofer, T. Märzinger, C. Eder, F. Pröll, and T. Pröll, "Particle mixing in bubbling fluidized bed reactors with continuous particle exchange," *Chemical Engineering Science*, Nov. 2018

These publications are included in the Appendix A.

Not included

[5] G. Hofer, "Heat transfer at immersed tube bundles in bubbling fluidized beds considering Geldart type B particles," in *12. Minisymposium Verfahrenstechnik*, pp. 9–12, TU Graz, Mar. 2016

[6] G. Hofer, J. Fuchs, G. Schöny, and T. Pröll, "Dimensioning tube bundle heat exchangers for a continuous temperature swing adsorption process," in *Proceedings of 12th International Conference on Fluidized Bed Technology (CFB-12)* (W. Nowak, M. Sciazko, and P. Mirek, eds.), pp. 465–473, May 2017

List of symbols

Abbreviations

AC alternating current
AD axial dispersion

BFB bubbling fluidized bed

CET central European time
CFM cold flow model
CO_2 carbon dioxide
CSTR continuous stirred tank reactor

DC direct current

H_2O water
HEX heat exchanger

ID inner diameter

OD outer diameter

PFR plug flow reactor
PID proportional–integral–derivative
PLC programmable logic controller
PSA pressure swing adsorption
PSD particle size distribution

RTD residence time distribution

SCR solids circulation rate
SMD Sauter mean diameter

TIS tanks-in-series
TSA temperature swing adsorption

Roman characters

Sign	Description	Unit
A_{fb}	Fluidized bed cross section	kg
A_{HEX}	Active surface area transferring heat	m^2
Ar	Archimedes number	1
Bo	Bodenstein number	1
C	Capacitance	F
C_{pulse}	Pulse input	1
$C_{response}$	Response to a pulse input	1
c	Coefficient	1
$c_{p,g}$	Gas specific heat capacity	$J\,kg^{-1}\,K^{-1}$
$c_{p,p}$	Particle specific heat capacity	$J\,kg^{-1}\,K^{-1}$
$\mathbf{D}$	Axial dispersion coefficient	$m^2\,s^{-1}$
d_{32}	Sauter mean diameter	m
d_{eff}	Effective particle diameter	m
d_p	Particle mean diameter determined by sieving	m
d_p^*	Dimensionless particle mean diameter	1
$d_{p,i}$	Particle size in the i^{th} size range	1
d_t	Tube outer diameter	m
E	Exit age distribution function	s^{-1}
E_{fit}	Modeled exit age distribution function	s^{-1}
F	Force, Cumulative exit age distribution function	$N, 1$
f_{dt}	Tube diameter corrective factor	1
f_{tb}	Tube bundle corrective factor	1
g	Acceleration of gravity	$m\,s^{-2}$
H_{fb}	Fluidized bed height	m
h	Wall-to-bed heat transfer coefficient	$W\,m^{-2}\,K^{-1}$
h_{gc}	Gas convective heat transfer coefficient	$W\,m^{-2}\,K^{-1}$
h_i	Apparent heat transfer coefficient	$W\,m^{-2}\,K^{-1}$
h_{max}	Maximum heat transfer coefficient	$W\,m^{-2}\,K^{-1}$
h_{pc}	Particle convective heat transfer coefficient	$W\,m^{-2}\,K^{-1}$
h_r	Radiative heat transfer coefficient	$W\,m^{-2}\,K^{-1}$

Sign	Description	Unit
h_{total}	Overall heat transfer coefficient	$\mathrm{W\,m^{-2}\,K^{-1}}$
Δh_r	Heat transfer coefficient random measurement error	$\mathrm{W\,m^{-2}\,K^{-1}}$
Δh_s	Heat transfer coefficient systematic measurement error	$\mathrm{W\,m^{-2}\,K^{-1}}$
j	Imaginary unit	1
k_{max}	E_{fit}-curve maximum slope	$\mathrm{s^{-2}}$
L	Inductance, Characteristic length	$\mathrm{H, m}$
l_l	Laminar flow length	m
M	Molar mass	$\mathrm{kg\,mol^{-1}}$
m	Mass	kg
$\dot{m}_{H_2O}$	Water mass flow	$\mathrm{kg\,h^{-1}}$
m_p	Particle mass	kg
m_s	Solids mass	kg
$\dot{m}_s$	Solids mass flow	$\mathrm{kg\,h^{-1}}$
n_{stage}	Number of fluidized bed stages	1
Pr	Prandtl number	1
p	Pressure	Pa
p_{diag}	Diagonal tube pitch	m
p_h	Horizontal tube pitch	m
p_i	Partial pressure of the species i	Pa
p_{min}	Minimum tube pitch	m
p_v	Vertical tube pitch	m
Δp_{fb}	Fluidized bed pressure drop	Pa
Q	Power, Heat flow	W
$\Re$	Molar gas constant	$\mathrm{J\,K^{-1}\,mol^{-1}}$
R	Resistance	Ω
Re	Reynolds number	1
S_0	Straight line zeroing $C_{response}$	1
S_1	k_{max}-sloped straight line determining τ_1	1
s_{diag}	Diagonal tube spacing	1

Sign	Description	Unit
s_h	Horizontal tube spacing	1
s_v	Vertical tube spacing	1
T	Temperature	K
T_{fb}	Fluidized bed temperature	K
T_{pr}	Heat transfer measurement probe temperature	K
ΔT_m	Mean logarithmic temperature difference	K
t	Time	s
U	Superficial gas velocity	$\mathrm{m\,s^{-1}}$
U_{mb}	Minimum bubbling gas velocity	$\mathrm{m\,s^{-1}}$
U_{mf}	Minimum fluidization gas velocity	$\mathrm{m\,s^{-1}}$
U_{opt}	Superficial gas velocity at maximum heat transfer	$\mathrm{m\,s^{-1}}$
U_{se}	Solids entrainment gas velocity	$\mathrm{m\,s^{-1}}$
u	(Characteristic) velocity	$\mathrm{m\,s^{-1}}$
u^*	Dimensionless gas velocity	1
V_b	Bulk volume	$\mathrm{m^3}$
$\dot{V}_g$	Gas volume flow	$\mathrm{m^3\,h^{-1}}, \mathrm{Nm^3\,h^{-1}}$
$\dot{V}_{H_2O}$	Water vapor volume flow	$\mathrm{m^3\,h^{-1}}, \mathrm{Nm^3\,h^{-1}}$
V_{in}	AC input voltage (peak-peak)	V
V_{out}	AC output voltage (peak-peak)	V
V_p	Particle volume	$\mathrm{m^3}$
ΔV_{DC}	DC voltage change	V
w_i	Mass fraction of particles in the $\mathrm{i^{th}}$ size range	1
w_{tracer}	Mass fraction of tracer	1
x	X-coordinate	m
y	Y-coordinate	m
z	Z-coordinate	m

Greek characters

Sign	Description	Unit
β	Adsorbent loading	$\mathrm{mol\,kg^{-1}}$
γ	Accommodation coefficient	1
ϵ	Void fraction	1
ϵ_{mf}	Void fraction at minimum fluidization	1
ϑ	Temperature	°C
κ	Particle size parameter	1
Λ	Mean free path	m
λ_g	Gas thermal conductivity	$\mathrm{W\,m^{-1}\,K^{-1}}$
λ_p	Particle thermal conductivity	$\mathrm{W\,m^{-1}\,K^{-1}}$
λ_t	Tube wall thermal conductivity	$\mathrm{W\,m^{-1}\,K^{-1}}$
μ_g	Gas viscosity	Pa s
ϕ	Particle sphericity	1
ρ_b	Bulk density	$\mathrm{kg\,m^{-3}}$
ρ_g	Gas density	$\mathrm{kg\,m^{-3}}$
ρ_p	Particle density	$\mathrm{kg\,m^{-3}}$
τ	Mean residence time	s
τ_0	Time at maximum of C_{pulse}	s
τ_1	Breakthrough time at S_1=0	s
τ_2	Breakthrough time at the occurrence of k_{max}	s
τ_3	Breakthrough time at maximum of $C_{response}$	s
τ_{fit}	Mean residence time calculated from E_{fit}	s
τ_{hyd}	Hydraulic residence time	s
ω	Angular frequency	$\mathrm{rad\,s^{-1}}$
ψ_{HEX}	Tube bundle void fraction	1

Dimensionless groups

The ratio of forces due to gravitation and viscosity is given by the Archimedes number (Equation 0.1) and is used to characterize the motion of liquids based on their difference in density.

$$Ar = \frac{\rho_g \cdot {d_p}^3 \cdot (\rho_p - \rho_g) \cdot g}{{\mu_g}^2} \tag{0.1}$$

The ratio of convection current to dispersion current is given by the Bodenstein number (Equation 0.2) and is used to characterize solids backmixing or dispersion, respectively. The inverse is referred to the term vessel dispersion number $\mathbf{D}/(u \cdot L)$ in the literature [7].

$$Bo = \frac{u \cdot L}{\mathbf{D}} \tag{0.2}$$

The dimensionless particle mean diameter is given by Equation 0.3. The quantity is used to categorize fluidized bed flow regimes.

$$d_p^* = \sqrt[3]{Ar} \tag{0.3}$$

The ratio of viscous diffusion to thermal diffusion is given by the Prandtl number (Equation 0.4).

$$Pr = \frac{\mu_g \cdot c_{p,g}}{\lambda_g} \tag{0.4}$$

Within a fluid the ratio of forces due to inertia and viscosity is given by the Reynolds number. In particular, the Reynolds number for gas-solid flows is given by Equation 0.5, wherein the particle mean diameter of a respective powder represents the characteristic length.

$$Re_p = \frac{\rho_g \cdot d_p \cdot U}{\mu_g} \tag{0.5}$$

The dimensionless gas velocity is given by Equation 0.6. Such as the dimensionless particle diameter, the quantity is used to categorize fluidized bed flow regimes.

$$u^* = \frac{Re_p}{\sqrt[3]{Ar}} \tag{0.6}$$

Contents

Chapter 1

Introduction

1.1 Problem definition

Newton's first law is illustrated by the given Equation 1.1. In brief, the absence of a net force neither causes acceleration nor deceleration.

$$\sum F = 0 \iff \frac{du}{dt} = 0 \tag{1.1}$$

Newton's second law is illustrated by the given Equation 1.2. Under the assumption of a constant mass system, the net force is directly proportional to the object's acceleration or deceleration, respectively.

$$F = m \cdot \frac{du}{dt} \tag{1.2}$$

Newton's third law is illustrated by the given Equation 1.3. For every action there exists reaction, directed oppositely and equal in its magnitude.

$$F_A = -F_B \tag{1.3}$$

Although Newton's laws neglect the object's size and shape by reducing it substantially to a single point mass — *particle*, we want to utilize them for the description and characterization of occurrences and processes in view of the *Anthropocene*. Not yet recognized as a geological time, the term Anthropocene was introduced in the year 2000 by Crutzen and Stoermer to represent the major and still growing impacts of human activities on earth and atmosphere [8]. Climate policy or protection of biodiversity in the Anthropocene must no longer be just goals that serve to permanently preserve the human life or to avoid future costs, rather than declaring the non-human world of living things, landscapes, the climate, the oceans and water cycles to be independent values worthy of protection [9].
Certainly, an unforseenly different era was introduced with the industrial revolution. With machines taking over hand production methods, terms such as mass production and automation rapidly became common. Currently, Industry 5.0 is on the doorstep [10]. Knowing that the industrial revolution rang in just about 200 years ago accompanied by a swift growth of the population, we inevitably get to feel Newton's first and second law. Having more and more minds available to invent even faster inherently unleashes an unprecedented force. On the one hand, a force that enables the lives of so many people. Doubling the value of 1990, more than $25{\cdot}10^{15}$Wh of electricity were produced in 2017, therefrom 25% generated by renewable sources [11]. On the other hand, Newton's third law implies that action causes reaction, in other words, every protagonist has its antagonist, or according to Equation 1.3, every force has its counterforce — *climate change*.

Living as a human in the 21st century possibly comprises having a great deal of resources available to understand, think and act. At the moment, the human race seems to understand what industrialization caused and still causes, and some of us already vehemently try to mitigate those changes. With regard to thinking and acting, carbon capture and storage and/or utilization have gained wide acceptance within the international climate change policy community as a practical mitigation option [12]. Many attempts have been made to capture atmospheric CO_2 at its source, whereby liquid amine gas treating is the leading post-combustion technology easily retrofittable to modern pulverized coal power plants or natural gas combined cycle power plants [13]. Although liquid amine scrubbing was optimized in view of the process energy consumption over the past decades, the minimum energy demand is expected to be as high as 3.7GJ per tonne of CO_2 captured [14]. Superficially, mass transfer poses an obstacle preventing from further improvement.

1.2 Recent development

The utilization of amine-functionalized particles in temperature swing adsorption (TSA) is investigated contingently possibly representing an energy-efficient alternative to the state-of-the-art liquid amine scrubbing process [15, 16]. The basic principle of a continuously operated TSA process for CO_2 capture from flue gas streams is illustrated in Figure 1.1.
The reactors, namely adsorber and desorber, could be designed as moving bed columns favoring thermodynamics by the establishment of counter-current flows of the gas phase to be treated and the solids transferring heat to and from the solids-immersed heat exchangers. However, heat transfer is crucial when carrying out TSA and heat transfer coefficients are poor in the moving bed regime hampering efficient heat exchange realizing the temperature swing. Operating the reactors in the fluidized bed regime may help to overcome the limitation in heat transfer, subsequently comprising a thermodynamic limitation in the cyclic sorbent capacity. This implies that the CO_2 concentration in the desorber off-gas is crucially limited in single-stage systems when a high CO_2 capture efficiency is desired leading to excessive desorber stripping gas requirements and sorbent circulation rates. In conclusion, the process must allow for counter-current flow of the gas and sorbent streams accompanied by sufficient heat transfer and excellent mass transfer.
Because of the mentioned necessities leading to a feasible process implementation, a TSA plant design based on double loop, multistage bubbling fluidized bed (BFB) reactors was proposed by Pröll et al. [15]. Comprehensive experimental work was performed with a fully functional TSA unit in bench scale by Schöny et al. [16, 17] and Dietrich et al. [18, 19]. The unit featured five fluidized bed stages each in the adsorber and desorber. Fluid dynamics were investigated alongside the CO_2 capture efficiency using simulated flue gas mixtures and nitrogen or steam as stripping agents. Critical process parameters such as the

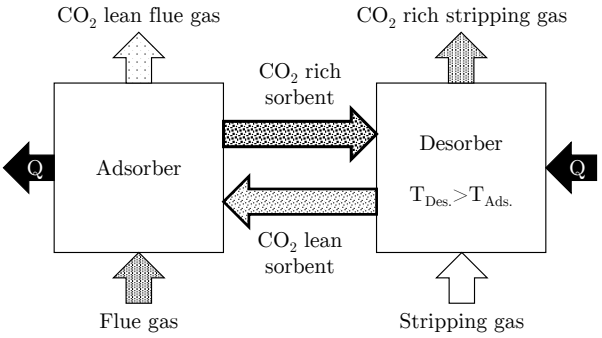

Figure 1.1: TSA process principle.

adsorption and desorption temperature, the solids circulation rate and the solids inventory were varied during these tests with promising outcomes in terms of the capture efficiency (≈90%). However, it was noted that the CO_2 capture performance was limited by insufficient heat transfer in the fluidized bed stages. In addition, extensive computational studies with regard to the optimization of the stage number and heat integration on the TSA process efficiency were performed by Pirklbauer et al. [20, 21]. It was concluded that at least three stages had to be implemented in each reactor in order to limit the energy demand and to create a competitive process. However, the larger the fluidized bed stage number the higher the capital expenditures for carbon capture systems based on TSA. Fluid-dynamic studies by means of cold flow modeling were conducted by Zehetner et al. [22, 23] to optimize the design of the adsorber and desorber as well as the solids transport systems between the reactors in view of the construction of a pilot unit.

1.3 Aim

To account for the crucial importance of heat and mass transfer in TSA systems and supplementary to the work performed by others as mentioned in Section 1.2, two specific aims were defined to be treated in the course of this thesis.

1. Determine the design of the in-bed heat exchangers capable to transfer the required sensible and latent heat considering rather shallow fluidized beds in the adsorber and low stripping gas flows for desorption purposes.

2. Investigate the fluid-dynamic behavior in the fluidized bed stages of the adsorber and desorber with regard to the mass transfer depending on particle mixing characteristics.

Based on the given aims defined by the Items 1 and 2 and in view of designing a temperature swing adsorption pilot unit, the following research questions were derived.

a. What are the achievable wall-to-bed heat transfer coefficients between bubbling fluidized beds of Geldart group *B* particles and immersed tube bundle heat exchangers?

b. What are the residence time distribution characteristics within a bubbling fluidized bed of Geldart group *B* particles under continuous solids exchange?

Chapter 2

Background

The fundamentals of adsorption are summarized in Section 2.1. The process proposed for post-combustion carbon capture by means of fluidization-based TSA is briefly described in Section 2.2. Section 2.3 condenses the relevant theory on gas-solid fluidization by elaborating on the emerging fluidization regimes and calculation methods. The models available for the estimation of wall-to-bed heat transfer coefficients are presented in Section 2.4. The theoretical background in view of the residence time distribution (RTD) characteristics of particles in BFB with continuous solids exchange is discussed in Section 2.5.

2.1 Adsorption fundamentals

Adsorption refers to a process in which a substance — the *adsorptive* — adheres to a substance usually different in its aggregate phase — the *(ad)sorbent* [24]. In every sense, the adsorption of gases onto solids is of great importance in gas separation processes. Mass transfer during adsorption is a consequence of the energy available on the sorbent's surface. Thereby, the bonding mechanism may differ in its nature, i.e. chamical — *chemisorption* — or physical — *physisorption*. Whereas the prevalent chemical reactions during chemisorption strongly depend on the participating components, the bonds formed are usually stronger compared to physically adsorbed reagents. Adsorption usually is an exothermic process. However, in case a molecule dissociates and the respective energy is larger than the bond formation energy, the process can be endothermic [25]. Thus, chemisorption may be either exothermic or endothermic (rare).
According to Bathen and Breitbach [26], adsorption and desorption consist of a complex interaction of mass transfer processes based on convection and diffusion alongside to thermal conduction and heat transfer. Subsequently, the process of adsorption is graphically illustrated in Figure 2.1 and characterized by the following steps:

1→2 Convective and diffusive transfer of the gas molecule to the boundary layer of the sorbent material.

2→3 Diffusive transport through the boundary layer.

3→4 Diffusive transport in the pores of the adsorbent.

4→5 Adsorption, an exothermic accumulation of gas molecules onto the sorbent's surface. Usually the preceding transport processes are slower, why adsorption is not the limiting step.

5→6 The heat of adsorption is transported mainly by heat conduction to the surface of the adsorbent particle and through the boundary layer.

6→7 Governed by heat convection, the heat of adsorption is transported to the contacting phase.

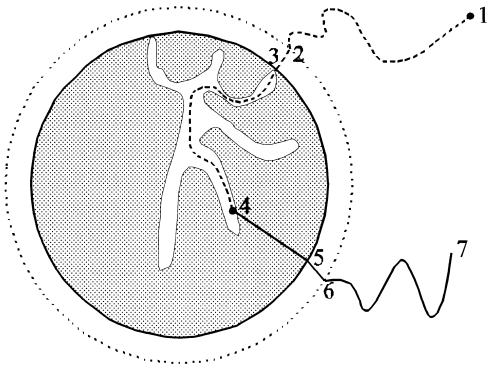

Figure 2.1: The principle of adsoption in seven steps, taken from Bathen and Breitbach [26].

For the mathematical description of the adsorption so-called isotherms are used [27]. They provide a basis for the calculation of data in view of the adsorption equilibrium as a function of the gas concentrations, pressures and temperatures. Because of the exothermic nature of adsorbing CO_2, the adsorption capacity of a respective sorbent material decreases with an increase in the process temperature. By way of example, adsorption isotherms, i.e. adsorbent loadings β as a function of the partial pressure of a respective gaseous species p_i for different temperatures are shown in Figure 2.2 [28].
The regeneration of the sorbent is referred to the term *desorption*, which can be achieved by an increase in the temperature — *temperature swing*, reduction of the pressure — *pressure swing*, by the reduction of the partial pressure or by applying a stronger sorbent [29]. As for the design of a continuous adsorption unit by means of a solid sorbent coupled with fluidized bed technology, particle handling is a crucial aspect naturally ruling out pressure swing adsorption (PSA) because of the fact that it is difficult to seal the reactor columns against each other. It is concluded that amine-based sorbents are able to capture CO_2 selectively and efficiently [30] and that regeneration by means of a temperature swing with steam as stripping agent constitutes the only option relevant for practical applications [28].

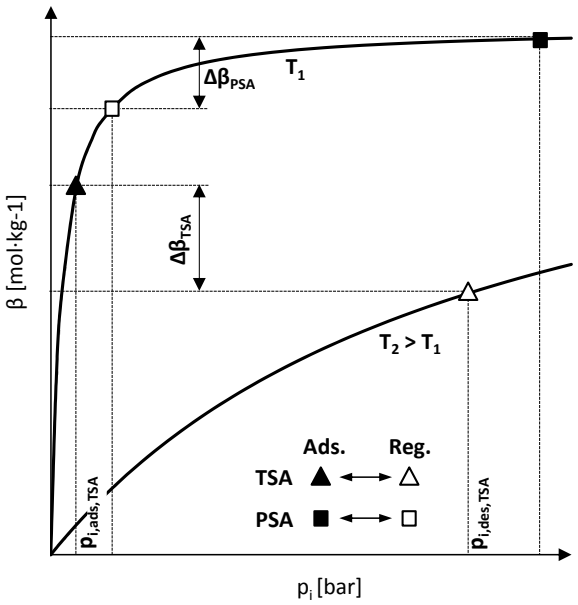

Figure 2.2: Temperature dependent adsorption isotherms illustrating sorbent regeneration by temperature swing adsorption and pressure swing adsorption, taken from Schöny [28].

2.2 Fluidization-based temperature swing adsorption

Figure 2.3 illustrates the principle of the gas-solid fluidization-based double-loop reactor system proposed by Pröll et al. [15] realizing the continuous TSA process utilizing an amine-functionalized solid sorbent. Similar process implementations can be found in the literature [31, 32]. In the given configuration, both the adsorber and desorber feature five BFB stages for efficient CO_2 capture resulting in capture efficiencies up to 90% [16]. A comprehensive discussion concerned with the number of stages in view of the process efficiency is given by Pirklbauer et al. [20].
The top-down moving sorbent particles are fluidized by the introduction of raw flue gas at the bottom of the adsorber column. CO_2 is progressively removed from the gas mixture while contacting the sorbent material in quasi-counter-current flow. After the separation process when the loaded (rich) sorbent exits the bottom stage of the adsorber, the particles are transported to the desorber column for regeneration. A riser manages the solids lift. The desorber is operated at higher temperatures accomplishing the temperature swing. In the proposed setup, steam is used to fluidize the top-down streaming sorbent actively stripping the CO_2. A gas mixture containing steam and pure CO_2 is obtained at the top freeboard of the desorber. To close the loop of solids, the regenerated (lean) sorbent is lifted through a riser from the bottom of the desorber to the top of the adsorber for further CO_2 separation.

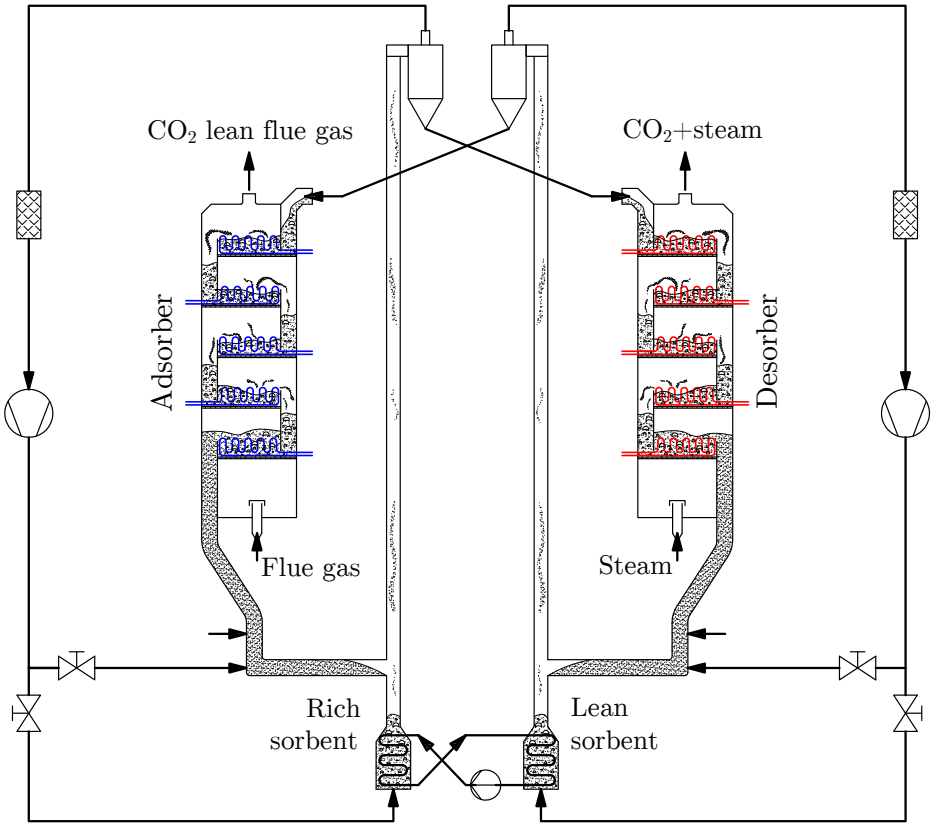

Figure 2.3: Principle of the continuous temperature swing adsorption process and relevant heat exchange requirements (blue=cooling, red=heating).

Because of the exothermic nature of the adsorption of CO_2, a certain amount of heat must be removed from the multiple particle beds fluidized in the stages of the adsorber. Contrarily, the regeneration step requires about the same amount of heat to be introduced during

desorption. In-bed tube bundle heat exchangers (HEXs) shall execute the task of efficient heat transfer. Further process optimization might utilize additional HEXs, particle-wise arranged downstream of the adsorber and desorber, allowing for the exchange of sensible heat tempering the solids before entering the respective other reactor column.
Considering the proposed process from a fluidized bed point of view reveals two possible bottlenecks. One the one hand, heat transfer between the fluidized beds and the immersed HEXs must be sufficient since excessive temperatures during adsorption lead to limited sorbent loadings [30], and insufficient heating in the desorber leads to poor sorbent regeneration. On the other hand, the fluidized bed stages must be designed in view of sufficient mass transfer, i.e. an efficient residence time of the particles for adsorption and desorption alongside adequate particle mixing to involve the largest possible amount of amine-functionalized solids in the chemical reaction by means of avoiding dead spaces. From this point of view especially the design of the desorber is challenging taking the limited steam flow rate due to the minimization of the energy requirement for gas separation into account. Low amounts of steam used for fluidization most likely correlate to low wall-to-bed heat transfer coefficients and poor solids mixing.

2.3 Gas-solid fluidization fundamentals

By the 13$^{\text{th}}$ of December 2018, 11a.m. CET, sciencedirect.com provided 282,409 results searching for the term *fluidized bed*, whereof 170,864 results were research articles. Hence, this thesis does not claim completeness when it comes to (mathematical) models available for the description and calculation of fluidized bed specific properties and pragmatically focuses on approaches with regard to the tasks defined in Section 1.3.

2.3.1 Powder characterization

Particle size and sphericity

The relevant particle size for fluidized bed calculations is the surface area moment mean [33, 34], also referred to as Sauter mean diameter (SMD) and often represented by the symbol d_{32}. The SMD gives larger weight to the finer fractions of a bulk material featuring a certain particle size distribution (PSD). For a single particle, the definition of the SMD is the diameter of a notional sphere with the same ratio of external surface area to volume compared to the original particle. Sieving is often the most practicable method of size analysis, whereby Equation 2.1 results in the particle mean diameter d_p.

$$d_p = d_{32} = \left(\sum \frac{w_i}{d_{p,i}} \right)^{-1} \tag{2.1}$$

Consequently, the relationship between the effective particle diameter d_{eff} and d_p is of interest. For particles not deviating too much from the spherical shape, Equation 2.2 correlates d_{eff} and d_p by the introduction of the particle sphericity ϕ [35]. ϕ is defined as the ratio of the external surface area of a sphere to that of a particle of equivalent volume [36] and ranges from zero to one, whereby for spheres ϕ=1 applies.

$$d_{eff} = \phi \cdot d_p \tag{2.2}$$

Particle and bulk density

The density of a particle is defined by Equation 2.3, i.e. the ratio of particle mass to particle volume. In the absence of pores, the density of the particles is equal to the material density,

while in the presence of pores, the volume of the particles is defined by the virtual contour that encloses the voids.

$$\rho_p = \frac{m_p}{V_p} \tag{2.3}$$

Whereas the particle density is an intrinsic particle property, the bulk density is not, since it depends on the degree of compaction, i.e. the bed voidage. The bulk density is defined by Equation 2.4, i.e. the ratio of the solids mass to the volume occupied by the bulk of solids.

$$\rho_b = \frac{m_s}{V_b} \tag{2.4}$$

Void fraction

Based on the particle sphericity, in 1966 Wen and Yu proposed a correlation for the calculation of the void fraction of bulk materials [37]. In the state of a fixed bed (refer to Section 2.3.2), the ratio of the particle interstice volume to the total volume occupied by the bulk of solids is represented by the bed voidage at minimum fludization ϵ_{mf}. The mathematical formula is given in Equation 2.5 and leads to fair approximations of ϵ_{mf} for practical purposes.

$$\epsilon_{mf} \approx \sqrt[3]{\frac{1}{14 \cdot \phi}} \tag{2.5}$$

Minimum fluidization gas velocity

The minimum fluidization gas velocity U_{mf} constitutes a characteristic velocity with respect to fluid flow through particulate systems, i.e. the state where the drag force of the upward moving gas balances the buoyed weight of the fluidized solids. In this state, the particles are suspended in the flow of gas. It is part of the mathematical models available for the prediction of the wall-to-bed heat transfer and thus a key feature in designing in-bed HEXs. The minimum fluidization gas velocity can be derived from the Ergun equation [38] (Equation 2.6), which is widely accepted for the calculation of the pressure drop caused by residing bulk material, i.e. the basis for calculating the drag force in the fixed bed regime.

$$\Delta p_{fb} = \left[150 \cdot \frac{(1-\epsilon)^2}{\epsilon^3} \cdot \frac{\mu_g \cdot U}{\phi^2 \cdot {d_p}^2} + 1.75 \cdot \frac{1-\epsilon}{\epsilon^3} \cdot \frac{\rho_g \cdot U^2}{\phi \cdot d_p} \right] \cdot H_{fb} \tag{2.6}$$

For laminar gas flows where Reynolds numbers are less than unity, the term dominates where the superficial gas velocity U appears linear, accounting for the viscous energy losses. In the case of turbulent flows with Reynolds numbers exceeding 10^3, the term dominates where U appears quadratic, accounting for the kinetic energy losses. Equation 2.6 equals Equation 2.7 at minimum fluidization conditions, whereby $\epsilon{=}\epsilon_{mf}$ and $U{=}U_{mf}$ holds true. Therein, the particle weight reduced by the buoyancy force represents the pressure drop of a bulk material in the fluidized state. In case of $\rho_g \ll \rho_p$ the fluidized bed pressure drop might be approximated by the fraction of the solids weight and the fluidized bed cross-section (Equation 2.7) elucidating Δp_{fb} being constant for $U_{mf}{<}U{<}U_{se}$, as shown in Figure 2.4.

$$\Delta p_{fb} = (1-\epsilon) \cdot (\rho_p - \rho_g) \cdot g \cdot H_{fb} \approx \frac{m_s \cdot g}{A_{fb}} \tag{2.7}$$

By simplifying, rearranging and introducing the Archimedes number Ar as well as the Reynolds number at minimum fludization Re_{mf}, Equation 2.8 is deduced from equating Equation 2.6 and Equation 2.7. Therein, both coefficients c_1 and c_2 are a function of the void fraction at minimum fluidization ϵ_{mf}.

$$Ar = c_1 \cdot Re_{p,mf} + c_2 \cdot {Re_{p,mf}}^2 \tag{2.8}$$

The correlation for calculating U_{mf} is obtained by solving and rearranging Equation 2.8. The resulting formula is given by Equation 2.9.

$$U_{mf} = \frac{\mu_g}{\rho_g \cdot d_p} \cdot \left(\sqrt{{c_1}^2 + c_2 \cdot Ar} - c_1 \right) \tag{2.9}$$

Grace recommends c_1=27.2 and c_2=0.0408 [39], which were used for the calculations performed in the scope of this thesis. Other authors recommend diverging values for c_1 and c_2. However, it is stated that inaccuracies of up to 40% in respect of U_{mf} are tolerable when designing in-bed HEXs from a practical point of view [40]. Comprehensive summaries on the various equations available for the calculation of the minimum fluidization gas velocity U_{mf} are given in the literature [41, 42].

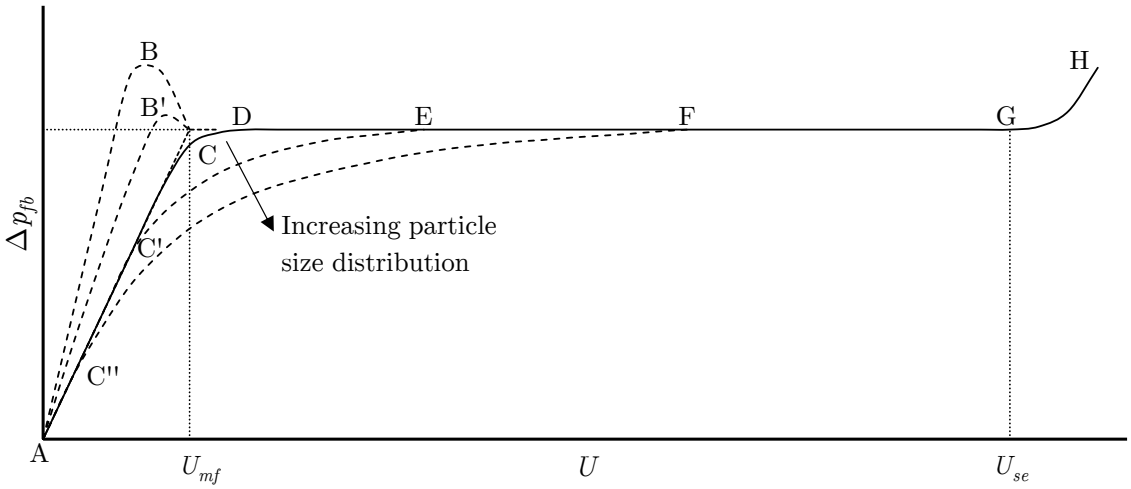

Figure 2.4: Fluidized bed pressure drop as a function of superficial gas velocity, adapted from Yang [43] (ABDEF and AB'DEF=powder in a narrow tube or compacted; AC'EFG and AC"FG=wide size distribution, fluidization indicating particle segregation; ACDEFG=normal fluidization curve; FG=fully fluidized region; GH=solids entrainment).

Fluidized bed void fraction

Considering Equation 2.7, the pressure drop across a fluidized bed Δp_{fb} is determined by the density of the solids ρ_p and gas phase ρ_g, the bed height H_{fb} and voidage ϵ. Because of the fact that the mass of the fluidized particles in a BFB is constant, the fluidized bed pressure drop is constant over a more or less wide range of superficial gas velocity (refer to Figure 2.4). However, the increase in gas flow will cause the bed to expand, i.e. increase in height. To quantify the extent of the change in volume, Hsiung and Thodos developed a model to calculate the void fraction in the fluidized state [44]. The formula is given by Equation 2.10.

$$\epsilon = \epsilon_{mf} \cdot \left(\frac{Re_p - \kappa}{Re_{p,mf} - \kappa} \right)^{0.28} \tag{2.10}$$

Thereby, κ represents the dimensionless particle size parameter, to be calculated according to Equation 2.11.

$$\kappa = 0.216 \cdot Re_{p,mf}^{1.2} - 0.35 \tag{2.11}$$

Geldart's powder classification

In 1973 Geldart proposed a powder categorization with respect to their behavior when fluidized [45]. The classification is reproduced in Figure 2.5. Dense, non-cohesive materials

such as glass or sand most likely are of group B. Bubble formation occurs at the onset of fluidization, that is, reaching the minimum fluidization gas velocity U_{mf}. Thus, the excess gas causes the formation of bubbles conceivably growing to considerable size.
Particles such as catalysts for fluid catalytic cracking with mean sizes in the range of 20...100µm are considered to be of group A. Powders of this group tend to exhibit slightly cohesive behavior causing the bed to expand smoothly above U_{mf} without the formation of bubbles [46]. Stable bubbles limited in size are shown to exist [47] at gas velocities well beyond U_{mf}.
Powders of group C, even smaller and/or lighter than those of group A, clearly exhibit cohesive behavior based on the large ratio volume/mass. Rather than forming bubbles, gas flow through the particle bed occurs in channels. High gas velocities and/or vibration may be applied to overcome cohesion.
Group D particles, either of high density or considerably large in size, tend to spout when fluidized characterized by severe bed motion [48].

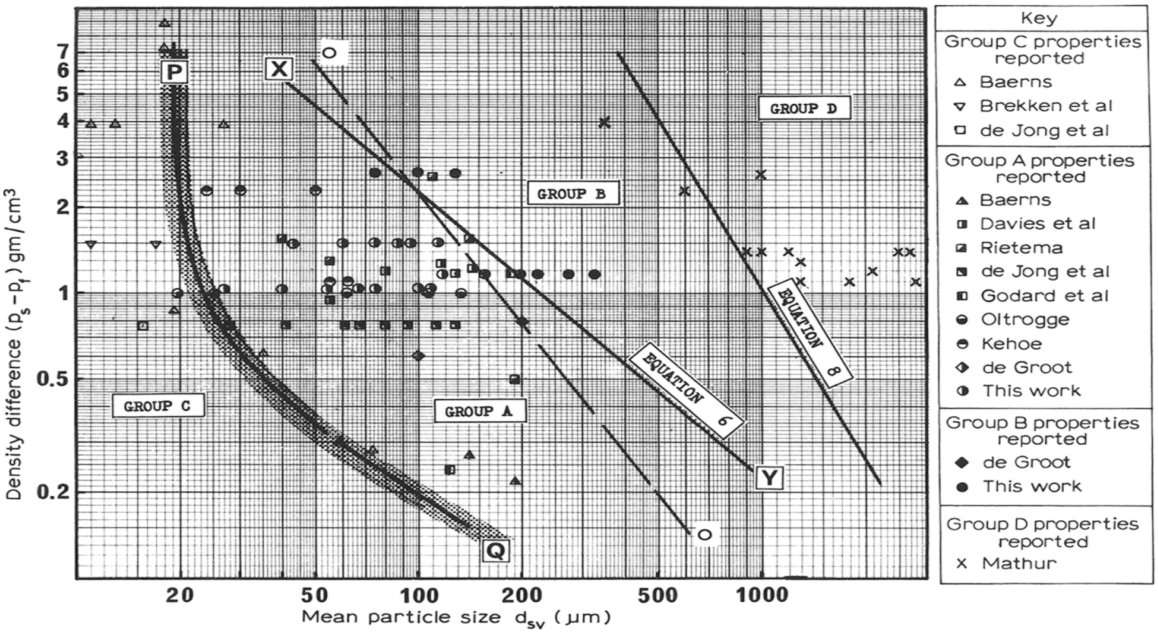

Figure 2.5: Powder classification diagram for fluidization with air at ambient conditions (ρ_s=ρ_p, ρ_f=ρ_g), taken from Geldart [45].

2.3.2 Flow regime mapping

In the following, a description of the occurring flow regimes during gas-solid fluidization is given. Supplementary, Figure 2.6 illustrates them graphically.
Respective regime mapping diagrams are shown in Figure 2.7, whereby the fluidized bed regimes are plotted as a function of the dimensionless particle diameter d_p^* (Equation 0.3) and the dimensionless gas velocity u^* (Equation 0.6). The presented data is based on experiments conducted by a number of researchers under various conditions (T_{fb}=293...573K, p=1·10^5...85·10^{5}Pa) [49].
An accumulation of loose solids featuring a certain PSD, particle density ρ_p and sphericity ϕ, residing on a porous plate. With the porous plate evenly distributing a flow of gas across the bed cross-section, the void fraction allows for throughflow of this bottom-up directed gas stream, whereby $\rho_g \ll \rho_p$ applies. An increase in gas flow inherently causes the drag force on the individual particle to increase simultaneously. This is characterized by a surge in the pressure drop across the particle bed (Figure 2.4, f.i. section AC). Thereby, the drag force

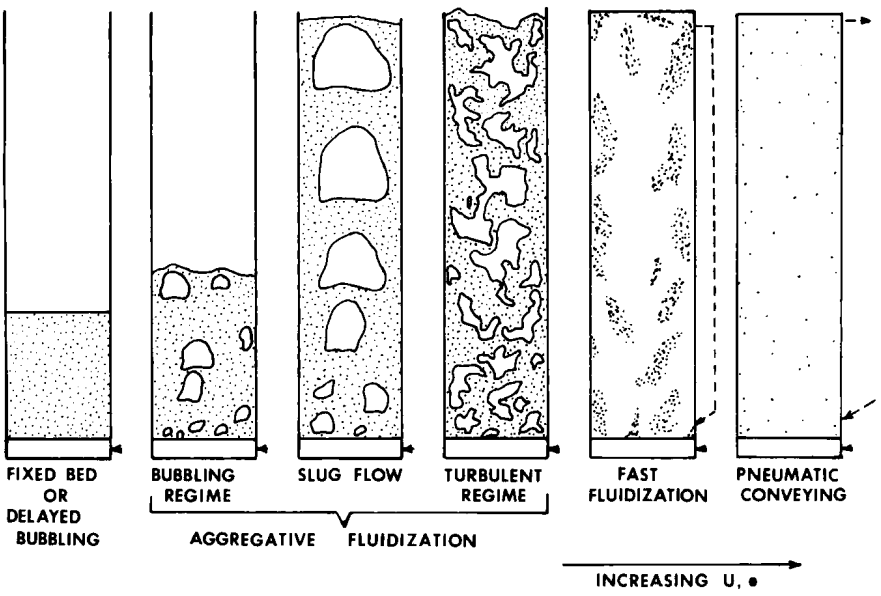

Figure 2.6: Flow regimes, taken from Grace [50].

is smaller than the effective weight of the particle bed — the *fixed bed.*
In case the gas velocity is high enough, i.e. the minimum fluidization gas velocity U_{mf} is reached, particle movement sets in and the bed of solids begins to expand by increasing its void fraction. The pressure drop across the particle bed, that is, the drag force by the upward moving gas equals the area-specific weight of the solids remains constant over a wide range of gas velocities (Figure 2.4, f.i. section DG). Because of the fluid-like behavior the particle bed is said to be in a fluidized state — the *fluidized bed.*
Whereas liquid-solid fluidization is mostly described as being homogeneous, the phenomenon is also observed during gas-solid fluidization. It is stated that homogeneous fluidization mainly depends on the suitable combination of gas velocity and particle size [51]. However, the range of gas velocity where homogeneous fluidization occurs is narrow.
Powders belonging to the Geldart groups A and B (to be defined in Section 2.3.1) fluidized above minimum fluidization cause the gas to form bubbles, referred to as heterogeneous, aggregative, or — *bubbling fluidized bed.* The movement of gas bubbles significantly affects solids mixing, entrainment as well as heat and mass transfer [52]. The gas velocity at which bubbles are first observed is referred to as minimum bubbling velocity U_{mb}.
In BFBs, bubbles coalesce and grow while rising. If the bed is small enough in its cross-section combined with being deep enough, the bubbles may eventually spread across the vessel — *slugging* occurs. Thereby, the portion of the bed above the bubble is pushed upward, as by a piston [49].
Further increasing the superficial gas velocity causes the upper surface of the bed to disappear and solids entrainment is observed alongside the turbulent motion of solids clusters and voids of gas. A distinct decrease in pressure fluctuations characterizes the onset of the *turbulent regime.*
Subsequently, solids strands are formed and the density of particles in the freeboard rises. With the increase of the gas velocity, and under the assumption that any entrained particles are recycled to the fluidized bed, the pressure drop further increases (Figure 2.4, section GH) — *fast fluidization.* Further increasing the gas velocity then leads to *pneumatic conveying.*

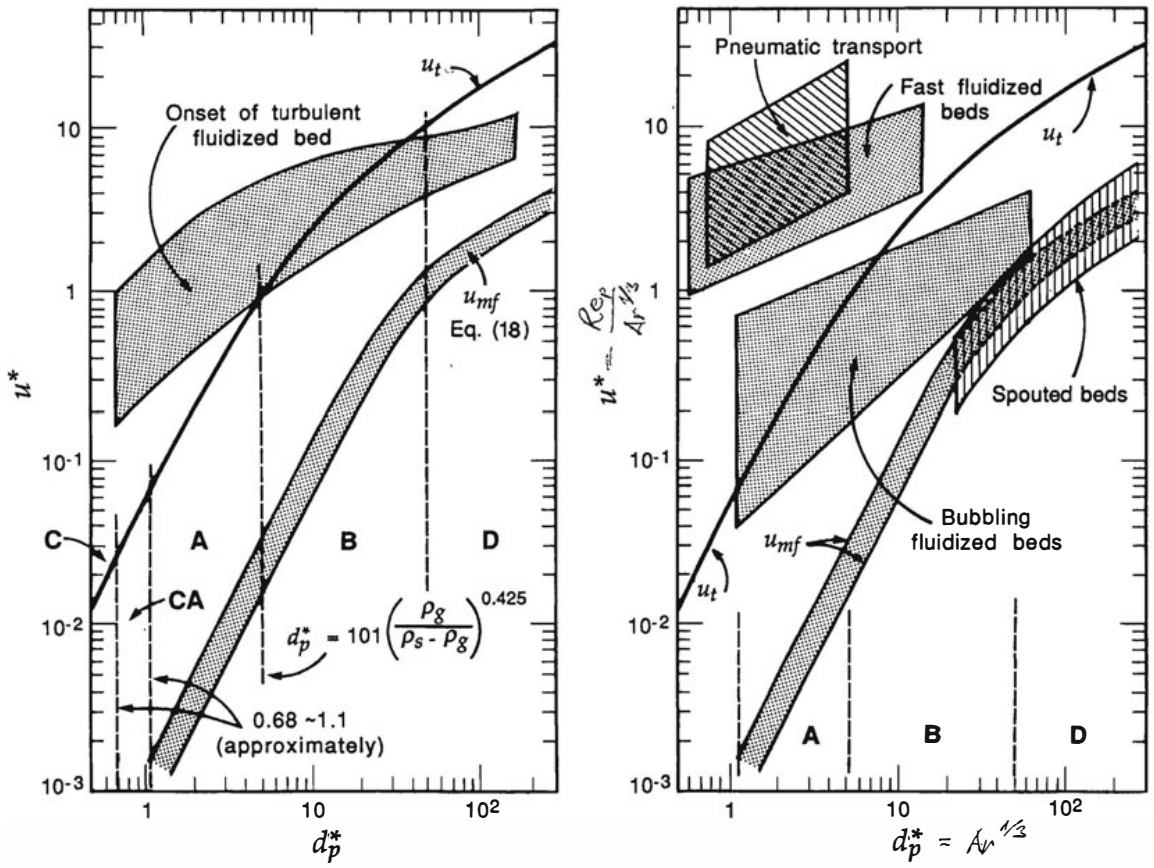

Figure 2.7: Flow regime mapping diagrams, taken from Kunii and Levenspiel [49], originally adapted from Grace [50], including information from Čatipović et al. [53], van Deemter [54] and Horio et al. [55]; the letters A to D referring to the Geldart classification of solids [45].

2.4 Wall-to-bed heat transfer

In this sense, the fluidized bed resembles a liquid with relatively high heat capacity and of a uniquely low vapor pressure transferring heat to and from in-bed HEXs [56]. Thereby, the wall-to-bed heat transfer is affected by the solids migration at the immersed HEX. Generally spoken, therein the reason for heat transfer to increase with an increase in particle motion lies. Thus, relatively low heat transfer coefficients are observed in the fixed bed regime ($U<U_{mf}$) or, depending on the velocity of the gaseous phase, in the absence of particles ($U>U_{se}$). By way of example, the circumstance is illustrated in Figure 2.8.
Considering the fluidization regime, the wall-to-bed heat transfer in the fixed bed is governed by gas-convection. With the formation of the fluidized bed, particle convection causes heat transfer to increase to a greater or lesser extent, identified as a distinct increase in heat transfer exceeding U_{mf} [57, 40]. Increasing the gas velocity causes heat transfer to decrease to a lesser or greater extent. Exceeding the solids entrainment gas velocity U_{se}, when all particles are entrained, the overall wall-to-bed heat transfer again equals the appearing gas-convective heat transfer. For Geldart group B particles, the described behaviour is shown in Figure 2.8.
Besides heat transfer being influenced by the fluidization regime, it equally is a function of the fluidized bed temperature and the particle size. Therefore, a heat transfer mode map was proposed by Flamant et al. [58] and enhanced by Fan and Zhu [52], shown in Figure 2.9. Accordingly, the overall wall-to-bed heat transfer coefficient consists of the three cumulative mechanisms gas convection, particle convection and radiation, illustrated by the

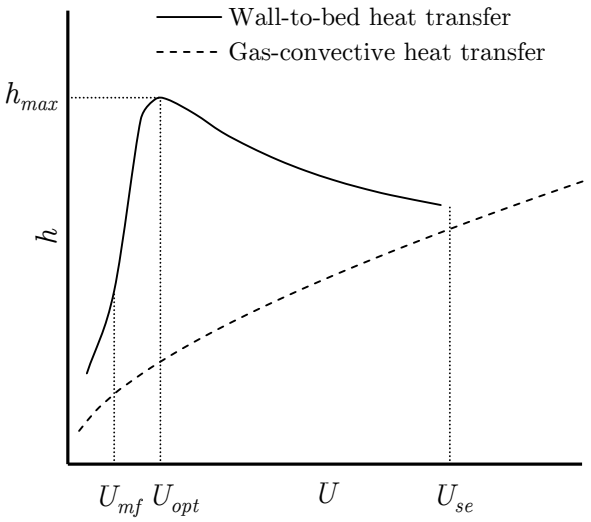

Figure 2.8: Typical behavior of the wall-to-bed heat transfer as a function of the gas velocity in bubbling fluidized beds of Geldart group B particles vs. the gas-convective heat transfer.

given Equation 2.12. Because of the moderate temperatures of the proposed TSA process, both during adsorption and desorption, the effect of radiation is neglected in view of the considerations made in this thesis.

$$h = h_{gc} + h_{pc} + h_r \tag{2.12}$$

Maximum wall-to-bed heat transfer coefficients as a function of the particle size are shown in Figure 2.10 [59]. Low heat transfer coefficients are observed for powders classified as Geldart group C, caused by inter-particulate forces hindering the efficient mixing of solids. Fluidized group A powders lead to the highest wall-to-bed heat transfer coefficients, followed by group B powders. Particle convection dominates heat transfer for both types of solids. Simultaneously, with an increase in particle size the gas-convective heat transfer increases.

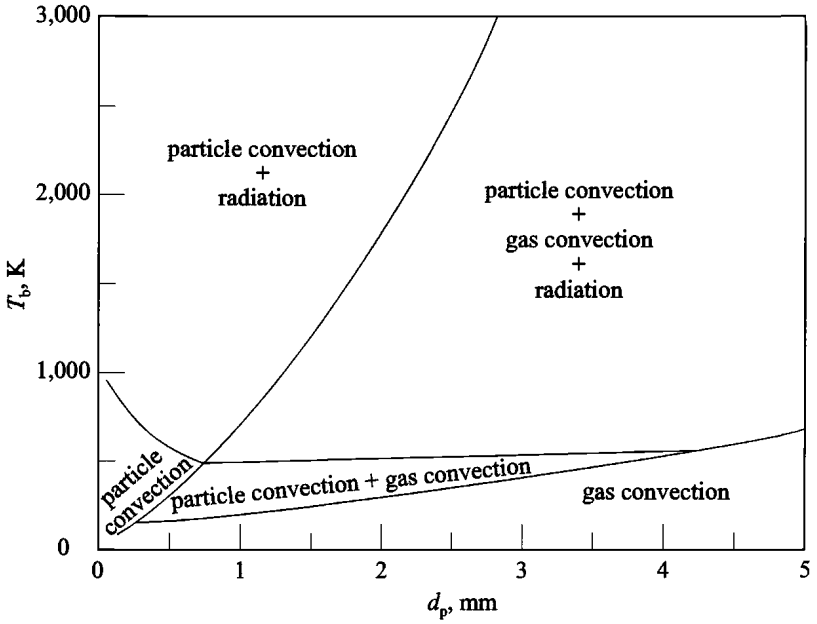

Figure 2.9: Heat transfer mode diagram (T_b=T_{fb}), taken from Fan and Zhu [52].

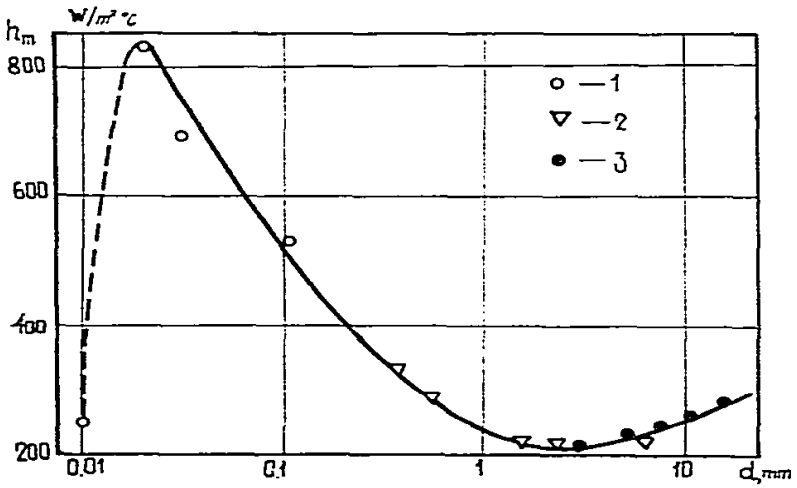

Figure 2.10: Maximum wall-to-bed heat transfer coefficient as a function of the particle size (d=d_p, h_m=h_{max}), taken from Baskakov et al. [59].

The progression of heat transfer as a function of the superficial gas velocity strongly depend on the particle size, as depicted in Figure 2.11 [60]. Whereas wall-to-bed heat transfer coefficients are observed to be higher for fine-grained powders, the maximum in heat transfer is reached at rather high excess gas velocities $U-U_{mf}$ or fluidization numbers U/U_{mf}, i.e. at the onset of the circulating fluidized bed regime. Coarse-grained particles of $d_p \geq 2$mm reveal a somewhat similar behaviour, reaching a maximum in heat transfer at higher fluidization numbers U/U_{mf}, but with significantly lower wall-to-bed heat transfer coefficients. Compared to fine-grained particles, it was found that the steep increase in heat transfer is observed at a much smaller range of excess gas velocity [40]. For particles ranging in size from $\approx 150 \ldots 2 \cdot 10^3$µm a slightly different behavior is reported. Maximum heat transfer occurs at rather low excess gas velocities, followed by a more or less pronounced decrease. The described behavior is illustrated in Figure 2.11.
A considerable number of authors thoroughly investigated the phenomenon of wall-to-bed heat transfer considering the following parameters:

1. Particle properties, i.e. size d_p, sphericity ϕ, density ρ_p, heat capacity $c_{p,p}$ and heat conductivity λ_p [61, 62, 63, 64, 65, 66, 67, 68, 69, 70, 71, 72, 73, 58, 74, 75, 76, 77, 78, 79, 2].

2. Gas properties, i.e. density ρ_g, heat capacity $c_{p,g}$, heat conductivity λ_g and viscosity μ_g [63, 80, 81, 74, 82, 83, 75, 84, 85, 86, 87].

3. The tube diameter d_t [88, 60, 89, 73, 90].

4. The tube orientation, i.e. horizontal or vertical [64, 91, 89, 48, 92, 93, 94, 95, 96, 97, 98].

5. The tube bundle geometry, i.e. horizontal/vertical tube spacing s_h/s_v and the arrangement, e.g. in-line, staggered or cross-over [99, 60, 100, 89, 76, 101, 2].

6. The surface character, e.g. threaded, finned, etc. [64, 60, 65, 102, 103, 104, 105, 106, 107].

7. The tube circumferential angle [99, 108, 109, 110, 111, 112, 113, 114],

8. the gas distributor design [115, 116, 117].

9. Fluidized bed hydrodynamics [115, 118, 119, 120, 121, 122, 123, 124, 125, 126, 127, 128, 129, 130, 131, 132, 3].

Literature reviews with regards to the wall-to-bed heat transfer including comprehensive reference listings condensing the basic characteristics of the numerously conducted experiments are available, e.g. by Gutfinger and Abuaf [133], Saxena et al. [134] as well as Molerus and Wirth [40]. Since the main focus of this thesis is based on establishing a proper design of in-bed HEXs optimized for the efficient removal respectively introduction of heat from and to the TSA reactors, this work emphasizes on the achievable overall heat transfer coefficients with specific attention to the Items 1, 3, 5 and 9 listed on page 15.

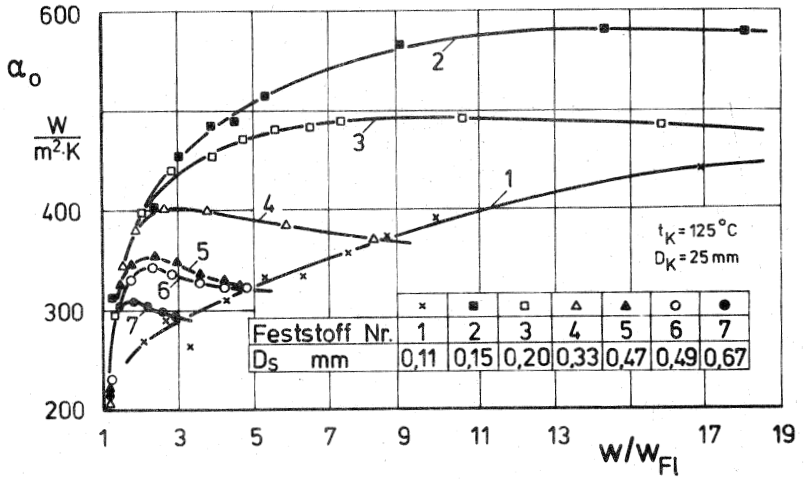

Figure 2.11: Wall-to-bed heat transfer coefficient as a function of the fluidization number (w/w_{Fl}=U/U_{mf}, α_0=h, D_S=d_p, D_K=d_t and t_K=T_{fb}), taken from Natusch et al. [60].

2.4.1 Modeling single tube heat transfer coefficients

Although (in-bed) HEXs often are designed with tubes arranged in an array (tube bundle), by far the larger number of the available publications deal with wall-to-bed heat transfer of an individual tube immersed in fluidized beds.

Maximum heat transfer

Quite a number of the mathematical models developed for the estimation of wall-to-bed heat transfer coefficients are designed to predict maximum values h_{max} [135, 63, 136, 60] (also refer to Equation 2.16). In addition, some authors provide correlations to calculate the optimal superficial gas velocity U_{opt} at which h_{max} exists. Martin [137] recommends a fairly simple term for the rough estimation of U_{opt} in view of practical purposes, given by Equation 2.13.

$$U_{opt} \approx 7.5 \cdot \sqrt{g \cdot d_p} \tag{2.13}$$

Conveniently, it is desired to design the TSA process flexible in view of the dynamic sorbent loading, i.e. the adsorber and desorber will be operated under varying solids exchange rate and gas velocity. In any case, it has to be ensured that the occurring heat load is transported efficiently to and from the reactor's HEXs. From this point of view it seems even more important to investigate heat transfer as a function of the fluidization number and the following considerations might be of special interest.

Heat transfer as a function of the gas velocity

The model developed by Natusch et al. [60] is given by Equation 2.14, with the constants c_i being a function of the particle size as indicated by the data given in Table 2.1. The

experiments were conducted with glass beads and air as fluidization gas. Based on their findings, the overall heat transfer coefficient for plain tubes and the considered powders with mean bead sizes in the range of 110...670µm is represented with good accuracy by the proposed formula and deviations between calculation and measurement were smaller than 3%.

$$h = c_1 \cdot Ar^{c_2} \cdot \left(\frac{U}{U_{mf}} - 1\right)^{c_3} \cdot \left[c_4 + \exp\left(-c_5 \cdot \left(\frac{U}{U_{mf}} - 1\right)\right)\right] \cdot \frac{\lambda_g}{d_p} \tag{2.14}$$

Table 2.1: Coefficients c_i for the calculation of the wall-to-bed heat transfer coefficient according to Equation 2.14, proposed by Natusch et al. [60].

d_p [µm]	c_1 [1]	c_2 [1]	c_3 [1]	c_4 [1]	c_5 [1]
110	0.2045	0.1034	0.2878	2.038	0.8828
150	0.4027	0.1354	0.2693	1.527	0.1005
200	0.5226	0.1561	0.2580	1.037	0.1995
330	0.7366	0.2110	0.3564	0.445	0.3186
470	0.8158	0.2209	0.3629	0.5038	0.6656
490	0.8236	0.2241	0.3848	0.4803	0.6848
670	0.8236	0.2768	0.5669	0.2693	1.175

The model proposed by Martin [137, 138] is given by Equation 2.15. Therein, the first term merely represents heat transfer due to particle convection (h_{pc}). The maximum heat transfer coefficient is calculated according to Schlünder [139] (Equation 2.16). The second term adds the gas-convective component (h_{gc}) and was originally proposed by Baskakov [59]. Heat transfer coefficients calculated with the model by Martin were compared within wide ranges of all the relevant parameters with experimental data from different sources [138]. However, the equations are not able to predict heat transfer coefficients for fine powders of mean bead sizes <40µm, since there is a clear tendency to underestimate heat transfer for such materials.

$$\begin{aligned} h =& \frac{\lambda_g}{d_p} \cdot (1-\epsilon) \cdot \frac{1}{6} \cdot \frac{\rho_p \cdot c_{p,p}}{\lambda_g} \cdot \sqrt{\frac{g \cdot d_p \cdot (\epsilon - \epsilon_{mf})}{5 \cdot (1-\epsilon_{mf}) \cdot (1-\epsilon)}} \\ & \cdot \left[1 - \exp\left(-\frac{h_{max} \cdot d_p}{c \cdot \lambda_g \cdot \sqrt{\frac{g \cdot d_p \cdot (\epsilon - \epsilon_{mf})}{5 \cdot (1-\epsilon_{mf}) \cdot (1-\epsilon)}}}\right)\right] + 0.009 \cdot \frac{\lambda_g}{d_p} \cdot \sqrt[3]{Pr} \cdot \sqrt{Ar} \end{aligned} \tag{2.15}$$

Martin [138] noted that c in Equation 2.15 was determined experimentally resulting in the numerical value of 2.6. The quantity is a measure for the contacting time between particles and the in-bed HEX.

$$h_{max} = \frac{\lambda_g}{d_p} \cdot 4 \left[\left(1 + \frac{4 \cdot \Lambda \left(\frac{2}{\gamma} - 1\right)}{d_p}\right) \cdot ln\left(1 + \frac{d_p}{4 \cdot \Lambda \left(\frac{2}{\gamma} - 1\right)}\right) - 1\right] \tag{2.16}$$

$$\Lambda = \sqrt{\frac{2 \cdot \pi \cdot \Re \cdot T}{\mathrm{M}}} \cdot \frac{\lambda_g}{p \cdot (2 \cdot c_{p,g} - \Re \cdot \mathrm{M})} \tag{2.17}$$

For air under ambient conditions (ϑ=25°C) the accommodation coefficient γ=0.9 applies representing the measure of imperfection of the energy exchange between the HEX and the gas molecules [138].
The model developed by Molerus et al. [121, 75] is given by Equation 2.18, whereby the laminar flow length l_l is calculated according to Equation 2.19. The model is valid for particle sizes in the range of $74 \ldots 4{\cdot}10^3$µm and densities of $26 \ldots 11.8{\cdot}10^3 \mathrm{kg\,m^{-3}}$. The excess gas velocity $U{-}U_{mf}$ may get up to $2.5 \mathrm{m\,s^{-1}}$. It is stated that radiation does not contribute to the total wall-to-bed heat transfer up to a fluidized bed temperature of 1,050K [75].

$$h \cdot \frac{l_l}{\lambda_g} = \frac{0.125 \cdot (1-\epsilon_{mf}) \cdot \left(1 + 33.3 \cdot \left(\sqrt[3]{\frac{U-U_{mf}}{U_{mf}}} \cdot \sqrt[3]{\frac{\rho_p \cdot c_{p,p}}{\lambda_g \cdot g}} \cdot (U-U_{mf})\right)^{-1}\right)^{-1}}{1 + \left(\frac{\lambda_g}{2 \cdot c_{p,p} \cdot \mu_g}\right) 0.28 \cdot (1-\epsilon_{mf})^2 \cdot \sqrt{\frac{\rho_g}{\rho_p - \rho_g}} \cdot \left(\sqrt[3]{\frac{\rho_p \cdot c_{p,p}}{\lambda_g \cdot g}} \cdot (U-U_{mf})\right)^2 \cdot \frac{U_{mf}}{U-U_{mf}}}$$
$$+0.165 \cdot \sqrt[3]{Pr} \cdot \sqrt[3]{\frac{\rho_g}{\rho_p - \rho_g}} \cdot \left(1 + 0.05 \cdot \frac{U_{mf}}{U-U_{mf}}\right)^{-1} \tag{2.18}$$

$$l_l = \left(\frac{\mu_g}{\sqrt{g} \cdot (\rho_p - \rho_g)}\right)^{2/3} \tag{2.19}$$

Influence of the tube diameter

The effect of the tube diameter on the wall-to-bed heat transfer was observed by a number of authors (refer to the list given on page 15, Item 3). It is stated that the so-called shielding effect increases with the increase of the tube diameter causing a reduction in heat transfer. Thereby, the shielding effect influences the optimum particle concentration and movement [60]. Petrie et al. [88] proposed a mathematical model merely dependent on the tube diameter d_t to be implemented by multiplication of the corrective factor f_{dt} to a respective model available for the estimation of single tube heat transfer coefficients. The correlation is given by Equation 2.20.

$$f_{dt} = \left(\frac{d_t}{33.7 \cdot 10^{-3}\mathrm{m}}\right)^{-1/3} \tag{2.20}$$

2.4.2 Modeling tube bundle heat transfer coefficients

The wall-to-bed heat transfer at immersed tube bundles is equal or lower than for an immersed single tube. The reason is the arrangement of tubes hindering particle mixing, i.e. the smaller the spacing the larger the hindrance.

Influence of the tube alignment

With respect to the findings documented in the literature, arrays of vertical tubes may prevent bubble coalescence [98]. In view of the proposed TSA system this behavior is identified desirable, since the splitting of bubbles may enhance mass transfer resulting in an increased adsorption and regeneration efficiency. However, it seems likely that vertical tubes get encased by the rising bubbles hindering heat transfer most notably in the upper areas of the fluidized bed where bubbles may still reach significant sizes. Concurrently, bubbles encasing the HEX tubes may promote gas slipping.
Similar to vertical tube arrays it is reported that arrays of horizontal tubes promote bubble breaking and limit bubble size as well as the bubble rise velocity [134, 140, 141, 49], possibly improving mass transfer. However, it is stated that, due to bubble separation caused by the tube bundle, smaller bubbles may lead to a decrease in heat transfer [142].
Although it seems that the larger number of experiments was performed with single vertical

tubes, it is stated that the heat transfer coefficients show no significant differences [40]. In the end, the manufacturability may decide whether to choose vertical or horizontal tubes.

Influence of the tube bundle geometry

The main dimensions of a respective tube bundle are illustrated in Figure 2.12. For the formulation of equations, the normalized tube pitch is often used, which is referred to as tube spacing. It is defined by the quotient of the tube pitch and tube diameter (e.g. s_h=p_h/d_t).

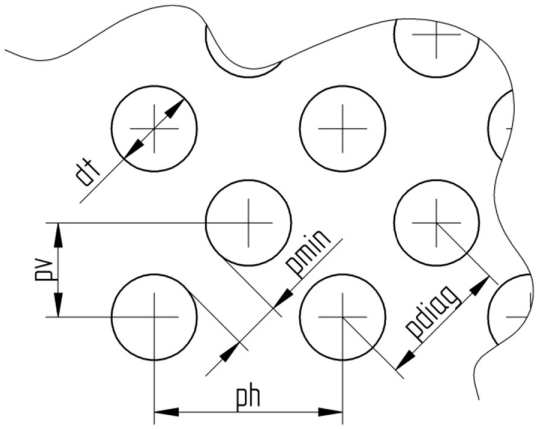

Figure 2.12: Main dimensions of a tube bundle.

Correction factors may be applied to account for the particle hindrance effect of an immersed tube bundle. In the following, two so-called tube bundle reduction factors are presented. Thereby, f_{tb} can be applied by multiplication to a respective single tube model.
The model developed by Natusch et al. [60] is given by Equation 2.21. It merely is a function of the horizontal tube spacing s_h and applicable to plain tubes only. Natusch et al. also note that the vertical tube pitch must not be smaller than $10 \ldots 20 \cdot d_p$. Gel'perin et al. [136] and Moawed et al. [101] reported that the neglection of the vertical tube spacing seems justified, because it was found that the change in either the arrangement (in-line or staggered) or in the vertical spacing hardly affects the wall-to-bed heat transfer.

$$f_{tb} = \left(1 - \frac{1}{s_h}\right)^{0.25} \tag{2.21}$$

Quite recently, Lechner et al. [143] proposed a more comprehensive corrective factor for tube bundles. The formula is given by Equation 2.22. The model is valid for Geldart group A particles only and limited to the application with the single tube model by Molerus et al. [75] (refer to Equation 2.18).

$$\begin{aligned} f_{tb} = &\left(\frac{d_t}{80 \cdot 10^{-3}\mathrm{m}}\right)^{-0.3} \cdot \left(1 - \frac{1}{s_h}\right)^{0.36} \\ &\cdot \left(1 - \frac{1}{s_{diag}}\right)^{0.24} \cdot \left(1 - \frac{d_p}{p_{min}}\right)^{4} \cdot \left(\frac{d_t}{22 \cdot 10^{-3}\mathrm{m}}\right)^{0.09} \end{aligned} \tag{2.22}$$

2.5 Solids residence time distribution

The tracer method was selected to study the solids residence time distribution (RTD) and particle mixing in BFBs. The first objective was to understand the BFB mixing behavior in view of stagnant zones (dead spaces) and channeling (bypassing or short-cuircuiting). The

second objective is to determine a suitable model able to represent the BFB flow characteristics for further analysis of the occurring flow behavior by means of characteristic quantities.

2.5.1 Tracer experiment

During the tracer experiment a nonreactive (inert) tracer is pulsed creating the input signal at the particle feed transporting solids to the BFB (t=0). Subsequently, the output signal obtained at the particle drain reveals information about the BFB reactor characteristics. Typical input and output signals are illustrated in Figure 2.13.

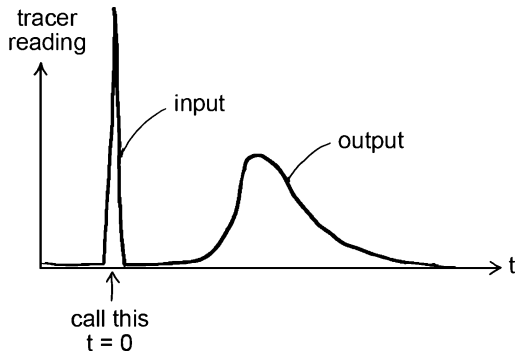

Figure 2.13: Typical output signal resulting from a pulse input, taken from Levenspiel [144].

Input signal

For an ideal input signal, i.e. a Dirac delta function (δ-function), the modeling of the output signal is rather simple omitting the deconvolution process [7]. Therefore, it is desired to create sharp input pulses of a time span negligible compared to the duration of the output signal.

Output signal

As previously mentioned, the input signal (C_{pulse}) obtained at the solids feed and the output signal ($C_{response}$) obtained at the solids drain are recorded in the course of the tracer experiment. The RTD, often referred to as exit age distribution function or E-curve, is derived from these data with the formula given by Equation 2.23. Integrating the E-curve by definition equals one, which is why the described process often is referred to the term normalization. Respecting the closed vessel boundary condition, the tracer enters and leaves the reaction zone, i.e. the BFB one time only.

$$E = \frac{C_{response}}{\int_0^\infty C_{response}\, dt} \tag{2.23}$$

Mean residence time

Considering the output signal represented by the exit age distribution function, the average time span of a particle residing in the reaction zone is given by Equation 2.24, referred to as mean residence time.

$$\tau = \int_0^\infty t \cdot E\, dt \tag{2.24}$$

Cumulative exit age distribution

The cumulative exit age distribution function is defined with the formula given by Equation 2.25, whereby F equals one for $t \to \infty$. F is a measure for the fraction of the particles in the exit stream which are younger than the age t.

$$F = \int_0^t E \, dt \tag{2.25}$$

Hydraulic residence time

In terms of a BFB resembling the mixing characteristics of a continuous stirred tank reactor (CSTR), the mean residence time of the solids continuously conveyed through the BFB equals the hydraulic residence time, given by Equation 2.26. The correlation is helpful to perform material balance checks, i.e. to compare τ_{hyd} to mean residence time resulting from an experiment or model, respectively.

$$\tau_{hyd} = \frac{m_s}{\dot{m}_s} \tag{2.26}$$

2.5.2 Modeling reactor characteristics

Ideal reactors

The obtained E-curves can be fitted with mathematical models for further evaluation. These models are referred to the term compartment model leading to certain characteristic quantities depending on the used mathematical model. Different models are available for different types of flow characteristics, e.g. ideal models for mixed flow (CSTR, Equation 2.27) and plug flow (plug flow reactor (PFR), Equation 2.28). Both models are a function of the characteristic mean residence time τ_{CSTR} or τ_{PFR}, respectively.
As for the CSTR, the added fluid is assumed to be distributed immediately and evenly throughout the reacting mixture resulting in the exponential decay of the exit age distribution function.
As for the PFR, all the particles leaving the reactor spent exactly the same amount of time in the reaction zone. Thus, the mathematical model is represented by the time delay τ_{PFR}.

$$E_{CSTR} = \frac{1}{\tau_{CSTR}} \cdot \exp\left[\frac{-t}{\tau_{CSTR}}\right] \tag{2.27}$$

$$E_{PFR} = \delta\left(t - \tau_{PFR}\right) \tag{2.28}$$

Non-ideal reactors

Non-ideal reactors, i.e. real vessels, may differ to a greater or lesser extent from the above-mentioned ideal systems. Modeling these can be accomplished by applying the tanks-in-series (TIS) model, the dispersion model or the convection model. In particular, the convection model is used to fit residence time distribution functions obtained from experiments with laminar flow reactors and thus not applicable for modeling BFB reactors. The TIS model specifically may be applicable for modeling multistage BFB reactor systems and is given by Equation 2.29, wherein n_{stage} equals the reactor's stage number and τ_i is the mean residence time of a single stage, that is $\tau_i = \tau / n_{stage}$.

$$E_{TIS} = \frac{t^{n_{stage}-1}}{(n_{stage}-1)! \cdot {\tau_i}^{n_{stage}}} \cdot e^{\frac{-t}{\tau_i}} \tag{2.29}$$

In an analogous manner to Fick's law, the dispersion model is given by Equation 2.30. Therein, $\mathbf{D}$ is the axial dispersion (AD) coefficient representing the degree of particle back-mixing.

$$\frac{\partial C}{\partial t} = \mathbf{D} \cdot \frac{\partial^2 C}{\partial x^2} \tag{2.30}$$

In case an ideal pulse of tracer material is imposed onto a continuous flow of solids, dispersion causes the pulse to widen, i.e. the tracer experiences a certain spreading into the surrounding solids while moving through the reaction zone. The behavior is illustrated by Figure 2.14. For small extents of dispersion the solution of Equation 2.30 is given by Equation 2.31.

$$E_{PFR,AD} = \sqrt{\frac{u^3}{4 \cdot \pi \cdot \mathbf{D} \cdot L}} \cdot \exp\left[-\frac{L - u \cdot t}{4 \cdot \mathbf{D} \cdot L/u}\right] \tag{2.31}$$

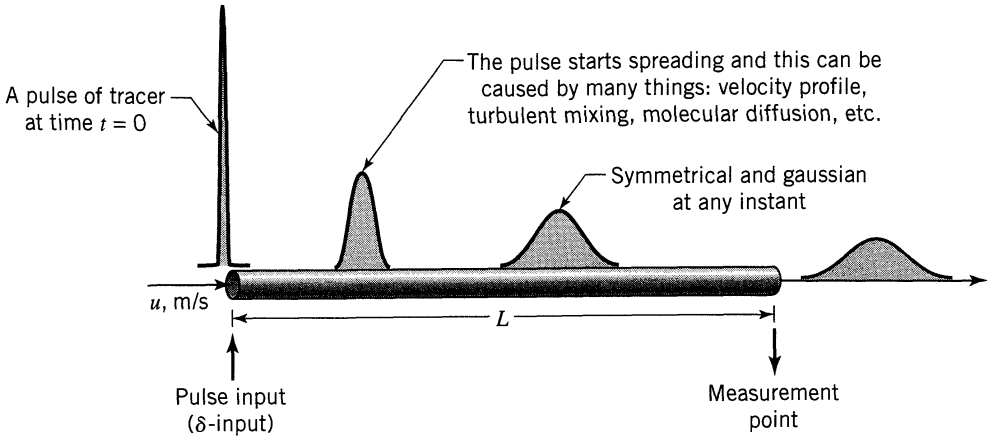

Figure 2.14: Tracer spreading due to dispersion, taken from Levenspiel [7].

Chapter 3

Materials and methods

3.1 Cold flow model

Cold flow models CFMs are often used to make fluidized bed phenomena observable in practical scale by overcoming the necessity to heat/cool and/or pressurize/depressurize. Depending on the setup, certain laws may have to be considered when scaling fluidized beds [145]. Because of the fact that heat transfer is reported to increase (slightly) with an increase in the fluidized bed temperature [60] and because of the moderate process parameters of the proposed TSA system, it was decided to operate the CFM at ambient conditions leading to a conservative design of the in-bed heat exchangers.
The experimental work carried out in respect of Papers [1] to [4] was performed with the CFM presented in the following sections. In the course of the test campaigns the CFM was adapted to improve the measurement technique and to enhance its features. Additionally, the CFM was upgraded to enable for the measurements in view of the particle residence time distribution when superimposing a solids cross-flow to the bubbling bed. The stages of enhancement are referred to as Stage I, Stage II and Stage III.

3.1.1 Stage I

Fluidizing solids

The CFM was mostly made of acrylic glass allowing for the visual observation of the fluidization behavior. The CFM was designed specifically for the determination of wall-to-bed heat transfer coefficients in view of the TSA process. Thus, its dimensions were opted big enough to hold a representative amount of tubes immersed in the fluidized bed, i.e. to simulate the fluidized bed stages of the adsorber or desorber, respectively. The cross-sectional dimension of the fluidized bed was 400mm in length and 200mm in width. The overall bed height could get up to 400mm. A differential pressure sensor (Kalinsky, DS2-420, 100mbar range) was used to determine the pressure drop across the entire bed height. Additionally, the pressure drop across a specified height was recorded (Kalinsky, DS2-420, 100mbar range), i.e. 67mm at a distance of 50mm measured from the gas distributor. This allowed for the calculation of the bed voidage. The freeboard was equipped with an exhaust gas filter preventing the release of fines. The CFM in Stage I configuration is shown in Figure 3.1.

Operating the cold flow model

A process control system was installed to operate the CFM and to accomplish all arising control tasks via a programmable logic controller (PLC). A touchscreen interface was installed to set the desired operational parameters. Sensor data were recorded to a thumb drive

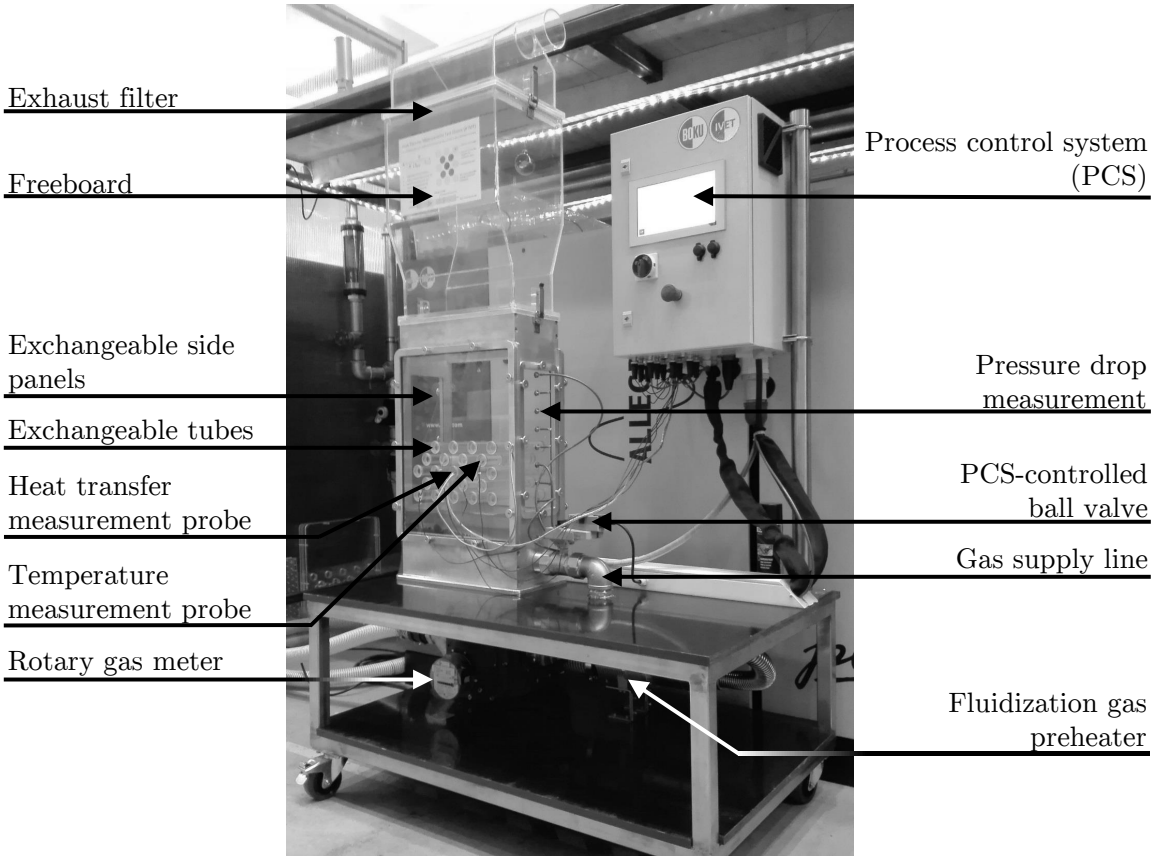

Figure 3.1: Cold flow model in Stage I configuration.

for subsequent data analysis. Thereby, the recording interval was one second. A detailed description of the used sensors and their accuracy will be given the following subsections.

Supplying gas

Compressed air was used for fluidization. The gas was provided by a screw-type compressor and dried right after compression. The pressure of the gas supply line was limited to ≈700mbar gauge prior introduction to the CFM. A rotary gas meter (Elster Instromet, RABO G250) was used to measure the actual gas volume flow. The gas meter allowed for tapping the gas temperature and pressure. The gas temperature was measured redundantly by two resistance thermometers (Pt100, 1/3DIN standard). The pressure was measured by a differential pressure sensor (Kalinsky, DS2-420, 1000mbar range). The measurement accuracy of these devices is given in Table 3.1. Furthermore, it was possible to preheat the gas in a controlled manner by an installed air heater (Herz, XL92). A ball valve was used to manipulate the fluidization gas flow, which was controlled by the PLC via the feedback signal obtained from the rotary gas meter.

Distributing gas

Two types of gas distributors were used during the experimental campaigns. Both gas distributors were designed to provide sufficient pressure drop ensuring homogeneous gas distribution.
Gas distributor *A* was utilized for measurements at lower gas velocities (Papers [3] and [4]). It featured 74 individual G1/2" sintered metal filters incorporated in an aluminum plate of 6mm in thickness. The maximum gas flow rate was limited to $80\mathrm{Nm}^3\,\mathrm{h}^{-1}$ due to the

relatively high pressure drop originated by the gas distributor. The permeable metal filters hindered solids from draining into the windbox when the gas supply was switched off.
Gas distributor B was used to measure heat transfer at larger gas volume flows, which could go up to $300\mathrm{Nm}^3\,\mathrm{h}^{-1}$ (Papers [1] and [2]). The aluminum plate of 6mm in thickness featured 155 holes of 3mm in diameter evenly distributed across the cross section.

Sensing heat transfer

Tubular sensing probes were used to measure wall-to-bed heat transfer coefficients in the course of the experiments conducted with regard to Papers [1] to [3]. Two main types of probes existed — the *heat transfer measurement probe* and the *temperature measurement probe*.
A typical heat transfer measurement probe is shown in Figure 3.2a. It consisted of a heatable copper cylinder 100mm in length placed in between acrylic glass tips isolating the heated component in axial direction. The length of both acrylic pieces was 50mm. The copper cylinder incorporated an electrical heating cartridge (200W, 6mm OD). The probe temperature T_{pr} was dermined with at least one resistance thermometer (Pt100, 1/3DIN standard, 3mm OD), also placed in the copperous part. Because of the specific design of the heat transfer measurement probe it was assumed that the entire heat introduced is transported to the contacting fluidized bed phase. The probe was heated to a temperature of 333K and kept constant throughout the entire measuring period by a proportional–integral–derivative (PID) controller algorithm.
Because of the high heat conductivity of copper it is assumed that the copper cylinder's intrinsic temperature gradient is negligibe. Because of the applied measurement principle the obtained heat transfer coefficients cumulate heat transfer due to gas and particle convection and do not distinguish between them. Because of the moderate temperatures the radiative heat transfer is assumed to be insignificant [58, 146].
A typical temperature measurement probe is shown in Figure 3.2b. The probe was made of a cylindrical piece of acrylic glass incorporating a single resistance thermometer (Pt100, 1/3DIN standard, 3mm OD). A circular recess allowed the resistance thermometer to be properly covered by the fluidized bed. Four temperature measurement probes were used to determine the fluidized bed temperature T_{fb} at different spots.

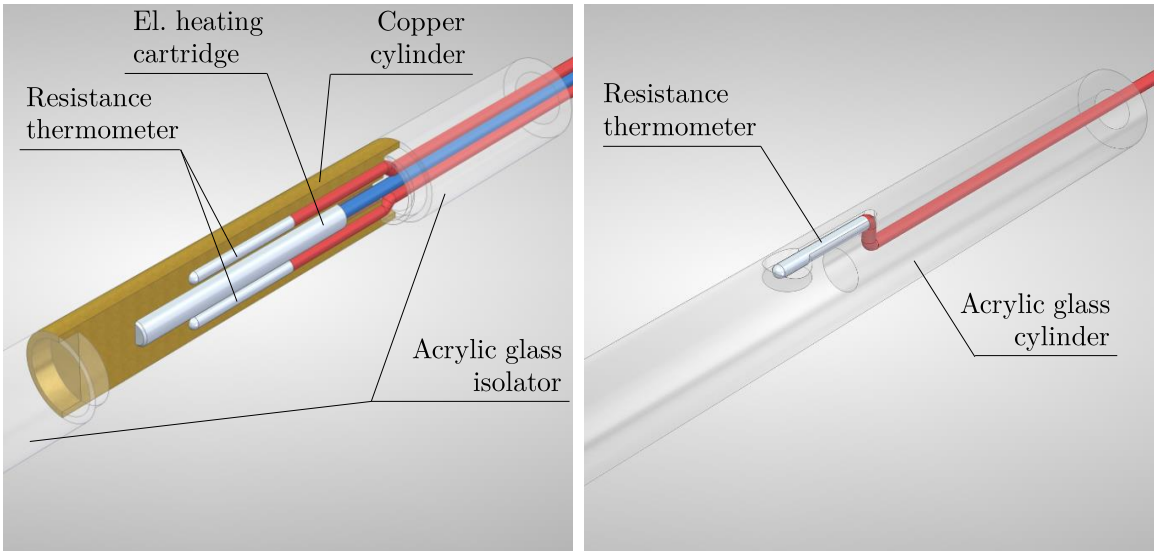

(a) Heat transfer measurement probe. (b) Temperature measurement probe.

Figure 3.2: Heat transfer sensing devices.

Calculating heat transfer coefficients

The data obtained from the heat transfer measurement probe, i.e. the electrical power consumption Q, the temperature of the heated copper cylinder T_{pr} as well as the average fluidized bed temperature T_{fb} measured by four temperature measurement probes were used to calculate the apparent wall-to-bed heat transfer coefficient h_i. The formula is given by the following Equation 3.1.

$$h_i = \frac{Q}{T_{pr} - T_{fb}} \tag{3.1}$$

Measurement accuracy

During the experiments two types of measurement errors occured — the *systematic error* and the *random error*.
Systematic measurement errors arise from the measurement accuracy of the respective measurement device, given in Table 3.1. The calculation of the overall systematic heat transfer measurement error Δh_s is given by Equation 3.2 (propagation of uncertainty). For typical CFM operating conditions, i.e. ambient fluidized bed temperature and T_{pr}=333K, the overall measurement accuracy Δh_s was lower than ±3% in terms of the calculated value h_i.

$$\Delta h_s = \left|\frac{\partial h_i}{\partial Q}\right| \cdot \Delta Q + \left|\frac{\partial h_i}{\partial T_{pr}}\right| \cdot \Delta T + \left|\frac{\partial h_i}{\partial T_{fb}}\right| \cdot \Delta T \tag{3.2}$$

The operation of the CFM was standardized in view of the variation of the fluidization gas flow assuring reproducibility of the results. Starting at low gas velocities, the gas flow was increased incrementally to a specified maximum. Every setting of gas flow was kept constant for 120s. After reaching the maximum gas flow, the process control system was programmed to decrease the gas flow by the same increments as it was increased. Hence, the fluidized bed heat transfer was measured twice for each setting of gas volume flow, gas velocity or fluidization number, respectively. Subsequently, the arithmetic mean wall-to-bed heat transfer coefficient h and the correlating standard deviation were calculated for each setting of gas velocity according to Equation 3.3. The standard deviation may be referred to as random measurement error Δh_r, originating in the alternating contact of the measurement probes with the different phases of the BFB, i.e. solids and gas phase. A detailed graphical illustration of the applied evaluation procedure is given in Paper [2], Figure 5.

$$h = \frac{1}{t}\sum h_i \pm \Delta h_r \tag{3.3}$$

Table 3.1: Technical specifications of the used measurement devices.

Device	Measurement accuracy
Electric power consumption of the heat transfer measurement probe	$\Delta Q = \pm 0.1\text{W}$
Resistance thermometers (Pt100, 1/3DIN standard)	$\Delta T = \pm 1/3 \cdot (0.3°\text{C} + 0,005 \cdot \vartheta)$
Pressure sensor compressed air supply	Linearity error: $\Delta p = \pm 0.5\%$ Temperature error (0 ... 50°C): $\Delta p = \pm 1\%$
Pressure sensors fluidized bed	Linearity error: $\Delta p = \pm 0.8\%$ Temperature error (0 ... 50°C): $\Delta p = \pm 1\%$
Rotary gas meter	$\dot{V}_g = 2.5 \ldots 64\text{m}^3\,\text{h}^{-1}$: $\Delta\dot{V}_g = \pm 2\%$ $\dot{V}_g = 64 \ldots 400\text{m}^3\,\text{h}^{-1}$: $\Delta\dot{V}_g = \pm 1\%$

Process flow diagram

The process flow diagram depicting the components of the CFM in Stage I configuration is given in the Appedix B, Figure B.1.

3.1.2 Stage II

Mastering electrostatics

Fluidization of bulk materials naturally provokes particle movement and causes interparticulate friction alongside the friction between the solids and the enclosing walls. Friction may cause the solids to accumulate electrostatic charge. Not removing the charge from the particles was found to induce particle agglomeration subsequently leading to false heat transfer readings.
Charge dissipating devices such as copper rods or copper bands are often used to divert the charge. The downside of these devices is that particles increasingly adhere during discharge, i.e. solids stick to the charge dissipating equipment. Placing rods may thus cause hindrance to the free particle movement. Hence in the present work, the increased conductivity of humidified air was exploited to minimize the influence on the particle movement and to efficiently remove electrostatic charge. In practice, the gas stream was humidified with purified water. By increasing the relative humidity of the fluidization gas to ≈50% electric discharges and agglomeration of particles were reduced sufficiently.
A dosing pump controlled by the PLC was used to dynamically modulate the amount of water sprayed into the gas stream. A nozzle was used to atomize the water for proper evaporation, which was positioned in a tube bend directing the the spray in-line to the gas flow, as shown in Figure 3.3. The total gas volume flow $\dot{V}_g + \dot{V}_{H_2O}$ increased by the vaporized mass flow of water $\dot{m}_{H_2O}$ was calculated on-line via the process control system.

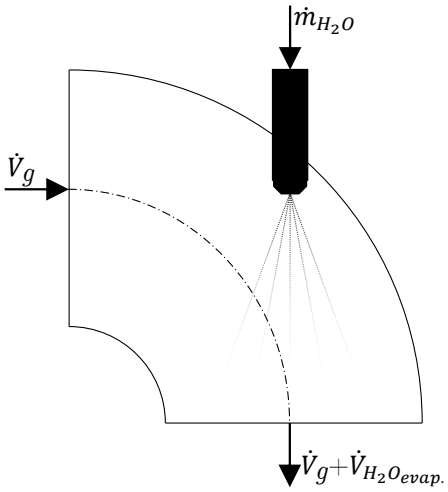

Figure 3.3: Principle of gas humidification.

Enlarging the freeboard

When the CFM was designed the freebaord was built with a total height of 0.57m. Operating the CFM at high gas velocities caused particles, i.e. especially fines, to accumulate in the exhaust filer. Hence, the height of the freeboard was extended by 0.77m (Figure 3.4). The modification sufficiently allowed particles to decelerate and revert to the fluidized bed.

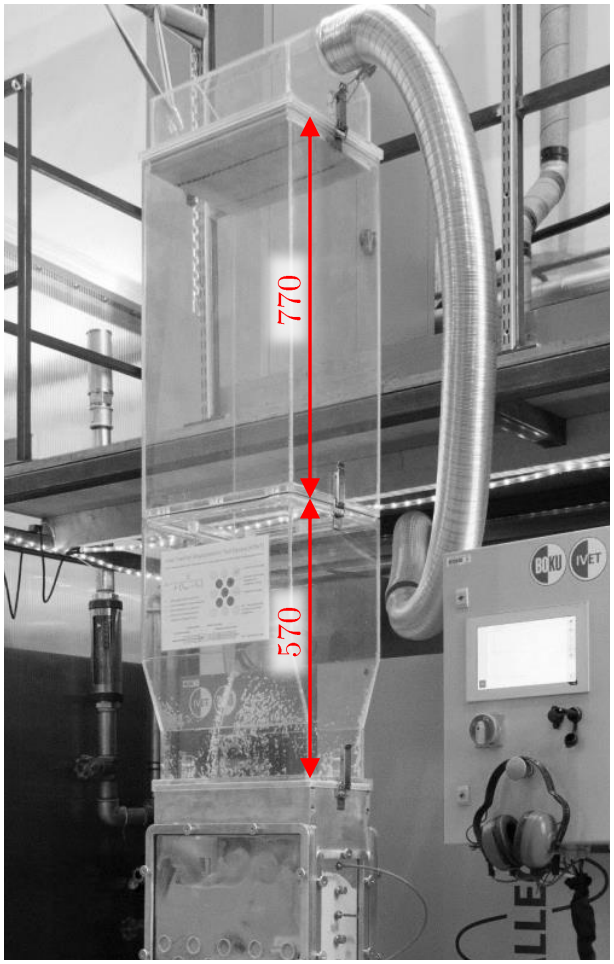

Figure 3.4: Freeboard extension, dimensions in mm.

Process flow diagram

The process flow diagram of the CFM in Stage II configuration featuring the components used for humidification of the fluidization gas stream is given in the Appedix B, Figure B.2.

3.1.3 Stage III

The CFM was modified for a continuous solids transport crosswise to the fluidized bed. The configuration still allowed for the investigation of heat transfer, but also enabled for conducting experiments in view of the particle RTD and particle mixing.

Superimposing solids crossflow

During operation, particles were continuously extracted from the fluidized bed and recirculated for introduction at another spot. For this, the narrower walls enclosing the fluidized bed were replaced with plates featuring ports allowing for the bed material to flow to and from the fluidized bed. A screw conveyor was used to maintain a constant flow of solids, which was driven by a frequency-controlled motor. A compartment was located at the discharge of the screw conveyor. Particles entering this compartment were fluidized with humidified air for electrostatic charge dissipation, albeit it was not possible to adjust humidification in a controlled manner. The gas flow was set by means of a manual needle valve and a float-type flow meter (Krohne, VA40). The flow meter featured a measurement accuracy of 1% with reference to the measured value. The solids were then lifted in a riser of 36mm ID connected

to the compartment. A particle separator was connected at the uppermost position of the riser separating the solids from the gas stream. While the gaseous phase exited the particle transport system being redirected to the freeboard of the CFM, the particles were directed downwards reverting back into the bubbling bed. The downcomer was made of an acrylic glass tube of 63mm ID. The solids and the gas flow is illustrated in the process flow diagram given in the Appendix B, Figure B.3.

Quantifying the solids circulation rate

It was assumed that the screw conveyor used for the particle transport provided a constant mass flow of solids. The process control system was used to set the solids circulation rate (SCR), whereby the SCR was translated to a frequency signal by a frequency converter (Siemens Micromaster 420) driving the AC motor.
The system was calibrated in view of the interpretation of the user input in relation to the frequency-controlled output signal. For different settings of frequencies, the SCR was measured by blocking the solids flow at the lower end of the downcomer, i.e. at the solids feed at the BFB exit port. A measuring grid added at the vertical section of the downcomer was used to determine the increase of the particle volume while extracting solids from the fluidized bed outlet port. The increase of the bulk height was recorded with a camera (Canon 500D) for subsequent analysis with respect to the time frame dependent solids height inside the downcomer. The actual SCR was calculated based on the bulk density of the respective bulk material. The described procedure is illustrated in Figure 3.5.

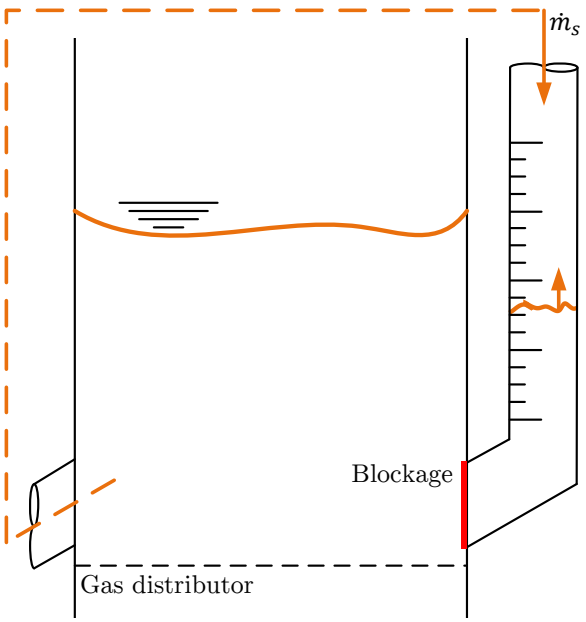

Figure 3.5: Solids circulation rate measurement principle.

Quantifying the solids residence time distribution

The principle of magnetic tracer detection was utilized for the purpose of measuring particle RTDs by means of tracer experiments. The main requirements for a potential measuring system were defined as follows:

1. High sensitivity — small amounts of tracer should be detectable.

2. High signal-to-noise ratio — the level of the signal should be considerably higher than the level of the noise.

3. High temporal resolution — to ensure that the tracer is detected even at high particle velocities.

4. Linearity — ideally, the output signal is proportional to the detected amount of tracer. In case the measuring system shows a non-linear behavior, it should at least have known characteristics which allow the user to consider them by the implementation of suitable (mathematical) correlations.

Based on previous work conducted by Guío-Pérez et al. [147], a tracer detection device was designed. Inductors were used to detect the tracer, i.e. ferromagnetic steel particles influencing the coil's inductance L while passing. The change in inductance was processed by means of electrical circuitry and recorded for subsequent analysis.
Fundamentally, a tracer detection device consisted of a coil integrated into an alternating current (AC) Maxwell-Wien bridge, shown in Figure 3.6. During the experiments, the bridge was used in null-balanced mode and designed according to the balancing conditions given by the Equations 3.4, 3.5 and 3.6. Balancing the bridge was accomplished by adjusting R_1, R_2 and R_3 as well as selecting C in response to variations in the other arm that carries the sensor, resulting in V_{out}≈0V. Null bridges have superior linearization characteristics and in small ranges of measurements the signal output may be considered to be quasi-linear [148]. The linearity characteristics of the detection device is discussed in Chapter 4, Section 4.4.1.

$$\frac{R_L + j \cdot \omega \cdot L}{R_1} = \frac{R_2 \cdot (1 + R_3 \cdot j \cdot \omega \cdot C)}{R_3} \tag{3.4}$$

$$C = \frac{L}{R_1 \cdot R_2} \tag{3.5}$$

$$R_3 = \frac{R_1 \cdot R_2}{R_L} \tag{3.6}$$

The AC signal obtained from the Maxwell-Wien bridge was processed by means of a lock-in amplifier, which was designed according to the application information provided in the data sheet of the Analog Devices balanced modulator/demodulator AD630 [149]. The principle of the detection device is described by the schematics given in Figure 3.7, illustrating the basic components and signal processing.
The reference signal, an AC signal with the amplitude V_{in} obtained from an analogue sine wave generator and amplified before used for driving the measurement bridge, was phase-shifted and processed by the demodulator. The signal obtained from the measurement bridge was amplified once again and processed by the demodulator as well.

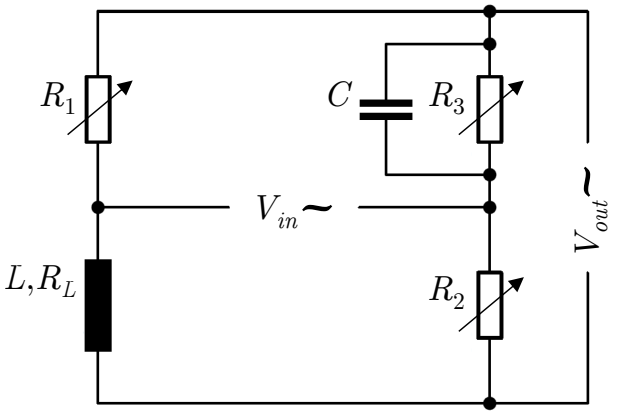

Figure 3.6: Maxwell-Wien bridge circuit.

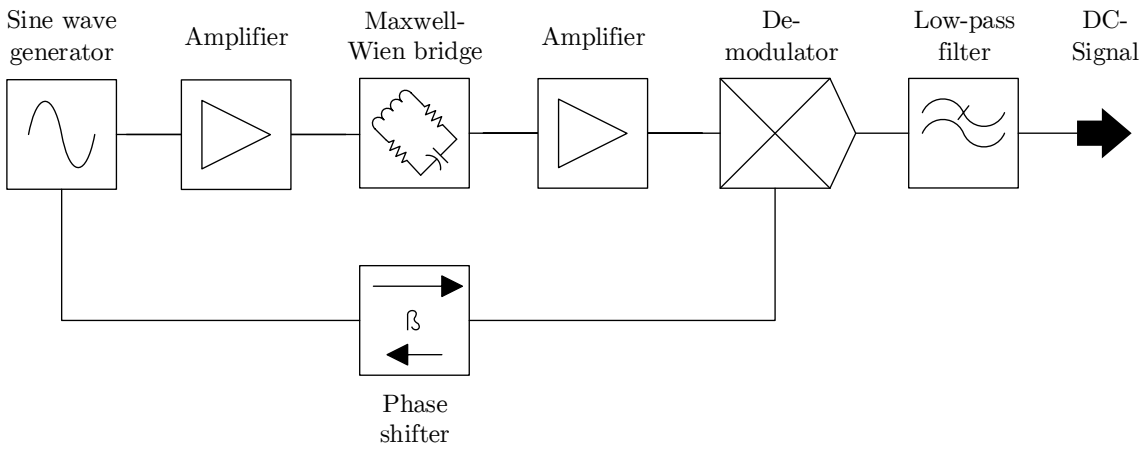

Figure 3.7: Schematics of the tracer detection device.

A low-pass filter was used to obtain a direct current (DC) signal, i.e. the change in the DC output voltage ΔV_{DC} being a function of the tracer mass fraction w_{tracer}. The phase shifter was adjusted with respect to the voltage of the DC-signal. The circuitry and its amplification factors were designed to create adequate DC signals of high quality despite minimum amounts of tracer material introduced.
In the scope of quantifying particle RTDs, the circuitry design was brought to printed circuitry boards. For data acquisition and data analysis two types of devices were manufactured — the *detector unit* and the *main unit*. Both devices are shown in Figure 3.8.

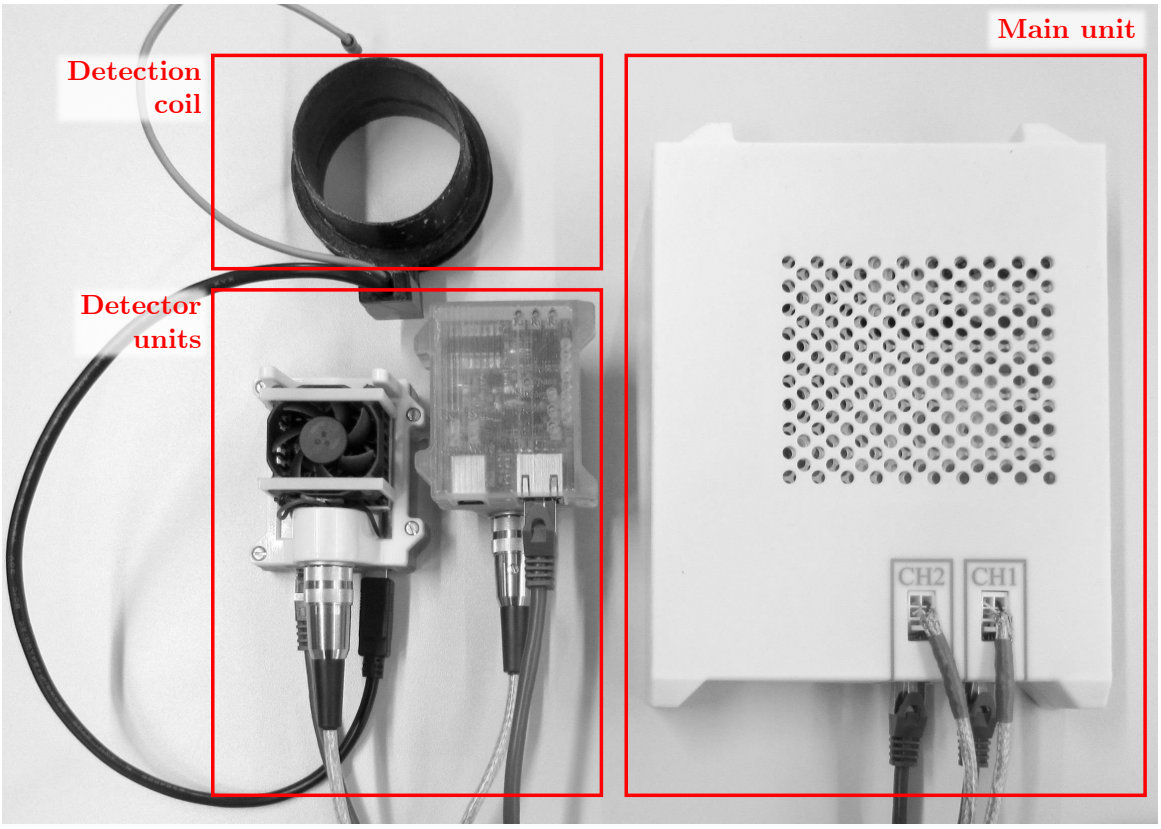

Figure 3.8: Tracer detection equipment.

The detector unit contained the circuitry realizing the signal processing principle given by the schematics depicted in Figure 3.7. The detection coil was connected externally and thus easily installable at the CFM. In the current setup two coils connected to separate detector units were used. The first coil was mounted at the downcomer recording the input signal, whereas the second coil was placed at the point of solids extraction. The positioning of the coils is illustrated in Figure 3.9. The temperature of the detector unit was kept constant by means of a PID controlled Peltier element to obtain stable and high quality measurement signals.
The main unit consisted of a custom-designed extension board connected to a single-board computer (Raspberry Pi 3, Model B) and is used to control the power output to the Peltier elements and to record the RTD-relevant data obtained from the detector units. Up to four extension boards may be connected to a single single-board computer allowing for the connection of up to eight detector units.

Injecting the tracer

Neodymium magnets, 40x10x5mm in size, were incorporated into 3D-printed half shells and mounted on the outside of the downcomer acting as separation device separating the ferromagnetic tracer particles from the continuous flow of inert bulk material. The positioning of the shells is shown in Figure 3.9. Initially, the entire amount of ferromagnetic solids of 200g in weight was kept in place on the inner surface of the downcomer. At some point, the shells were removed releasing the tracer detected as a pulse by the detection coil 1 (C_{pulse}). The magnetic shells were put back onto the downcomer immediately after injection to recollect the ferromagnetic solids and to avoid unintended reintroduction of the circulated tracer. The tracer concentration at the exit of the BFB was recorded by detection coil 2 ($C_{response}$).

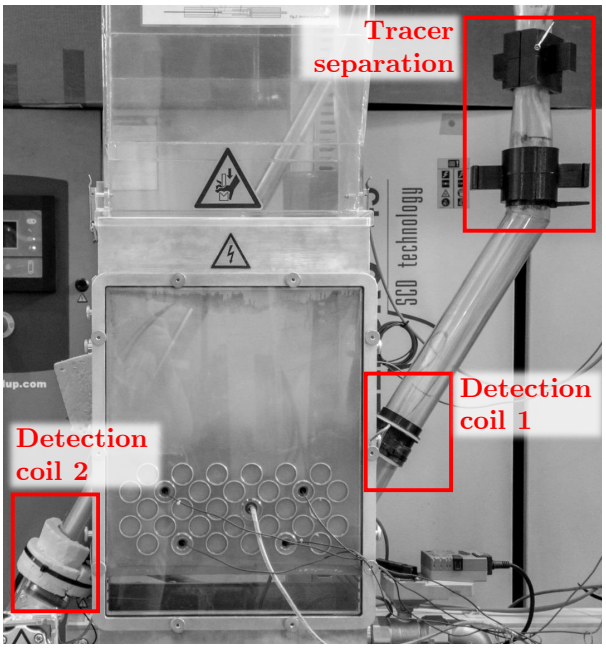

Figure 3.9: Positioning of the detection coils and the magnetic tracer separation device.

Modeling exit age distributions

For signal processing, the continuous response signal recorded at the particle drain $C_{response}$ was truncated based on the input pulse C_{pulse}. Thereby, the peak of the input pulse determined the beginning of the measurement, i.e. t=0, referred to as τ_0. Although the detector units were kept at constant temperature, the DC-signal may be subjected to a slight drift.

To account for the bias, 150 data points at the beginning, starting at τ_0, as well as 150 data points at the end of the response signal were averaged to level the $C_{response}$-curve zero. That is, both mean values were used for imprinting the straight line S_0 to be subtracted from the $C_{response}$ data points. The evaluation procedure is illustrated in Paper [4], Figure 11.
The experiments were repeated five times for each combination of gas velocity U and solids circulation rate $\dot{m}_s$. The recorded data $C_{response}$ were then synchronized in time, whereby τ_0 served as a basis for the starting point. For each $C_{response}$-curve the exit age distribution E was calculated with the formula given by Equation 2.23. With the data already synchronized in time, the respective E-curves were averaged for further analysis.
A suitable model able to approximate the flow characteristics of the CFM was designed. Therefore, the CSTR was selected to stand for the CFM's single BFB stage with continuous exchange of solids. The model representing the tubular sections of the solids feed and drain was designed as PFR with imprinted AD, involving additional degrees of freedom compared to a PFR without AD. A graphical representation is given by the compartment flow model shown in Figure 3.10.

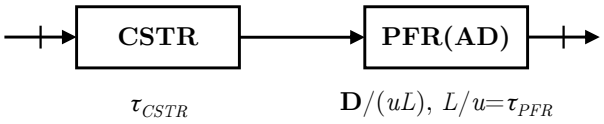

Figure 3.10: Compartment flow model.

Conclusively, the mathematical model was derived by convolution of a CSTR (Equation 2.27) and an axial dispersion PFR (Equation 2.31) by means of the software Mathematica [150]. The resulting formula is given by Equation 3.7. Therein, the interval $[a, b]$ was defined by the time when the tracer is detected at the particle feed τ_0 and the time when the last tracer particle is detected at the particle drain.

$$\begin{aligned} E_{fit} =& E_{CSTR} * E_{PFR,AD} = \int_a^b E_{CSTR}\left(t'\right) \cdot E_{PFR,AD}\left(t - t'\right)\, dt' \\ =& \frac{1}{2 \cdot \tau_{CSTR} \cdot u^{3/2}} \cdot \sqrt{\mathbf{D}} \cdot \exp\left[\frac{\mathbf{D} \cdot L + \tau_{CSTR} \cdot u^2 \cdot (L - u \cdot t)}{{\tau_{CSTR}}^2 \cdot u^3}\right] \cdot \sqrt{L} \\ & \cdot \sqrt{\frac{u^3}{\mathbf{D} \cdot L}} \cdot \operatorname{erf}\left[\frac{2 \cdot \mathbf{D} \cdot L + \tau_{CSTR} \cdot u^2 \cdot (L - u \cdot t)}{2 \cdot \sqrt{\mathbf{D}} \cdot \sqrt{L} \cdot \tau_{CSTR} \cdot u^{3/2}}\right]_a^b \end{aligned} \tag{3.7}$$

The mathematical fit function was then used to obtain characteristic data in view of the RTD and particle mixing, given by the Items 1 to 7. An example of the designed mathematical correlation fitting a respective E-curve is shown in Figure 3.11a. Additionally, a graphical illustration of the characteristic values is presented in Figure 3.11b.

1. k_{max}, the maximum slope occurring at the 'take-off' of the E_{fit}-curve, used to construct the straight line S_1.

2. τ_2, the breakthrough time at the occurrence of k_{max}.

3. τ_1, the breakthrough time resulting from the straight line S_1 intersecting the time axis.

4. τ_3, the duration from τ_0 until the E-curve reaches its absolute maximum.

5. τ, the mean residence time calculated from the experimental E-curve.

6. τ_{fit}, the mean residence time stemming from the modeled E_{fit}-curve.

7. $\mathbf{D}/(u \cdot L)$ and its individual components $\mathbf{D}$ and L/u=τ_{PFR}.

As for Item 5, it is noted that the fit-function did not meet the criterion E=0 after completion of the experiment, specifically holding true for low SCR scenarios. Therefore, a termination criterion was defined. By calculating the cumulative exit age distribution function F based on the E_{fit}-curve and normalizing it to unity in view of the time at the completion of the experiment, the time when the cumulative exit age distribution equals 0.632 was determined ($t_{0.632}$). The procedure is illustrated by Figure 3.11c. Ultimately, τ_{fit} was calculated with Equation 2.24 and the defined interval [τ_0,5·$t_{0.632}$]. A modeled E_{fit}-curve terminated by the 5·$t_{0.632}$-criterion is shown in Figure 3.11d.

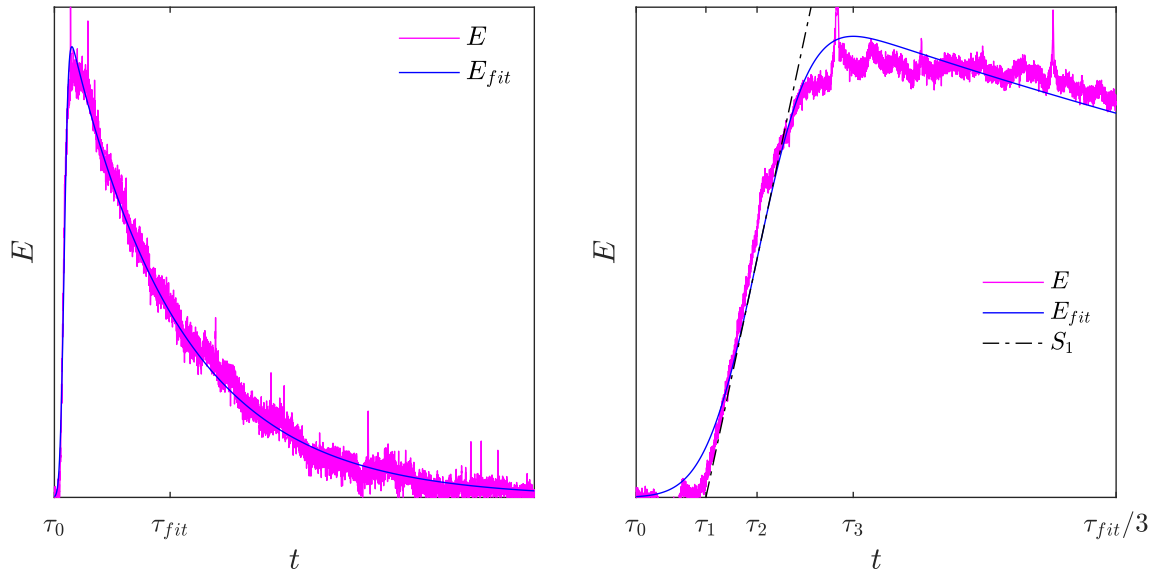

(a) Fitting experimentally obtained E-curves.

(b) Determining characteristic breakthrough times τ_1, τ_2 and τ_3.

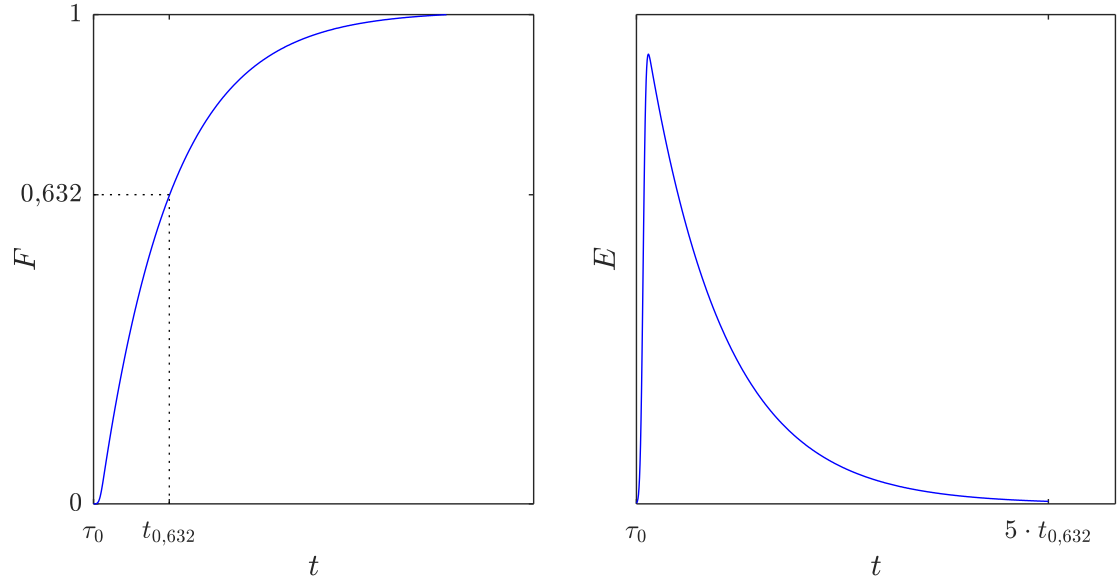

(c) Cumulative exit age distribution determining 5·$t_{0.632}$ based on F=0.632.

(d) Applying the termination criterion 5·$t_{0.632}$ to the modeled exit age distribution.

Figure 3.11: Mathematical fitting and analysis of the residence time distribution.

Process flow diagram

The process flow diagram of the CFM in Stage III configuration including the components used for the continuous circulation of solids is given in the Appendix B, Figure B.3.

3.2 Bulk materials

3.2.1 Bed materials

Three different bulk materials were selected, subsequently referred to as bulk material A, B and C. The main properties are given in Table 3.2. Figure 3.12 reveals that the three bulk materials are clearly classified as Geldart group B [45]. The PSD analyses of the bulk materials A, B and C can be found in the Appendix C.
Experiments considering the wall-to-bed heat transfer were on the one hand conducted with bulk material A at varying superficial gas velocity U in the range of $0.1 \ldots 0.8\,\mathrm{m\,s^{-1}}$, i.e. the fluidization number U/U_{mf} ranging from $5 \ldots 42$. On the other hand, for bulk material B the superficial gas velocity U was varied in the range of $0.1 \ldots 1\,\mathrm{m\,s^{-1}}$, i.e. the fluidization number U/U_{mf} ranging from $3 \ldots 26$. At all times, the bed height was set to 250mm at a superficial gas velocity U of $0.1\,\mathrm{m\,s^{-1}}$. For the experiments with tube bundles immersed in the fluidized bed, the superficial gas velocity U corresponds the introduced gas flow with reference to the total cross section of the CFM without accounting for the constriction caused by the tubes. This means that the onset of fluidization is expected at superficial gas velocities smaller than U_{mf} in the case of immersed bundles. In view of the heat transfer tests with bulk material C, the superficial gas velocity U was varied in the range of about $0.04 \ldots 0.3\,\mathrm{m\,s^{-1}}$, i.e. the fluidization number U/U_{mf} ranging from $0.2 \ldots 1.5$. The bed height was set to 360mm at a superficial gas velocity U of $0.04\,\mathrm{m\,s^{-1}}$.
The residence time or exit age distribution was investigated for bulk material A at different superficial gas velocities and solids circulation rates. The superficial gas velocity U was varied in the discrete steps $0.08\,\mathrm{m\,s^{-1}}$, $0.15\,\mathrm{m\,s^{-1}}$ up to $0.23\,\mathrm{m\,s^{-1}}$, i.e. the fluidization numbers U/U_{mf} equaling 4.7, 8.8 and 13.5. The SCR $\dot{m}_s$ was set to $88\,\mathrm{kg\,h^{-1}}$, $206\,\mathrm{kg\,h^{-1}}$ and $323\,\mathrm{kg\,h^{-1}}$ for each of the three investigated gas velocities or fluidization numbers, respectively.

Table 3.2: Bulk material specifications.

Bulk material		A Papers [2]&[4]	B Papers [1]&[2]	C Paper [3]	Flow tracer Paper [4]
d_p	[µm]	130	200	677	72
ϕ	[1]	≈1	≈1	≈1	≈1
ρ_p	$[\mathrm{kg\,m^{-3}}]$	2,450	2,450	890[(1)]	7,579
ρ_b	$[\mathrm{kg\,m^{-3}}]$	1,570	n/a	550[(2)]	n/a
$c_{p,p}$	$[\mathrm{J\,kg^{-1}\,K^{-1}}]$	840	840	2,250	500
ϵ_{mf}	[1]	0.41	0.41	0.42	0.41
Ar[(3)]	[1]	188	686	9,653	99
U_{mf}[(4)]	$[\mathrm{m\,s^{-1}}]$	0.017	0.039	0.146	0.016

[(1)] Assumed particle density under TSA operating conditions.
[(2)] Assumed bulk density under TSA operating conditions.
[(3)] Calculated with Equation 0.1.
[(4)] Calculated with Equation 2.9.

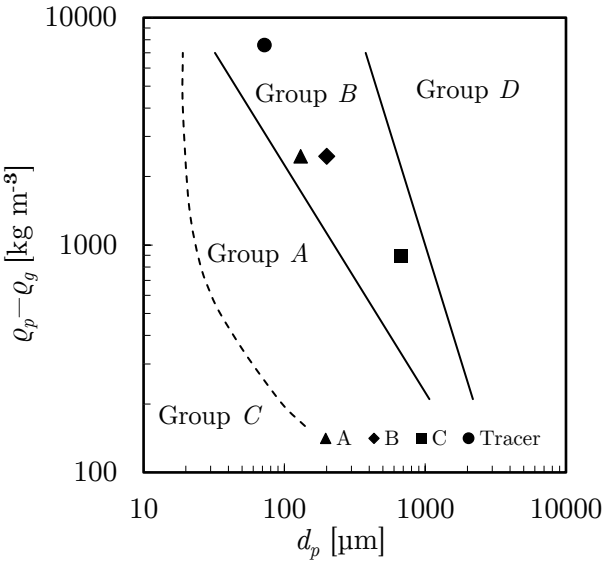

Figure 3.12: Classification of used bulk materials according to Geldart [45].

3.2.2 Flow tracer

Because of the large difference in their properties compared to other bulk materials, i.e. the magnetic permeability, and because they proved to be suitable in the past [151], steel particles were selected as the tracer used to measure particle RTDs. The material of the flow tracer was ferritic stainless steel designated as 1.4742. The combination of the used bed material and flow tracer ought to achieve an optimal match in the fluid-dynamic properties, i.e. similarity in minimum fluidization gas velocity U_{mf}. Also, the flow tracer is considered to be of the Geldart group B [45]. Regarding the best possible combination of the bulk materials available, bulk material A was used for the experiments conducted in view of the solids RTD and particle mixing.

3.3 Heat exchanger configurations

The larger walls, i.e. side panels of the CFM confining the fluidized bed were designed to be exchangeable (Figure 3.1). This allowed for the measurement of heat transfer at either a single tube or tube bundles of different geometries, respectively.

3.3.1 Single tube

Many models designed for the calculation of heat transfer in (bubbling) fluidized beds are valid for single tubes (refer to Chapter 2, Section 2.4). Hence, the first tests with the CFM were performed in view of the achievable single tube heat transfer rates to verify the validity of the measurement principle. Thereby, merely one heat transfer measurement probe and four temperature measurement probes were immersed in the fluidized bed. Thereby, the heat transfer measurement probe was positioned in the center of the fluidized bed. The temperature measurement probes were placed in maximum distance from the heat transfer measurement probe.

3.3.2 Tube bundles

Five different side panels were manufactured, able to hold tubes of different ODs. Thus, the combination of side panels with tubes of different diameters add up to tube bundles of

different properties in view of the resulting geometry. A tube bundle is characterized by its properties such as the diameter of the tubes d_t, horizontal and vertical tube pitch p_h and p_v as well as the diagonal and minimum tube pitch p_{diag} and p_{min}.
For further considerations, the panels are referred to side panel *A* to *D*. The specific properties of the panels are given in Table 3.3, including the possible combinations with tubes differing in OD resulting in the tube bundles *I* to *X*. In addition, the minimum tube pitch p_{min} as well as the heat exchanger void fraction ψ_{HEX} is presented.
Specifically, side panels *A* to *C* could be used with tubes of 20, 25 and 30mm OD. The properties of the nine resulting configurations (Tube bundles *I* to *IX*) are presented in more detail in Paper [2], Table 2.
Side panel *D* was able to hold 16mm OD tubes only and is referred to as tube bundle *X*. This setting was used when measurements for Paper [3] were performed in view of the distribution of heat transfer coefficients in the lateral and vertical position of the fluidized bed. A comprehensive description of the methodology is given in Paper [3], Chapter 2.

Table 3.3: Tube bundle specifications.

Side panel		*A*			*B*			*C*			*D*
p_h	[mm]	55			70			85			30
p_v	[mm]	27.5			35			42.5			26
p_{diag}	[mm]	38.9			49.5			60.1			30
Tube bundle		*I*	*II*	*III*	*IV*	*V*	*VI*	*VII*	*VIII*	*IX*	*X*
d_t	[mm]	20	25	30	20	25	30	20	25	30	16
p_{min}	[mm]	18.9	13.9	8.9	29.5	24.5	19.5	40.1	35.1	30.1	14
ψ_{HEX}	[1]	0.71	0.64	0.57	0.78	0.72	0.66	0.82	0.77	0.72	0.58

Chapter 4

Results and discussion

4.1 Heat exchange requirement in temperature swing adsorption

A mathematical correlation for estimating the necessary heat exchanger surface to be immersed in the fluidized bed stages of the adsorber and desorber considering a defined flow of heat is presented in Paper [1]. Therein, the flow of heat is based on the heat released during CO_2 adsorption and the necessary heat supply for the sorbent regeneration. Practically, thin tube walls with high thermal conductivity λ_t and turbulent flow of liquid or condensing steam on the inside of the tubes are assumed. Under these assumptions the conclusion is drawn that

> *the wall-to-bed heat transfer coefficient constitutes the limiting factor within the overall heat transfer coefficient.*

Equation 4.1 incorporates parameters characterizing particle and fluidized bed properties such as the pressure drop across a reactor stage Δp_{fb}, the void fraction ϵ as well as the densities of the gaseous phase ρ_g and the particles ρ_p. Furthermore, the parameters d_t, s_h and s_v characterize the geometry of the in-bed HEXs, whereas $x{\cdot}y$ yields the cross section of the respective reactor column.

$$A_{HEX} = \frac{x \cdot y \cdot \pi}{d_t \cdot s_h \cdot s_v} \cdot \frac{\Delta p_{fb} \cdot n_{stage}}{(1-\epsilon) \cdot (\rho_p - \rho_g) \cdot g} \approx \frac{Q}{\Delta T_m} \cdot \frac{1}{h_{total}} \tag{4.1}$$

Considering Paper [1] and following the development of Equation 4.1, the correlation given by Equation 4.2 is derived expressing that the total pressure drop Δp_{fb} of the contacting column, which is critical in CO_2 capture processes, is inversely proportional to h_{total}.

$$\Delta p_{fb} \propto \frac{1}{h_{total}} \tag{4.2}$$

In general it is noted that

> *low heat transfer coefficients or a badly distributed heat surface load leading to local shortages in heat transfer causes the fluidized bed to increase in pressure drop for a desired CO_2 capture efficiency.*

In specific view of the process design proposed for TSA it is noted that high pressure drops across the reactor columns must be avoided to achieve the best possible process efficiency and thus to limit the process in its capital and operational expenditures.

4.2 Wall-to-bed heat transfer – single tube

4.2.1 Comparison of models

Three models for the estimation of heat transfer coefficients between fluidized beds and immersed single tubes as a function of the superficial gas velocity are presented in Section 2.4.1. Paradigmatically, these models have been considered to predict heat transfer in view of bulk material B (refer to Table 3.2, Chapter 3). The results are shown in Figure 4.1.
It is evident that each one of the models leads to a different characteristic how heat transfer progresses as a function of the superficial gas velocity or fluidization number, respectively. For the selected bulk material, the model proposed by Natusch et al. [60] predicts a maximum heat transfer coefficient of $\approx$460W m^{-2} K^{-1} occurring at a fluidization number U/U_{mf} $\approx$10. From this point on, heat transfer is predicted to stay roughly constant up to a fluidization number U/U_{mf}=60.
Maximum heat transfer occurs at about the same fluidization number considering the model by Molerus et al. [75]. The model projects a slight decrease in heat transfer for the higher gas velocities. From a practical point of view, the differences in terms of the quantity and quality in heat transfer between the models by Natusch et al. and Molerus et al. seem to be negligible.
With regard to the model by Martin [138] it is noted that the predicted heat transfer coefficients differ in quality and quantity from the ones obtained considering the models by Natusch et al. [60] and Molerus et al. [75]. After a steep increase in heat transfer starting at U/U_{mf} $\approx$1 a maximum is reached at a rather low fluidization number U/U_{mf} $\approx$2. Furthermore, the maximum heat transfer coefficient is predicted to be as high as $\approx$710W m^{-2} K^{-1}, significantly larger compared to the other models. After reaching U/U_{mf} $\approx$5 heat transfer is predicted to decrease rather rapidly, intersecting the curves obtained with the models by Natusch et al. and Molerus et al. at fluidization numbers ranging from 35 to 45. At U/U_{mf}=60 the model by Martin predicts the lowest heat transfer coefficient, compared to the other models with a value of $\approx$340W m^{-2} K^{-1}.

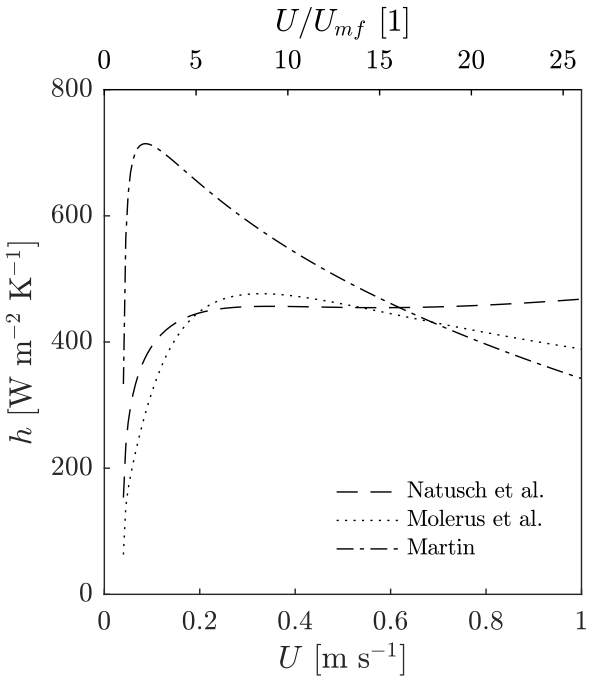

Figure 4.1: Comparison of calculated heat transfer coefficients, bulk material B, single tube.

4.2.2 Comparison of model and experiment

Experimental work was conducted with the bulk materials A and B (refer to Section 3.2, Table 3.2). In the course of this thesis merely the results obtained from the measurements with bulk material A are presented. A comprehensive discussion of all results is given in the Paper [2]. The heat transfer data are given in Tables A1 and A2 in the Appendix of the same manuscript.
The experimentally obtained wall-to-bed heat transfer coefficients are shown in 4.2a, whereby calculated wall-to-bed heat transfer coefficients obtained from the models by Natusch et al. [60] and Molerus et al. [75] are presented alongside. Both models neglect the effect of the tube diameter on heat transfer, whereas the dependency is clearly indicated by the experimental results. The highest heat transfer coefficients were observed for the tube of 20mm OD and, concurrently, the lowest values are found for the tube of 30mm OD.
Therefore, the corrective factor proposed by Petrie et al. [88] (refer to Equation 2.20) was used to account for the effect of the tube diameter on the wall-to-bed heat transfer. The mathematical correlation was applied to the respective single tube models, whereby the results are discussed in detail in Paper [2]. By way of example, the results obtained from calculations for single tubes of different diameter are shown in Figure 4.2b. Depending on the suitability of the model used for the estimation of heat transfer coefficients at single tubes,

> *the application of the model by Petrie et al. accounting for the influence of the tube diameter on the wall-to-bed heat transfer leads to promising results.*

Furthermore, the experimental data shows a distinct increase in heat transfer at U/U_{mf} in the approximate range of 5 to 20, followed by more or less constant heat transfer coefficients. Thereby, heat transfer seems to increase slightly more rapid for the tube of 20mm OD than for the larger sizes. The model by Molerus et al. nicely resembles heat transfer coefficients up to $U{\approx}0.4\,\mathrm{m\,s^{-1}}$. At gas velocities higher than that the model tends to underestimate heat transfer. The model by Natusch et al. also shows a pronounced increase in heat transfer starting at U/U_{mf} ≈5, however predicts a continuous increase clearly overestimating heat transfer for the higher values of the superficial gas velocity.

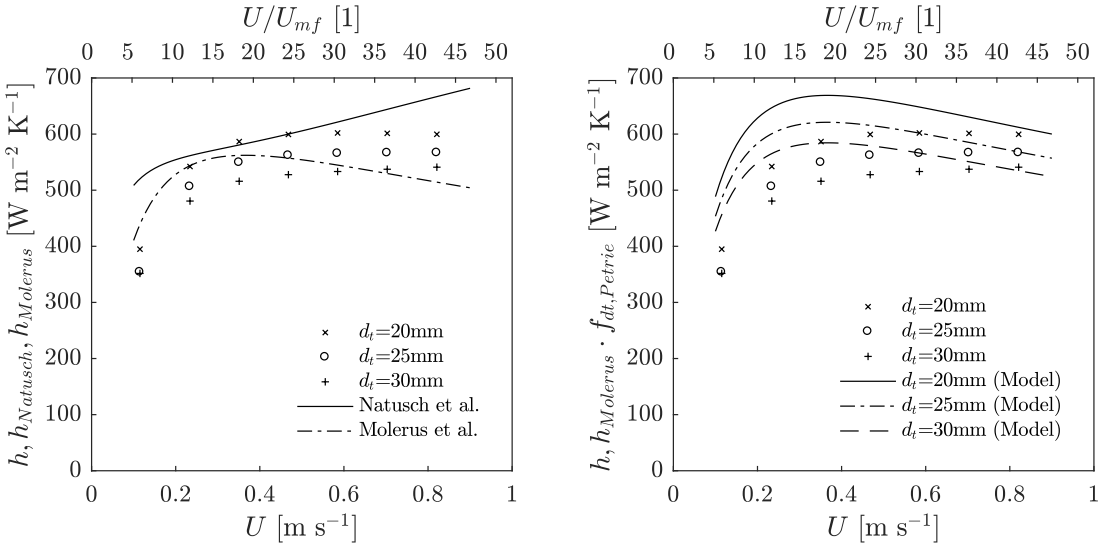

(a) Comparison of the model quality.

(b) Influence of the tube diameter.

Figure 4.2: Experimental and modeled wall-to-bed heat transfer coefficients, bulk material A, single tubes.

Based on the presented findings it is evident that

> *the experimental results more or less differ in quantity and quality compared to the heat transfer coefficients calculated with the models available in the literature.*

Conclusively, depending on the considered bulk material better results are achieved with one or the other calculation model. It is assumed that deviations between experimental and modeled heat transfer coefficients are based on:

1. The fact, that the actual solids PSDs vary from one experiment to another. However, the Sauter mean diameter used for the calculations merely represents a mean particle size.

2. The varying designs of experimental setups used to measure wall-to-bed heat transfer coefficients, i.e. differing in their gas distributor designs, cross-sectional shapes and bed heights, etc.

4.3 Wall-to-bed heat transfer – tube bundle

Experiments were conducted with the tube bundles *I* to *IX* (refer to Section 3.3, Table 3.3) and the bulk materials *A* and *B* (refer to Section 3.2, Table 3.2). In the course of this thesis, merely the results obtained from the measurements with bulk material *A* are discussed in Section 4.3.1 and in detail in Paper [2].
In addition, the main results obtained from the experiments with the tube bundle *X* and bulk material *C* are presented in Section 4.3.2. A detailed analysis is given in Paper [3]. During these experiments, the heat transfer measurement probe was inserted at different locations of the tube bundle, i.e. heat transfer as a function of the horizontal and vertical fluidized bed position.

4.3.1 Influence of the tube bundle geometry

The results obtained with tube bundles *II*, *V* and *VIII* compared to heat transfer coefficients measured with a single tube of 25mm OD are shown in Figure 4.3a. Thereby, heat transfer at the single tube was found to be highest and decreases when the tubes are arranged in an array. The narrower the tubes are arranged, the lower the achievable heat transfer coefficients are. This behavior is also described in the literature and is based on the fact that particle movement is hindered by the immersed tubes, especially when arranged in an array [134]. As for tube bundle *VIII* (s_h=3.4), heat transfer is slightly lower than for the single tube of the same outer diameter. Heat transfer seems to decrease marginally at $U \approx 0.8\,\mathrm{m\,s^{-1}}$. This behavior is even more pronounced for the other tube bundles *II* and *V* (s_h=2.8 and s_h=2.2).
Experimental results obtained with the tube bundles *I* to *IX* were compared to heat transfer coefficients calculated with the models by Molerus et al. [75], which was adapted with the model by Natusch et al. [60] accounting for the hindering effect of the respective tube bundle. The results are presented in Figure 4.3b. Except for the tube bundle *VII* (s_h=4.25), all of the calculated heat transfer coefficients lie within a boundary of ±20%.
Based on the findings it is concluded that

> *the adequacy with regard to the match between experimental and calculated data for tube bundles strongly depends on the combination of the used models.*

Thus, the Items 1 and 2 listed in Section 4.2 apply as well to the observations made with tube bundles.

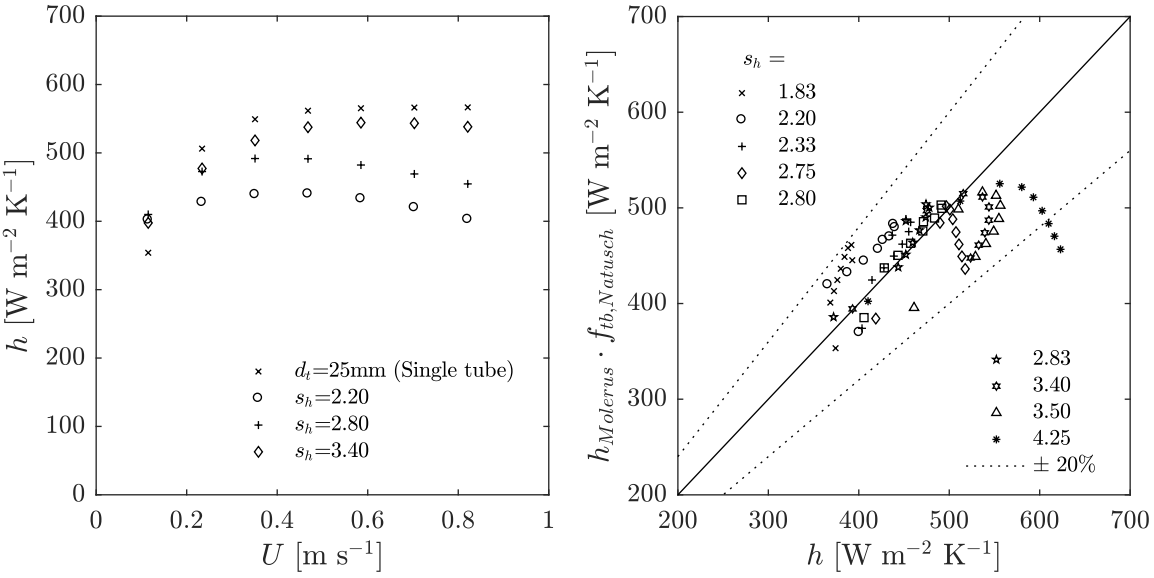

(a) Experimental heat transfer coefficients, single tube vs. tube bundles *II*, *V* and *VIII*.

(b) Experimental vs. modeled heat transfer coefficients, tube bundles *I* to *IV*.

Figure 4.3: Experimental and modeled wall-to-bed heat transfer coefficients, bulk material A, tube bundles.

4.3.2 Zoning of heat transfer

As shown in Figure 4.4a, the findings clearly indicate that heat transfer strongly depends on the investigated fluidized bed position, referred to as zone. Lower heat transfer coefficients are observed in the wall-zone ($y \rightarrow 0.2$m), whereas heat transfer increases moving toward the core-zone ($y \rightarrow 0$m). It was furthermore found that heat transfer coefficients near the gas distributor ($z = -0.13$m) seem to be slightly lower as they are in the upper area ($z = 0.13$m). This behavior is discussed in detail in Paper [3], Figure 11.
Regardless of the examined zone, the higher the gas velocity the higher the heat transfer coefficients. Nevertheless, the deviation between heat transfer in the core-zone and wall-zone decreases with an increase in the gas velocity. Both circumstances, that is the decrease of heat transfer near the wall and near the gas distributor are in accordance to the findings presented in the literature [136, 115].
To counteract the described phenomenon of diverging heat transfer coefficients an uneven gas distribution was deliberately forced. The results are shown in Figure 4.4b. It is evident that heat transfer could be increased significantly in the wall-zone.

> *Although the averaged results regarding the core-zone and wall-zone clearly indicate that heat transfer is distributed more evenly with the modified gas distributor, an increase of the overall wall-to-bed heat transfer was not observed.*

Nevertheless, it is evident that a more uniform heat transfer across the in-bed heat exchanger is equivalent to improved uniformity in view of particle mixing and, concurrently, the distribution of the HEX heat load. Interpreted in another way, consistent solids mixing behavior may lead to an improvement in both heat and mass transfer.

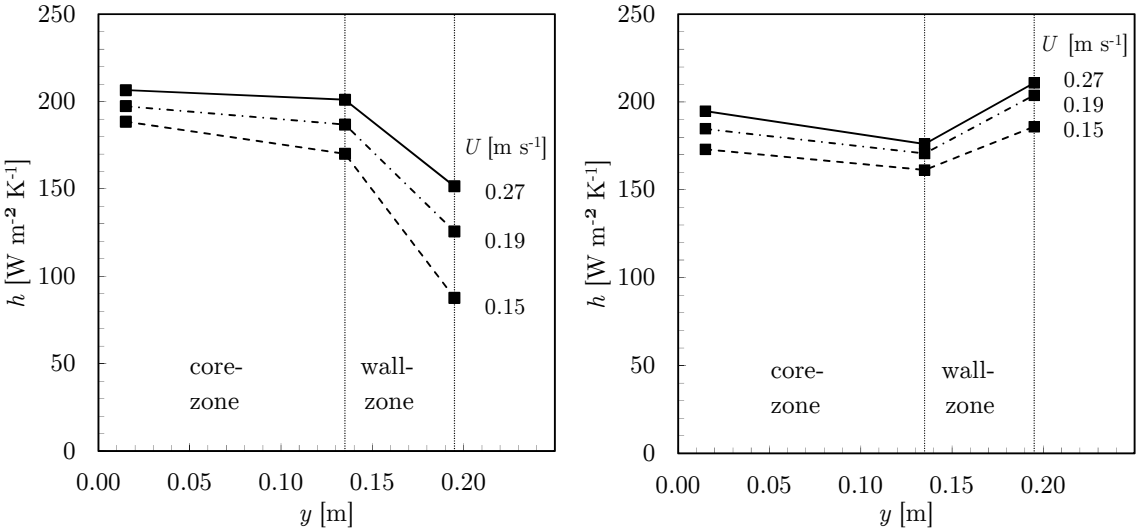

(a) Uniform nozzle grid.

(b) Modified nozzle grid.

Figure 4.4: Position-dependent heat transfer coefficients for selected superficial gas velocities, bulk material C, tube bundle X.

4.4 Solids residence time distribution

4.4.1 Suitability of the measurement system

The linearity characteristics of the inductive measurement system were analyzed by preparing fixed bed mixtures with different amounts of tracer added to the bulk of inert solids, i.e. bulk material A (refer to Table 3.2, Chapter 3). The samples were well mixed before placed in the core of the detection coil. The obtained results are illustrated in Figure 4.5a.
It is shown that the glass beads are in fact inert meaning no change in the output signal ΔV_{DC} was detected when no tracer was present. The output signal increases with the increase in the ferromagnetic tracer concentration. Thereby, the linear fit seems to be a fair approximation for tracer concentrations up to 15wt%. This insures the validity of the recorded C-curves without the necessity to account for any non-linearity effects.
Considering the duration of the input signal C_{pulse}, it is noted that the pulse duration of just $\approx$1s is significantly lower than the duration of the entire experiment ($\approx$20...60min). The exit age distributions of typical input and output signals are shown in Figure 4.5b. Thus, it is justifiable to assume the Dirac delta function as input when modeling RTD functions.

4.4.2 Solids residence time and mixing

The solids mean residence time as a function of the fluidization number U/U_{mf} and solids mass flow $\dot{m}_s$ was calculated from the data recorded during the RTD experiments, i.e. the exit age distributions derived from the $C_{response}$-signal by applying Equation 2.23 (refer to Section 2.5). τ_{fit}, the mean residence time of a respective (tracer) particle in between the detection coils was compared to the hydraulic residence time τ_{hyd}. The results are presented in Figure 4.6a.
It is shown that the hydraulic residence time is constant for the different superficial gas velocities, but varies with the solids mass flow. The circumstance is explained by Equation 2.26. For the lowest solids mass flow of $\dot{m}_s$=88kg h^{-1}, the divergence between τ_{fit} and τ_{hyd} decreases with an increase in gas velocity. Thereby, the lowest mean residence time is

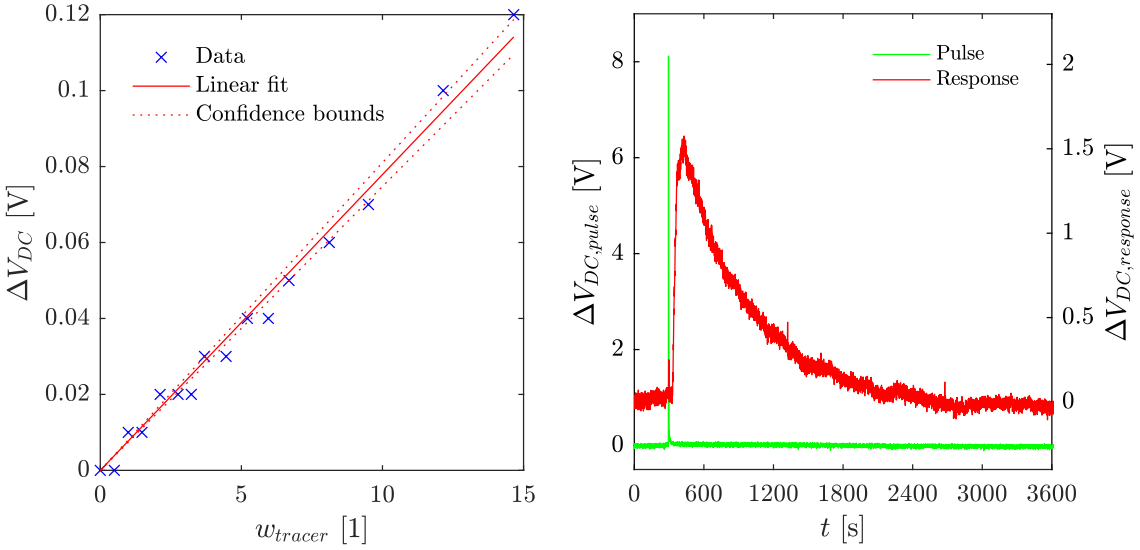

(a) DC-signal change as a function of tracer mass fraction.

(b) Signal-to-noise ratio of the pulse and response signal.

Figure 4.5: Suitability of the measurement system.

observed for the lowest fluidization number of U/U_{mf}=4.7. Therefore, it is concluded that

> *the formation of dead-spaces and short-circuit flows were observed at fluidization numbers around five.*

The result is tracer material accumulating in the stagnant zones of the fluidized bed. With an increase of the gas velocity the lack of particle mixing vanishes, resulting in τ_{fit} resembling τ_{hyd} for the highest fluidization number U/U_{mf}=13.5. The deviation between τ_{fit} and τ_{hyd} at the higher SCRs stems from imperfect tracer separation by the magnetic shells.
In addition, the mean residence time of particles in the feed and drain section transporting solids to and from the fluidized bed, represented by $\tau_{PFR}=L/u$, was compared to the hydraulic residence time τ_{hyd}. Thereby, τ_{hyd} equals the ratio of the particle mass contained in the feed and drain tubing and the apparent solids circulation rate. The results are illustrated in Figure 4.6b.
For the three tested SCRs it is shown that τ_{PFR} increasingly approximates τ_{hyd} with an increase in the superficial gas velocity or fluidization number, respectively. This means that

> *the more extensive the particle movement gets, the more the mixing characteristics of the bubbling fluidized bed is represented by mixed flow conditions.*

As for the lower fluidization numbers, it is evident that the reactor characteristics are additionally influenced by the characteristics of a plug flow reactor with imprinted axial dispersion.
As for the low fluidization number of U/U_{mf}=4.7, it was already discussed that stagnant fluid and short-circuiting occurred during the experiments. This is substantiated by the exit age distributions obtained from the $C_{response}$-signals, which are presented in the Figures 4.7a, 4.7b and 4.7c. These figures contain the recorded RTD data E (magenta), the fitted exit age distributions E_{fit} (blue) and the signal data obtained when the gas velocity was increased after the actual experiment $E_{U/U_{mf}=13.5}$ (cyan). For the lowest SCR of $\dot{m}_s$=88kg h^{-1} it is shown that a significant amount of tracer material accumulated in the fluidized bed kept in the dead spaces until the gas velocity was increased. With an increase in the SCR this amount decreases significantly. However, it must be noted that the mean

residence time obtained from these experiments is lower than the hydraulic residence time τ_{hyd}. With reference to Figure 1 in Paper [4] it is observed that

> *the exit age distribution indicates slow internal circulation of the fluidized bulk material at fluidization numbers around five.*

Caused by the stagnant zones, the active reactor volume seems decreased by the volume of the dead spaces resulting in the lower mean residence time of solids. As mentioned above, both results obtained at the higher SCRs indicate short-circuiting. This behavior is described as sharp early peak occurring during the tracer experiment (refer to Figure 1 in Paper [4]). Obviously, the effect of the dead spaces is superimposed by the effect of short-circuiting. Although an exact quantification of both effect is not possible, the $E_{U/U_{mf}=13.5}$-curves shown in the Figures 4.7b and 4.7c indicate that fluid stagnation was decreased by the increase of the SCR. The higher the SCR, the more the short-circuiting is pronounced.
To examine the formation of dead spaces at higher fluidization numbers, the gas velocity was again increased for the experiment conducted at the operational parameters U/U_{mf}=8.8 and $\dot{m}_s$=206kg h^{-1}. Thereby, the data presented in Figure 4.7e neither indicates significant amounts of tracer material kept back in stagnant zones nor the formation of short-circuiting.

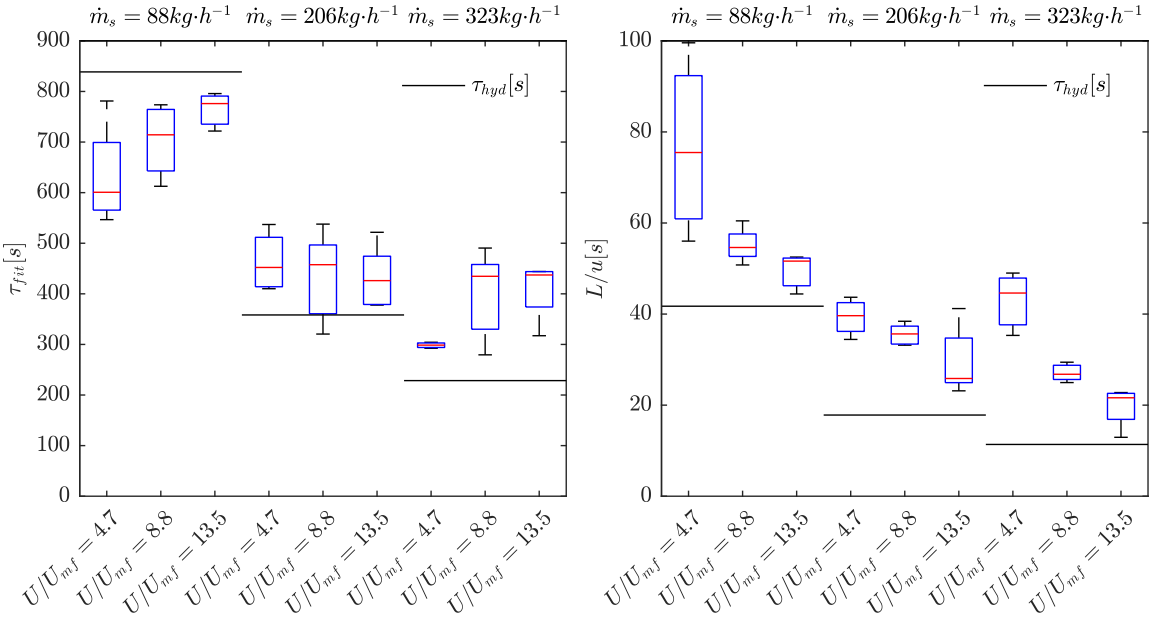

(a) τ_{fit} as a function of U/U_{mf} and $\dot{m}_s$ compared to τ_{hyd}.

(b) τ_{PFR} as a function of U/U_{mf} and $\dot{m}_s$ compared to τ_{hyd}.

Figure 4.6: Mean residence time of the entire reactor volume and of the particle feed and drain representing a plug flow reactor with axial dispersion.

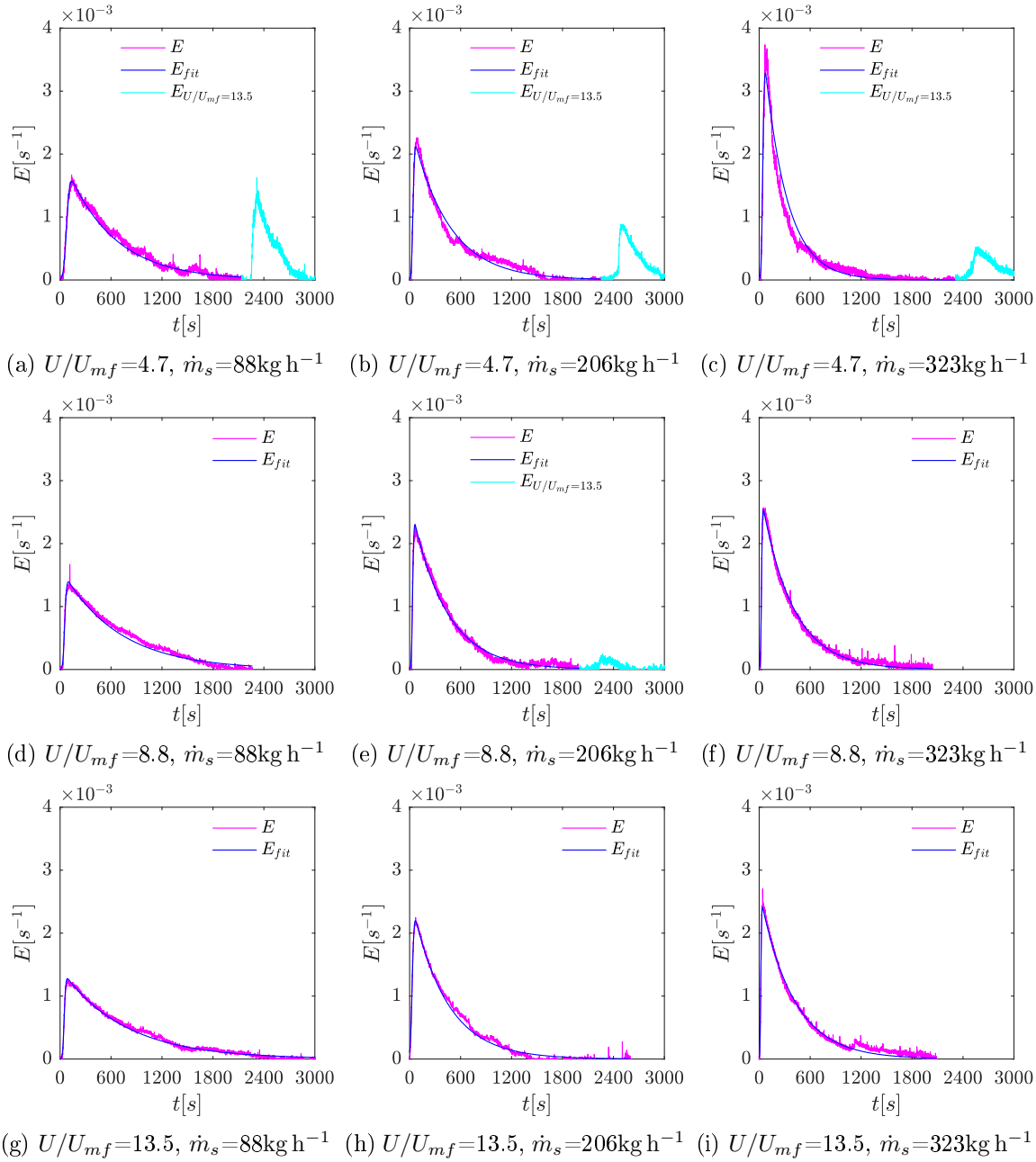

(a) U/U_{mf}=4.7, $\dot{m}_s$=88kg h^{-1} (b) U/U_{mf}=4.7, $\dot{m}_s$=206kg h^{-1} (c) U/U_{mf}=4.7, $\dot{m}_s$=323kg h^{-1}

(d) U/U_{mf}=8.8, $\dot{m}_s$=88kg h^{-1} (e) U/U_{mf}=8.8, $\dot{m}_s$=206kg h^{-1} (f) U/U_{mf}=8.8, $\dot{m}_s$=323kg h^{-1}

(g) U/U_{mf}=13.5, $\dot{m}_s$=88kg h^{-1} (h) U/U_{mf}=13.5, $\dot{m}_s$=206kg h^{-1} (i) U/U_{mf}=13.5, $\dot{m}_s$=323kg h^{-1}

Figure 4.7: Experimental and modeled exit age distributions for different fluidization numbers U/U_{mf} and solids circulation rates $\dot{m}_s$.

Chapter 5

Conclusion and outlook

The conclusions of this thesis are subdivided into those stemming from the investigations with regard to wall-to-bed heat transfer presented in Section 5.1, whereas Section 5.2 is dedicated to the conclusions drawn in view of the solids residence time distribution and particle mixing. A brief outlook will be given in Section 5.3. In addition, a closing remark with respect to the thesis' introduction is provided in Section 5.4.

5.1 Wall-to-bed heat transfer

Although a number of models for the estimation of heat transfer coefficients between gas-fluidized solids and immersed tube bundle heat exchangers is available in the literature, the applicability for an exact and profound heat exchanger design is questionable. Thereby a couple of factors impede from doing so:

1. The number of mathematical models available for the calculation of wall-to-bed heat transfer coefficients is limited and the predicted heat transfer coefficients differ in their quality and quantity. Furthermore, these models are designed for the calculation of heat transfer at single tubes only.

2. In practice, a bundle of tubes is defined by its properties such as the tube diameter and the tube arrangement. Other models can be used to take these quantities into account, again increasing the uncertainty in the course of designing in-bed heat exchangers.

3. Every setup more or less differs from another, be it the structure enclosing the fluidized bed, the gas distributor or the powder properties.

Considering the stated items it seems inevitable to conduct preliminary tests utilizing for instance cold flow models in the course of designing fluidization based processes relying on excellent heat transfer characteristics.
Nevertheless for the tested particle collectives and single tubes, the models proposed by Natusch et al. [60] and Molerus et al. [40] lead to fair approximations of the wall-to-bed heat transfer coefficients. The fairly simple model by Petrie et al. [88] is recommended to account for the effect of the tube diameter on heat transfer. As for tube bundles, the model by Natusch et al. [60] leads to fair results by merely taking the horizontal tube spacing into account.

5.2 Solids residence time distribution

It was shown that the proposed inductance measuring method is suitable for the determination of residence time distributions of gas-solid fluidization based reactors. Although the

tracer separation was insufficient during the tests conducted, the particle mixing was investigated successfully by means of the utilized cold flow model with a bubbling bed subjected to continuous solids exchange. Surprisingly, the formation of dead spaces was observed at fluidization numbers $U/U_{mf} \approx 5$. Thereby it is concluded that the design of the gas distributor most likely influences solids mixing characteristics.

5.3 Outlook

After improving the tracer separation further experimental work is going to be performed in view of the solids residence time distribution and the coupled particle mixing characteristics under the influence of in-bed heat exchangers. It is assumed that the clear dominance of the mixed flow regime in the bubbling phase increasingly changes towards a more pronounced plug flow reactor with superimposed axial dispersion, especially with a significant decrease in the tube spacing, respectively. Because of the fact that the cold flow model will be equipped with heat transfer measurement probes, simultaneously the effect of the solids circulation rate on heat transfer will be examined.
The heat transfer coefficients determined with the cold flow model were used for the design of the in-bed heat exchangers for a temperature swing adsorption plant in pilot scale. The occurring heat transfer coefficients under real world conditions will be compared to those obtained from the experimental campaigns conducted with the cold flow model.

5.4 Closing remark

Introducing the term Anthropocene to represent the human's impact on the environment seems to be a big step already. Alongside other technologies proposed and increasingly available for mitigating climate change, the invention and advancement of the temperature swing adsorption process may shorten the time line to CO_2 capture implementation and this constitute a small but important step towards the protection of the human's home — *the Earth*. It is a pity that we have to fight hard to preserve the most valuable gift — *life*. However, it is an even greater pity that the ideas born are reduced to their costs in the end evaluating them in view of the expected profit and/or prestige. Rather than doing what is best for ourselves on a short-term basis, i.e. to think in terms of maximizing the economic output or monetary wealth, we must do what is best for the entirety on the longer term presumably beginning with the redefinition of our values.

Bibliography

[1] G. Hofer, J. Fuchs, G. Schöny, and T. Pröll, "Heat transfer challenge and design evaluation for a multi-stage temperature swing adsorption process," *Powder Technology*, vol. 316, pp. 512–518, July 2017.

[2] G. Hofer, G. Schöny, J. Fuchs, and T. Pröll, "Investigating wall-to-bed heat transfer in view of a continuous temperature swing adsorption process," *Fuel Processing Technology*, vol. 169, pp. 157–169, Jan. 2018.

[3] G. Hofer, G. Schöny, and T. Pröll, "Acting on hydrodynamics to improve the local bed-to-wall heat transfer in bubbling fluidized beds," *Chemical Engineering Research and Design*, vol. 134, pp. 309–318, June 2018.

[4] G. Hofer, T. Märzinger, C. Eder, F. Pröll, and T. Pröll, "Particle mixing in bubbling fluidized bed reactors with continuous particle exchange," *Chemical Engineering Science*, Nov. 2018.

[5] G. Hofer, "Heat transfer at immersed tube bundles in bubbling fluidized beds considering Geldart type B particles," in *12. Minisymposium Verfahrenstechnik*, pp. 9–12, TU Graz, Mar. 2016.

[6] G. Hofer, J. Fuchs, G. Schöny, and T. Pröll, "Dimensioning tube bundle heat exchangers for a continuous temperature swing adsorption process," in *Proceedings of 12th International Conference on Fluidized Bed Technology (CFB-12)* (W. Nowak, M. Sciazko, and P. Mirek, eds.), pp. 465–473, May 2017.

[7] O. Levenspiel, *Chemical Reaction Engineering*. Paperbackshop UK Import, 1998.

[8] P. J. Crutzen and E. F. Stoermer, "The "Anthropocene."," *Global Change Newsletter, International Geosphere–Biosphere Programme (IGBP)*, vol. 41, pp. 17–18, 2000.

[9] E. Horn, "Jenseits der Kindeskinder. Nachhaltigkeit im Anthropozän," *Merkur*, vol. 71, pp. 5–17, 2017.

[10] V. Özdemir and N. Hekim, "Birth of industry 5.0: Making sense of big data with artificial intelligence, "the internet of things" and next-generation technology policy," *OMICS: A Journal of Integrative Biology*, vol. 22, pp. 65–76, Jan. 2018.

[11] Enerdata, "Electricity production." https://yearbook.enerdata.net/electricity/world-electricity-production-statistics.html, Sept. 2018.

[12] J. Meadowcroft and O. Langhelle, *Caching the Carbon: The Politics and Policy of Carbon Capture and Storage*. Edward Elgar Pub, 2011.

[13] IPCC, *Carbon Dioxide Capture and Storage: Special Report of the Intergovernmental Panel on Climate Change*. United Nations, 2005.

[14] G. D. Pirngruber, F. Guillou, A. Gomez, and M. Clausse, "A theoretical analysis of the energy consumption of post-combustion CO_2 capture processes by temperature swing adsorption using solid sorbents," *International Journal of Greenhouse Gas Control*, vol. 14, pp. 74–83, May 2013.

[15] T. Pröll, G. Schöny, G. Sprachmann, and H. Hofbauer, "Introduction and evaluation of a double loop staged fluidized bed system for post-combustion CO_2 capture using solid sorbents in a continuous temperature swing adsorption process," *Chemical Engineering Science*, vol. 141, pp. 166–174, Feb. 2016.

[16] G. Schöny, E. Zehetner, J. Fuchs, T. Pröll, G. Sprachmann, and H. Hofbauer, "Design of a bench scale unit for continuous CO_2 capture via temperature swing adsorption—fluid-dynamic feasibility study," *Chemical Engineering Research and Design*, vol. 106, pp. 155–167, Feb. 2016.

[17] G. Schöny, F. Dietrich, J. Fuchs, T. Pröll, and H. Hofbauer, "A multi-stage fluidized bed system for continuous CO_2 capture by means of temperature swing adsorption – first results from bench scale experiments," *Powder Technology*, vol. 316, pp. 519–527, July 2017.

[18] F. Dietrich, G. Schöny, J. Fuchs, and H. Hofbauer, "Parameter variation in a multi-stage fluidized bed system for continuous CO_2 capture by means of temperature swing adsorption," in *Proceedings of 12th International Conference on Fluidized Bed Technology (CFB-12)* (W. Nowak, M. Sciazko, and P. Mirek, eds.), pp. 475–482, May 2017.

[19] F. Dietrich, G. Schöny, J. Fuchs, and H. Hofbauer, "Experimental study of the adsorber performance in a multi-stage fluidized bed system for continuous CO_2 capture by means of temperature swing adsorption," *Fuel Processing Technology*, vol. 173, pp. 103–111, May 2018.

[20] J. Pirklbauer, G. Schöny, F. Zerobin, T. Pröll, and H. Hofbauer, "Optimization of stage numbers in a multistage fluidized bed temperature swing adsorption system for CO_2 capture," *Energy Procedia*, vol. 114, pp. 2173–2181, July 2017.

[21] J. Pirklbauer, G. Schöny, T. Pröll, and H. Hofbauer, "Impact of stage configurations, lean-rich heat exchange and regeneration agents on the energy demand of a multistage fluidized bed TSA CO_2 capture process," *International Journal of Greenhouse Gas Control*, vol. 72, pp. 82–91, May 2018.

[22] E. Zehetner, G. Schöny, J. Fuchs, T. Pröll, and H. Hofbauer, "Fluid-dynamic study on a multistage fluidized bed column for continuous CO_2 capture via temperature swing adsorption," *Powder Technology*, vol. 316, pp. 528–534, July 2017.

[23] E. Zehetner, G. Schöny, and H. Hofbauer, "L-valve design study for a continuous temperature swing adsorption CO_2 capture unit," in *Proceedings of 12th International Conference on Fluidized Bed Technology (CFB-12)* (W. Nowak, M. Sciazko, and P. Mirek, eds.), pp. 199–206, May 2017.

[24] O. Blüh and N. Stark, *Die Adsorption.* Springer Fachmedien Wiesbaden GmbH, 1929.

[25] C. G. Hill, *An Introduction to Chemical Engineering Kinetics and Reactor Design.* JOHN WILEY & SONS INC, 1977.

[26] D. Bathen and M. Breitbach, *Adsorptionstechnik.* Springer Berlin Heidelberg, 2001.

[27] J. Keller and R. Staudt, *Gas Adsorption Equilibria.* Springer-Verlag GmbH, 2004.

[28] G. Schöny, *Post combustion CO_2 capture based on temperature swing adsorption – from process evaluation to continuous bench scale operation.* PhD thesis, TU Wien, 2015.

[29] W. J. T. Barry Crittenden, *Adsorption Technology & Design.* Butterworth Heinemann, 1998.

[30] R. Veneman, N. Frigka, W. Zhao, Z. Li, S. Kersten, and W. Brilman, "Adsorption of H_2O and CO_2 on supported amine sorbents," *International Journal of Greenhouse Gas Control*, vol. 41, pp. 268–275, Oct. 2015.

[31] H. M. Rowson, "Fluid bed adsorption of carbon disulfide," *British Chemical Engineering*, vol. 8, no. 3, pp. 180–184, 1963.

[32] D. A. Avery and D. H. Tracey, "Application of fluidized beds of activated carbon in solvent recovery from air or gas streams," *IChemE Symp. Ser. (Fluid.)*, vol. 30, pp. 28–33, 1968.

[33] A. Abrahamsen and D. Geldart, "Behaviour of gas-fluidized beds of fine powders part i. homogeneous expansion," *Powder Technology*, vol. 26, pp. 35–46, May 1980.

[34] D. Geldart, "Estimation of basic particle properties for use in fluid-particle process calculations," *Powder Technology*, vol. 60, pp. 1–13, Jan. 1990.

[35] H. Wadell, "Volume, shape, and roundness of quartz particles," *The Journal of Geology*, vol. 43, pp. 250–280, Apr. 1935.

[36] R. R. Irani and C. F. Callis, *Particle Size: Measurement, Interpretation, and Application.* John Wiley and Sons, 1963.

[37] C. Y. Wen and Y. H. Yu, "A generalized method for predicting the minimum fluidization velocity," *AIChE Journal*, vol. 12, pp. 610–612, May 1966.

[38] S. Ergun, "Fluid flow through packed columns," *Fluid Flow through Packed Columns*, vol. 48, no. 2, pp. 89–94, 1952.

[39] J. R. Grace, "Fluidized-bed hydrodynamics," in *Handbook of Multiphase Systems* (G. Hetsroni, ed.), Washington: Hemisphere, 1982.

[40] O. Molerus and K.-E. Wirth, *Heat Transfer in Fluidized Beds.* Springer Netherlands, 1997.

[41] G. Löffler, *A Modeling Study on Fuel-nitrogen Conversion to NO and N_2O Related to Fluidized Bed Combustion.* PhD thesis, TU Wien, 2001.

[42] A. Anantharaman, R. A. Cocco, and J. W. Chew, "Evaluation of correlations for minimum fluidization velocity (U) in gas-solid fluidization," *Powder Technology*, vol. 323, pp. 454–485, Jan. 2018.

[43] W.-C. Yang, *Handbook of Fluidization and Fluid-Particle Systems.* CRC Press, 2003.

[44] T. H. Hsiung and G. Thodos, "Expansion characteristics of gas-fluidized beds," *The Canadian Journal of Chemical Engineering*, vol. 55, pp. 221–224, Apr. 1977.

[45] D. Geldart, "Types of gas fluidization," *Powder Technology*, vol. 7, pp. 285–292, May 1973.

[46] L. Davies and J. F. Richardson, "Gas interchange between bubbles and continuous phase in a fluidised bed," *Trans. Inst. Chem. Engrs.*, vol. 44, no. 8, pp. 293–305, 1966.

[47] M. Horio and A. Nonaka, "A generalized bubble diameter correlation for gas-solid fluidized beds," *AIChE Journal*, vol. 33, pp. 1865–1872, Nov. 1987.

[48] M. Pell, *Gas Fluidization (Handbook of Powder Technology)*. Elsevier Science, 1989.

[49] D. Kunii and O. Levenspiel, *Fluidization Engineering*. Butterworth Heinemann, 2 ed., 1991.

[50] J. R. Grace, "Contacting modes and behaviour classification of gas-solid and other two-phase suspensions," *The Canadian Journal of Chemical Engineering*, vol. 64, pp. 353–363, June 1986.

[51] J. D. Jong and J. Nomden, "Homogeneous gas-solid fluidization," *Powder Technology*, vol. 9, pp. 91–97, feb 1974.

[52] L.-S. Fan and C. Zhu, *Principles of Gas-Solid Flows*. Cambridge University Press, 1998.

[53] N. M. Čatipović, G. N. Jovanovic, and T. J. Fitzgerald, "Regimes of fluidization for large particles," *AIChE Journal*, vol. 24, pp. 543–547, May 1978.

[54] J. J. van Deemter, "Mixing patterns in large-scale fluidized beds," in *Fluidization*, pp. 69–89, Springer US, 1980.

[55] M. Horio, A. Nonaka, M. Hoshiba, K. Morishita, Y. Kobukai, J. Naito, O. Tachibana, K. Watanabe, and N. Yoshida, "Coal combustion in a transparent circulating fluidized bed," in *Circulating Fluidized Bed Technology*, pp. 255–262, Elsevier, 1986.

[56] J. S. M. Botterill, *Fluid-bed Heat Transfer*. Academic Press Inc, 1975.

[57] H. Martin, "Heat transfer between gas fluidized beds of solid particles and the surfaces of immersed heat exchanger elements, part II," *Chemical Engineering and Processing: Process Intensification*, vol. 18, pp. 199–223, July 1984.

[58] G. Flamant, N. Fatah, and Y. Flitris, "Wall-to-bed heat transfer in gas-solid fluidized beds: Prediction of heat transfer regimes," *Powder Technology*, vol. 69, pp. 223–230, Mar. 1992.

[59] A. P. Baskakov, B. V. Berg, O. K. Vitt, N. F. Filippovsky, V. A. Kirakosyan, J. M. Goldobin, and V. K. Maskaev, "Heat transfer to objects immersed in fluidized beds," *Powder Technology*, vol. 8, pp. 273–282, Nov. 1973.

[60] H.-J. Natusch, B. Neukirchen, and R. Noack, "Lokale Wärmeübergangszahlen für ein Einzelrohr und für Rohrbündel verschiedener Anordnung in Wirbelschichten," tech. rep., Forschungs-Gesellschaft Verfahrenstechnik e.V. (GVT), 1975.

[61] H. S. Mickley and C. A. Trilling, "Heat transfer characteristics of fluidized beds," *Industrial & Engineering Chemistry*, vol. 41, pp. 1135–1147, June 1949.

[62] E. Wicke and F. Fetting, "Wärmeübertragung in Gaswirbelschichten," *Chemie Ingenieur Technik*, vol. 26, pp. 301–310, June 1954.

[63] A. Mersmann, "Zum Wärmeübergang in Wirbelschichten," *Chemie Ingenieur Technik - CIT*, vol. 39, pp. 349–353, Mar. 1967.

[64] B. Neukirchen and H. Blenke, "Gestaltung horizontaler Rohrbündel in Gas-Wirbelschichtreaktoren nach wärmetechnischen Gesichtspunkten," *Chemie Ingenieur Technik*, vol. 45, pp. 307–312, Mar. 1973.

[65] N. Grewal, S. Saxena, A. Dolidovich, and S. Zabrodsky, "Effect of distributor design on heat transfer from an immersed horizontal tube in a fluidized bed," *The Chemical Engineering Journal*, vol. 18, pp. 197–201, Jan. 1979.

[66] H. Martin, "Fluid-bed heat exchangers—a new model for particle convective energy transfer," *Chemical Engineering Communications*, vol. 13, pp. 1–16, Dec. 1981.

[67] N. Grewal, "A correlation for maximum heat transfer coefficient between a horizontal tube and a gas-solid fluidized bed of small particles," *Letters in Heat and Mass Transfer*, vol. 9, pp. 377–384, Sept. 1982.

[68] D. R. Pitts, R. S. Figliola, and K. M. Hamlyn, "Heat transfer between a horizontal cylinder and a mixed particle size fluidized bed," *Journal of Heat Transfer*, vol. 104, no. 3, pp. 563–565, 1982.

[69] H.-J. Bock, J. Schweinzer, and O. Molerus, "Strömungsmechanik und Wärmeübergang in einer Wirbelschicht mit grobkörnigen Partikeln," *Chemie Ingenieur Technik*, vol. 55, no. 3, pp. 224–225, 1983.

[70] N. S. Grewal and S. C. Saxena, "Experimental studies of heat transfer between a bundle of horizontal tubes and a gas-solid fluidized bed of small particles," *Industrial & Engineering Chemistry Process Design and Development*, vol. 22, pp. 367–376, July 1983.

[71] R. L. Adams, "Heat transfer in large particle bubbling fluidized beds," *Journal of Heat Transfer*, vol. 106, no. 1, pp. 85–90, 1984.

[72] R. S. Figliola, E. G. Suarez, and D. R. Pitts, "Mixed particle size distribution effects on heat transfer in a fluidized bed," *Journal of Heat Transfer*, vol. 108, no. 4, pp. 913–915, 1986.

[73] J. G. H. Borkink and K. R. Westerterp, "Influence of tube and particle diameter on heat transport in packed beds," *AIChE Journal*, vol. 38, pp. 703–715, May 1992.

[74] O. Molerus and W. Mattmann, "Heat transfer mechanisms in gas fluidized beds. Part 3: Heat transfer in circulating fluidized beds," *Chemical Engineering & Technology*, vol. 15, pp. 291–294, Oct. 1992.

[75] O. Molerus, A. Burschka, and S. Dietz, "Particle migration at solid surfaces and heat transfer in bubbling fluidized beds—i. Particle migration measurement systems," *Chemical Engineering Science*, vol. 50, pp. 871–877, Mar. 1995.

[76] J. Wiman and A. Almstedt, "Hydrodynamics, erosion and heat transfer in a pressurized fluidized bed: influence of pressure, fluidization velocity, particle size and tube bank geometry," *Chemical Engineering Science*, vol. 52, pp. 2677–2695, Aug. 1997.

[77] N. Masoumifard, N. Mostoufi, A.-A. Hamidi, and R. Sotudeh-Gharebagh, "Investigation of heat transfer between a horizontal tube and gas–solid fluidized bed," *International Journal of Heat and Fluid Flow*, vol. 29, pp. 1504–1511, Oct. 2008.

[78] A. Blaszczuk and W. Nowak, "Bed-to-wall heat transfer coefficient in a supercritical CFB boiler at different bed particle sizes," *International Journal of Heat and Mass Transfer*, vol. 79, pp. 736–749, Dec. 2014.

[79] J. Ngoh and E. W. C. Lim, "Effects of particle size and bubbling behavior on heat transfer in gas fluidized beds," *Applied Thermal Engineering*, vol. 105, pp. 225–242, July 2016.

[80] J. S. M. Botterill and M. Desai, "Limiting factors in gas-fluidized bed heat transfer," *Powder Technology*, vol. 6, pp. 231–238, Oct. 1972.

[81] C. Beeby and O. E. Potter, "Heat transfer between a horizontal tube bundle and fine particles with air or steam," *AIChE Journal*, vol. 30, pp. 977–980, Nov. 1984.

[82] H. Ackeskog, A. Almstedt, and V. Zakkay, "An investigation of fluidized-bed scaling: heat transfer measurements in a pressurized fluidized-bed combustor and a cold model bed," *Chemical Engineering Science*, vol. 48, no. 8, pp. 1459–1473, 1993.

[83] G. Flamant, J. D. Lu, and B. Variot, "Radiation heat transfer in fluidized beds: A comparison of exact and simplified approaches," *Journal of Heat Transfer*, vol. 116, no. 3, pp. 652–659, 1994.

[84] Z. H. Fang, J. R. Grace, and C. J. Lim, "Radiative heat transfer in circulating fluidized beds," *Journal of Heat Transfer*, vol. 117, no. 4, pp. 963–968, 1995.

[85] J. Yamada, Y. Kurosaki, I. Satoh, and K. Shimada, "Radiative heat exchange between a fluidized bed and heated surface," *Experimental Thermal and Fluid Science*, vol. 11, pp. 135–142, Aug. 1995.

[86] J. Yamada, Y. Kurosaki, and T. Nagai, "Radiation heat transfer between fluidizing particles and a heat transfer surface in a fluidized bed," *Journal of Heat Transfer*, vol. 123, no. 3, pp. 458–465, 2001.

[87] S. W. Kim and S. D. Kim, "Heat transfer characteristics in a pressurized fluidized bed of fine particles with immersed horizontal tube bundle," *International Journal of Heat and Mass Transfer*, vol. 64, pp. 269–277, Sept. 2013.

[88] J. C. Petrie, W. A. Freeby, and J. A. Buckham, "In-bed heat exchangers," *Chem. Eng. Prog.*, vol. 64, pp. 45–51, Jan. 1968.

[89] S. Fukusako, S. Ishiguro, and N. Seki, "Heat-transfer characteristics from a bundle of horizontal tubes immersed in aggregative fluidized bed," *Wärme- und Stoffübertragung*, vol. 22, pp. 13–22, Jan. 1988.

[90] M. Merzsch, S. Lechner, and H. J. Krautz, "Heat-transfer from single horizontal tubes in fluidized beds: Influence of tube diameter, moisture and diameter-definition by Geldart C fines content," *Powder Technology*, vol. 235, pp. 1038–1046, Feb. 2013.

[91] A. Mathur, S. C. Saxena, and A. Chao, "Heat transfer from an immersed vertical tube in a gas-fluidized bed," *Industrial & Engineering Chemistry Process Design and Development*, vol. 25, pp. 156–163, Jan. 1986.

[92] S. Ouyang, X.-G. Li, G. Davies, and O. Potter, "Heat transfer between a vertical tube bundle and fine particles in a CFB downcomer with and without circulation of solids," *Chemical Engineering and Processing: Process Intensification*, vol. 35, pp. 21–27, Jan. 1996.

[93] S. Furui, H. Umekawa, K. Hayashi, M. Ozawa, and N. Takenaka, "Bubble behavior in vertical tube banks installed in a fluidized bed," *Heat Transfer—Asian Research*, vol. 32, pp. 727–739, Nov. 2003.

[94] B. A. Abid, J. M. Ali, and A. A. Alzubaidi, "Heat transfer in gas–solid fluidized bed with various heater inclinations," *International Journal of Heat and Mass Transfer*, vol. 54, pp. 2228–2233, Apr. 2011.

[95] M. Rüdisüli, T. J. Schildhauer, S. M. A. Biollaz, and J. R. van Ommen, "Radial bubble distribution in a fluidized bed with vertical tubes," *Industrial & Engineering Chemistry Research*, vol. 51, pp. 13815–13824, Oct. 2012.

[96] M. Rüdisüli, T. J. Schildhauer, S. M. A. Biollaz, and J. R. van Ommen, "Bubble characterization in a fluidized bed with vertical tubes," *Industrial & Engineering Chemistry Research*, vol. 51, pp. 4748–4758, Mar. 2012.

[97] R. Sundaresan and A. K. Kolar, "Axial heat transfer correlations in a circulating fluidized bed riser," *Applied Thermal Engineering*, vol. 50, pp. 985–996, Jan. 2013.

[98] V. Verma, T. Li, J.-F. Dietiker, and W. A. Rogers, "Hydrodynamics of gas-solids flow in a bubbling fluidized bed with immersed vertical u-tube banks," *Chemical Engineering Journal*, vol. 287, pp. 727–743, Mar. 2016.

[99] B. Dahlhoff and H. v. Brachel, "Wärmeübergang an horizontal in einem Fluidatbett angeordneten Rohrbündeln," *Chemie Ingenieur Technik*, vol. 40, pp. 372–376, Apr. 1968.

[100] N. Grewal, "A generalized correlation for heat transfer between a gas-solid fluidized bed of small particles and an immersed staggered array of horizontal tubes," *Powder Technology*, vol. 30, pp. 145–154, Nov. 1981.

[101] M. A. Moawed, N. S. Berbish, A. A. Allam, A. R. El-Shamy, and K. M. El-Shazly, "Heat transfer between fluidized bed and horizontal bundle of tubes in a vertical channel," *International Journal of Chemical Reactor Engineering*, vol. 8, Jan. 2010.

[102] W. B. Krause and A. R. Peters, "Heat transfer from horizontal serrated finned tubes in an air-fluidized bed of uniformly sized particles," *Journal of Heat Transfer*, vol. 105, no. 2, pp. 319–324, 1983.

[103] I. Goel, S. C. Saxena, and A. F. Dolidovich, "Heat transfer from rough and finned horizontal tubes in a gas fluidized bed," *Journal of Heat Transfer*, vol. 106, no. 1, pp. 91–97, 1984.

[104] N. S. Grewal, T. K. Cheung, and S. C. Saxena, "Heat transfer between horizontal finned tubes and a gas-solid fluidized bed," *Industrial & Engineering Chemistry Process Design and Development*, vol. 24, pp. 458–471, Apr. 1985.

[105] A. K. Kolar and V. Sastri, "Extended surface heat transfer in fluidized beds," *Chemical Engineering and Processing: Process Intensification*, vol. 22, pp. 1–17, July 1987.

[106] S. Rasouli, M. Golriz, and A. Hamidi, "Effect of annular fins on heat transfer of a horizontal immersed tube in bubbling fluidized beds," *Powder Technology*, vol. 154, pp. 9–13, June 2005.

[107] C. Penny, D. Rosero, D. Naylor, and J. Friedman, "Heat transfer to flat strips immersed in a fluidized bed," *Journal of Heat Transfer*, vol. 133, no. 7, 2011.

[108] R. Noack, "Lokaler Wärmeübergang an horizontalen Rohren in Wirbelschichten," *Chemie Ingenieur Technik*, vol. 42, pp. 371–376, Mar. 1970.

[109] H. K. Lese and R. I. Kermode, "Heat transfer from a horizontal tube to a fluidized bed in the presence of unheated tubes," *The Canadian Journal of Chemical Engineering*, vol. 50, pp. 44–48, Feb. 1972.

[110] R. Chandran, J. C. Chen, and F. W. Staub, "Local heat transfer coefficients around horizontal tubes in fluidized beds," *Journal of Heat Transfer*, vol. 102, no. 1, pp. 152–157, 1980.

[111] A. I. Karamavruç and N. N. Clark, "A fractal approach for interpretation of local instantaneous temperature signals around a horizontal heat transfer tube in a bubbling fluidized bed," *Powder Technology*, vol. 90, pp. 235–244, Mar. 1997.

[112] S. W. Kim, J. Y. Ahn, S. D. Kim, and D. H. Lee, "Heat transfer and bubble characteristics in a fluidized bed with immersed horizontal tube bundle," *International Journal of Heat and Mass Transfer*, vol. 46, pp. 399–409, Jan. 2003.

[113] F. D. Natale and R. Nigro, "A critical comparison between local heat and mass transfer coefficients of horizontal cylinders immersed in bubbling fluidised beds," *International Journal of Heat and Mass Transfer*, vol. 55, pp. 8178–8183, Dec. 2012.

[114] P. Ostermeier, A. Vandersickel, M. Becker, S. Gleis, and H. Spliethoff, "Hydrodynamics and heat transfer around a horizontal tube immersed in a Geldart b bubbling fluidized bed," *International Journal of Computational Methods and Experimental Measurements*, vol. 6, pp. 71–85, Oct. 2017.

[115] H.-J. Bock and O. Molerus, "Einfluß der Strömungsmechanik auf den Wärmeübergang in Gas/Feststoff-Wirbelschichten," *Chemie Ingenieur Technik*, vol. 52, no. 3, pp. 260–261, 1980.

[116] T. Aihara, S. Maruyama, M. Hongoh, and S. Aya, "Heat transfer and pressure loss of a very shallow fluidized-bed heat exchanger part 1. experiment with a single row of tubes," *Experimental Thermal and Fluid Science*, vol. 1, pp. 315–323, Oct. 1988.

[117] S. Maruyama, T. Aihara, Y. Tanaka, and K. Kasahara, "Heat transfer and pressure loss of a very shallow fluidized-bed heat exchanger part 2. experiment with multirow tube banks," *Experimental Thermal and Fluid Science*, vol. 1, pp. 325–333, Oct. 1988.

[118] R. L. Adams and J. R. Welty, "An analytical study of bubble and adjacent tube influence on heat transfer to a horizontal tube in a gas fluidized bed," *Journal of Heat Transfer*, vol. 104, no. 1, pp. 206–209, 1982.

[119] D. Moslemian, M. Chen, and B. Chao, "Heat transfer to horizontal tubes in a fluidized bed: The role of superficial gas and local particle velocities," *Experimental Thermal and Fluid Science*, vol. 4, pp. 76–89, Jan. 1991.

[120] O. Molerus and W. Mattmann, "Heat transfer in gas fluidized beds. Part 2: Dependence of heat transfer on gas velocity," *Chemical Engineering & Technology*, vol. 15, pp. 240–244, Aug. 1992.

[121] O. Molerus, A. Burschka, and S. Dietz, "Particle migration at solid surfaces and heat transfer in bubbling fluidized beds—II. Prediction of heat transfer in bubbling fluidized beds," *Chemical Engineering Science*, vol. 50, pp. 879–885, Mar. 1995.

[122] M. Ozawa, H. Umekawa, T. Matsuda, N. Takenaka, A. Tsuruno, and M. Matsubayashi, "Void fraction profile in tube-banks of a simulated fluidized-bed heat exchanger," *Nuclear Instruments and Methods in Physics Research Section A: Accelerators, Spectrometers, Detectors and Associated Equipment*, vol. 377, pp. 144–147, July 1996.

[123] C. C. Wu and G. J. Hwang, "Flow and heat transfer characteristics inside packed and fluidized beds," *Journal of Heat Transfer*, vol. 120, no. 3, pp. 667–673, 1998.

[124] O. Molerus, "Fluid mechanics and heat transfer in fluidized beds," *KONA Powder and Particle Journal*, vol. 18, no. 0, pp. 121–130, 2000.

[125] J. C. Chen, "Surface contact—its significance for multiphase heat transfer: Diverse examples," *Journal of Heat Transfer*, vol. 125, no. 4, pp. 549–566, 2003.

[126] H. Yurong, L. Huilin, S. Qiaoqun, Y. Lidan, Z. Yunhua, D. Gidaspow, and J. Bouillard, "Hydrodynamics of gas-solid flow around immersed tubes in bubbling fluidized beds," *Powder Technology*, vol. 145, pp. 88–105, July 2004.

[127] S. Ahn, S. Bae, B. Lee, W. Kim, and M. Bae, "Fluid flow and heat transfer in fluidized bed vertical shell and tube type heat exchanger," *International Communications in Heat and Mass Transfer*, vol. 32, pp. 224–232, Jan. 2005.

[128] A. A. B. Pécora and M. R. Parise, "Heat transfer coefficient in a shallow fluidized bed heat exchanger with a continuous flow of solid particles," *Journal of the Brazilian Society of Mechanical Sciences and Engineering*, vol. 28, Sept. 2006.

[129] A. Stefanova, H. Bi, C. Lim, and J. Grace, "Heat transfer from immersed vertical tube in a fluidized bed of group a particles near the transition to the turbulent fluidization flow regime," *International Journal of Heat and Mass Transfer*, vol. 51, pp. 2020–2028, Apr. 2008.

[130] K. Pisters and A. Prakash, "Investigations of axial and radial variations of heat transfer coefficient in bubbling fluidized bed with fast response probe," *Powder Technology*, vol. 207, pp. 224–231, Feb. 2011.

[131] A. Stefanova, H. Bi, J. Lim, and J. Grace, "Local hydrodynamics and heat transfer in fluidized beds of different diameter," *Powder Technology*, vol. 212, pp. 57–63, Sept. 2011.

[132] V. Rimpiläinen, L. M. Heikkinen, and M. Vauhkonen, "Moisture distribution and hydrodynamics of wet granules during fluidized-bed drying characterized with volumetric electrical capacitance tomography," *Chemical Engineering Science*, vol. 75, pp. 220–234, June 2012.

[133] C. Gutfinger and N. Abuaf, "Heat transfer in fluidized beds," in *Advances in Heat Transfer Volume 10*, pp. 167–218, Elsevier, 1974.

[134] S. Saxena, N. Grewal, J. Gabor, S. Zabrodsky, and D. Galershtein, "Heat transfer between a gas fluidized bed and immersed tubes," in *Advances in Heat Transfer*, pp. 149–247, Elsevier, 1979.

[135] S. S. Zabrodsky, *Hydrodynamics and Heat Transfer in Fluidized Beds*. The MIT Press, 1966.

[136] N. I. Gel'perin, V. G. Ajnstejn, and A. V. Zajkovskij, "Hydraulische und wärmetechnische Eigenschaften eines Fließbettes mit waagerechten Rohrbündeln," *Chimiceskoe i Neftjanoe Masinostroenie*, vol. 3, pp. 17–20, 1968.

[137] H. Martin, "Wärme- und Stoffübertragung in der Wirbelschicht," *Chemie Ingenieur Technik*, vol. 52, no. 3, pp. 199–209, 1980.

[138] H. Martin, "M5 heat transfer in fluidized beds," in *VDI Heat Atlas*, pp. 1301–1310, Springer Berlin Heidelberg, 2010.

[139] E. U. Schlünder, "Wärmeübergang an bewegte Kugelschüttungen bei kurzfristigem Kontakt," *Chemie Ingenieur Technik*, vol. 43, pp. 651–654, June 1971.

[140] J. Yates, R. Ruiz-Martinez, and D. Cheesman, "Prediction of bubble size in a fluidized bed containing horizontal tubes," *Chemical Engineering Science*, vol. 45, no. 4, pp. 1105–1111, 1990.

[141] T. W. Asegehegn and H. J. Krantz, "Hydrodynamic simulation of gas-solid bubbling fluidized bed containing horizontal tubes," in *Proceedings of the 20th International Conference on Fluidized Bed Combustion* (G. Yue, H. Zhang, C. Zhao, and Z. Luo, eds.), (Berlin, Heidelberg), pp. 864–869, Springer Berlin Heidelberg, 2010.

[142] S. Andersson, F. Johnsson, and B. Leckner, "Fluidization regimes in non-slugging fluidized beds," in *The 10th International Conference on Fluidized Bed Combustion*, (San Francisco, USA), The American Society of Mechanical Engineers, 1989.

[143] S. Lechner, M. Merzsch, and H. J. Krautz, "Heat-transfer from horizontal tube bundles into fluidized beds with Geldart A lignite particles," *Powder Technology*, vol. 253, pp. 14–21, Feb. 2014.

[144] O. Levenspiel, *Tracer Technology*. Springer New York, 2012.

[145] L. R. Glicksman, "Scaling relationships for fluidized beds," *Chemical Engineering Science*, vol. 43, no. 6, pp. 1419–1421, 1988.

[146] J. Werther, *Fluidized-Bed Reactors*. Wiley Online Library, 2007.

[147] D. C. Guío-Pérez, T. Pröll, J. Wassermann, and H. Hofbauer, "Design of an inductance measurement system for determination of particle residence time in a dual circulating fluidized bed cold flow model," *Industrial & Engineering Chemistry Research*, vol. 52, pp. 10732–10740, July 2013.

[148] P. H. Sydenham and R. Thorn, eds., *Handbook of Measuring System Design*. John Wiley & Sons, Ltd, July 2005.

[149] AnalogDevices, *Balanced Modulator/Demodulator AD630*, 2015. Rev. G.

[150] W. R. Inc., "Mathematica, Version 11.2," 2017. Champaign, IL, 2018.

[151] D. C. Guío-Pérez, T. Pröll, and H. Hofbauer, "Measurement of ferromagnetic particle concentration for characterization of fluidized bed fluid-dynamics," *Powder Technology*, vol. 239, pp. 147–154, May 2013.

List of figures

List of tables

Appendix A

Publications

Paper [1]

Powder Technology 316 (2017) 512–518

Contents lists available at ScienceDirect

Powder Technology

journal homepage: www.elsevier.com/locate/powtec

Heat transfer challenge and design evaluation for a multi-stage temperature swing adsorption process

G. Hofer [a,*], J. Fuchs [b], G. Schöny [b], T. Pröll [a]

[a] University of Natural Resources and Life Sciences, Department of Material Sciences and Process Engineering, Peter-Jordan-Str. 82, 1190 Vienna, Austria
[b] TU Wien, Institute of Chemical Engineering, Getreidemarkt 9/166, 1060 Vienna, Austria

ARTICLE INFO

Article history:
Received 25 April 2016
Received in revised form 28 October 2016
Accepted 19 December 2016
Available online 22 December 2016

Keywords:
Temperature swing adsorption
TSA
Carbon capture
Heat transfer
Fluidized bed
Heat exchanger design

ABSTRACT

Functionalized solid amine-based temperature swing adsorption (TSA) processes have recently been proposed as a potential way to reduce the energy-penalty of post-combustion carbon capture processes. Thereby, multi-stage fluidized bed contactors with immersed heat exchanger surfaces and counter-current flow of solids and gas phase may solve the heat transfer challenge while maintaining the thermodynamic process requirements. Hence, the present work develops design requirements for TSA stages based on achievable heat transfer rates in bubbling fluidized beds. The considered particles are Geldart Type B. It is shown that the pressure drop of multi-stage fluidized bed TSA units for flue gas CO_2 capture is practically determined by the heat exchange requirement. Scalability, maintainability and durability of different heat exchanger geometries are considered. The net movement and mixing of particles within the bubbling bed stage must be maintained in spite of the immersed heat exchangers concerning possible dead zones in the area of the tube bundles. Comprehensive models are used to predict heat transfer coefficients for tubes immersed in fluidization. A heat transfer measurement test device for optimization of the heat exchanger geometry has been put into operation and heat exchange measurement results are compared to calculated heat transfer coefficients. It is shown that experimentally obtained heat transfer rates for single tubes are in good agreement with modeled values. A model proposed for Geldart A particles is used to estimate heat transfer rates for two particular tube bundles with a tube diameter of 25 mm and horizontal tube spacing of 2.2 and 2.8. It is shown that the calculated results represent heat transfer rates qualitatively and quantitatively for tube bundle heat exchangers immersed in Geldart Type B particle fluidized beds. Although this article has been motivated by heat exchange in TSA, it may be of interest for other applications concerned with heat transfer between bubbling fluidized beds and immersed heat exchanger surfaces.

1. Introduction

A double loop, multi-staged fluidized bed system operated with functionalized solid amine sorbents, by means of temperature swing adsorption (TSA), has been introduced for continuous post-combustion CO_2 separation tasks [1,2]. In this process configuration, staged bubbling fluidized bed columns are used for the adsorber and desorber, respectively. For continuous operation it is necessary to extract the heat of adsorption from the adsorber and to supply about the same amount of heat into the desorber. In addition, the sensible heat caused by the temperature swing has to be transferred. Thermodynamically, the contactors could be favorably designed as fixed or moving beds. However, heat transfer rates are poor for fixed and moving bed regime and heat transfer is crucial in TSA [3]. Hence, fluidized bed contactors with counter-current flow of solids and gas may solve the heat transfer challenge while maintaining the thermodynamic process requirements.

On the one hand, it is important to achieve high heat transfer coefficients in order to limit the pressure drop across the adsorber column, because of the major influence on blower power consumption. On the other hand, high heat transfer rates are equally important with concern to the desorber. The restriction on stripping steam demand for desorption has limiting influence on fluidization and, therefore, on fluidized bed volume to accommodate heat exchanger geometries. Furthermore, with increasing pressure drop difference between adsorber and desorber it gets harder to seal them against each other, and the possibility of purging supply lines increases. Since adsorption kinetics are known to be fast and mass transfer is efficient in fluidized beds, we formulate the hypothesis that the required heat exchanger surface will determine the dimensions of the fluidized bed stages. This would mean that the practically achieved heat transfer rates, the resulting compactness of the heat exchanger bundles and the operational expenditures would determine the overall costs of such a continuous TSA device.

* Corresponding author.
E-mail address: gerhard.hofer@boku.ac.at (G. Hofer).

http://dx.doi.org/10.1016/j.powtec.2016.12.062
0032-5910/

Fig. 1 shows the principle of the double loop fluidized bed system including the relevant heat exchangers in the adsorber and desorber reactor columns featuring five stages each for efficient CO_2 separation with resulting capture efficiencies up to 90% or more. The top-down moving sorbent particles are fluidized by introducing raw exhaust gas at the bottom of the adsorber column. While contacting the sorbent in counter-current flow, CO_2 is progressively removed from the flue gas. After the separation process, when the rich sorbent reaches the bottom of the adsorber, these particles are lifted through a riser system to the desorber, that is operated at higher temperatures. For regeneration, stripping steam is used to fluidize the top-down streaming sorbent in the desorber. On top of the desorber, a gas mixture containing steam and CO_2 is obtained. In order to obtain pure CO_2 the steam is condensed downstream of the desorber. To close the particle circulation loop, the lean sorbent is lifted from the bottom of the desorber column to the adsorber for further CO_2 separation.

As mentioned previously, heat exchange is expected to be the dominant limiting factor when carrying out TSA. Therefore, the present work focuses on the application of established heat exchange calculation methods for immersed surfaces in bubbling fluidized beds; in particular single tubes [6–9] and tube bundles [10–14]. Previously defined TSA process design parameters [1,2,4] are considered as input data. Furthermore, the calculated results are used to develop an awareness for practical heat exchanger design possibilities. In spite of already accomplished investigations regarding heat exchange in bubbling fluidized beds, a heat transfer measurement test device (HTMT) has been deployed to conduct heat exchange measurements at immersed single tubes and, preferably, tube bundles in various settings. It is shown, that the theoretically achievable heat transfer coefficients calculated with the model proposed by Lechner et al. [19], valid for Geldart Type A particles only, is also able to predict coefficients for Geldart Type B bulk material.

2. Heat exchange in TSA

2.1. Prediction of necessary heat exchanger surface area

Based on Fourier's law the heat flow Q to be transported in the adsorber and desorber can be written as

$$Q = h \cdot A_{hex} \cdot \Delta T_m \tag{1}$$

where h is the overall heat transfer coefficient applied to the outside diameter d_o of the heat exchanging tube

$$h = \left[\frac{d_o}{d_i}\cdot\frac{1}{h_i} + \frac{d_o}{2\cdot\lambda}\cdot \ln\left(\frac{d_o}{d_i}\right) + \frac{1}{h_{fb}}\right]^{-1} \tag{2}$$

For thin tube walls with high heat conductivity λ and turbulent flow of liquid in the tubes we may assume

$$\frac{d_o}{2\cdot\lambda}\cdot \ln\left(\frac{d_o}{d_i}\right) \ll \frac{d_o}{d_i}\cdot\frac{1}{h_i} \approx \frac{1}{h_i} < \frac{1}{h_{fb}} \tag{3}$$

and thus

$$h \approx \left[\frac{1}{h_i} + \frac{1}{h_{fb}}\right]^{-1} \tag{4}$$

Assuming that the reactor design has a rectangular cross sectional area with the lengths a and b and, furthermore, 100% of this area is used to accommodate heat exchanger tubes, the total heat exchanging surface area A_{hex} can be estimated by

$$A_{hex} = \frac{a\cdot b\cdot \pi}{d_o\cdot s_h\cdot s_v}\cdot H_{fb} \tag{5}$$

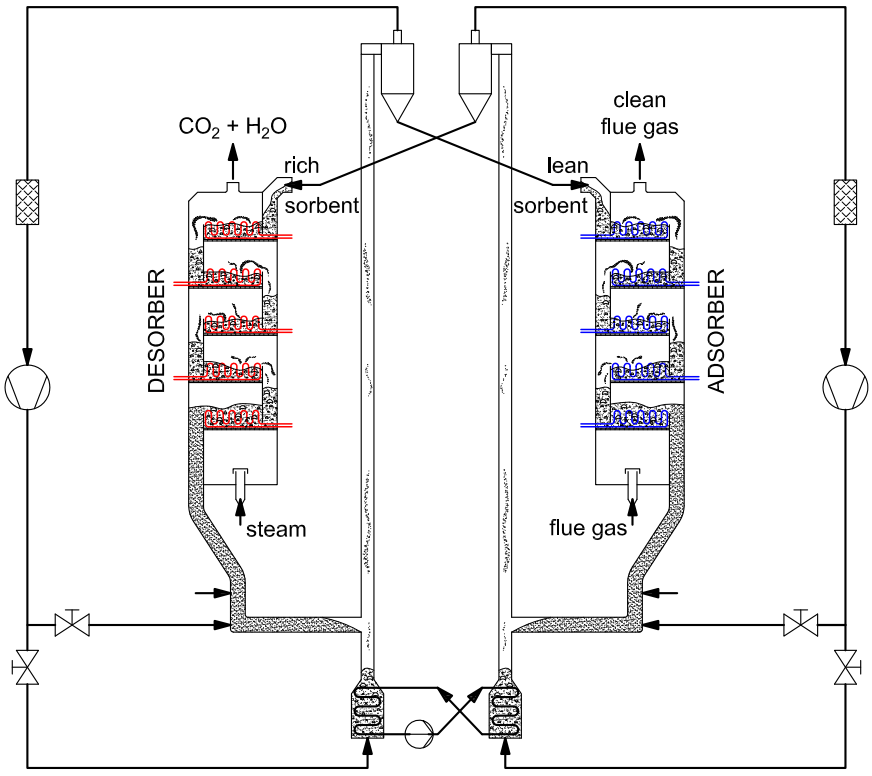

Fig. 1. Principle of the continuous TSA CO_2 separation process with relevant heat exchange requirements featuring five stages in the adsorber and desorber (blue = cooling requirement, red = heating requirement).

where s_h characterizes the horizontal and s_v the vertical tube spacing

$$\left.\begin{aligned} s_h &= \frac{p_h}{d_o} \\ s_v &= \frac{p_v}{d_o} \end{aligned}\right\} \tag{6}$$

Generally, the accumulated height of all fluidized beds H_{fb} contained in the reactor columns can be calculated by the following equation.

$$H_{fb} = \frac{\Delta p_{fb} \cdot n_{stage}}{(1-\varepsilon) \cdot \left(\rho_p - \rho_g\right) \cdot g} \tag{7}$$

Thus, an approximation of A_{hex} for either horizontal or vertical tubes can be derived.

$$A_{hex} = \frac{a \cdot b \cdot \pi}{d_o \cdot s_h \cdot s_v} \cdot \frac{\Delta p_{fb} \cdot n_{stage}}{(1-\varepsilon) \cdot \left(\rho_p - \rho_g\right) \cdot g} \approx \frac{Q}{\Delta T_m} \cdot \left[\frac{1}{h_i} + \frac{1}{h_{fb}}\right] \tag{8}$$

Assuming a given amount of heat to be transferred (Q), Eq. (8) leads to a simplified correlation between Δp_{fb}, the pressure drop across the fluidized bed each reactor stage contains, and the overall heat transfer coefficient h.

$$\Delta p_{fb} \sim \frac{1}{h} \tag{9}$$

Eq. (9) shows that high heat transfer rates engender a decrease of required Δp_{fb} and, concurrently, the reduction of the required heat exchanger surface area. Since there is a focus on attaining minimum pressure drops, especially across the adsorber column, it is even more important to achieve high heat transfer rates when designing heat exchangers for TSA.

Furthermore, Eqs. (7) and (8) can be used to deduce a correlation between the mean logarithmic temperature difference ΔT_m and the fluidized bed height H_{fb}. The obtained results, displayed in Fig. 2, are calculated with assumed TSA and heat exchanger parameters, reported in Table 1. The heat of adsorption Q is determined with the adsorption enthalpy taken from [4] for an assumed absolute CO_2 capture rate of 100 kg/d. It should be noted that these calculations neglect the transport of sensible heat, caused by the temperature swing, between the adsorber and desorber. It is evident that the decrease of ΔT_m causes an increase of the required fluidized bed height H_{fb} and, thus, of the fluidized bed pressure drop (at constant superficial gas velocity). For example, for the heat duty shown in Table 1 and a bed height of 60 mm [2], a ΔT_m of about 25 K would be required at a superficial gas velocity of 0.39 m/s, for which a maximum fluidized bed heat transfer rate of 350 W/(m^2 K) occurs (Fig. 4). Thus, for reasonable temperature differences below 30 K, the total bed inventory is determined by the required heat exchanger surface rather than by limitations because of fluidized bed hydrodynamics or adsorption itself.

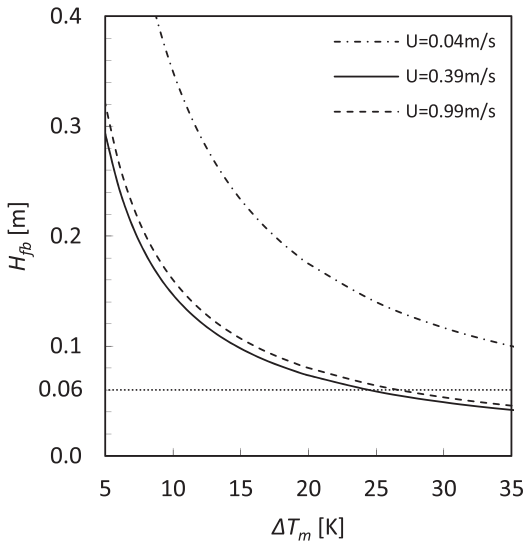

Fig. 2. Fluidized bed height H_{fb} as a function of the mean logarithmic temperature difference ΔT_m.

Table 1
Assumed TSA parameters.

Parameter	Value	Unit
a	0.15	[m]
b	0.15	[m]
d_o	0.025	[m]
$d_{p,m}$	200	[μm]
h_{fb}	Lechner et al. d_o = 25 mm, s_h = 2.8 (Fig. 4)	[W/(m^2 K)]
h_i	3000	[W/(m^2 K)]
n_{stage}	5	[−]
Q	1653	[W]
s_h	2.8	[−]
s_v	1.4	[−]

2.2. Single tube and tube bundle heat transfer rates

On the one hand, it is important to derive accurate heat transfer coefficients for heat exchanger surfaces immersed in bubbling fluidized beds. On the other hand, the heat exchanger design should not stand in contrast to the crosswise particle movement in each reactor stage. Therefore, a certain minimum pipe spacing must be maintained. Since TSA processes are operating at temperatures below 425 K and considered particle diameters are less than 500 μm, the gas-convective heat transfer and heat transfer due to radiation can be neglected [5]. Thus, the decisive factor is heat transfer due to particle convection.

Many studies have been published to describe heat transfer in bubbling fluidized beds concerning single tubes [6–9] and tube bundles [10–14] in either horizontal or vertical alignment with different tube arrangements, such as in-line, staggered or crossover. In addition, the effect of finned tubes on heat transfer has been investigated [15,16]. In many of the stated studies at least one fluidized bed parameter (gas velocity, particle size) or heat exchanger design parameter (tube diameter and/or pitch) has been varied in order to investigate the influence on heat exchange. More comprehensive calculation models to predict heat transfer coefficients pertaining immersed single tubes in bubbling fluidized beds may be those developed by Molerus et al. [17] and Martin [18]. This is because of the fact that these models do not just lead to maximum heat transfer rates for applied fluidized bed parameters, but comprise a relation to (minimum) fluidization velocity as well as (minimum) bed voidage and likewise consider gas and particle properties, such as thermal conductivity and specific heat capacity. Since the abovementioned calculation methods of Molerus et al. and Martin merely consider single tubes, Lechner et al. [19] developed a model to modify the single tube models by Molerus et al. and Martin for particular tube bundle designs. The model represents a reduction factor regarding heat transfer at immersed tube bundles by implementing terms respecting tube diameter, spacing and arrangement. Despite the fact that the correlation by Lechner et al. [19] has been validated for Geldart A particles only, it might be useful for a first approximation of heat transfer rates with Geldart B particles relevant for TSA processes.

Fig. 3 shows the theoretically achievable heat transfer coefficients at adsorber and desorber conditions between immersed single tube heat exchangers and the contacting particles, calculated with Molerus et al. [17] concerning reasonable mean particle diameters $d_{p,m}$. Higher heat

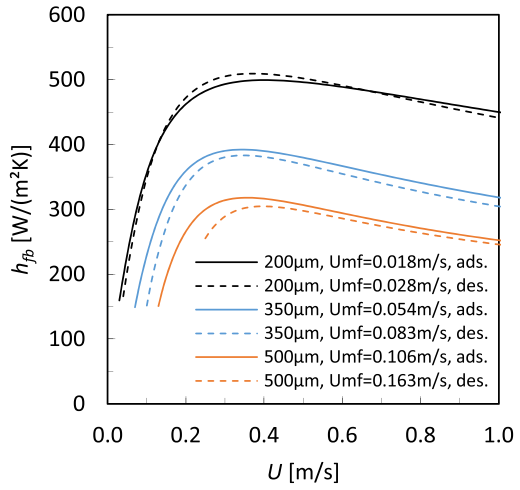

Fig. 3. Single tube heat transfer rates, calculated with the model by Molerus et al. [17] for 200 µm, 350 µm and 500 µm sorbent particles. Minimum fluidization velocity calculated for adsorber and desorber gas atmosphere.

transfer rates are achieved with smaller particles. Heat transfer increases with increasing fluidization number until a certain point is reached, where heat exchange again begins to decrease.

As mentioned before, the developed model by Lechner et al. [19] for tube bundles was validated for Geldart Type A particles only. However, to acquire an awareness concerning heat exchange between immersed tube bundles and the contacting particles, the model is applied to the calculation results obtained with the model by Molerus et al. [17]. Fig. 4 shows the results for particular tube bundle designs with two different tube diameters (d_o = 25 and 30 mm) and horizontal tube spacing (s_h = 2.2 and 2.8). A vertical tube spacing of $s_v = s_h/2$ is assumed. When the models of Molerus et al. and Lechner et al. are used to predict heat transfer rates in bubbling fluidized beds it is evident, that tube spacing has significant influence on the achievable heat transfer rates, whereas the influence of the tube diameter is rather small.

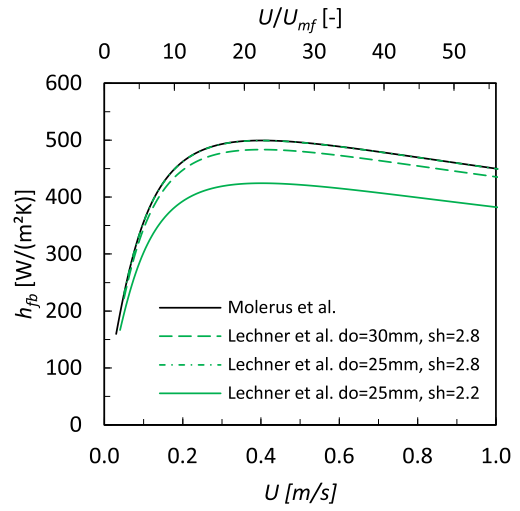

Fig. 4. Comparison of single tube and tube bundle heat transfer rates, calculated with the model by Molerus et al. [17] for 200 µm sorbent particles at adsorber conditions, modified by applying the model by Lechner et al. [19] for specific tube bundle heat exchanger configurations.

2.3. Practical stage design

In essence, there are not too many possibilities of how a practical heat exchanger design might look like. For reasons concerning capital and operational expenditures, the stage heat exchangers will most likely be constructed as tube bundles. However, this simple and well-established design approach leaves a few possibilities for options regarding tube diameter, arrangement and tube alignment inside the fluidized bed. Conceivably, tubes might be aligned horizontally or vertically. Furthermore, the resistance to particle flow and the resulting residence time distribution of particles must be considered. Therefore, it might be inevitable to align tubes longitudinal to the particle movement, as this is illustrated with the blue arrow in Fig. 5. At the present stage of investigation it is unclear if this particular design has a disadvantage on heat transfer compared to transversal oriented tubes. Another disadvantage of the just-mentioned heat exchanger design might be the relatively poor capability regarding scale up to large reactor units, because large tube lengths must be supported accordingly as oscillating mechanical forces will act on the tubes. However, a badly designed support would have a significant drag on particle flux. Hence, vertical tubes might have an advantage when it comes to forces caused by the rising bubbles and the moving particles of the fluidized bed. Furthermore, the maintainability of different heat exchanger designs must be considered.

3. Experimental setup

Although many studies regarding heat transfer in bubbling fluidized beds are available in the literature, a heat transfer measurement test device has been commissioned. Compressed dry air, with a volume flow in the range of 2.5–400 Nm^3/h, fluidizes the bulk material the HTMT contains. The heat transfer measurement device has a rectangular cross sectional area of 400 × 200 mm and the bubbling bed height can get up to approximately 400 mm. Fig. 6 shows the actual device in horizontal tube bundle configuration. Exchangeable front covers with varying horizontal hole pitch (30, 38, 55, 70 and 85 mm) accommodate dummy tubes with different diameters (16, 20, 25 and 30 mm).

The design of the cylindrical heat transfer measurement probes was inspired by the work of Lechner et al. [19]. A typical probe is made of an electrically heated copper part in between of two acrylic glass ends (Fig. 7). The acrylic glass ensures that the entire amount of introduced heat is transported to the contacting particles of the fluidized bed by isolating the probe from the HTMT casing. The electrical power consumption of the heating cartridge is measured and resistance thermometers determine the temperature of the heated probe. Four other tube dummies of each diameter are as well equipped with resistance thermometers to measure the temperature of the surrounding fluidized bed. With

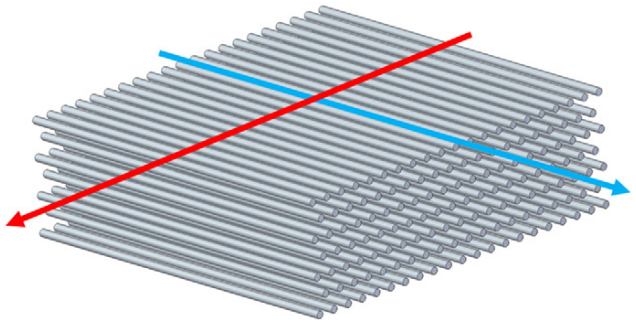

Fig. 5. Horizontal tube bundle and possible particle flow (blue = longitudinal, red = transversal).

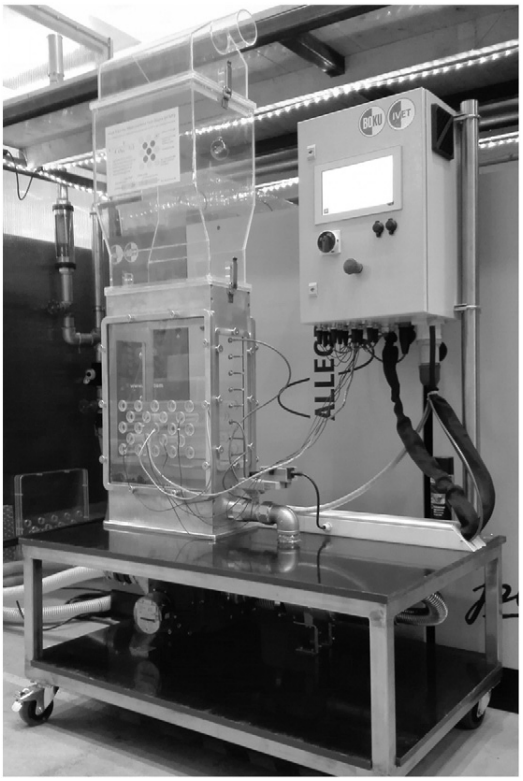

Fig. 6. Heat transfer measurement test device in horizontal tube bundle configuration.

the known surface area of the copper part, the heat transfer coefficient can be calculated.

4. Results and discussion

In the following, first results obtained from measurements with the previously introduced HTMT will be presented. The measurements were conducted with glass bead bulk material with a mean particle diameter of 200 μm and a particle density of 2450 kg/m^3 at ambient conditions.

At first, heat transfer at a single tube with a tube diameter d_o = 25 mm was investigated. Furthermore, two distinct tube bundle heat exchanger settings were tested. The tube diameter d_o was 25 mm and horizontal tube spacing s_h was set to 2.2 and 2.8. The vertical tube spacing was $s_v = s_h/2$. Each measurement was conducted with varying superficial gas velocity up to about 1 m/s. The relevant data (temperatures of the fluidized bed and heat transfer measurement probe, heat duty and gas volume flow) was logged continuously.

The data obtained from the single tube measurement was then compared to the model developed by Molerus et al. [17]. The data obtained from the tube bundle measurements was compared to the heat transfer rates calculated with Molerus et al. [17] with applied tube bundle reduction factor proposed by Lechner et al. [19].

4.1. Single tube

Fig. 8 illustrates the test results regarding an immersed single tube compared to calculated heat transfer rates. It should be noted that the indicated standard deviation has been doubled for reasons of visibility. It is shown that the measured data agree well to the modeled data until a superficial gas velocity of about 0.5 m/s is reached, which is equal to a fluidization number U/U_{mf} of 15. The model predicts decreasing heat exchange rates for high gas velocities, whereas actual heat transfer seems to remain approximately constant for the investigated range of superficial gas velocity. Hence, after exceeding 0.5 m/s, the measured heat exchange rates are no longer in good agreement with the modeled values.

4.2. Tube bundle

Fig. 9 illustrates measurement results regarding heat transfer coefficients obtained with two different tube bundle settings (d_o = 25 mm, s_h = 2.2 and 2.8, $s_v = s_h/2$). Herein, the superficial gas velocity equals the gas velocity without any tubes immersed in the fluidized bed. These results are compared to heat transfer coefficients calculated with Molerus et al. [17], which were modified using the model proposed by Lechner et al. [19].

It is shown that the measured heat transfer coefficients drop with decreasing tube spacing, as this is also predicted by the modeled data. The values calculated with the model by Lechner et al. are in good qualitative and quantitative agreement to the measured values. It seems, that the tube bundle reduction factor, determined by measurements with Geldart A particles, is also applicable to tube bundle heat exchangers immersed in Geldart Type B particle fluidized beds.

With regard to the illustrated standard deviations it should be noted that the higher values occurring for the measurement with smaller tube spacing (HTMT, d_o = 25 mm, s_h = 2.2, $s_v = s_h/2$) are the result of increased electrostatic charges between the particles.

5. Conclusion and outlook

Different models from literature are available to predict heat transfer coefficients for heat exchangers immersed in bubbling fluidized beds. Molerus et al. [17] proposed a model for single tube heat transfer coefficients. Lechner et al. [19] proposed a model, valid for Geldart Type A particles only, to calculate heat transfer rates for tube bundles immersed in fluidized beds, when single tube rates are known. A cold flow model was designed and commissioned in order to validate the stated models with experimental results obtained for Geldart Type B particles (glass beads). Heat transfer coefficients were measured for different heat exchangers with horizontal tube alignment (single tube/tube bundles with different tube spacing) at varying superficial gas velocity.

With regard to single tubes the results clearly indicate that the measured heat transfer rates are in good agreement with the model by Molerus et al. At low gas velocities heat transfer begins to increase until a maximum of about 500 W/(m^2 K) is reached. After exceeding U/U_{mf} of about 10, the model predicts decreasing heat transfer coefficients, which was not observed during the experiments. Instead, nearly

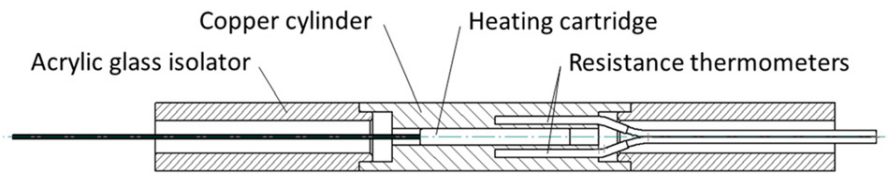

Fig. 7. Construction of a heat transfer measurement probe with plain surface design.

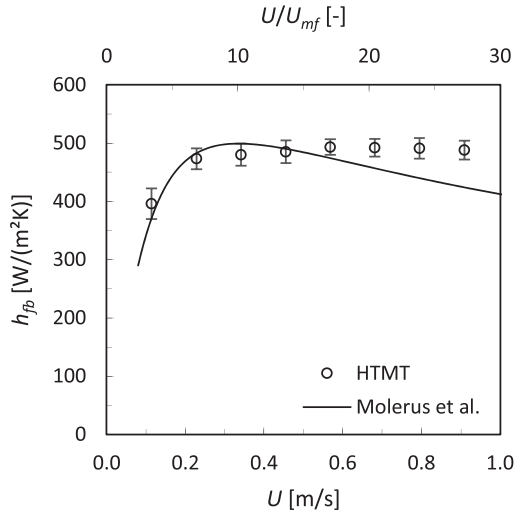

Fig. 8. Single tube heat exchange measurement results compared to heat transfer rates calculated with the model by Molerus et al. [17].

constant heat exchange rates at superficial gas velocities up to 1 m/s (U/U_{mf} of about 30) were measured.

Concerning the investigated tube bundles it was found that the model by Lechner et al. is able to predict heat exchange qualitatively as well as quantitatively for Geldart Type B particles. The tube bundle with a horizontal tube spacing of 2.8 showed heat transfer rates similar to the ones observed for a single tube. Reduced heat transfer coefficients occurred for smaller tube spacing, an effect that was also predicted by the model. In contrast to the single tube results heat exchange rates drop when the superficial gas velocity exceeds a characteristic optimum ($U/U_{mf} = 10$ for 200 μm glass beads).

Future experiments with the introduced heat transfer measurement test device will be conducted utilizing different particles matching Geldart Type B criteria. Further tests campaigns will investigate heat transfer at finned, pinned and threaded tubes in horizontal and vertical alignment with different tube spacing and bulk materials, respectively.

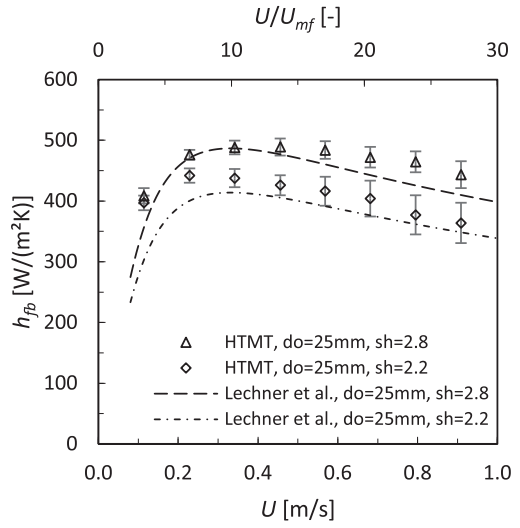

Fig. 9. Tube bundle heat exchange measurement results compared to heat transfer rates calculated with the model by Molerus et al. [17] and applied tube bundle reduction factor according to Lechner et al. [19].

Notation

a Length a (of fluidized bed), [m]
A_{hex} Area of heat exchanger surface, [m^2]
b Length b (of fluidized bed), [m]
d_i Inner diameter of a heat exchanger tube, [m]
d_o Outer diameter of a heat exchanger tube, [m]
$d_{p,m}$ Mean particle diameter, [m]
g Acceleration due to gravity, [m/s^2]
h Heat transfer coefficient, [$W/(m^2\,K)$]
h_{fb} Wall to bed heat transfer coefficient, [$W/(m^2\,K)$]
h_i Wall to fluid heat transfer coefficient, [$W/(m^2\,K)$]
H_{fb} Height of fluidized bed, [m]
n_{stage} Number of stages in adsorber/desorber, [−]
Δp_{fb} Pressure drop across a TSA fluidized bed stage, [Pa]
p_h Horizontal tube pitch, [m]
p_v Vertical tube pitch, [m]
Q Heat flow, [W]
s_h Horizontal tube spacing, [−]
s_v Vertical tube spacing, [−]
ΔT_m Mean logarithmic temperature difference, [K]
U Superficial gas velocity, [m/s]
U_{mf} Minimum fluidization gas velocity, [m/s]
ε Fluidized bed voidage, [−]
λ Thermal conductivity of heat exchanger tubes, [W/(m K)]
ρ_g Gas density, [kg/m^3]
ρ_p Particle density, [kg/m^3]

Acknowledgements

The authors appreciate the financial support by the Austrian Climate and Energy Fund (FFG project no. 845022) and gratefully acknowledge funding and publication permission from Shell Global Solutions International BV, The Hague, in the framework of the ViennaGreenCO2 project.

References

[1] T. Pröll, G. Schöny, G. Sprachmann, H. Hofbauer, Introduction and evaluation of a double loop staged fluidized bed system for post-combustion CO_2 capture using solid sorbents in a continuous temperature swing adsorption process, Chem. Eng. Sci. 141 (2016) 166–174.
[2] G. Schöny, E. Zehetner, J. Fuchs, T. Pröll, G. Sprachmann, H. Hofbauer, Design of a bench scale unit for continuous CO_2 capture via temperature swing adsorption - fluid-dynamic feasibility study, Chem. Eng. Res. Des. 106 (2016) 155–167.
[3] G. Schöny, F. Dietrich, J. Fuchs, H. Hofbauer, T. Pröll, A multi-stage fluidized bed system for continuous CO_2 capture by means of temperature swing adsorption – first results from bench scale experiments, in: J. Chaouki, F. Berruti, X. Bi, R. Cocco (Eds.),Fluidization XV, ECI Symposium Series, 2016 http://dc.engconfintl.org/fluidization_xv/83.
[4] D.J. Fauth, M.L. Gray, H.W. Pennline, H.M. Krutka, S. Sjostrom, A.M. Ault, Investigation of porous silica supported mixed-amine sorbents for post-combustion CO_2 capture, Energy Fuel 26 (2012) 2483–2496.
[5] J. Werther, Fluidized-Bed Reactors. Ullmann's Encyclopedia of Industrial Chemistry, 2007.
[6] R. Noack, Lokaler Wärmeübergang an horizontalen Rohren in Wirbelschichten, Chem. Ing. Tech. 42 (6) (1970) 371–376.
[7] A. Stefanova, H.T. Bi, C.J. Lim, J.R. Grace, Heat transfer from immersed vertical tube in a fluidized bed of group A particles near the transition to the turbulent flow regime, Int. J. Heat Mass Transf. 51 (2008) 2020–2028.
[8] A. Mathur, S.C. Saxena, A. Chao, Heat transfer from an immersed vertical tube in a gas-fluidized bed, Ind. Eng. Chem. Process. Des. Dev. 25 (1986) 156–163.
[9] D. Kunii, O. Levenspiel, Fluidization Engineering, second ed. Butterworth-Heinemann, USA, 1991.
[10] N.S. Grewal, S.C. Saxena, Experimental studies of heat transfer between a bundle of horizontal tubes and a gas-solid fluidized bed of small particles, Ind. Eng. Chem. Process. Des. Dev. 22 (1983) 367–376.
[11] S. Fukusako, S. Ishiguro, N. Seki, Heat-transfer Characteristics from a Bundle of Horizontal Tubes Immersed in Aggregative Fluidized Bed, vol. 22, Wärme Stoffübertragung, 1988 13–22.
[12] S.W. Kim, J.Y. Ahn, S.D. Kim, D.H. Lee, Heat transfer and bubble characteristics in a fluidized bed with immersed horizontal tube bundle, Int. J. Heat Mass Transf. 46 (2003) 399–409.
[13] M.A. Moawed, N.S. Berbish, A.A. Allam, A.R. El-Shamy, K.M. El-Shazly, Heat transfer between fluidized bed and horizontal bundle of tubes in a vertical channel, Int. J. Chem. React. Eng. 8 (2010) (Article A105).

[14] Q.F. Hou, Z.Y. Zhou, A.B. Yu, Gas–solid flow and heat transfer in fluidized beds with tubes - effects of material properties and tube array settings, Powder Technol. 296 (2015) 59–71.
[15] N.S. Grewal, T.K. Cheung, S.C. Saxena, Heat transfer between horizontal finned tubes and a gas-solid fluidized bed, Ind. Eng. Chem. Process. Des. Dev. 24 (1985) 458–471.
[16] S. Rasouli, M.R. Gloriz, A.A. Hamidi, Effect of annular fins on heat transfer of a horizontal immersed tube in bubbling fluidized beds, Powder Technol. 154 (2005) 9–13.
[17] O. Molerus, A. Burschka, S. Dietz, Particle migration at solid surfaces and heat transfer in bubbling fluidized beds 2, Chem. Eng. Sci. 50 (5) (1995) 879–885.
[18] H. Martin, Wärmeübergang in Wirbelschichten (chap. M5), VDI Wärmeatlas, 11th ed. Springer-Verlag, Berlin Heidelberg, 2013.
[19] S. Lechner, M. Merzsch, H.J. Krautz, Heat-transfer from horizontal tube bundles into fluidized beds with Geldart a lignite particles, Powder Technol. 253 (2013) 14–21.

Paper [2]

Fuel Processing Technology 169 (2018) 157–169

Contents lists available at ScienceDirect

Fuel Processing Technology

journal homepage: www.elsevier.com/locate/fuproc

Research article

Investigating wall-to-bed heat transfer in view of a continuous temperature swing adsorption process

G. Hofer[a,*], G. Schöny[b], J. Fuchs[b], T. Pröll[a]

[a] University of Natural Resources and Life Sciences, Institute of Chemical and Energy Engineering, Peter-Jordan-Str. 82, 1190 Vienna, Austria
[b] TU Wien, Institute of Chemical Engineering, Getreidemarkt 9/166, 1060 Vienna, Austria

ARTICLE INFO

Keywords:
Temperature swing adsorption
TSA
Heat transfer
Bubbling fluidized bed
Model vs. experiment

ABSTRACT

Heat transfer between bubbling fluidized beds and immersed heat exchanger surfaces is studied in view of continuously operated temperature swing adsorption processes for post-combustion CO_2 capture. A novel heat transfer measurement test device was used to measure wall-to-bed heat transfer coefficients. The present work focuses on the comparison of experimentally obtained and calculated heat transfer coefficients. Heat transfer at horizontal single tubes and tube bundles immersed in fluidized particle beds of glass beads with 140 µm and 200 µm in Sauter mean diameter is investigated. It is shown that the experimental results for single tubes are in mediocre agreement to established mathematical models, such as the ones proposed by Natusch et al. (1975) and Molerus et al. (1995), and that heat transfer is significantly influenced by the tube diameter. The model by Petrie et al. (1968) was considered to take the effect of the tube diameter into account, which lead to promising results. Furthermore, measured heat transfer coefficients at tube bundles of different geometries are compared to predictions using the models by Natusch et al. (1975) and Lechner et al. (2013). Some of the tube bundle reduction factors predicted by the model by Lechner et al. (2013) are larger than one, which stands in contrast to the finding that the highest heat transfer coefficients occur at single tubes. However, both models lead to adequate results when calculating heat transfer coefficients for different tube bundle geometries.

1. Introduction

Previously conducted studies have shown that heat transfer has a dominant or even limiting effect on the CO_2 capture performance of continuous temperature swing adsorption (TSA) processes [1,2]. For reasons concerning the overall process economy it may be necessary to achieve shallow bubbling beds with minimized pressure drop across the reactor stages. The pressure drop across a fluidized bed is known to be practically constant in the range of U_{mf} (minimum fluidization gas velocity) to U_t (terminal gas velocity). However, the fluidization gas velocity has a major influence on the bed expansion and, thus, on the available space for the placement of in-bed heat exchangers. Concurrently, the fluidization rate affects the achievable heat transfer coefficient between the immersed heat exchangers and the fluidized particles. The particles considered for the application in the TSA process are of Geldart Type B.

In general, it is recognized that there are three mechanisms of heat transfer between a fluidized bed and immersed heat exchanger surfaces – namely (1) particle convection, (2) gas convection and (3) radiation. Due to the relatively low temperatures occurring in the TSA process radiation may be neglected [3]. In most dense gas-solid fluidized beds solids mixing is the primary cause for the particle convective heat transfer [4]. Thus, heat transfer coefficients are low at low superficial gas velocities, where particles are in the state of a fixed bed. With an increase of the gas velocity and the formation of bubbles the increase in particle movement results in a sharp rise of the heat transfer coefficient until a characteristic maximum is reached, as shown in Fig. 1. A further increase in gas velocity yields to a decrease in heat transfer, which may be pronounced to a greater or lesser extent. The reason for the described behavior is based on the alternation between the particle and gas convective heat transfer [4]. The particle convective heat transfer reaches a maximum at the optimal gas velocity U_{opt}, whereas the gas convective heat transfer increasingly takes on greater significance beyond this point.

For relatively deep bubbling fluidized beds with a height/diameter-ratio larger than one and Geldart Type B particles it is widely accepted that the solids flow occurs in upward movement in the bed center. This behavior is explained by the growth and coalescence of bubbles while they are rising. Concurrently, a downward flow is observed at the walls enclosing the bubbling bed. We may conclude that a certain lateral

* Corresponding author.
E-mail address: gerhard.hofer@boku.ac.at (G. Hofer).

http://dx.doi.org/10.1016/j.fuproc.2017.09.024
Received 18 June 2017; Received in revised form 14 September 2017; Accepted 25 September 2017

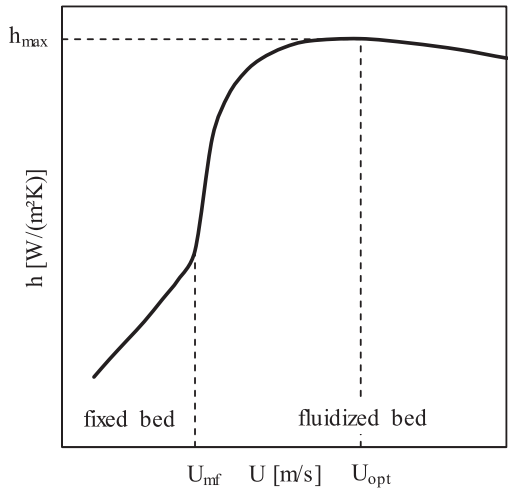

Fig. 1. Typical behavior of wall-to-bed heat transfer as a function of gas velocity in bubbling fluidized beds of Geldart Type B particles.

distribution of axial particle velocities exists. With an increase in gas velocity the lateral particle velocity becomes more uniform [5]. The described pattern of the solids flow is also observed while heat exchanger surfaces, i.e. tube bundles, are immersed in emulsified particle beds [5,6]. Yao et al. [7] correlated all the described phenomena to the packet renewal model, which was published first by Mickley and Fairbanks in 1955 [8]. Furthermore, we conclude that heat transfer may be not uniform across the fluidized beds cross-section. However, this phenomenon is not investigated in this study.

In a qualitative manner, the immersed tubes have an influence on bubble growth and, concurrently, on solids mixing. Rüdisüli et al. [6] conducted experiments to examine the lateral bubble distribution in fluidized beds with immersed vertical tubes. In a quantitative manner, they reported that the number of bubbles decreases with increasing bed height if there is no bundle of tubes present. This can be attributed to the typical coalescence of bubbles. It is mentioned that the number of bubbles remains almost constant over bed height if a tube bundle is inserted to the bubbling bed. Rüdisüli et al. [6] concluded that '*bubble coalescence in beds with vertical tubes is either inhibited or compensated by more frequent bubble splitting*'.

In the past, a great number of experimental and computational studies on wall-to-bed heat transfer were conducted in fixed beds, fluidized beds in bubbling and turbulent regime as well as in circulating fluidized beds. Lately, Merzsch et al. [9] and Lechner et al. [10] have contributed an extensive literature and empirical research concerning the influence of tube diameter, tube bundle arrangement and particle moisture on bubbling bed heat transfer for Geldart Type A and C bulk materials.

It is summarized that there are numerous models relevant for single tubes, such as those introduced by Zabrodsky [11], Noack [12], Mathur et al. [13], Kunii et al. [14] or Stefanova et al. [5] – to name just a few. Most of the available models are designed to estimate maximum heat transfer coefficients for a certain optimum fluidization gas velocity. Effectively, just a couple of models are able to describe the overall fluidized bed heat transfer coefficient as a function of superficial gas velocity, which is of special importance when it comes to dimensioning heat exchangers for TSA. As to that, the models of Natusch et al. [15], Molerus et al. [16] and Martin [17] may be of special interest.

However, the mentioned models disregard the influence of the tube diameter on heat transfer. Natusch et al. [15] reported that – according to Vreedenberg [18], Gel'perin and Einstein [19] and Zabrodsky [11] – the influence is negligible for tube diameters larger than 15 mm. Nevertheless, Petrie et al. [20], Molerus et al. [21] as well as other authors have shown that the tube diameter has significant influence on heat transfer and suitable models were developed.

Regarding heat transfer at tube bundles immersed in fluidized beds, many models were introduced by different authors. Some of the proposed tube bundle models lead, in analogy to single tube models, to maximum heat transfer coefficients correlated to optimum gas velocities. However, other models are designed to calculate so-called tube bundle reduction factors [10,15], which are applicable multiplicatively to available single tube models. The expression 'tube bundle reduction factor' implies, that heat transfer is reduced by the implementation of in-bed tube bundle heat exchangers. Hence, heat transfer coefficients decrease at some point, i.e. if the tube spacing is low enough. This leads to the conclusion that particle movement is hindered by the placement of in bed heat exchangers.

This work will investigate and discuss the difference between

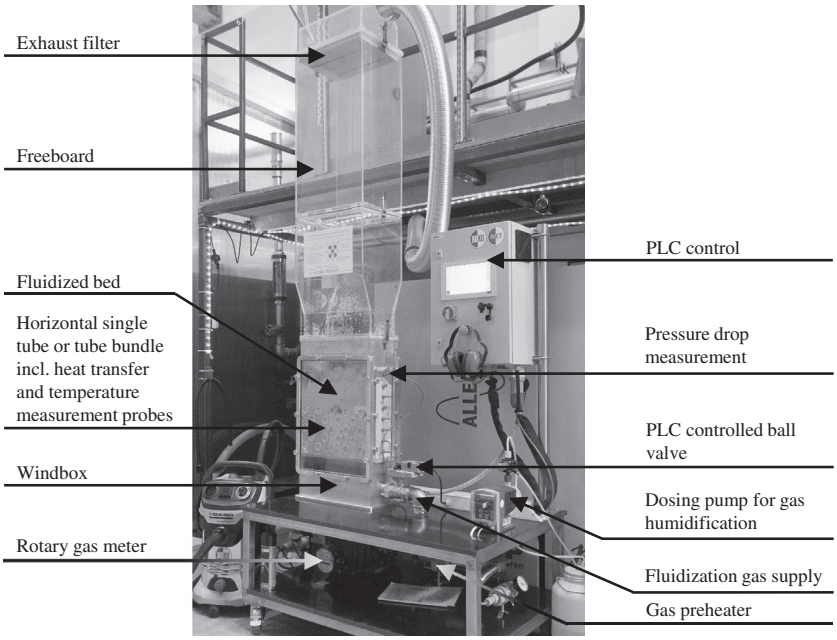

Fig. 2. Heat transfer measurement test device (HTMT).

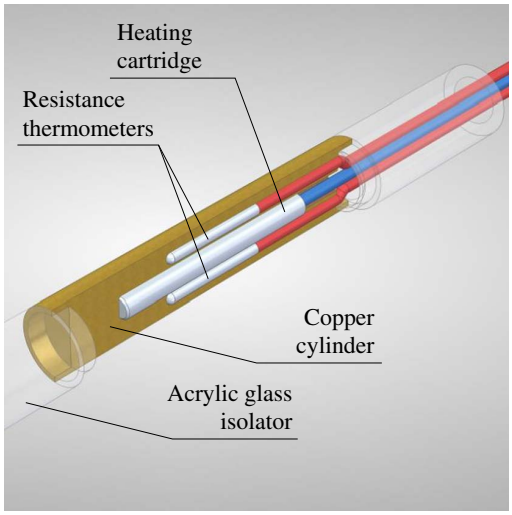

Fig. 3. Heat transfer measurement probe.

experimentally measured heat transfer coefficients and calculated values obtained with selected models for single tubes of varying diameter as well as horizontal tube bundles of different geometry with varying tube diameter and pitch.

2. Materials and methods

2.1. Experimental setup

A cold flow model, referred to as heat transfer measurement test device (HTMT), was used for the measurement of cumulated gas- and particle-convective heat transfer coefficients. The HTMT and a description of its main components is shown in Fig. 2.

The HTMT is mostly made of acrylic glass to allow for the observation of the fluidized bed behavior. The dimensions of the fluidized bed are 400 × 200 mm in length and width. Thereby, the overall bed height can get up to about 400 mm. Compressed, dry air is used to fluidize the particles within the HTMT. The gas volume flow $\dot{V}$ is measured with a rotary gas meter and regulated with a PLC controlled ball valve. A perforated plate with 155 bore holes of 3 mm in diameter was used as gas distributor, that provided sufficient pressure drop and gas distribution throughout the tested operating conditions. The

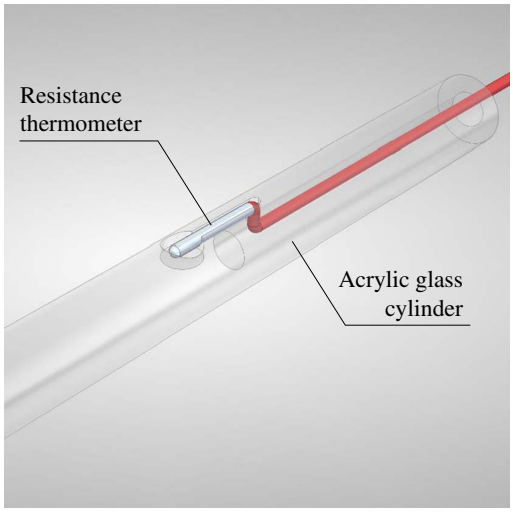

Fig. 4. Fluidized bed temperature measurement probe.

introduced fluidization gas may be preheated. To reduce electrostatic effects, all metal parts are grounded and the air used for fluidization may be humidified in a controlled manner prior introduction into the unit. Additionally, the pressure drop across the entire fluidized bed height is measured as well as across a specific bed height, which allows for calculation of the current bed voidage.

Tubular probes are used to measure fluidized bed heat transfer coefficients. The design of the probes was inspired by the work of Lechner et al. [10]. A typical heat transfer measurement probe is shown in Fig. 3. A probe consists of a copper cylinder of 100 mm in length placed in between acrylic glass ends isolating the probe from the environment. The length of both acrylic ends is 50 mm. Thus, it is assumed that the entire heat introduced to the system is transported to the contacting fluidized bed. The copper cylinder is equipped with an electrical heating cartridge and two resistance thermometers (1/3DIN standard).

During operation, the electric power consumption Q and the temperature T_{Probe} are recorded. The temperature of the measurement probe is kept constant by regulating the power consumption of the heating cartridge via the PLC control unit. Furthermore, the heat transfer surface area A of the copper cylinder is well defined. The temperature of the fluidized bed T_{fb} is determined with four temperature measurement probes immersed at different bed positions. Each of these probes is equipped with one resistance thermometer (1/3DIN standard). A typical fluidized bed temperature measurement probe is shown in Fig. 4.

The apparent wall-to-bed heat transfer coefficient h_i is calculated with Eq. (1).

$$h_i = \frac{Q}{A \bullet (T_{Probe} - T_{fb})} \tag{1}$$

During the tests with the HTMT two types of errors occur, systematic and random errors. Systematic measurement errors are caused by the used measurement devices. The measurement accuracies for the used devices are given in Table 1. Taking the given accuracies of the heaters power consumption measurement as well as of the resistance thermometers into account, the overall systematic measurement error Δh_s due to error propagation is given in Eq. (2). For typical HTMT operating conditions the overall measurement accuracy Δh_s is lower than ± 3% of h_i.

$$\Delta h_s = \left|\frac{1}{A \bullet (T_{Probe} - T_{fb})}\right| \bullet (\pm 0.1W) + \left|-\frac{Q}{A \bullet (T_{Probe} - T_{fb})^2}\right| \bullet \left[\pm\frac{1}{3} \bullet (0.3^{\circ}C + 0.005 \bullet T_{Probe})\right] + \left|\frac{Q}{A \bullet (T_{Probe} - T_{fb})^2}\right| \bullet \left[\pm\frac{1}{3} \bullet (0.3^{\circ}C + 0.005 \bullet T_{fb})\right] \tag{2}$$

To assure reproducibility of the conducted measurements the operation of the HTMT is standardized regarding the variation of the fluidization gas flow. Starting at low gas velocities the gas flow is

Table 1
Measurement accuracies of the used devices.

Device	Measurement accuracy
Rotary gas meter	$\dot{V}$ = 2.5…64m³/h: $\Delta\dot{V}$ = ± 2% max. $\dot{V}$ = 64…400m³/h: $\Delta\dot{V}$ = ± 1% max.
Electric power consumption of the heat transfer measurement probe	ΔQ = ± 0.1 W
Resistance thermometers (1/3DIN standard)	ΔT = ± 1/3·(0.3 °C + 0,005·T)
Pressure sensor compressed air supply	Linearity error: Δp = ± 0.5% max. Temperature error (0–50 °C): Δp = ± 1% max.
Pressure sensors fluidized bed	Linearity error: Δp = ± 0.8% max. Temperature error (0–50 °C): Δp = ± 1% max.

increased incrementally to a specified maximum gas velocity. Every setting of gas flow is kept constant for 2 min. The data provided by the sensors is recorded every second. Reaching the maximum gas flow the HTMT is programmed to decrease gas flow incrementally once again. Therefore, the fluidized bed heat transfer coefficient h is measured twice for each setting of gas volume flow. For the recorded data at constant superficial gas velocities the arithmetic mean heat transfer coefficients and the correlating standard deviations are calculated.

The occurring standard deviation may be referred to as random error Δh_r. The random measurement error originates from the alternating contact of the heat transfer measurement probe with different phases of the bubbling fluidized bed, which are (1) solid phase and (2) gas phase. Therefore, the arithmetic mean heat transfer coefficient for each superficial gas velocity is calculated with Eq. (3). The applied procedure for the analysis of the recorded data is illustrated in Fig. 5. The averaged heat transfer coefficients including the occurring standard deviations for the experimentally obtained data are presented in Tables A1 and A2 in the Appendix.

$$h = \frac{1}{t}\sum h_i \pm \Delta h_r \tag{3}$$

It must be noted that the superficial gas velocity U corresponds to the ratio of the introduced gas flow to the total cross section of the HTMT without accounting for the constriction caused by the tubes and tube bundles, respectively. Due to the applied measurement principle, the measured heat transfer coefficients cumulate heat transfer due to gas and particle convection and do not distinguish between them. Since temperatures are below 425 K heat transfer due to radiation is negligible [3]. The minimum temperature difference between the heated measurement probe (Fig. 3) and the fluidized bed was set to at least 30 K. Every experiment was conducted with only one heat transfer measurement probe positioned in the center of the fluidized bed.

Heat transfer was investigated for spherical glass beads with two selected Sauter mean diameters (SMD) of particles d_p of 140 µm and 200 µm. Both particles are clearly in the Geldart Type B range [22], as indicated in Fig. 6.

Thereby, horizontal single tubes with plain surface of different outer diameters d_t (20 mm, 25 mm and 30 mm) as well as horizontal tube bundles with varying geometry were used. The main variables describing the tube bundle properties (d_t = tube outer diameter, p_{diag} = diagonal tube pitch, p_{min} = minimum tube pitch, p_h = horizontal tube pitch, p_v = vertical tube pitch) are illustrated in Fig. 7.

The investigated heat exchanger geometries are shown in Table 2,

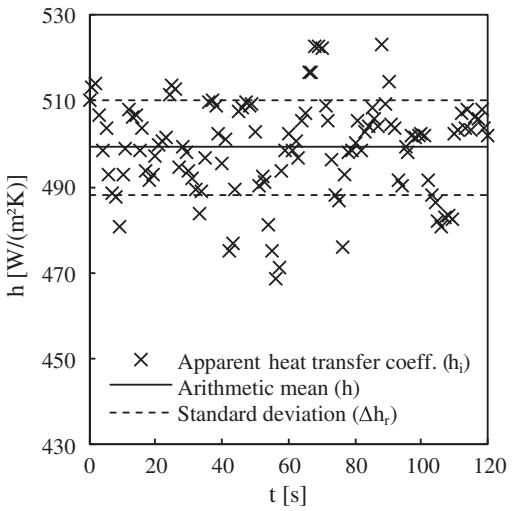

Fig. 5. Recorded heat transfer coefficients including mean value and standard deviation.

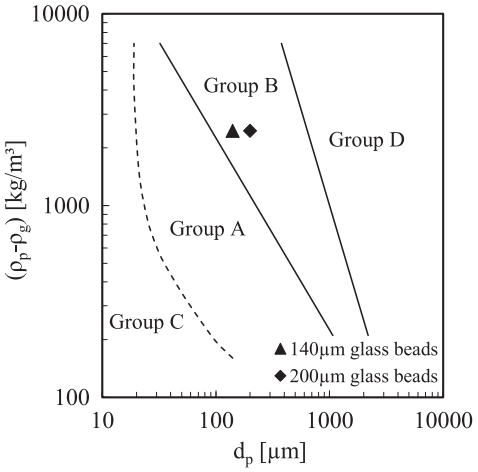

Fig. 6. Particle classification according to Geldart [22].

arranged in the order of increasing horizontal tube spacing s_h. The normalized horizontal and diagonal tube spacing are defined as $s_h = d_t/p_h$ and $s_{diag} = d_t/p_{diag}$, respectively. Each tube bundle consisted of five tube rows. The number of tube columns varies but is chosen in a way, that the whole width of the fluidized bed is filled by the tube bundle. The heat transfer measurement probe was positioned in the center of the bundle, i.e. in the vertical as well as in the horizontal direction.

Experiments conducted with the 140 µm glass beads were carried out at varying superficial gas velocity U in the range of 0.1 m/s to 0.8 m/s, which is equivalent to fluidization numbers U/U_{mf} in the range of 5 to 42 (U_{mf} = 0.019 m/s). Regarding the 200 µm glass bead bulk material the superficial gas velocity U was varied in the range of 0.1 m/s to 1.0 m/s, which is equivalent to fluidization numbers U/U_{mf} in the range of 3 to 26 (U_{mf} = 0.039 m/s). The fluidized bed height was set to 0.25 m at a superficial gas velocity of 0.1 m/s.

2.2. Mathematical models

Selected models from literature were used to calculate heat transfer coefficients for gas and particle properties corresponding to the experimental conditions. The main properties and features of the selected models are summarized in Table A3 in the Appendix.

The empirical single tube results obtained with the 140 µm and 200 µm glass bead bulk material were compared to the models proposed by Natusch et al. [15] and Molerus et al. [16]. Both models were

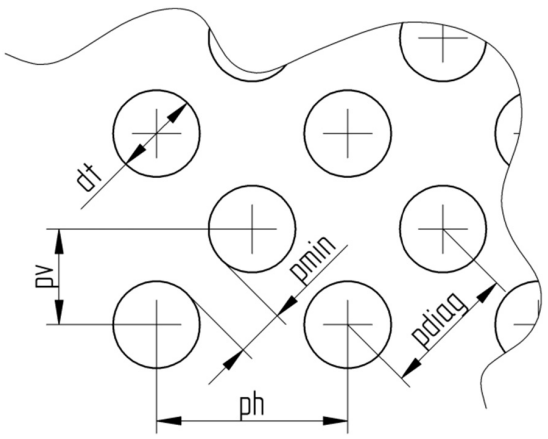

Fig. 7. Essential variables describing the properties of a tube bundle.

Table 2
Tube bundle geometries.

s_h [−]	1.83	2.20	2.33	2.75	2.80	2.83	3.40	3.50	4.25
s_{diag} [−]	1.30	1.56	1.65	1.94	1.98	2.00	2.40	2.47	3.01
d_t [mm]	30	25	30	20	25	30	25	20	20
p_h [mm]	55	55	70	55	70	85	85	70	85
p_v [mm]	27.5	27.5	35	27.5	35	42.5	42.5	35	42.5
p_{min} [mm]	8.9	13.9	19.5	18.9	24.5	30.1	35.1	29.5	40.1

Table 3
Coefficients C_1 to C_5 according to Natusch et al. [15].

d_p [μm]	C_1 [−]	C_2 [−]	C_3 [−]	C_4 [−]	C_5 [−]
150	0.4027	0.1354	0.2693	1.5270	0.1005
200	0.5226	0.1561	0.2580	1.0370	0.1195

developed based on different gas and particle properties. Eq. (4) presents the model by Natusch et al. [15] with the relevant coefficients C_1 to C_5 displayed in Table 3, also taken from [15]. Since coefficients for particles of 140 μm in SMD are unavailable, the shown values for 150 μm particles were used for the calculation of achievable fluidized bed heat transfer coefficients. The model proposed by Molerus et al. [16] is presented with Eq. (5).

$$h_{Natusch} = C_1 \cdot Ar^{C_2} \cdot \left(\frac{U}{U_{mf}} - 1\right)^{C_3} \cdot \left\{C_4 + e^{-C_5 \cdot \left(\frac{U}{U_{mf}} - 1\right)}\right\} \cdot \frac{k_g}{d_p} \tag{4}$$

$$h_{Molerus} = \left\{ \frac{0.125 \cdot (1-\varepsilon_{mf}) \cdot \left(1 + 33.3 \cdot \left(\sqrt[3]{\frac{U-U_{mf}}{U_{mf}}} \cdot \sqrt[3]{\frac{\rho_p \cdot c_{p,p}}{k_g \cdot g}} \cdot (U-U_{mf})\right)^{-1}\right)^{-1}}{1 + \left(\frac{k_g}{2 \cdot c_{p,p} \cdot \mu_g}\right) \cdot \left(1 + 0.28 \cdot (1-\varepsilon_{mf})^2 \cdot \sqrt{\frac{\rho_g}{\rho_p - \rho_g}} \cdot \left(\sqrt[3]{\frac{\rho_p \cdot c_{p,p}}{k_g \cdot g}} \cdot (U-U_{mf})\right)^2 \cdot \frac{U_{mf}}{U-U_{mf}}\right)} + 0.165 \cdot Pr^{1/3} \cdot \left(\frac{\rho_g}{\rho_p - \rho_g}\right)^{1/3} \cdot \frac{1}{1 + 0.05 \cdot \frac{U_{mf}}{U-U_{mf}}} \right\} \cdot k_g \cdot \left(\frac{\mu_g}{\sqrt{g} \cdot (\rho_p - \rho_g)}\right)^{-2/3} \tag{5}$$

Calculations with the model developed by Martin [17] were also performed in this study. Comparing the results obtained with this model lead to significant quantitative and qualitative differences to heat transfer coefficients derived with the above-mentioned single tube models as well as to the measured values. The model leads to an excessive rise of the heat transfer coefficients starting at low gas velocities followed by a significantly overrated value for the occurring maximum in heat transfer. After the narrow plateau in maximum heat transfer a rapid decrease of heat transfer is predicted. Therefore, the model by Martin [17] was not further taken into considerations.

Since the experimental campaign also included a variation of the diameter of the heat exchanger tubes, the model proposed by Petrie et al. [20], taken from [9] and given in Eq. (6), was considered to calculate the tube diameter-dependent factor f_{dt}. This factor was applied to results obtained with the models by Natusch et al. [15] and Molerus et al. [16]. The results were then compared to the empirical single tube heat transfer coefficients obtained with the HTMT.

$$f_{d_t,Petrie} = \left(\frac{d_t}{33.7 \cdot 10^{-3}\,m}\right)^{-1/3} \tag{6}$$

To compare theoretical and experimental heat transfer coefficients for tube bundles the models proposed by Natusch et al. [15] and Lechner et al. [10] were considered. Both models represent reduction factors, which can be applied to heat transfer coefficients predicted with models available for single tubes. The bundle reduction factor developed by Natusch et al. [15], valid for plain tubes in different arrangements, such as in-line or staggered, is given in Eq. (7).

$$f_{tb,Natusch} = \left(1 - \frac{1}{s_h}\right)^{0.25} \tag{7}$$

Eq. (8) represents the tube bundle reduction factor developed by Lechner et al. [10]. It is noted that the model is valid for Geldart Type A particles only. Although the model by Lechner et al. [10] is specifically designed to be applied to the single tube model by Molerus et al. [16], calculations in combination with the model by Natusch et al. [15] were performed.

$$f_{tb,Lechner} = \left(\frac{d_t}{80 \cdot 10^{-3}\,m}\right)^{-0.3} \cdot \left(1 - \frac{1}{s_h}\right)^{0.36} \cdot \left(1 - \frac{1}{s_{diag}}\right)^{0.24} \cdot \left(1 - \frac{d_p}{p_{min}}\right)^4 \cdot \left(\frac{d_t}{22 \cdot 10^{-3}\,m}\right)^{0.09} \tag{8}$$

3. Results and discussion

3.1. Single tubes

The measured heat transfer coefficients with varying fluidization velocity for both 140 μm and 200 μm glass beads are shown in Figs. 8 and 9. Furthermore, the theoretical single tube heat transfer coefficients, calculated with the models by Natusch et al. [15] and Molerus et al. [16], are presented in these figures. As mentioned before, both models are neglecting the effect of the tube diameter on heat transfer, whereas the influence is clearly indicated by the experimental results. Regarding the 140 μm glass beads it is shown that the highest heat transfer coefficients are achieved with the tube of 20 mm in outer diameter and, concurrently, the lowest values are found for the 30 mm

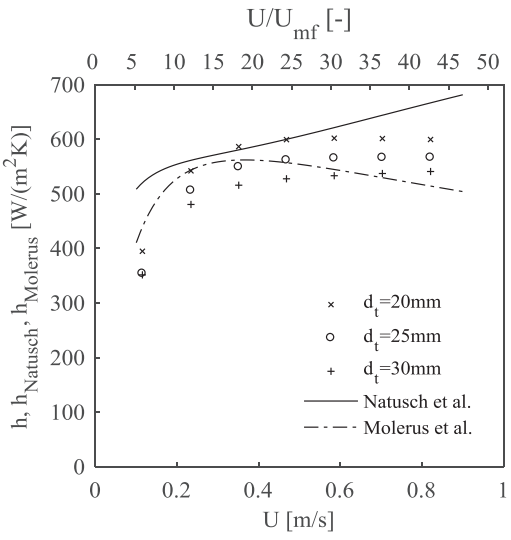

Fig. 8. Experimental vs. modeled heat transfer coefficients for single tubes and 140 μm glass beads.

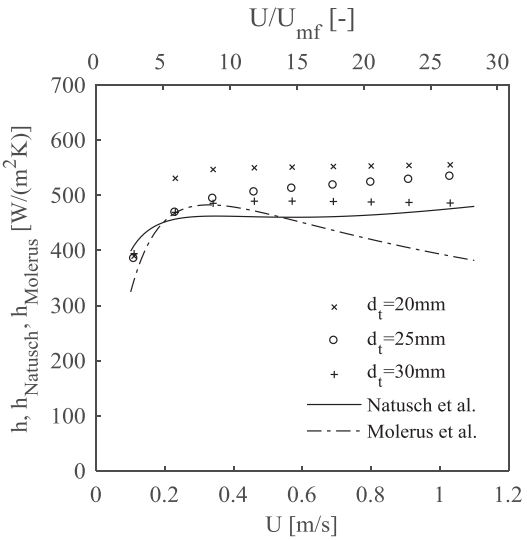

Fig. 9. Experimental vs. modeled heat transfer coefficients for single tubes and 200 µm glass beads.

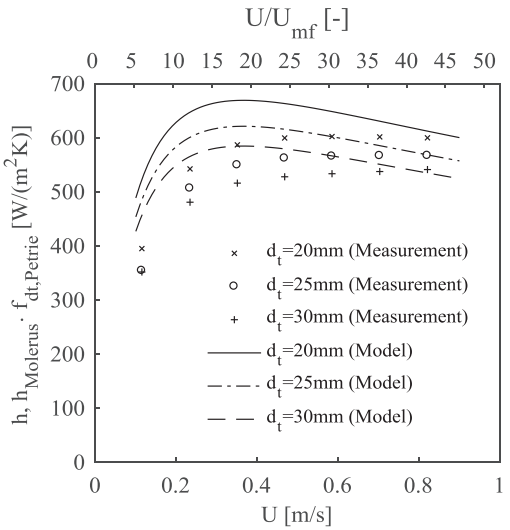

Fig. 11. Experimental vs. modeled heat transfer coefficients for single tubes and 140 µm glass beads.

tube. Furthermore, both models show qualitative and quantitative differences regarding their estimation of heat transfer coefficients as a function of superficial gas velocity. Whereas the model by Natusch et al. [15] clearly overestimates heat transfer at high gas velocity, the model by Molerus et al. [16] tends to underestimate the heat transfer values.

The constancy in heat transfer of the measured values starting at a gas velocity of about 0.5 m/s can be explained by the explained mechanisms of particle and gas convective heat transfer. It seems that the decrease of the particle convective heat transfer is counteracted by the increase of the gas convective effect with increasing gas velocity.

Equal behavior concerning the dependency of tube diameter is shown for the 200 µm particles. Starting at a superficial gas velocity of about 0.3 m/s ($U/U_{mf} = 8$) the model by Natusch et al. [15] is in good agreement with the measured data by predicting more or less constant heat transfer coefficients. For gas velocities below 0.5 m/s both models are in good agreement with the experimental data. The model by Molerus et al. [16] significantly underestimates heat transfer for higher superficial gas velocities.

In general, it is observed that heat transfer coefficients are lower for the 200 µm particles and that both models tend to underestimate heat transfer for these particles. In contrast to this conclusion the model by Natusch et al. [15] clearly overestimates heat transfer for the 140 µm glass beads at gas velocities higher than 0.6 m/s.

Fig. 10 shows a comparison of experimental data for single tubes and diameter-corrected heat transfer coefficients calculated with Eq. (4), adapted with Eq. (6) for the 140 µm glass beads. Fig. 11 illustrates the results obtained with the model by Molerus et al. [16], given in Eq. (5), adapted with Eq. (6) for tubes of different outer diameter.

The results for 200 µm glass beads are presented in Figs. 12 and 13, respectively. Thereby, the best fit of heat transfer coefficients is observed by comparing the measured results observed for the 200 µm particles and coefficients calculated with the combination of the models by Natusch et al. [15] and Petrie et al. [20].

3.2. Tube bundles

Experimental results from tube bundle measurements with tubes of 20 mm, 25 mm and 30 mm in outer diameter and varying tube pitch of

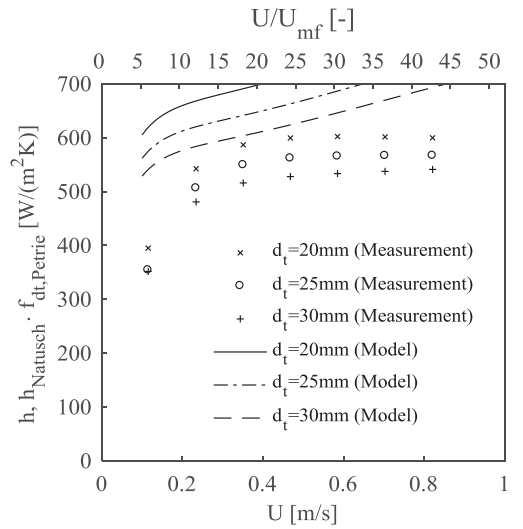

Fig. 10. Experimental vs. modeled heat transfer coefficients for single tubes and 140 µm glass beads.

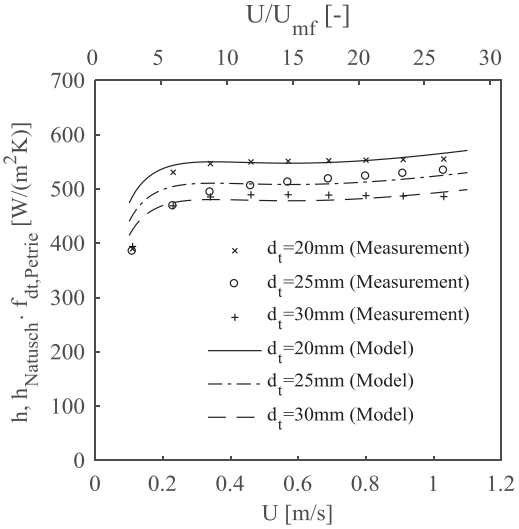

Fig. 12. Experimental vs. modeled heat transfer coefficients for single tubes and 200 µm glass beads.

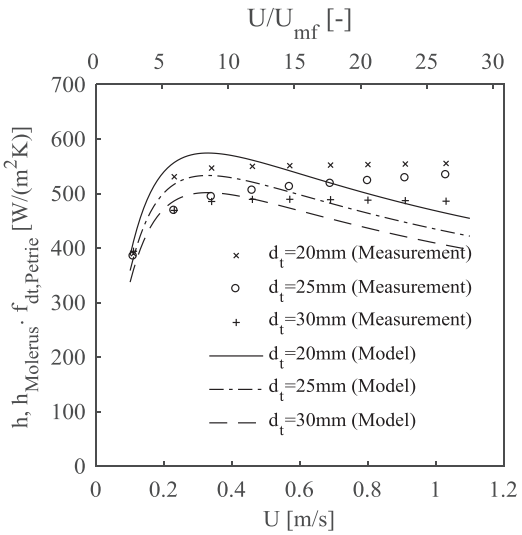

Fig. 13. Experimental vs. modeled heat transfer coefficients for single tubes and 200 μm glass beads.

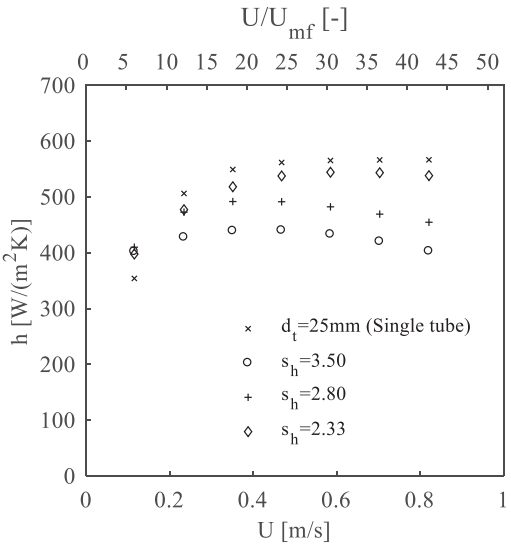

Fig. 15. Experimental heat transfer coefficients for a single tube and different tube bundles with tubes of 25 mm in outer diameter.

55 mm, 70 mm and 85 mm are illustrated in Figs. 14–16. In the figures, the tube bundle properties are given in form of the dimensionless horizontal tube spacing s_h. The measured data derived with the single tubes of equal diameter is presented as well. The figures show results that were measured with the 140 μm glass beads only, since the data obtained with 200 μm bulk material lead to the same conclusions.

Figs. 14–16 indicate that heat transfer decreases with decreasing tube pitch and tube spacing, respectively. This behavior is also predicted by both tube bundle reduction factors f_{tb} proposed by Natusch et al. [15] and Lechner et al. [10] and can be explained by the hindrance of the particle mixing by the immersed bundle of tubes. Concurrently, the highest heat transfer coefficients are observed at single tubes. The tube bundle reduction factors calculated with both models are presented in Table 4. Although the tube bundle reduction factor proposed by Lechner et al. [10], given in Eq. (8), can take values larger than one. This finding stands in contradiction to the fact that the highest heat transfer coefficients occur at single tubes.

The following parity plots given in Figs. 17–22 are used to discuss the differences between experimentally obtained heat transfer coefficients and modeled data regarding tube bundles with varying horizontal tube spacing s_h.

The measurement results compared to modeled data derived with Eq. (5) and adapted for tube bundles with Eq. (7) are presented in Fig. 17 for 140 μm and in Fig. 18 for 200 μm glass beads. Regarding the bulk material of 140 μm in SMD the tube bundle model by Natusch et al. [15] is in mediocre agreement to the experimental data, but heat transfer is underestimated for the specific tube bundle with the largest spacing of 4.25. For 200 μm particles the combination of the mentioned models tends to clearly underestimate heat transfer, especially for tube bundles with large horizontal tube pitch.

Experimental results compared to calculated data derived with the model by Molerus et al. [16] adapted for tube bundles with the model

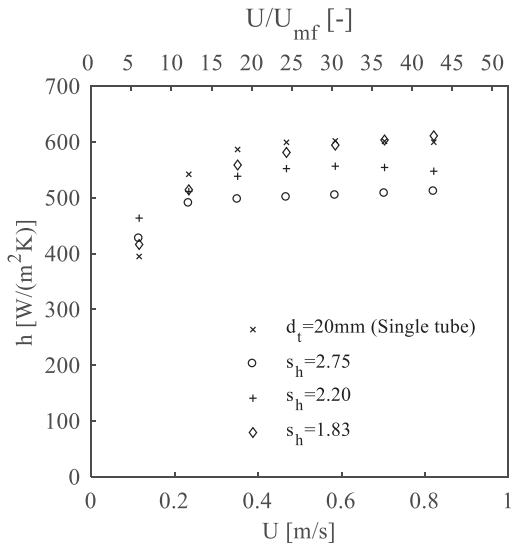

Fig. 14. Experimental heat transfer coefficients for a single tube and different tube bundles with tubes of 20 mm in outer diameter.

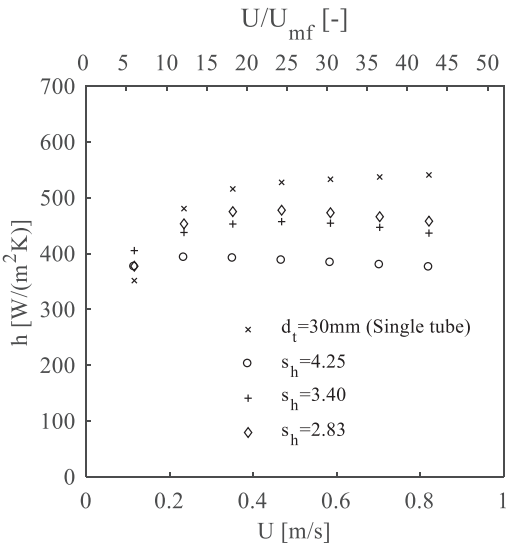

Fig. 16. Experimental heat transfer coefficients for a single tube and different tube bundles with tubes of 30 mm in outer diameter.

Table 4
Tube bundle reduction factors calculated with the model by Natusch et al. [15] and Lechner et al. [10].

s_h [−]	1.83	2.20	2.33	2.75	2.80	2.83	3.40	3.50	4.25
$f_{tb,Natusch}$ [−]	0.82	0.86	0.87	0.89	0.90	0.90	0.92	0.92	0.94
$f_{tb,Lechner}$ [−]	0.67	0.85	0.87	1.03	1.00	0.97	1.09	1.14	1.21

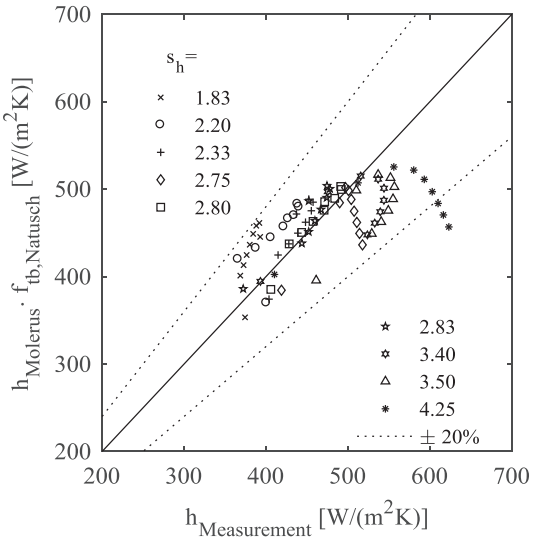

Fig. 17. Experimental vs. modeled heat transfer coefficients for different tube bundles and 140 µm glass beads.

by Lechner et al. [10] are displayed in Fig. 19 for 140 µm and in Fig. 20 for 200 µm glass beads.

It is concluded that the predicted heat transfer coefficients with regard to the 200 µm glass bead particles are in better agreement to the measured data than these for the 140 µm glass beads. This stands in contrast to the fact that the model by Lechner et al. [10] is valid for Geldart Type A particles only and that the model by Molerus et al. [16] does not overestimate heat transfer at single tubes. As mentioned

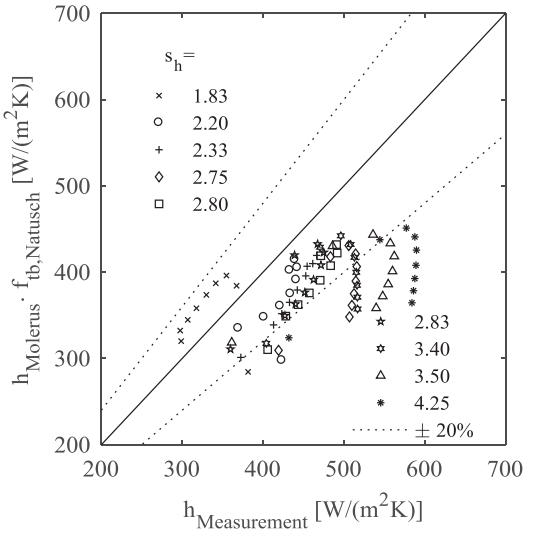

Fig. 18. Experimental vs. modeled heat transfer coefficients for different tube bundles and 200 µm glass beads.

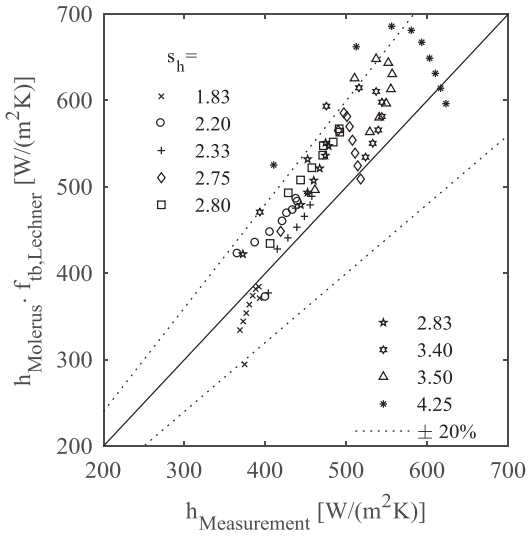

Fig. 19. Experimental vs. modeled heat transfer coefficients for different tube bundles and 140 µm glass beads.

before, some of the calculated tube bundle reduction factors with the model by Lechner et al. [10], given in Table 4, are larger than one. This is contrary to the observation that the highest heat transfer coefficients occur at single tubes.

In general, it is observed that good results are obtained for the 200 µm glass beads having the presented single tube models by Natusch et al. [15] and Molerus et al. [16] adapted for the different tube diameters with the model by Petrie et al. [20] and accounting for tube bundles with either the model by Natusch et al. [15] or Lechner et al. [10]. These results are shown in Figs. 21–24. However, it is evident that the model by Lechner et al. [10] leads to heat transfer coefficients which seem to be spread more widely.

Looking at the results given in Fig. 10 reveals that the just mentioned combination of models leads to a significant overestimation of heat transfer coefficients for the 140 µm glass beads. Therefore, these results are not presented in this study.

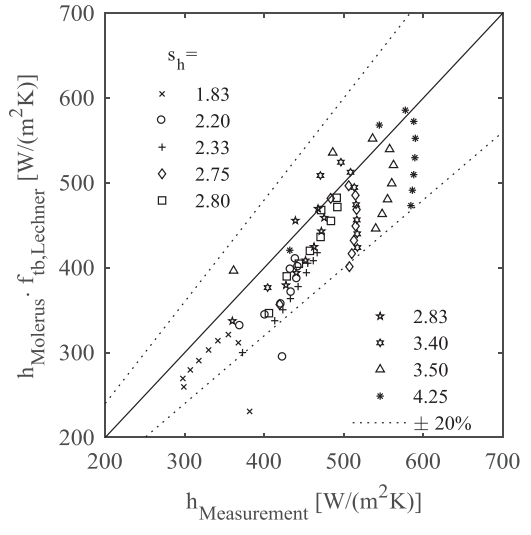

Fig. 20. Experimental vs. modeled heat transfer coefficients for different tube bundles and 200 µm glass beads.

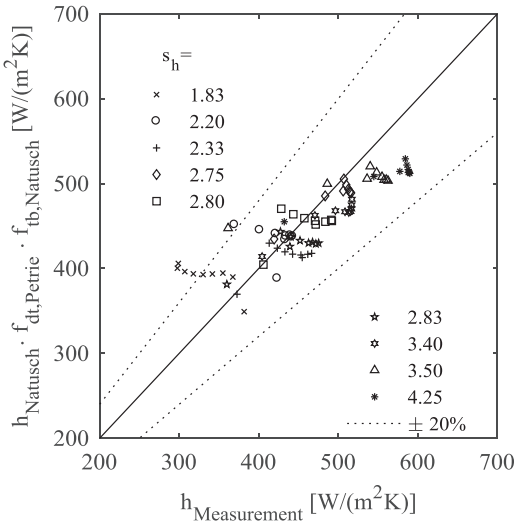

Fig. 21. Experimental vs. modeled heat transfer coefficients for different tube bundles and 200 µm glass beads.

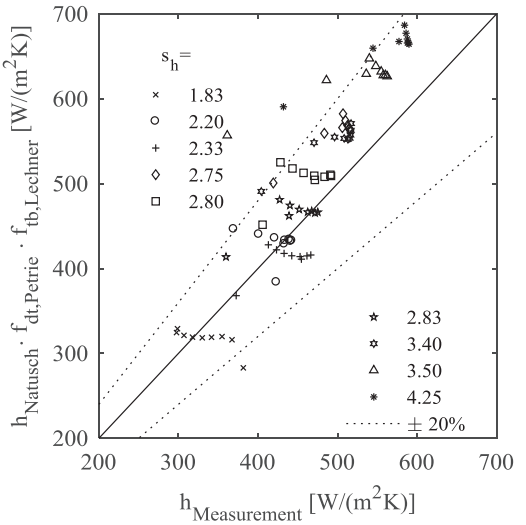

Fig. 23. Experimental vs. modeled heat transfer coefficients for different tube bundles and 200 µm glass beads.

3.3. General aspects

Both, the results for single tubes as well as the obtained results for tube bundles show quantitative and qualitative differences between the modeled and the experimental wall-to-bed heat transfer coefficients. It is assumed that these deviations are caused by

(1) the fact, that the actual particle size distributions of the solids used for the measurement of heat transfer coefficients vary from one experiment to another. However, the SMD used for the calculations is an average of particle size.
(2) the differences of the used measurement devices. The experiments were conducted with various apparatuses, i.e. different designs of gas distributors and different cross-sectional fluidized bed shapes.

4. Conclusion and outlook

Regarding heat transfer between bubbling fluidized beds of Geldart Type B particles (140 µm and 200 µm spherical glass beads) and immersed single tubes experiments have shown that the tube diameter has significant influence on the achievable heat transfer coefficients. Therefore, it is inevitable to consider models to account for the described effect. The model proposed by Petrie et al. [20] is in good qualitative agreement with the measured results presented in this work.

Nevertheless, the considered models by Natusch et al. [15] and Molerus et al. [16] used for the prediction of single tube heat transfer coefficients as a function of superficial gas velocity lead to significant qualitative and quantitative differences – with concern to the respective other model as well as with respect to experimental heat transfer coefficients.

The measurements conducted with respect to heat transfer at tube

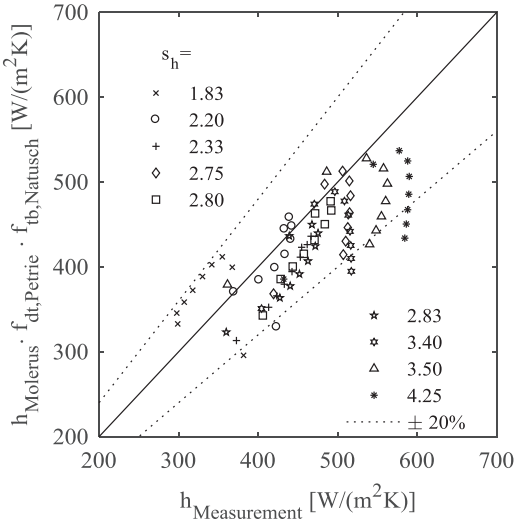

Fig. 22. Experimental vs. modeled heat transfer coefficients for different tube bundles and 200 µm glass beads.

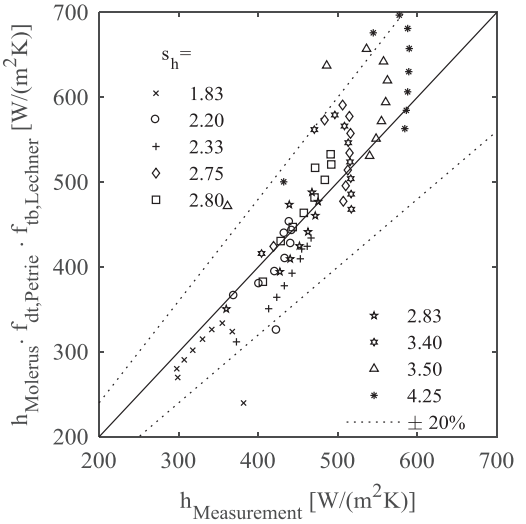

Fig. 24. Experimental vs. modeled heat transfer coefficients for different tube bundles and 200 µm glass beads.

bundles have shown that heat transfer coefficients decrease with decreasing tube spacing. This general behavior is also predicted by the models introducing a so-called tube bundle reduction factor, such as these proposed by Natusch et al. [15] or Lechner et al. [10]. Concurrently, the highest heat transfer coefficients are observed at single tubes.

Tube bundle heat transfer coefficients have been calculated with the model by Molerus et al. [16] adapted with the model by Natusch et al. [15] on the one hand, and with the model by Lechner et al. [10] on the other hand. The comparison of the experimentally obtained heat transfer coefficients with modeled data revealed that both models available for tube bundles are in moderate agreement to the experimental data. However, the model by Lechner et al. [10] leads to tube bundle reduction factors larger than one. This stands in contrast to the finding, that the highest heat transfer coefficients are observed at single tubes.

It is evident that the models for predicting wall-to-bed heat transfer coefficients available in literature lead to diverse results and that the suitability of these models strongly depends on the particles considered for a specific application. It is therefore unclear for which model the user should decide when dimensioning a tube bundle heat exchanger. For an accurate design of the proposed TSA process, utilized for post-combustion carbon capture, it is highly advisable to measure heat transfer coefficients to achieve best process performances. Nevertheless, the models available in literature are essential for the identification of the trends and mechanisms of in-bed heat transfer as well as for a first design of such heat exchangers.

Ongoing experiments with the heat transfer measurement test device are planned. Thereby, the influence of fluidized beds with continuous particle exchange, i.e. crosswise flow of the solids, on heat transfer will be investigated. Future improvements of the HTMT will be made to measure residence time distributions of solids in these crosswise moving particle beds and to determine essential reactor characteristics of fluidized bed TSA processes.

Notation

Symbols

Symbol	Parameter	Unit
A	Surface area of heat transfer measurement probe	m^2
Ar	Archimedes number	–
$c_{p,p}$	Heat capacity of particles	J/(kg·K)
d_p	Sauter mean diameter of particles	m
d_t	Tube outer diameter	m
f_{dt}	Tube diameter factor	–
f_{tb}	Tube bundle reduction factor	–
h	(Averaged) heat transfer coefficient	W/(m^2·K)
h_i	Apparent, measured heat transfer coefficient	W/(m^2·K)
h_{max}	Maximum heat transfer coefficient at U_{opt}	W/(m^2·K)
Δh_r	Random measurement error	W/(m^2·K)
Δh_s	Systematic measurement error	W/(m^2·K)
k_g	Thermal conductivity of gas phase	W/(m·K)
p	Pressure	Pa
p_{diag}	Diagonal tube pitch	m
p_h	Horizontal tube pitch	m
p_{min}	Minimum tube pitch	m
p_v	Vertical tube pitch	m
Pr	Prandtl number	–
Q	Power consumption	W
s_{diag}	Diagonal tube spacing	–
s_h	Horizontal tube spacing	–
t	Time	s
T	Temperature	K
T_{fb}	Temperature of fluidized bed	K
T_{Probe}	Temperature of heat transfer measurement probe	K
U	Superficial gas velocity	m/s
U_{mf}	Minimum fluidization gas velocity	m/s
U_{opt}	Optimal gas velocity	m/s
$\dot{V}$	Gas volume flow	m^3/h
ε_{mf}	Bed voidage at minimum fluidization gas velocity	–
μ_g	Viscosity of gas phase	Pa·s
ρ_g	Density of gas phase	kg/m^3
ρ_p	Density of particles	kg/m^3

Abbreviations

Abbreviation	Full name
HTMT	Heat transfer measurement test device
PLC	Programmable logic controller
SMD	Sauter mean diameter

Acknowledgements

The authors appreciate the financial support by the Austrian Climate and Energy Fund (FFG project no. 845022) and gratefully acknowledge funding and publication permission from Shell Global Solutions International B.V., The Hague. The authors want to thank Thomas Märzinger, who contributed a great deal of work in editing the figures. Furthermore, we acknowledge the critical and productive feedback of the reviewers, which helped to enrich and broaden the article with useful information.

Appendix

Table A1
Experimental heat transfer coefficients for single tubes and tube bundles (140 μm glass beads).

U [m/s]	h [W/(m²K)]											
	d_t = 20 mm	d_t = 25 mm	d_t = 30 mm	s_h = 1.83	s_h = 2.20	s_h = 2.33	s_h = 2.75	s_h = 2.80	s_h = 2.83	s_h = 3.40	s_h = 3.50	s_h = 4.25
0,12	412 ± 21	360 ± 37	353 ± 26	378 ± 23	400 ± 9	406 ± 10	427 ± 12	450 ± 13	372 ± 15	402 ± 17	462 ± 13	418 ± 21
0,23	545 ± 14	508 ± 20	487 ± 17	392 ± 8	429 ± 9	439 ± 8	487 ± 12	489 ± 8	446 ± 22	477 ± 10	513 ± 13	511 ± 14
0,35	579 ± 11	539 ± 16	511 ± 19	391 ± 8	437 ± 9	450 ± 7	507 ± 12	510 ± 11	480 ± 22	519 ± 10	533 ± 11	562 ± 19
0,47	598 ± 18	570 ± 19	530 ± 15	379 ± 6	438 ± 11	457 ± 12	496 ± 15	526 ± 14	476 ± 17	539 ± 13	555 ± 12	584 ± 15
0,59	604 ± 13	566 ± 22	538 ± 17	387 ± 8	439 ± 14	456 ± 15	509 ± 13	536 ± 15	470 ± 10	547 ± 13	556 ± 12	593 ± 17
0,70	599 ± 16	568 ± 14	539 ± 15	385 ± 8	424 ± 20	446 ± 12	512 ± 13	532 ± 17	468 ± 15	547 ± 16	551 ± 13	604 ± 17
0,82	597 ± 15	563 ± 16	538 ± 19	370 ± 15	404 ± 20	438 ± 13	506 ± 15	525 ± 17	462 ± 14	533 ± 14	547 ± 13	610 ± 15

Table A2
Experimental heat transfer coefficients for single tubes and tube bundles (200 μm glass beads).

U [m/s]	h [W/(m²K)]											
	d_t = 20 mm	d_t = 25 mm	d_t = 30 mm	s_h = 1.83	s_h = 2.20	s_h = 2.33	s_h = 2.75	s_h = 2.80	s_h = 2.83	s_h = 3.40	s_h = 3.50	s_h = 4.25
0,11	384 ± 46	390 ± 16	396 ± 13	388 ± 23	421 ± 9	387 ± 10	418 ± 12	409 ± 13	362 ± 11	408 ± 17	369 ± 26	438 ± 21
0,23	531 ± 17	469 ± 11	473 ± 9	377 ± 8	450 ± 9	456 ± 8	486 ± 12	476 ± 8	447 ± 6	473 ± 10	468 ± 26	540 ± 14
0,34	551 ± 11	493 ± 12	480 ± 10	372 ± 8	454 ± 9	469 ± 7	504 ± 12	488 ± 11	466 ± 7	495 ± 10	549 ± 16	572 ± 19
0,46	550 ± 13	503 ± 14	485 ± 10	347 ± 6	441 ± 11	461 ± 12	513 ± 15	489 ± 14	468 ± 7	505 ± 13	558 ± 13	583 ± 15
0,57	552 ± 18	506 ± 14	493 ± 7	326 ± 8	426 ± 14	454 ± 15	511 ± 13	484 ± 15	467 ± 7	513 ± 13	561 ± 13	584 ± 17
0,69	551 ± 14	521 ± 13	492 ± 8	314 ± 8	422 ± 20	444 ± 12	518 ± 13	472 ± 17	464 ± 7	514 ± 16	558 ± 12	590 ± 17
0,80	548 ± 17	530 ± 16	491 ± 9	304 ± 15	423 ± 20	426 ± 13	516 ± 15	465 ± 17	463 ± 7	521 ± 14	553 ± 14	581 ± 15
0,91	556 ± 16	527 ± 35	488 ± 8	291 ± 24	405 ± 16	421 ± 13	516 ± 16	443 ± 22	450 ± 7	522 ± 20	547 ± 15	587 ± 11
1,03	554 ± 21	525 ± 12	481 ± 7	290 ± 34	366 ± 25	N/A	502 ± 16	407 ± 28	421 ± 9	507 ± 22	545 ± 19	590 ± 10

Table A3
Features of the models selected from literature for the estimation of wall-to-bed heat transfer.

Reference	Model for	Effects/mechanisms on wall-to-bed heat transfer								Tube/bundle properties			Particle properties				
	s… Single tube b… Tube bundle	- Gas velocity	- Particle diameter	- Tube diameter	- Distance meas. probe/gas distributor	- Tube pitch/ spacing	- Finned tubes	- Bed height	pc… particle convection gs… gas convection r… radiation	Tube diameter [mm]	h… horizontal v… vertical	Distance to gas distributor (lowest row) [mm]	Geldart type	Particle material	Particle size [μm]	Particle density [kg/m^3]	Model uncertainty [%]
Natusch et al. [15]	s;b	x	x	x	–	x	x	–	pc;gc	25; 50	h	–	B	Glass	110–6-70	~2500	≤ ± 3
Molerus et al. [16]	s	x	x	–	–	–	–	–	pc;gc	–	v	–	A-D	Glass; sand; FCC	74–40-00	26–11800	–
Martin [17]	s	x	x	–	–	–	–	–	pc;gc;r	–	–	–	A-D	–	> 40	–	–
Petrie et al. [20]	s	–	–	x	–	–	–	–	–	–	–	–	–	–	–	–	–
Lechner et al. [10]	b	x	x	x	x	x	–	–	–	12–200	h	–	A, D	Lignite; plastic beads	73; 3000–-4000	–	± 10

References

[1] G. Schöny, F. Dietrich, J. Fuchs, T. Pröll, H. Hofbauer, A multi-stage fluidized bed system for continuous CO_2 capture by means of temperature swing adsorption – first results from bench scale experiments, Powder Technol. 316 (2017) 519–527.

[2] G. Hofer, J. Fuchs, G. Schöny, T. Pröll, Heat transfer challenge and design evaluation for a multi-stage temperature swing adsorption process, Powder Technol. 316 (2017) 512–518.

[3] J. Werther, Fluidized-bed reactors, Ullmann's Encyclopedia of Industrial Chemistry, 2007.

[4] L.-S. Fan, C. Zhu, Principles of Gas-Solid Flows, Cambridge University Press, 1998.

[5] A. Stefanova, H.T. Bi, C.J. Lim, J.R. Grace, Heat transfer from immersed vertical tube in a fluidized bed of group A particles near the transition to the turbulent flow regime, Int. J. Heat Mass Transf. 51 (2008) 2020–2028.

[6] M. Rüdisüli, T.J. Schildhauer, S.M.A. Biollaz, J.R. Van Ommen, Radial bubble distribution in a fluidized bed with vertical tubes, Ind. Eng. Chem. Res. 51 (2012) 13815–13824.

[7] X. Yao, Y. Zhang, C. Lu, X. Han, Systematic study on heat transfer and surface hydrodynamics of a vertical heat tube in a fluidized bed of FCC particles, AICHE J. 61 (1) (2015) 68–83.

[8] H.S. Mickley, D.F. Fairbanks, Mechanism of heat transfer to fluidized beds, AICHE J. 1 (3) (1955) 374–384.

[9] M. Merzsch, S. Lechner, H.J. Krautz, Heat transfer from single horizontal tubes in fluidized beds: Influence of tube diameter, moisture and diameter-definition by Geldart C fines content, Powder Technol. 235 (2013) 1038–1046.

[10] S. Lechner, M. Merzsch, H.J. Krautz, Heat-transfer from horizontal tube bundles into fluidized beds with Geldart A lignite particles, Powder Technol. 253 (2013) 14–21.

[11] S.S. Zabrodsky, Hydrodynamics and heat transfer in fluidized beds, MIT Press, Cambridge, Massachusetts, 1966.

[12] R. Noack, Lokaler Wärmeübergang an horizontalen Rohren in Wirbelschichten, Chem. Ing. Tech. 42 (6) (1970) 371–376.

[13] A. Mathur, S.C. Saxena, A. Chao, Heat transfer from an immersed vertical tube in a gas-fluidized bed, Ind. Eng. Chem. Process. Des. Dev. 25 (1986) 156–163.

[14] D. Kunii, O. Levenspiel, Fluidization Engineering, 2nd Ed., 1991 Butterworth-Heinemann, USA, 1991.

[15] H.-J. Natusch, B. Neukirchen, R. Noack, Lokale Wärmeübergangszahlen für ein Einzelrohr und für Rohrbündel verschiedener Anordnung in Wirbelschichten. Schlussbericht, GVT-Bericht 1975-8 Forschungs-Gesellschaft Verfahrenstechnik e.V. (GVT), 1975.

[16] O. Molerus, A. Burschka, S. Dietz, Particle migration at solid surfaces and heat transfer in bubbling fluidized beds 2, Chem. Eng. Sci. 50 (5) (1995) 879–885.

[17] H. Martin, Wärmeübergang in Wirbelschichten (chap. M5), VDI Wärmeatlas, 11th Ed., 2013 Springer-Verlag, Berlin Heidelberg, 2013.

[18] H.A. Vreedenberg, Heat transfer between a fluidized bed and a horizontal tube, Chem. Eng. Sci. Bd. 9 (1) (1958) 52–60.

[19] N.I. Gel'perin, V.G. Einstein, Heat Transfer in Fluidized Beds. Fluidization, Chap. 10, (1971).

[20] J.C. Petrie, W.A. Freeby, J.A. Buckham, In-bed heat exchangers, Chem. Eng. Prog. 64 (7) (1968) 45–51.

[21] O. Molerus, K.-E. Wirth, Heat Transfer in Fluidized Beds, 1st Ed., 1997 Springer-Verlag, Berlin Heidelberg, 1997.

[22] D. Geldart, Types of gas fluidization, Powder Technol. 7 (1973) 285–292.

Paper [3]

Contents lists available at ScienceDirect

Chemical Engineering Research and Design

journal homepage: www.elsevier.com/locate/cherd

Acting on hydrodynamics to improve the local bed-to-wall heat transfer in bubbling fluidized beds

Gerhard Hofer[a,*], Gerhard Schöny[b], Tobias Pröll[a]

[a] University of Natural Resources and Life Sciences, Institute for Chemical and Energy Engineering, Peter-Jordan-Str. 82, 1190 Vienna, Austria

[b] TU Wien, Institute of Chemical Engineering, Getreidemarkt 9/166, 1060 Vienna, Austria

ARTICLE INFO

Article history:
Received 17 July 2017
Received in revised form 5 April 2018
Accepted 9 April 2018
Available online 18 April 2018

Keywords:
Bubbling fluidized bed
Fluidized bed hydrodynamics
Gas distribution
Heat transfer
Mass transfer

ABSTRACT

Literature offers several excellent contributions in view of hydrodynamics and heat transfer characteristics of fluidized beds. Our investigations deal with the achievable wall-to-bed heat transfer rates at a tube bundle heat exchanger immersed in a bubbling bed of Geldart Type B particles. We confirm the findings of other authors, who described the lateral distribution of bed voidage as well as horizontal and vertical particle velocity and heat transfer. The heat transfer coefficients in the core of the bed are significantly higher than they are at the walls. An adapted gas distributor with a non-uniform nozzle-grid was used to overcome the disadvantage of unevenly distributed heat transfer. While the heat transfer coefficients close to the wall are 25–50% lower than in the core region when a uniform nozzle-grid is used, the effect can be fully balanced with the modified gas distributor. We conclude that a more even lateral distribution of heat transfer rates is possible while the overall heat exchange rate remains unchanged. Nevertheless, an increased uniformity in lateral particle mixing may indicate an improvement in heat surface load and mass transfer.

1. Introduction

Process design for different applications of fluidized bed reactors and fluidized bed systems requires an accurate understanding of fluidized bed hydrodynamics and of the correlated in-bed and wall-to-bed heat transfer. In the past, numerous studies have been performed to describe flow patterns and heat transfer characteristics of bubbling fluidized beds. Different methods have been selected for the investigation of the mentioned phenomena. Alongside of the various cold flow models in 2D and 3D configuration, computational fluid dynamic simulations revealed a great deal of information. Undoubtedly, every approach has its advantages and disadvantages. However, most of the conducted investigations with respect to hydrodynamics and wall-to-bed heat transfer lead to comparable conclusions.

As far as one is concerned with the hydrodynamics of a relatively deep bubbling bed (height/diameter-ratio >1) of Geldart Type B particles, Kunii and Levenspiel (1991) concluded that the particle flow occurs in upward movement at the centerline of the bed accompanied by a downward flow at the walls, illustrated in Fig. 1. Moreover, it is widely accepted that the described hydrodynamics of such bubbling beds evoke the formation of certain vortexes in between of the particle up- and down-flow paths. The movement of particles is caused by the rising bubbles and the correlating pressure gradients inside the fluidized bed.

The behavior of the emulsion flow according to Fig. 1 is underlined by the findings of Hamzehei (2011), who reported that the lateral '*void fraction profile is roughly uniform in the core of the bed with a slight decrease near the walls*'. Starting at the gas distributor, bubbles form, coalesce and grow while rising. Since bubbles tend to congregate toward the centerline of the bed with increasing gas flow, a lateral difference in bed voidage may be expected for deep bubbling fluidized beds in particular.

Many applications require fluidized bed reactors to be equipped with immersed heat exchangers, which are often designed as tube bundles. Lately, Gomez-Garcia et al. (2017) proposed to have tube bundle heat exchangers immersed in multi-stage fluidized beds for particle-receiver solar power plants. In order to create a fundamental understanding of such configurations, a number of authors investigated hydrodynamics and heat transfer having tube bundles immersed in bubbling beds.

* *Corresponding author.*
E-mail address: gerhard.hofer@boku.ac.at (G. Hofer).
https://doi.org/10.1016/j.cherd.2018.04.015

Nomenclature

Notation

A	Surface area of heat transfer measurement probe, m^2
d_t	Outer diameter of heat exchanger tubes, m
d_{sv}	Sauter mean diameter of particles, μm
h_{fb}	Fluidized bed heat transfer coefficient, $W\,m^{-2}\,K^{-1}$
$h_{fb,core}$	Fluidized bed heat transfer coefficient in the core-zone, $W\,m^{-2}\,K^{-1}$
$h_{fb,wall}$	Fluidized bed heat transfer coefficient in the wall-zone, $W\,m^{-2}\,K^{-1}$
$h_{fb,weighted}$	Weighted fluidized bed heat transfer coefficient, $W\,m^{-2}\,K^{-1}$
h_i	Apparent fluidized bed heat transfer coefficient, $W\,m^{-2}\,K^{-1}$
Δh_r	Random measurement error, W
Δh_s	Systematic measurement error, W
H_{hex}	Total height of heat exchanger, m
H_{max}	Maximum fluidized bed height, m
p_d	Pitch between gas distributor and heat exchanger, m
p_h	Horizontal tube pitch, m
p_v	Vertical tube pitch, m
Q	Power consumption of heat transfer measurement probe, W
t	Time, s
T_{fb}	Temperature of fluidized bed, K
T_{probe}	Temperature of heat transfer measurement probe, K
U	Superficial gas velocity, $m\,s^{-1}$
U_{mf}	Minimum fluidization gas velocity, $m\,s^{-1}$
x	x-coordinate, m
y	y-coordinate, m
z	z-coordinate, m
β_{hex}	Specific surface area, $m^2\,m^{-3}$
ρ_g	Density of gaseous phase, $kg\,m^{-3}$
ρ_p	Density of particles, $kg\,m^{-3}$
ψ_{hex}	Tube bundle void fraction, 1

Yurong et al. (2004) conducted a series of computational simulations having a single tube as well as a horizontal row of tubes immersed in fluidized particles with 1 mm in diameter and a particle density of 1600 $kg\,m^{-3}$. Their work presents results concerning the distribution of axial particle velocity as a function of radial distance from the fluidized bed wall. Thereby, the row of tubes was placed at a distance of 0.18 m from the gas distributor. Downward movement of particles at the wall and an upward flow of solids was observed in the center of the bed. Similar findings have also been reported by Li et al. (2011) and Verma et al. (2016), who performed extensive computational simulations with regards to the hydrodynamics at horizontal and vertical tube bundles. Rüdisüli et al. (2012) found somewhat similar behavior when they conducted measurements examining the radial bubble distribution (representing bed voidage and axial particle velocity) in a fluidized bed with immersed vertical tubes.

As early as in 1968 Gel'perin et al. reported that, having a bundle of horizontal tubes immersed in a bubbling bed, a significant drop in heat transfer can be observed near the walls. The same conclusions were drawn by Bock and Molerus (1980), Fukusako et al. (1988), Pisters and Prakash (2011) and Lechner (2012). However, Fukusako et al. (1988) mentioned that uniform heat transfer coefficients were measured for larger mean particle diameters (490 μm and 1145 μm). Both, Stefanova et al. (2008) and Yao et al. (2015) conducted extensive heat transfer measurements having a single vertical tube immersed in a bubbling fluidized bed. Stefanova et al. (2008) reported that the different heat transfer rates '*can be attributed to the different flow structures in the two regions*' (i.e. center- and wall-region). They also observed a dense layer of downward-moving mixture of gas and particles at the wall. With an increase in gas velocity the lateral heat transfer distribution became more uniform. Yao et al. (2015) correlated all these phenomena to the packet renewal model, first proposed by Mickley and Fairbanks (1955). They described that '*there are more bubbles in the bed center than near the wall*' and that this '*corresponds to more frequent packet renewal on tube surface in the bed center*'. Furthermore, it was mentioned that '*bubbles choose to dodge the near-wall region, which enables packets to stay on tube surface longer and become a resistance of heat transfer*'.

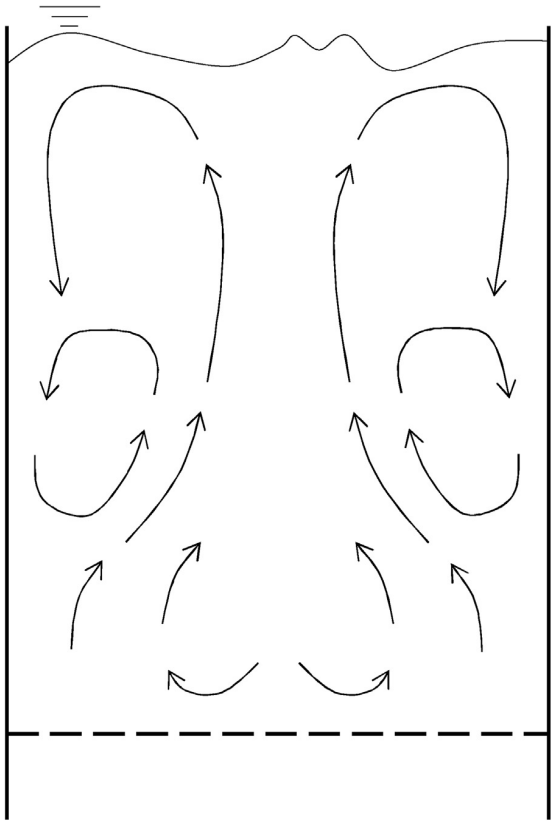

Fig. 1 – Movement of solids in deep bubbling beds of Geldart Type B particles according to Kunii and Levenspiel (1991).

We hypothesize that the phenomenon of decreasing heat transfer coefficients in the wall region may be insignificant for fluidized bed reactors of large dimension. However, especially when it comes to the design of relatively small but fully functional bubbling bed reactors (i.e. bench and pilot scale units) where high heat transfer rates may be necessary to optimize process operation, an accurate knowledge of local heat transfer coefficients is obligatory. This study is concerned with the determination of region-dependent heat transfer rates for a bubbling fluidized bed of particles in the Geldart Type B range. The expected effect of reduced heat transfer rates at the fluidized bed walls should be confirmed in a first step. Subsequently, a potential method is presented to improve lateral particle mixing and, thus, to increase heat transfer near the walls.

2. Materials and methods

A cold flow model, referred to as heat transfer measurement test device (HTMT), was used to experimentally obtain wall-to-bed heat transfer coefficients in bubbling fluidized beds. A picture of the HTMT is given in Fig. 2. The HTMT is designed

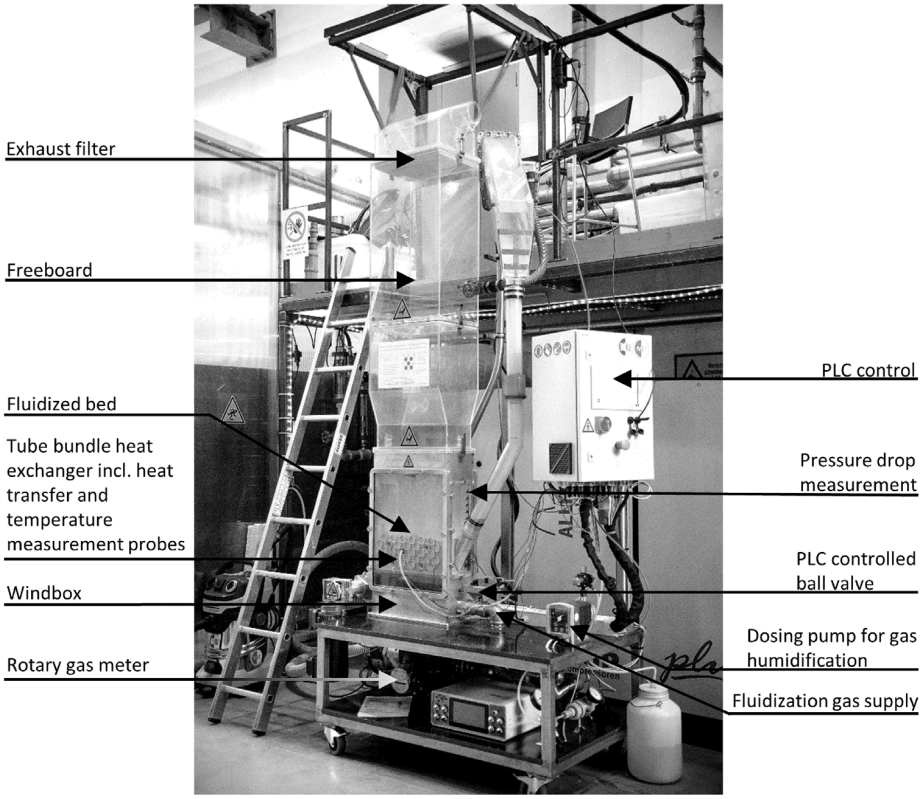

Fig. 2 – Heat transfer measurement test device.

to allow heat transfer investigations at single tubes as well as tube bundles of varying geometry.

The HTMT is mostly made of acrylic glass to allow the observation of the fluidized bed behavior. The dimensions of the fluidized bed are 0.4 × 0.2 m in length (y-axis) and width (x-axis) and the bed height (z-axis) can get up to 0.4 m. Particles are fluidized with compressed air, which is dried right after compression. The gas volume flow is measured with a rotary gas meter and regulated via a PLC controlled valve. The introduced fluidization gas may be preheated if necessary. To reduce electrostatic effects during operation, all metal parts are grounded and the air used for fluidization may be humidified in a controlled manner prior introduction into the unit. Additionally, the pressure drop across the entire fluidized bed is measured as well as across a specific bed height. That allows for calculation of the current bed voidage.

A tubular probe, referred to as heat transfer measurement probe, was used to obtain fluidized bed heat transfer coefficients (Fig. 3). The probe consists of a copper cylinder of 16 mm in diameter and 100 mm in length, placed in between acrylic glass tips isolating the probe from the environment. The length of both acrylic isolators is 50 mm. The total length of the heat transfer measurement probe adds up to 200 mm. The heated copper part of the heat transfer measurement probe covers 50% of the fluidized bed depth and consequently does not provide resolution in the x-axis. The copper cylinder is equipped with an electrical heating cartridge and two resistance thermometers. The power consumption Q and the temperature T_{probe} of the heat transfer measurement probe is recorded during the experiments. Thereby, the temperature of the measurement probe is kept constant by regulating the power consumption of the heating cartridge via PLC control. Furthermore, the surface area A of the heated copper cylinder is well defined. The fluidized bed temperature T_{fb} is obtained

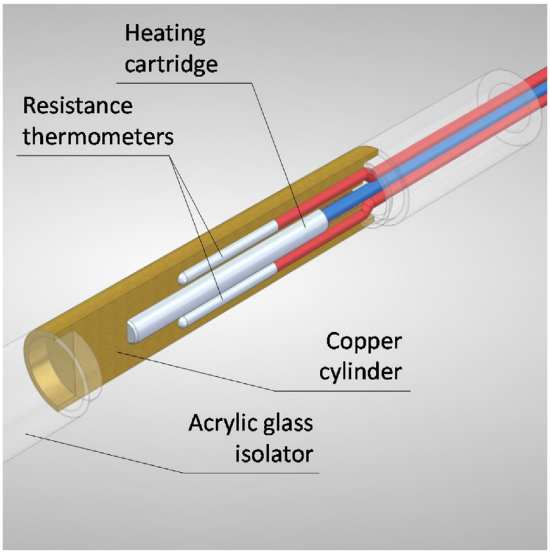

Fig. 3 – Heat transfer measurement probe.

with two temperature measurement probes. An in-bed temperature measurement probe is shown in Fig. 4. The outer diameter of these probes is 16 mm, just as the diameter of the heat transfer measurement probe and the other 'inert' tubes representing the tube bundle heat exchanger. The data provided by the sensors is recorded every second. Hence, the apparent wall-to-bed heat transfer rate h_i is calculated according to Eq. (1).

$$h_i = \frac{Q}{A \cdot \left(T_{probe} - T_{fb}\right)} \quad (1)$$

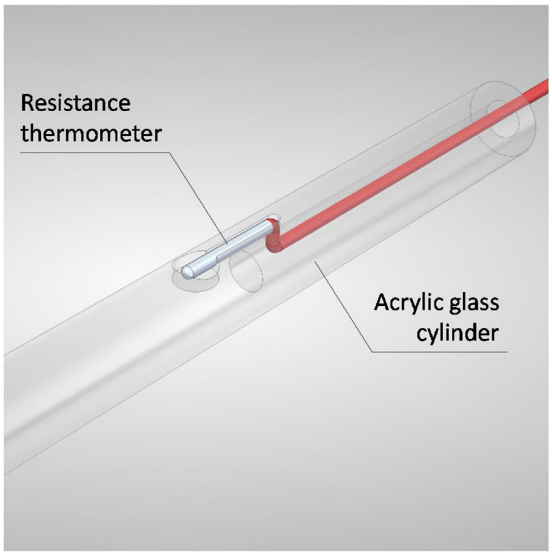

Fig. 4 – Fluidized bed temperature measurement probe.

The derived heat transfer coefficients cumulate heat transfer due to gas- and particle-convection and do not distinguish between them. Since temperatures are below 425 K heat transfer due to radiation is negligible (Werther, 2007). The temperature of the measurement probe was set to a temperature of 330 K. Since the fluidized bed is operated near ambient conditions, the temperature difference between the heated measurement probe and the fluidized bed was at least 30 K. Every experiment was conducted with only one heated measurement probe immersed in the fluidized bed.

All the used resistance thermometers are Pt100 and classified as 1/3DIN standard. The measurement accuracy regarding the electric power consumption of the heated probe is ±0.1 W. Taking these accuracies into account, the systematic measurement error Δh_s due to error propagation is derived with Eq. (2). For typical HTMT operating conditions the systematic error is lower than ±3% of h_i.

$$\Delta h_s = \left|\frac{1}{A\cdot\left(T_{Probe}-T_{fb}\right)}\right|\cdot(\pm 0.1\ \mathrm{W}) + \left|-\frac{Q}{A\cdot\left(T_{probe}-T_{fb}\right)^2}\right|\cdot \left(\pm\frac{1}{3}\cdot\left(0.3\,^{\circ}\mathrm{C}+0.005\cdot T_{probe}\right)\right) + \left|\frac{Q}{A\cdot\left(T_{probe}-T_{fb}\right)^2}\right| \cdot\left(\pm\frac{1}{3}\cdot\left(0.3\,^{\circ}\mathrm{C}+0.005\cdot T_{fb}\right)\right) \quad (2)$$

To ensure reproducibility of the conducted tests the operation of the HTMT is standardized regarding the variation of the fluidization gas flow. Starting at low gas velocity, the gas flow is increased incrementally up to a certain maximum gas velocity. Every setting of gas flow is kept constant for 120 s. When the maximum gas flow is reached, the HTMT is programmed to decrease gas flow incrementally once again. Therefore, the fluidized bed heat transfer rate as a function of superficial gas velocity is measured twice for each setting of gas volume flow. For the recorded heat transfer values the arithmetic mean heat transfer rate and standard deviation is calculated.

The occurring standard deviation may be referred to as random error Δh_r. The random measurement error originates in the heat transfer measurement probe contacting with the different phases of the bubbling bed, which are (a) solid phase and (b) gas phase. Therefore, the arithmetic mean fluidized bed heat transfer rate h_{fb} for each superficial gas velocity is calculated with Eq. (3). The averaged heat transfer rates including the occurring standard deviations regarding the experimentally obtained data are given in Tables A1 and A2 in the Appendix A.

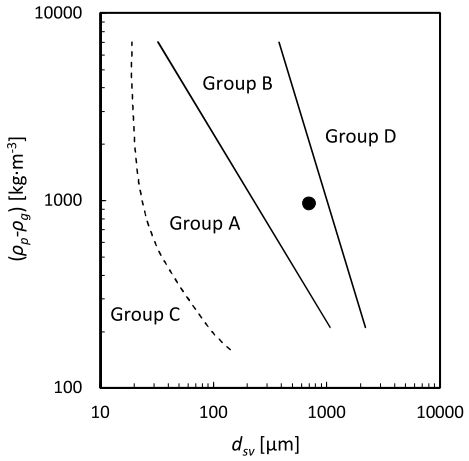

Fig. 5 – Powder classification diagram according to Geldart (1973).

Table 1 – Characteristic properties of the heat transfer measurement test device and the tube bundle heat exchanger.

Parameter	Symbol	Value	Unit
Heat transfer measurement test device			
Length of the fluidized bed	L	0.4	m
Width of the fluidized bed	W	0.2	m
Maximum fluidized bed height	H_{max}	0.4	m
Tube bundle heat exchanger			
Tube outer diameter	d_t	0.016	m
Horizontal tube pitch	p_h	0.030	m
Vertical tube pitch	p_v	0.026	m
Distance between gas distributor and the heat exchanger	p_d	0.010	m
Total height including the distance to the gas distributor	H_{hex}	0.364	m
Specific surface area	β_{hex}	64.50	m^2 m^{-3}
Void fraction	ψ_{hex}	0.58	1

$$h_{fb} = \frac{1}{t}\sum h_i \pm \Delta h_r \quad (3)$$

Heat transfer was investigated for a bundle of horizontal tubes immersed in particles with a Sauter mean diameter (SMD) d_{sv} of 695 µm and a particle density ρ_p of 965 kg m^{-3}. These solids are clearly classified as Geldart Type B particles (Geldart, 1973), illustrated in Fig. 5. The distinct heat exchanger geometry used for the experiments is given in Table 1. The void fraction ψ_{hex} of the tube bundle heat exchanger was calculated according to Gnielinski (2013), given in Eq. (4).

$$\psi_{hex} = 1 - \frac{\pi}{4\cdot s_h} \quad (4)$$

For every experiment the superficial gas velocity U was varied in the range of about 0.04 –0.3 m s^{-1}, which is equivalent to a fluidization number $U{\cdot}U_{mf}{}^{-1}$ of about 0.2–1.5 for ambi-

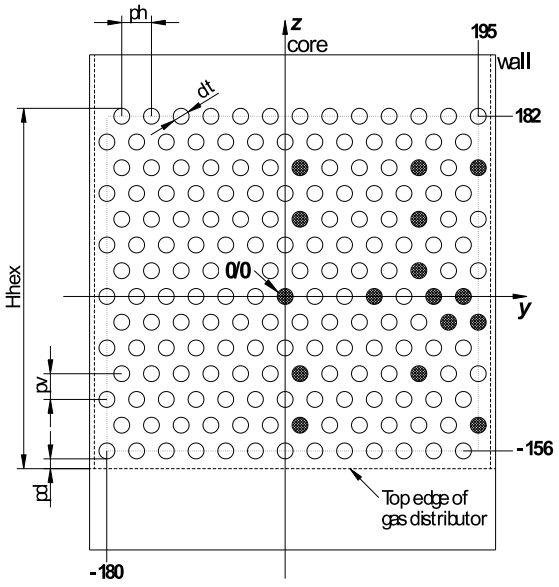

Fig. 6 – Layout of horizontal tube bundle and characteristic dimensions illustrating the tube positions at which heat transfer measurements were carried out.

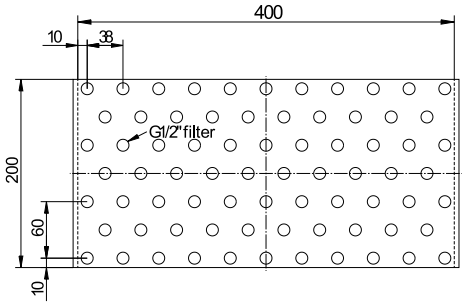

Fig. 7 – Constructional drawing of the gas distributor with uniform nozzle-grid.

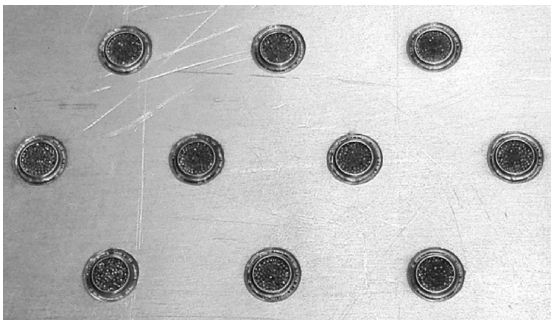

Fig. 8 – Nozzle-grid and individual sintered metal filters.

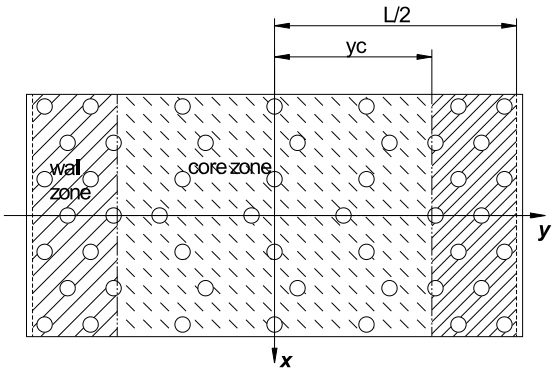

Fig. 9 – Gas distributor with modified nozzle-grid illustrating core-zone and wall-zone.

ent gas atmosphere ($U_{mf} = 0.2\,m\,s^{-1}$). It should be noted that the superficial gas velocity U is regarded as the gas velocity that occurs without the constriction of the free cross-section caused by the tubes immersed in fluidization. The actual averaged gas velocity is expected to be about 40% higher, as this is also indicated by the presented tube bundle voidage given in Table 1. The fluidized bed height at a superficial gas velocity of $0.04\,m\,s^{-1}$ was set to the height H_{hex}.

The heat transfer measurement probe was placed at different fluidized bed positions to obtain heat transfer coefficients as a function of the tube location relative to the walls and to the gas distributor. The selected positions are presented in Fig. 6. Thereby, 'inert' tubes adding up to the tube bundle have been replaced one by one with the heat transfer measurement probe. The positioning of the temperature measurement probes should provide information regarding the heat input of the heat transfer measurement probe. Thus, the first temperature measurement probe was placed right next to the heat transfer measurement probe. The second temperature measurement probe was placed in a distance of at least $6{\cdot}p_h$ to the heat transfer measurement probe. It was observed that the heat input of the heat transfer measurement probe has no effect on the fluidized bed temperature. Measurements in the negative y-coordinate were performed as well. It was confirmed that the heat transfer rates are symmetrical to the z-axis. However, these results are not presented in this work.

The individual tube locations are given in accordance with their actual distances along the y/z-axis to the point of reference 0/0. From there onwards, the distance in the y-direction de-/increases incrementally with each column of tubes ($p_h/2$), and thus ranges from −180 to 195. Accordingly, the z-coordinate de-/increases incrementally with p_v and ranges from −156 to 182. The labeling of the y/z-coordinates is illustrated in Fig. 6.

The gas distributor shown in Fig. 7 was used for the fluidized bed heat transfer rate measurements. It comprises 74 individual G1/2″ sintered metal filters screwed into an aluminum plate of 6 mm in thickness, illustrated in Fig. 8. Hence, the filters act as gas inlet nozzles. The number of nozzles was selected to ensure sufficient pressure drop across the gas distributor and thus to ensure homogeneous gas distribution. However, due to the relatively high pressure drop across the gas distributor, the maximum achievable gas flow rate is limited to about $80\,Nm^3\,h^{-1}$. The sintered metal filters further prevent solids from draining into the windbox below the gas distributor when the gas flow is switched off.

As mentioned earlier, other authors observed increased particle flow and thus improved heat transfer in the center of the fluidized bed. To increase the uniformity of heat exchange across the fluidized bed the gas distributor was adapted. For this, the pressure drop across the distributor was increased at the fluidized bed core. This was accomplished by sealing 25 individual gas nozzles in the core-region of the gas distributor. Hence, the introduced gas is forced toward the wall to enhance particle movement and thus heat transfer. The gas distributor with its remaining active nozzles is shown in Fig. 9.

The fluidized bed was divided into two distinct regions referred to as core-zone and wall-zone, as this is illustrated in Fig. 9. The width of the core-zone is characterized by a given

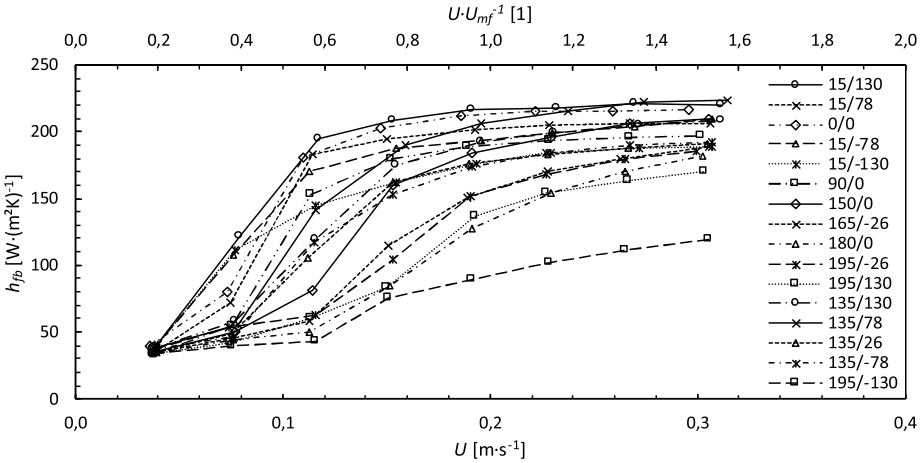

Fig. 10 – Heat transfer coefficients as a function of superficial gas velocity measured with the unmodified gas distributor (numbers in the legend indicate lateral/vertical position in the tube bundle with 0/0 representing the center).

length y_c. The zoning underlies the assumption, that particle circulation occurs according to Fig. 1 and thus symmetrical in the z-coordinate. Since the used measurement probes merely allow the determination of an average heat transfer rate along the tube axis, it was not possible to distinguish the heat transfer coefficient in the x-coordinate.

For further investigation, region-dependent mean heat transfer rates were calculated. This was accomplished by averaging the measured values in the z-coordinate for the characteristic positions $y = 0$, $y = y_c$ and $y = L/2$. In a further step, the calculation of arithmetic mean values of the obtained heat transfer rates in the range $y = 0 \ldots y_c$ lead to heat transfer coefficients in the fluidized bed core-zone ($h_{fb,core}$). This procedure was performed for the range $y = y_c \ldots L/2$ as well, which then represents heat transfer in the wall-zone ($h_{fb,wall}$). In a final step these zone-dependent heat transfer rates were weighted. Therefore, the ratio $(2 \cdot y_c)/L$ was introduced. Hence, the weighted heat transfer coefficients were calculated according to Eq. (5).

$$h_{fb,weighted} = h_{fb,core} \cdot \frac{2 \cdot y_c}{L} + h_{fb,wall} \cdot \left(1 - \frac{2 \cdot y_c}{L}\right) \quad (5)$$

3. Results and discussion

In Fig. 10 the experimental fluidized bed heat transfer rates for the tube bundle heat exchanger geometry presented in Table 1 are shown. Thereby, the gas distributor featuring the uniform nozzle-grid was used for fluidization.

It is shown that the achievable heat transfer coefficients are in the range of 40–220 $W\,m^{-2}K^{-1}$. The presented gas-velocity-dependency of heat transfer rates clearly follows the typical trends known from literature (Molerus and Wirth, 1997; Natusch et al., 1975). Hence, the lowest heat transfer coefficients are observed in the fixed bed regime ($U = 0.04\,m\,s^{-1}$). From this point on heat transfer increases with increasing superficial gas velocity. The reason for observing untypically high heat transfer rates at $U \cdot U_{mf}^{-1} < 1$ is the fact that the superficial gas velocity is regarded as the gas velocity not accounting for the constriction of the free cross-section by the immersed tubes.

The results clearly indicate that heat exchange strongly depends on the investigated fluidized bed region. Hence, relatively low heat transfer rates are measured at the wall of the

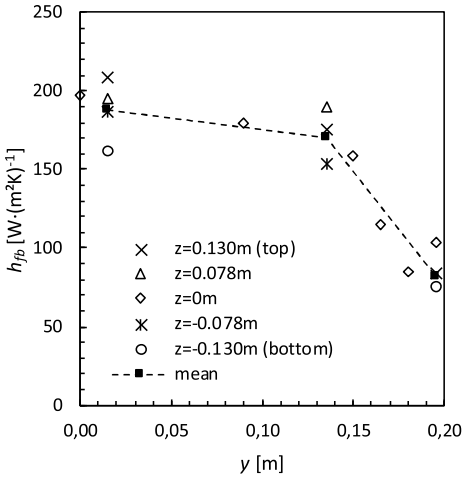

Fig. 11 – Position-dependent heat transfer coefficients at a superficial gas velocity $U = 0.15$ m/s.

HTMT (e.g. position 195/−26), whereas heat exchange tends to increase when moving toward the fluidized bed axis (e.g. position 15/78). Furthermore, the occurring heat transfer coefficients near the gas distributor (e.g. position 15/−130) seem to be lower as they are in the upper area (e.g. position 15/130). Fig. 11 summarizes the described phenomena by displaying heat transfer coefficients for a selected superficial gas velocity $U = 0.15\,m\,s^{-1}$ and varying y- and z-coordinate, which are now given in actual distances.

It is shown that heat transfer in the y-coordinate varies stronger than it does in the z-coordinate. Thus, mean heat transfer coefficients are calculated for the characteristic vertical positions $y = 0.015$ m, $y = 0.135$ m and $y = 0.195$ m and are shown in form of a linear interpolation (mean). Again, one can see that the heat transfer rates are highest in the fluidized bed axis ($y = 0.015$ m) and that relatively low rates are observed at the wall ($y = 0.195$ m). It seems that there is a specific distance ($y = y_c \approx 0.13$–0.15 m), in which heat transfer coefficients tend to drop more rapidly. This distance is about 0.06 m measured from the wall (which is equivalent to about $4 \cdot d_t$). Gel'perin et al. (1968) reported a characteristic distance of $2 \cdot d_t$, in which heat transfer decreases significantly.

The discussed evaluation procedure has been applied for three selected superficial gas velocities ($U = 0.15$, 0.19 and

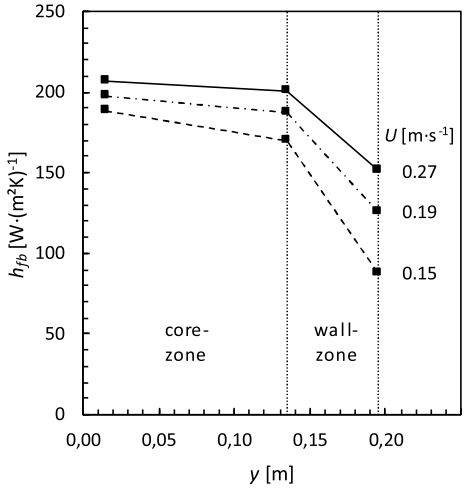

Fig. 12 – Position-dependent heat transfer coefficients for selected superficial gas velocities and the gas distributor with uniform nozzle-grid.

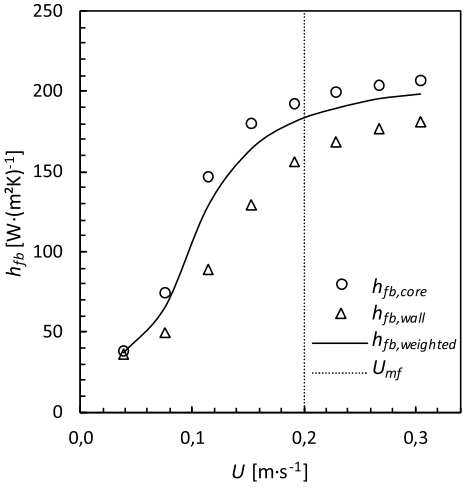

Fig. 13 – Averaged heat transfer rates in the fluidized bed core- and wall-zone and weighted heat transfer coefficients as a function of superficial gas velocity.

0.27 m s^{-1}). The calculated position-dependent mean heat transfer rates are presented in Fig. 12. With increasing fluidization gas velocity, a general increase of heat transfer is observed accompanied by significantly increased heat transfer at the wall.

According to the methodology described earlier gas-velocity-dependent heat transfer rates in the core-zone ($h_{fb,core}$) and wall-zone ($h_{fb,wall}$) were calculated. The results as well as the weighted heat transfer coefficients $h_{fb,weighted}$ are shown in Fig. 13.

As mentioned earlier, the curves displayed in Fig. 13 represent the averaged fluidized bed heat transfer coefficients for the core-zone and wall-zone, respectively. The weighted, overall fluidized bed heat transfer rate is expected to lie in between these curves. Since the core-zone represents about 70% of the entire fluidized bed cross section, the weighted curve is closer to the heat transfer coefficients measured in the core-zone.

To counteract the described phenomenon of diverging heat transfer coefficients in the core- and wall-zone, an uneven gas distribution was deliberately forced by utilizing the adapted gas distributor presented in Fig. 9. In Fig. 14 the measured heat transfer rates obtained during the experiments with the modified gas distributor are shown for selected y/z-coordinates.

While heat transfer seems to be slightly decreased in the core zone (e.g. positions 0/0 and 15/130), it more or less remains constant at position 135/26 and significantly increases in the wall-zone of the fluidized bed (e.g. positions 180/0, 195/130 and 195/−130). The previously applied calculation procedure has been used to calculate averaged heat transfer coefficients for the selected superficial gas velocities (U = 0.15, 0.19 and 0.27 m s^{-1}). The results are shown in Fig. 15. One can see that the heat transfer rates are now highest at the wall (y = 0.195 m). Inherently, with increasing local gas velocity also heat transfer increases. Fig. 16 summarizes the achievable heat transfer rates of the fluidized bed in the core- and wall-zone as well as the weighted results as a function of superficial gas velocity U.

Although the averaged results regarding the core- and wall-zone clearly indicate that heat transfer is distributed more evenly with the modified gas distributor, an increase of the overall wall-to-bed heat transfer was not observed (Fig. 17). Nevertheless, the presented method could be used to distribute the heat exchangers heat surface load more evenly. Furthermore, it is evident that uniform heat transfer rates across the in-bed heat exchanger is equivalent to uniform hydrodynamics of the fluidized bed. This can be synony-

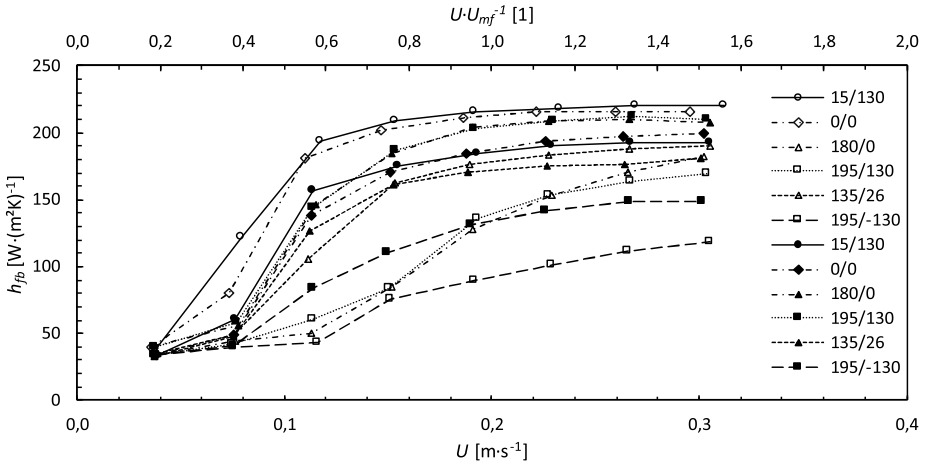

Fig. 14 – Comparison of heat transfer coefficients as a function of superficial gas velocity measured with the unmodified and modified gas distributor (blank markers = uniform nozzle-grid, solid markers = modified nozzle-grid).

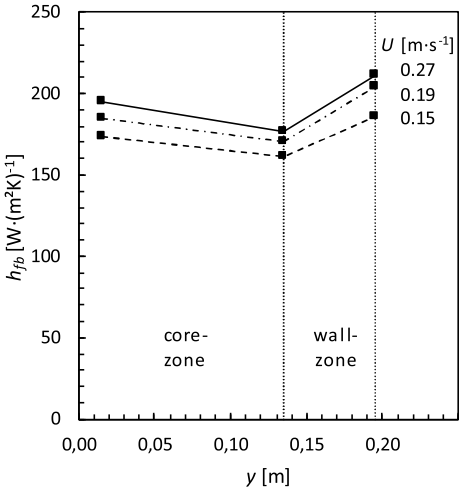

Fig. 15 – Position-dependent heat transfer coefficients for selected superficial gas velocities and the gas distributor with modified nozzle-grid.

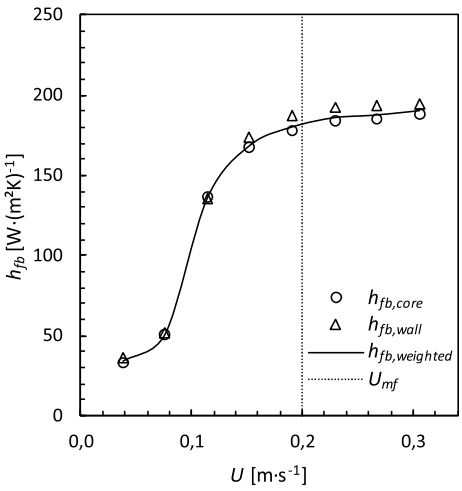

Fig. 16 – Averaged heat transfer rates in the fluidized bed core- and wall-zone and weighted heat transfer coefficients as a function of superficial gas velocity for the modified gas distributor.

mously interpreted as evenly distributed contact between the gas phase and solids. Therefore, a uniform fluidized bed mixing behavior may lead to improved mass-transfer.

4. Conclusion

In this study, it was shown that heat transfer between an in-bed heat exchanger (featuring tubes with 0.016 m in outer diameter and an equilateral tube pitch setting of 0.03 m) and the contacting particles (d_{sv} = 695 μm, ρ_p = 965 kg m^{-3}) strongly depends on the region of the fluidized bed. Therefore, the fluidized bed was divided into distinct regions referred to as

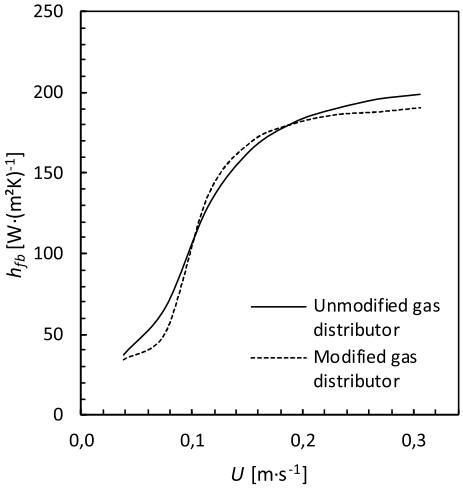

Fig. 17 – Comparison of weighted heat transfer coefficients for the unmodified and modified gas distributor.

core-zone and wall-zone. The used gas distributor is designed to evenly distribute the fluidization gas. Because of the fluidized bed hydrodynamics this distributor leads to relatively high heat transfer coefficients in the core-zone, but heat transfer in the wall-zone is decreased significantly. With the aim to increase the overall heat exchange rates, the gas distributor was modified to enforce particle movement in the wall-zone.

Regarding the uniformity of heat transfer rates across the different fluidized bed zones it is evident that the overall heat transfer rate may be distributed more evenly by implementing the modified gas distributor with lower pressure drop in the wall-zone. Even better results may be achieved by adapting the gas distributor more precisely, by means of a perforated plate with a larger number of holes of smaller and/or varying diameter. Hence, the perforation should feature bigger holes in the wall-zone and smaller ones in the core-zone, which would have an improving and more controllable effect on the deliberate gas distribution across the fluidized bed. The overall heat exchange rate of the bundle was not increased by the modification of the gas distributor. However, the presented method may lead to increased uniformity of the heat exchangers heat surface load. Additionally, the increased uniformity of heat transfer rates across the fluidized bed regions may be synonymously interpreted as evenly distributed contact between the gas phase and the solids. Thus, mass transfer may be improved by achieving a uniform fluidized bed mixing behavior.

Acknowledgments

The authors appreciate the financial support by the Austrian Climate and Energy Fund (FFG project no. 845022) and gratefully acknowledge funding and publication permission from Shell Global Solutions International B.V., The Hague.

Appendix A.

Table A1 – Experimental heat transfer rates including random measurement error values for different measurement probe positions and unmodified gas distributor.

	Position (y/z)							
U [m s^{-1}]	1/5	1/3	0/0	1/−3	1/−5	6/0	10/0	11/−1
	$h_{fb} \pm \Delta h_r$ [W m^{-2} K^{-1}]							
0.04	38 ± 4	35 ± 3	37 ± 3	38 ± 3	41 ± 4	34 ± 3	36 ± 3	35 ± 3
0.08	122 ± 24	72 ± 17	71 ± 13	108 ± 31	109 ± 6	54 ± 8	50 ± 5	46 ± 4
0.11	194 ± 12	183 ± 13	177 ± 11	170 ± 9	138 ± 7	153 ± 11	82 ± 17	58 ± 7
0.15	209 ± 13	195 ± 9	197 ± 8	187 ± 8	155 ± 7	179 ± 9	159 ± 9	115 ± 8
0.19	216 ± 6	201 ± 10	208 ± 8	193 ± 8	168 ± 7	188 ± 6	184 ± 9	151 ± 8
0.23	218 ± 8	204 ± 10	212 ± 7	199 ± 7	180 ± 8	193 ± 8	196 ± 8	170 ± 7
0.27	221 ± 8	206 ± 7	212 ± 8	204 ± 6	190 ± 9	196 ± 8	205 ± 6	180 ± 7
0.31	220 ± 6	206 ± 8	212 ± 6	209 ± 8	197 ± 8	197 ± 7	210 ± 7	188 ± 6

	Position (y/z)							
U [m s^{-1}]	12/0	13/−1	13/5	9/5	9/3	9/1	9/−3	13/−5
	$h_{fb} \pm \Delta h_r$ [W m^{-2} K^{-1}]							
0.04	34 ± 2	37 ± 2	34 ± 3	37 ± 4	39 ± 6	35 ± 3	38 ± 4	34 ± 3
0.08	44 ± 7	54 ± 5	42 ± 3	58 ± 6	56 ± 9	49 ± 7	47 ± 4	40 ± 3
0.11	50 ± 3	62 ± 6	61 ± 8	120 ± 14	142 ± 15	105 ± 14	117 ± 11	43 ± 4
0.15	85 ± 11	104 ± 15	84 ± 14	175 ± 11	190 ± 12	162 ± 7	153 ± 9	76 ± 8
0.19	128 ± 6	152 ± 7	136 ± 8	192 ± 6	206 ± 8	176 ± 10	174 ± 8	89 ± 5
0.23	154 ± 7	168 ± 6	154 ± 8	199 ± 9	215 ± 10	183 ± 8	184 ± 10	102 ± 6
0.27	170 ± 7	180 ± 7	164 ± 9	205 ± 8	222 ± 10	188 ± 7	189 ± 10	111 ± 6
0.31	182 ± 7	185 ± 6	170 ± 7	208 ± 11	224 ± 10	190 ± 8	192 ± 7	119 ± 2

Table A2 – Experimental heat transfer rates including random measurement error values for different measurement probe positions and modified gas distributor.

	Position (y/z)						
U [m s^{-1}]	1/5	0/0	12/0	13/5	9/1	13/−5	
	$h_{fb} \pm \Delta h_r$ [W m^{-2} K^{-1}]						
0.04	34 ± 4	34 ± 4	40 ± 7	40 ± 7	33 ± 4	34 ± 3	
0.08	61 ± 11	49 ± 6	56 ± 6	58 ± 10	47 ± 6	41 ± 3	
0.11	156 ± 15	138 ± 12	146 ± 30	144 ± 35	126 ± 22	84 ± 7	
0.15	175 ± 11	171 ± 12	185 ± 17	187 ± 21	161 ± 13	110 ± 6	
0.19	185 ± 10	185 ± 8	204 ± 13	203 ± 14	171 ± 10	131 ± 7	
0.23	190 ± 9	193 ± 12	209 ± 11	209 ± 11	175 ± 7	142 ± 6	
0.27	192 ± 7	197 ± 11	210 ± 12	212 ± 12	176 ± 7	148 ± 8	
0.31	193 ± 11	200 ± 14	208 ± 13	210 ± 10	181 ± 6	148 ± 10	

References

Bock, H.-J., Molerus, O., 1980. Einfluß der Strömungsmechanik auf den Wärmeübergang in Gas/Feststoff-Wirbelschichten. Chem. Ing. Tech. 52 (3), 260–261.

Fukusako, S., Ishiguro, S., Seki, N., 1988. Heat-transfer characteristics from a bundle of horizontal tubes immersed in aggregative fluidized bed. Wärme- und Stoffübertragung 22, 13–22.

Gel'perin, N.I., Ajnstejn, V.G., Zajkovsij, A.V., 1968. Hydraulische und wärmetechnische Eigenschaften eines Fließbettes mit waagrechten Rohrbündeln. Chimiceskoe i neftjanoe masinostroenie 3, 17–20.

Geldart, D., 1973. Types of gas fluidization. Powder Technol. 7, 285–292.

Gnielinski, V., 2013. Heat transfer in cross-flow around single rows of tubes and through tube bundles. In: VDI Heat Atlas, 2nd ed., 2010. Springer-Verlag, Berlin Heidelberg (Chapter G7).

Gomez-Garcia, F., Gauthier, D., Flamant, G., 2017. Design and performance of a multistage fluidised bed heat exchanger for particle-receiver solar power plants with storage. Appl. Energy 190, 510–523.

Hamzehei, M., 2011. Study of heat transfer and hydrodynamics in the fluidized bed reactors. In: Belmiloudi, A. (Ed.), Heat Transfer — Mathematical Modelling, Numerical Methods and Information Technology. InTech, ISBN: 978-953-307-550-1.

Kunii, D., Levenspiel, O., 1991. Fluidization Engineering, 2nd ed. Butterworth-Heinemann, USA.

Lechner, S., 2012. Untersuchungen zur Berechnung und Optimierung des Wärmeübergangs bei der Dampfwirbelschichttrocknung am Beispiel von Lausitzer Braunkohlen. PhD Thesis. Faculty of Mechanical, Electrical and Industrial Engineering, Brandenburg University of Technology, Brandenburg, Germany.

Li, T., Dietiker, J.-F., Zhang, Y., Shahnam, M., 2011. Cartesian grid simulations of bubbling fluidized beds with a horizontal tube bundle. Chem. Eng. Sci. 66, 6220–6231.

Mickley, H.S., Fairbanks, D.F., 1955. Mechanism of heat transfer to fluidized beds. AIChE J. 1 (3), 374–384.

Molerus, O., Wirth, K.-E., 1997. Heat Transfer in Fluidized Beds, 1st ed. Springer-Verlag, Berlin, Heidelberg.

Natusch, H.-J., Neukirchen, B., Noack, R., 1975. Lokale Wärmeübergangszahlen für ein Einzelrohr und für Rohrbündel verschiedener Anordnung in Wirbelschichten. Schlussbericht, GVT-Bericht 1975-8, Forschungs-Gesellschaft Verfahrenstechnik e.V. (GVT).

Pisters, K., Prakash, A., 2011. Investigations of axial and radial variations of heat transfer coefficient in bubbling fluidized bed with fast response probe. Powder Technol. 207, 224–231.

Rüdisüli, M., Schildhauer, T.J., Biollaz, S.M.A., Van Ommen, J.R., 2012. Radial bubble distribution in a fluidized bed with vertical tubes. Ind. Eng. Chem. Res. 51, 13815–13824.

Stefanova, A., Bi, H.T., Lim, C.J., Grace, J.R., 2008. Heat transfer from immersed vertical tube in a fluidized bed of group A particles near the transition to the turbulent flow regime. Int. J. Heat Mass Transf. 51, 2020–2028.

Verma, V., Li, T., Dietiker, J.-F., Rogers, W.A., 2016. Hydrodynamics of gas-solids flow in a bubbling fluidized bed with immersed vertical U-tube banks. Chem. Eng. J. 287, 727–743.

Werther, J., 2007. Fluidized-bed Reactors. Ullmann's Encyclopedia of Industrial Chemistry.

Yao, X., Zhang, Y., Lu, C., Han, X., 2015. Systematic study on heat transfer and surface hydrodynamics of a vertical heat tube in a fluidized bed of FCC particles. AIChE J. 68, 68–83.

Yurong, H., Huilin, L., Qiaoqun, S., Lidan, Y., Yunhua, Z., Gidaspow, D., Bouillard, J., 2004. Hydrodynamics of gas-solids flow around immersed tubes in bubbling fluidized beds. Powder Technol. 145, 88–105.

Paper [4]

ARTICLE IN PRESS

Chemical Engineering Science xxx (2018) xxx–xxx

Contents lists available at ScienceDirect

Chemical Engineering Science

journal homepage: www.elsevier.com/locate/ces

Particle mixing in bubbling fluidized bed reactors with continuous particle exchange ☆

G. Hofer *, T. Märzinger, C. Eder, F. Pröll, T. Pröll

University of Natural Resources and Life Sciences, Institute for Chemical and Energy Engineering, Peter-Jordan-Str. 82, 1190 Vienna, Austria

HIGHLIGHTS

- Tracer experiment used for bubbling bed particle mixing characterization.
- Bubbling bed mixing mostly characterized by ideally mixed flow.
- Axial dispersion plug flow superimposes mixed flow at fluidization number of 4.7.
- Dead spaces and short-circuit flows observed at fluidization number of 4.7.

ARTICLE INFO

Article history:
Received 29 June 2018
Received in revised form 3 September 2018
Accepted 2 October 2018
Available online xxxx

Keywords:
Bubbling fluidized bed
Tracer experiment
Residence time distribution
Particle mixing
Fluidized bed hydrodynamics

ABSTRACT

This paper reports on experiments conducted with a cold flow model utilized for the investigation of the particle residence time distribution and mixing characteristics in a bubbling fluidized bed with continuous solids exchange. The investigated system is of a rectangular cross section (0.4 × 0.2 m) with a bed height of 0.17 m. A measurement device based on an alternating current bridge circuitry coupled with lock-in amplifier technology was built in the scope of quantifying the solids residence time distribution, whereby a pulse-injected ferromagnetic tracer creates the input signal. The implementation of a profound mathematical routine ensures the reproducible calculation of the particles mean residence time and characteristic values describing particle mixing phenomena. Therefore, the *E*-curve was modeled by mathematical convolution of the exit age distributions available for an ideally mixed continuous stirred tank reactor and a plug flow reactor with axial dispersion. It is shown that the in-bed mixing is highly dependent on the fluidization rate as well as on the solids circulation rate. Albeit the lowest superficial gas velocity equals a fluidization number of 4.7, the formation of dead spaces and short-circuit flows was observed under these conditions. Axial dispersion coefficients in the range of $5 \cdot 10^{-3}$ to $7 \cdot 10^{-1}$ $m^2\,s^{-1}$ were obtained.

1. Introduction

Dimensioning fluidized bed reactors for chemical and thermal processes is of a challenging nature. A new process design or the optimization of an existing process often involves the deployment of cold flow models (CFMs) enabling the investigation of fluidized bed and/or solids transport phenomena for de-risking in view of prospective operational disturbances. Performant solids mixing and sufficient residence time in the reaction zone as well as adequate heat transfer alongside a smooth carryover of solids are the key factors for an optimal process design. Considering continuously operated bubbling fluidized bed (BFB) reactors with ongoing solids feed or exchange such as in combustion (Sette et al., 2015), temperature swing adsorption (Pröll et al., 2016) or drying (Chen et al., 2017), the particle residence time distribution (RTD) is of special interest when it comes to de-risking and optimization. The arrangement of particle feed and discharge and the placement of in-bed devices such as baffles or heat exchangers, potentially influence the exit age distribution, and thus the reactor efficiency.

For bubbling fluidized bed reactors it is stated that it seems reasonable to assume complete mixing, that is the fluidized bed behaves like an ideal continuous stirred tank reactor (CSTR), for (a) narrow particle size distribution (PSD), (b) no short-circuiting between the particle feed to the drain and (c) complete mixing of the particles, i.e. the absence of dead spaces (Yagi and Kunii, 1961). Modeling the RTD of a single staged CSTR is easy by applying Eq. (1), with only the MRT τ_{CSTR} to be varied. Albeit the model is of a simple nature, the comparison of the resulting *E*-curve with measured data from a tracer experiment might reveal quite a few reactor design flaws. A detailed discussion regarding the

☆ This document is a collaborative effort.

* Corresponding author.
E-mail address: gerhard.hofer@boku.ac.at (G. Hofer).

https://doi.org/10.1016/j.ces.2018.10.001
0009-2509/

Please cite this article in press as: Hofer, G., et al. Particle mixing in bubbling fluidized bed reactors with continuous particle exchange. Chem. Eng. Sci. (2018), https://doi.org/10.1016/j.ces.2018.10.001

List of symbols

Roman characters

Ar	archimedes number (1)
C	capacitance (F)
C_{pulse}	pulse input (1)
$C_{response}$	continuous response to a pulse input (1)
$\mathbf{D}$	axial dispersion coefficient ($m^2\ s^{-1}$)
$\mathbf{D}/(u{\cdot}L)$	vessel dispersion number (1)
d_{sv}	sauter mean diameter (m)
E	exit age distribution function (s^{-1})
E_{fit}	modeled exit age distribution function (s^{-1})
F	cumulative exit age distribution function (1)
U_{mf}	minimum fluidization bed height (m)
j	imaginary unit (1)
k_{max}	E_{fit}-curve 'take-off' maximum slope (s^{-2})
L	inductance, characteristic length (H, m)
m_s	solids mass (kg)
$\dot{m}_s$	solids mass flow ($kg\ h^{-1}$)
$m_{s,drain}$	drain-section solids mass (kg)
$m_{s,feed}$	feed-section solids mass (kg)
p	pressure (Pa)
R	resistance (Ω)
S_0	straight line zeroing $C_{response}$ (1)
S_1	k_{max}-sloped straight line determining τ_1 (1)
T	temperature (K)
t	time (s)
U	superficial gas velocity (ms^{-1})
U_{mf}	minimum fluidization gas velocity (ms^{-1})
U/U_{mf}	fluidization number (1)
u	characteristic velocity (ms^{-1})
ΔV_{DC}	DC voltage change (V)
V_{in}	AC bridge input voltage (peak-peak) (V)
V_{out}	AC bridge output voltage (peak-peak) (V)
$\dot{V}_g$	gas volume flow ($m^3\ h^{-1}$, $Nm^3\ h^{-1}$)
w_{tracer}	mass fraction of tracer (1)

Greek characters

β	phase shift (°)
θ	temperature(°C)
μ	electromagnetic permeability ($H\ m^{-1}$)
μ_0	permeability constant ($H\ m^{-1}$)
ϱ	bulk density ($kg\ m^{-3}$)
ϱ_p	particle density ($kg\ m^{-3}$)
τ	mean residence time (s)
tau_0	time at C_{pulse} = max (s)
tau_1	breakthrough time at $S_1 = 0$ (s)
τ_2	breakthrough time at the occurrence of k_{max} (s)
τ_3	breakthrough time at $C_{response}$ = max (s)
τ_{CSTR}	mean residence time of a CSTR (s)
τ_{fit}	mean residence time calculated from E_{fit} (s)
τ_{hyd}	haydraulic residence time (s)
τ_{PFR}	mean residence time of a PFR (s)
ω	angular frequency ($rad\ s^{-1}$)

List of abbreviations

AC	alternating current
AD	axial dispersion
BFB	bubbling fluidized bed
CAPEX	capital expenditure
CC	carbon capture
CCS	carbon capture and storage
CCU	carbon capture and utilization
CFB	circulating fluidized bed
CFM	cold flow model
CLC	chemical looping combustion
CO_2	carbon dioxide
CSTR	continuous stirred tank reactor
DC	direct current
DU	detector unit
FCC	fluid catalytic cracking
HEX	heat exchanger
HRT	hydraulic residence time
ID	inner diameter
LIA	lock-in amplifier
MU	main unit
MRT	mean residence time
OD	outer diameter
OPEX	operational expenditure
PCB	printed circuit board
PCS	process control system
PFD	process flow diagram
PFR	plug flow reactor
PID	proportional-integral-derivative
PLC	programmable logic controller
PSD	particle size distribution
RTD	residence time distribution
SBC	single-board computer
SCR	solids circulation rate
SMD	Sauter mean diameter
TSA	temperature swing adsorption
WTB	wall-to-bed

respective effects is given in the literature (Levenspiel, 1998), reproduced in Fig. 1. A more comprehensive approach in modeling RTDs of non-ideal reactors either involves the utilization of the tanks-in-series model or the dispersion model (Scott Fogler, 2015), or the combination of different models by means of mathematical convolution (Levenspiel, 1998).

$$E_{CSTR} = \frac{1}{\tau_{CSTR}} \cdot \exp\left[\frac{-t}{\tau_{CSTR}}\right] \quad (1)$$

Numerous studies concerned with the hydrodynamics and solids RTD of fluidized bed systems can be found in the literature. A comprehensive review considering the most suitable methods proposed for the measurement of particle RTDs and mixing behavior in (circulating) fluidized beds was put together by Harris et al. (2003). Later, other authors presented substantial reviews of articles concerned with the RTD as well as the models available to mathematically describe the related phenomena (Bruce Nauman, 2008; Gao et al., 2012). Most of the studies deal with circulating fluidized bed (CFB) reactors, because of them being widely used in industrial applications such as fluid catalytic cracking (FCC), chemical looping combustion (CLC) or gasification. With respect to bubbling fluidized bed reactors operated under continuous solids exchange, the variety of investigations focussed on the particle RTD is limited. Nilsson and Wimmerstedt (1988) as well as Bachmann and Tsotsas (2015) investigated the RTD in horizontal fluidized beds, followed by a comprehensive review concerned with the models available for the calculation of the dispersion coefficient **D** (Kunii and Levenspiel, 1991; Bachmann et al., 2016). Other investigations aim the deliberate manipulation of the fluidized bed hydrody-

Please cite this article in press as: Hofer, G., et al. Particle mixing in bubbling fluidized bed reactors with continuous particle exchange. Chem. Eng. Sci. (2018), https://doi.org/10.1016/j.ces.2018.10.001

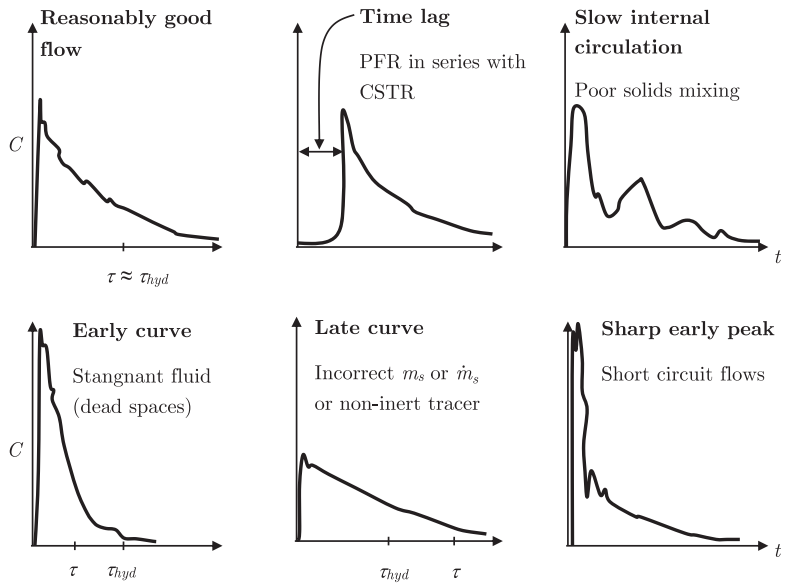

Fig. 1. Misbehaving mixed flow reactors, adapted from Levenspiel (1998).

namics by means of immersed baffles (Bachmann et al., 2017; Kong et al., 2018). In most cases, the focus lies on the characterization of particle mixing, mostly in view of batch-wise operated reactors but also applying the dispersion coefficient for the description of mixing phenomena (Bellgardt and Werther, 1986; Sette et al., 2014).

As mentioned earlier, different techniques are available to achieve the task of detecting diverse tracer materials. The present setup ought to be equipped with an non-intrusive online tracer detection system of high resolution in time also applicable to investigate CFBs of much lower mean residence times (MRTs), whereby the most important requirement is the use of a non-hazardous tracer. Additionally, the data to be derived has to be of low bias. Because it was proven feasible and reliable in the past, the principle of a magnetic tracer measurement was selected. First experiments utilizing magnetic tracers were conducted by Fitzgerald et al. (1977) at a semi industrial unit. However, the system was of low resolution, and thus the results barely reproducible. Avidan and Yerushalmi (1985) performed tests by using a setup similar to the one proposed by Fitzgerald et al. (1977), with a more successful outcome. More recently, the principle of inductance measurement was successfully applied for the determination of the solids RTDs in a CFM utilized for the investigation of the respective effects in a dual-CFB with MRTs in the order of 10 s (Guío-Pérez et al., 2013; Guío-Pérez et al., 2013).

In the scope of this work and based on the work of Guío-Pérez et al. (2013), the tracer detection device utilizing inductance measurement technique was improved to increase sensor dimensions and to avoid signal drifting during longer measurement periods in the order of 600 s. The device comprises a Maxwell-Wien bridge coupled with lock-in amplifier (LIA) technology utilized for signal processing, whereby a single-board computer (SBC) is used to record the data. The system was implemented to a CFM operated under BFB-conditions and able for particle circulation, that is, the continuous exchange of the fluidized solids. Measurements under the variation of the fluidization rate and the solids circulation rate (SCR) were conducted to prove suitability of the developed tracer detection device.

2. Experimental

2.1. The cold flow model

Most parts of the CFM were made of acrylic glass allowing for visual observation of the fluidization behavior. The cross-sectional dimension of the chamber enclosing the fluidized bed was 0.4 m in length by 0.2 m in width, whereby the overall height of the BFB can get up to about 0.4 m. A differential pressure sensor (Kalinsky, DS2-420, 100 mbar range) was used to determine the pressure drop across the entire bed height. Additionally, the pressure drop across a specified height was recorded as well (Kalinsky, DS2-420, 100 mbar range) allowing for the calculation of the bed voidage. The freeboard was equipped with an exhaust gas filter preventing the release of fines.

A process control system (PCS) was installed to operate the CFM and to assume all arising control tasks via the programmable logic controller (PLC). It enables the user to set the desired operational parameters at a touchscreen interface. Sensor data were written to a thumb drive for subsequent data evaluation. Thereby, the recording interval was set to 1 s.

A stream of dry air was supplied from a compressor unit. A rotary gas meter (Elster Instromet, RABO G250) was used to measure the actual gas volume flow. The gas meter allowed to tap the

Table 1
Measuring device accuracies.

Device	Measurement accuracy
Resistance thermometers (Pt100, 1/3DIN standard)	$\Delta T = \pm 1/3 \cdot (0.3\,^{\circ}\mathrm{C} + 0.005 \cdot \theta)$
Pressure sensor gas supply	Linearity error: $\Delta p = \pm 0.5\%$ Temperature error $(0 \ldots 50\,^{\circ}\mathrm{C}) : \Delta p = \pm 1\%$
Pressure sensors fluidized bed	Linearity error: $\Delta p = \pm 0.8\%$ Temperature error $(0 \ldots 50\,^{\circ}\mathrm{C}) : \Delta p = \pm 1\%$
Rotary gas meter	$\dot{V}_g = 2.5 \ldots 64\ \mathrm{m^3\ h^{-1}} : \Delta \dot{V}_g = \pm 2\%$ $\dot{V}_g = 64 \ldots 400\ \mathrm{m^3\ h^{-1}} : \Delta \dot{V}_g = \pm 1\%$

Please cite this article in press as: Hofer, G., et al. Particle mixing in bubbling fluidized bed reactors with continuous particle exchange. Chem. Eng. Sci. (2018), https://doi.org/10.1016/j.ces.2018.10.001

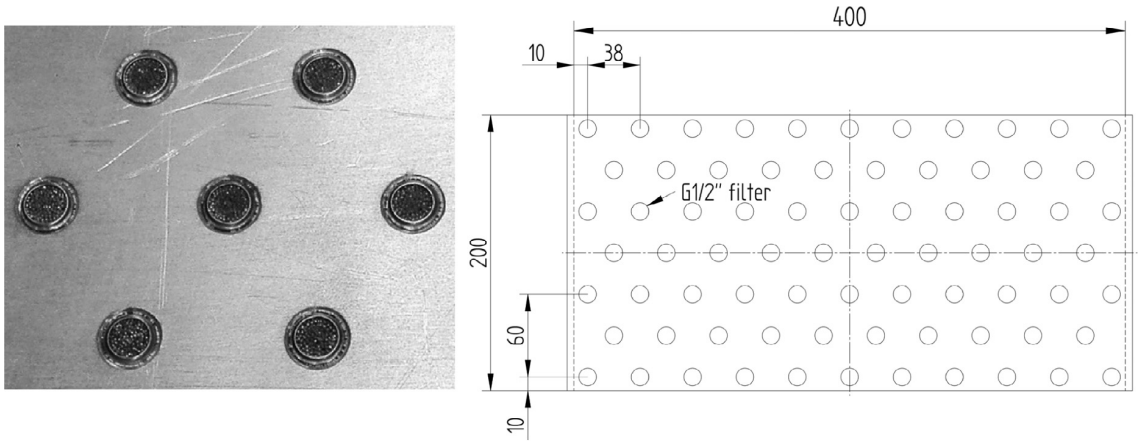

(a) Sintered metal filters. (b) Design drawing, dimensions in mm.

Fig. 2. Gas distributor.

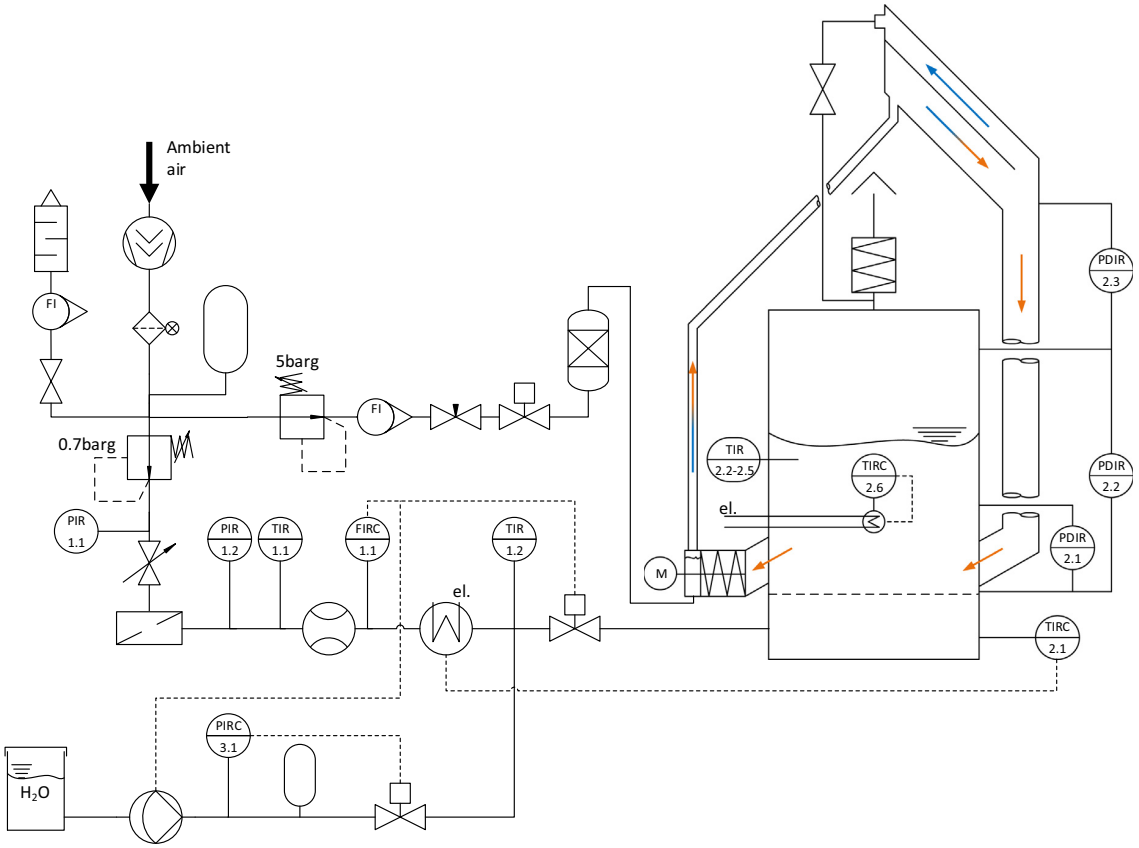

Fig. 3. PFD of the CFM illustrating particle circulation (orange = solids, blue = gas). (For interpretation of the references to color in this figure legend, the reader is referred to the web version of this article.)

gas temperature and pressure. The temperature was measured redundantly, i.e. with two resistance thermometers (Pt100, 1/3DIN standard). The supply pressure was measured by means of a differential pressure sensor (Kalinsky, DS2-420, 1000 mbar range). The measurement accuracy of these devices is given in Table 1. Humidified air was used to fluidize the bed material. A PLC-controlled dosing pump was used to dynamically adjust the amount of water sprayed into the gas stream achieving a certain humidity to reduce the effects of electrostatic charges occurring during fluidization. At the PCS the relative humidity was set, whereby the PLC calculated the mass flow of water to attain the desired humidity of the gas stream. A ball valve, controlled by the PLC, was used to manipulate the gas flow.

An aluminum plate of 6 mm in thickness featuring 74 individual G1/2 sintered metal filters was used for gas distribution. The sintered filters act as gas inlet nozzles and are shown in 2a. A design

Please cite this article in press as: Hofer, G., et al. Particle mixing in bubbling fluidized bed reactors with continuous particle exchange. Chem. Eng. Sci. (2018), https://doi.org/10.1016/j.ces.2018.10.001

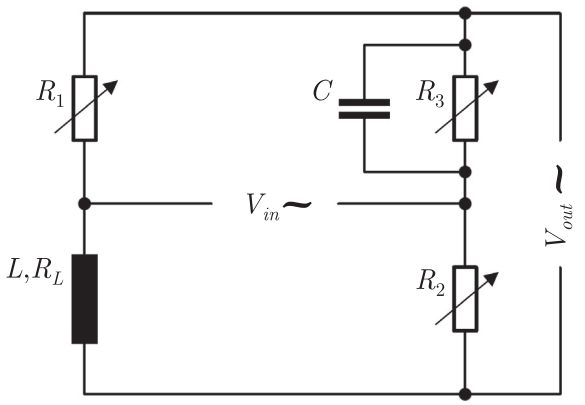

Fig. 4. Maxwell-Wien bridge circuit.

drawing of the gas distributor is given in Fig. 2b. The maximum gas flow rate was 80 $Nm^3\,h^{-1}$. The permeable metal filters hinder solids from draining into the windbox when the gas supply was switched off.

During operation, particles were continuously extracted from the fluidized bed, and recirculated for introduction opposite the point of withdrawal creating a net crosswise flow of gas and solids. For this, the narrower walls enclosing the fluidized bed were equipped with openings allowing the bed material to flow from and to the fluidized bed. A screw conveyor provided a constant flow of solids. The conveyor was driven by a frequency-controlled motor. A small compartment was located at the discharge of the screw conveyor. Particles entering this compartment were fluidized with humidified air, albeit it was not possible to adjust humidification in a controlled manner. The gas flow was set with a manual needle valve and a float-type flow meter (Krohne, VA40). Solids were lifted in a riser of 36 mm inner diameter (ID), which was connected to the described compartment at the lower end. A particle separator was connected at the risers uppermost position. While the gaseous phase exited the particle transport system being piped to the freeboard of the CFM, the particles were directed downwards reverting back into the BFB. The downcomer was made of an acrylic glass tube of 63 mm ID. The solids and the gas flow is illustrated in the process flow diagram (PFD) given in Fig. 3.

2.2. Measuring residence time distributions

The principle of magnetic tracer detection was utilized for the purpose of measuring particle RTDs. A tracer detection device was custom-designed based on previous work (Guío-Pérez et al., 2013). Inductors were used to detect ferromagnetic tracer particles influencing the coils' inductance L while passing. The change in inductance was processed by means of electrical circuitry. The obtained data was recorded for subsequent analysis.

2.2.1. Designing the measurement system

Fundamentally, the tracer detection device consisted of a coil integrated to a bridge circuit, i.e. an alternating current (AC)-driven Maxwell-Wien bridge (Fig. 4). The bridge was used in null-balanced mode and designed according to the balancing conditions given in the Eqs. (2)–(4). Practically, balancing the bridge was accomplished by adjusting R_1 to R_3 and selecting C in response to variations in the other arm that carries the sensor, resulting in $V_{out} \approx 0$ V. Null bridges have superior linearization characteristics and in small ranges of measurements the signal output may be considered to be quasi-linear (Sydenham and Thorn, 2005). Linearity characteristics of the custom-designed detection device are discussed at a later point.

The AC signal obtained from the Maxwell-Wien bridge was processed by means of a LIA, designed according to the applications information provided in the data sheet of the Analog Devices balanced modulator/demodulator AD630 (AnalogDevices, 2015). The principle of the detection device is schematically described in Fig. 5, illustrating the basic components and signal processing. The reference signal, an AC signal with the amplitude V_{in} obtained from an analogue sine wave generator and amplified before used for driving the measurement bridge, was phase-shifted and processed by the demodulator. The signal obtained from the measurement bridge was amplified once again and processed by the demodulator as well. A low-pass filter was used to obtain a direct current (DC)-signal, i.e. $\Delta V_{DC} = f(w_{tracer})$. The phase shift β was adjusted with respect to the voltage of the DC-signal. The circuitry and its amplification factors were designed to create adequate DC signals of high quality despite minimum amounts of tracer material introduced.

$$\frac{R_L + j \cdot \omega \cdot L}{R_1} = \frac{R_2 \cdot \left(\frac{1}{j \cdot \omega \cdot C} + R_3\right)}{\frac{R_3}{j \cdot \omega \cdot C}} \tag{2}$$

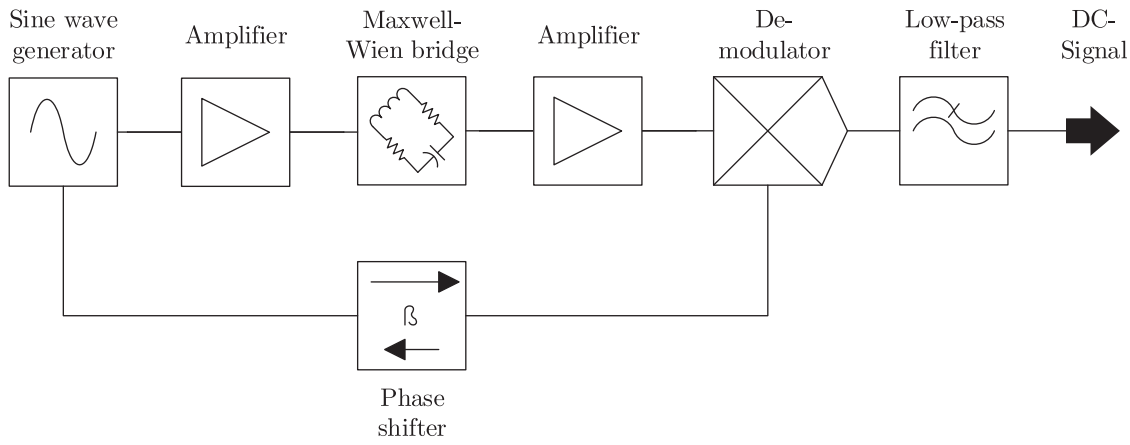

Fig. 5. Schematic of the tracer detection device.

Please cite this article in press as: Hofer, G., et al. Particle mixing in bubbling fluidized bed reactors with continuous particle exchange. Chem. Eng. Sci. (2018), https://doi.org/10.1016/j.ces.2018.10.001

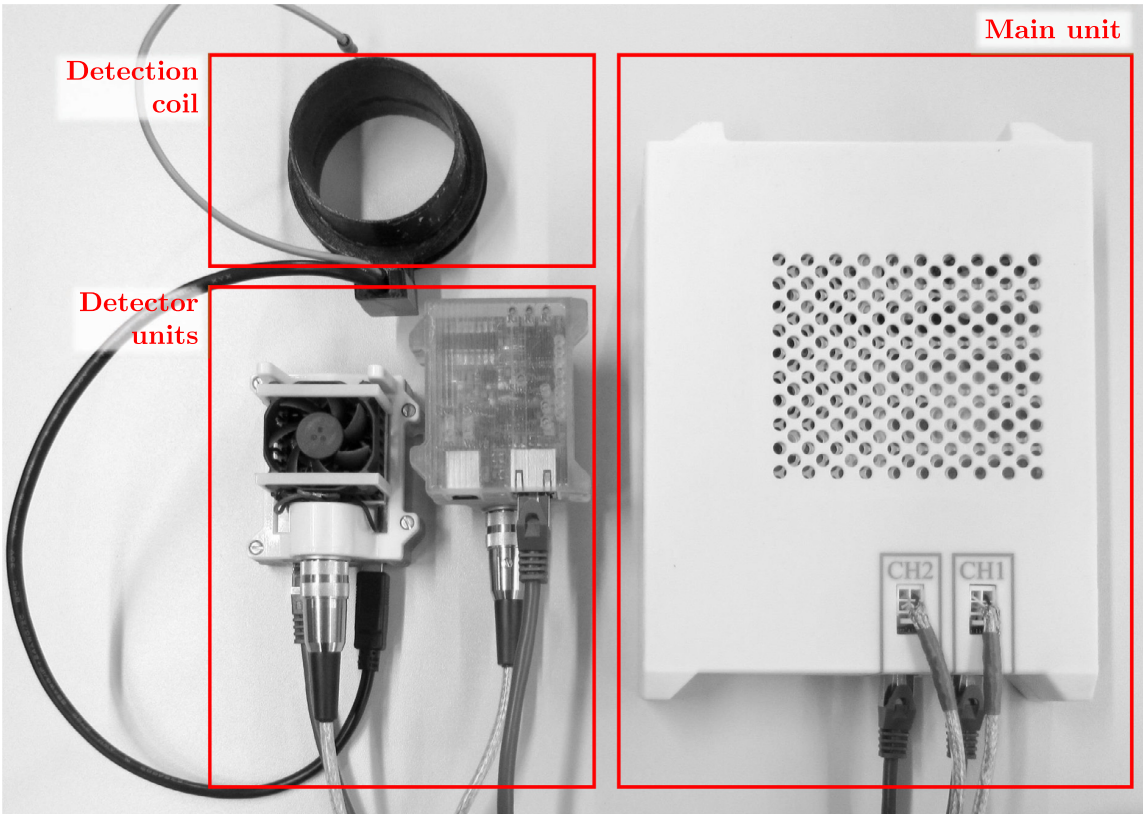

Fig. 6. Tracer detection equipment.

$$C = \frac{L}{R_1 \cdot R_2} \tag{3}$$

$$R_3 = \frac{R_1 \cdot R_2}{R_L} \tag{4}$$

The circuitry design was brought to printed circuit boards (PCBs). For data acquisition and data analysis two types of devices were available - the detector unit (DU) and the main unit (MU).

The DU, shown in Fig. 6, contained the circuitry depicted in Fig. 5 with the detection coil being connected externally. Therefore, the detection coil can be implemented easily to various particle transport lines. Considering the present setup, two coils were used for the measurement of the particle RTD. One coil was mounted at the lower end of the downcomer recording the input signal, whereas the second coil was placed at the point where particles are extracted from the fluidized bed. The positioning of the coils is illustrated in Fig. 7. The temperature of the DU was kept constant by means of a proportional-integral-derivative (PID)-controlled Peltier element to obtain stable and high quality measurement signals.

Two DUs were connected to the MU, a custom-designed extension board connected to a SBC (Raspberry Pi 3, Model B). Up to four extension boards may be connected to the SBC, allowing for the connection of up to eight DUs to a single MU. The MU, shown in Fig. 6, was used to drive the Peltier elements and to record the RTD-relevant data processed by the DUs.

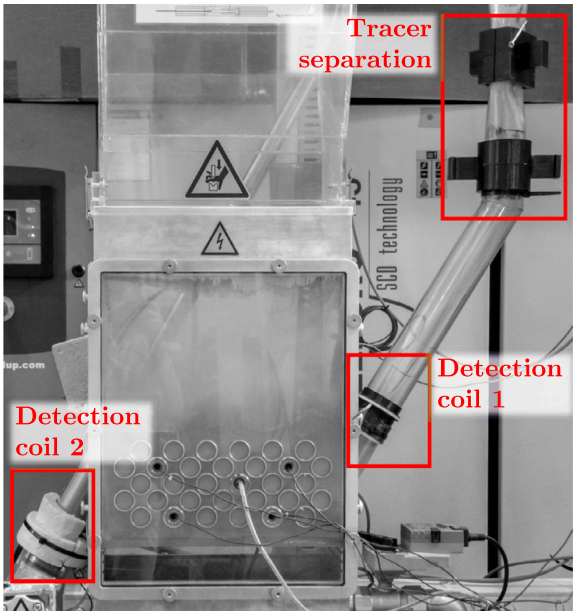

Fig. 7. Positioning of the detection coils and the magnetic tracer separation device.

2.2.2. Assessing linearity characteristics

Linearity of the measurement system was investigated by preparing fixed beds with different amounts of tracer added to the bulk of inert solids, i.e. the spherical glass beads. The prepared samples were well mixed before placed in the core of the detection coil. The results are illustrated in Fig. 8.

It is evident that the glass beads are in fact inert, meaning no change in the output signal ΔV_{DC} was detected having no tracer added. Continuously increasing the ferromagnetic tracer

Please cite this article in press as: Hofer, G., et al. Particle mixing in bubbling fluidized bed reactors with continuous particle exchange. Chem. Eng. Sci. (2018), https://doi.org/10.1016/j.ces.2018.10.001

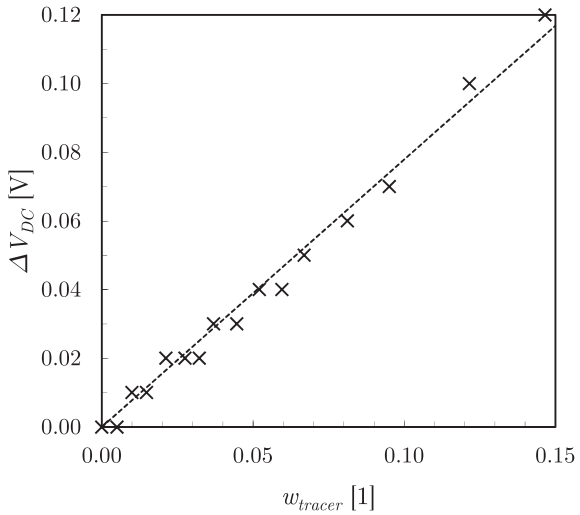

Fig. 8. Detector unit output signal change vs. mass fraction of steel tracer mixed in glass beads.

concentration causes the output signal to increase as well and the linear fit is a fair approximation for tracer concentrations up to 15 wt%.

2.2.3. Quantifying the solids circulation rate

It was assumed that the screw conveyor used for the particle transport provides a constant mass flow of solids. The PCS was used to set the SCR $\dot{m}_s$, translated to a frequency signal driving an AC motor, which was connected to the screw conveyor via a gearbox.

The system was calibrated in view of the interpretation of the user input in relation to the frequency-controlled signal output. For different settings of frequencies the mass flow was measured by blocking the solids flow at the lower end of the downcomer, i.e. at the entrance to the BFB (feed). Markings at the vertical section of the downcomer were used to determine the increase of the particle volume while extracting solids from the fluidized bed. The actual SCR was calculated based on the bulk density of the respective bulk material. The described procedure is illustrated in Fig. 9.

2.2.4. Handling the tracer

Magnetic separation devices, i.e. neodymium magnets ($40 \times 10 \times 5$ mm) incorporated to 3D-printed half-shells, were mounted on the outside of the downcomer and used to separate the ferromagnetic tracer particles from the inert bulk material. The position of the shells is shown in Fig. 7. Initially, the entire amount of ferromagnetic solids, 0.2 kg in weight, was kept in place on the inside of the downcomer by the magnetic separation devices. At some point, the shells were removed releasing the tracer. The magnetic shells were put back onto the downcomer right after injection, allowing the ferromagnetic solids to be circulated one time only. The tracer was transported to the inlet of the BFB for intermixing and detected by the downcomer-mounted coil (detection coil 1) connected to the first DU (C_{pulse}). While particles were still circulated, the tracer concentration $C_{response}$ at the outlet of the BFB was recorded with the tube-mounted coil (detection coil 2) connected to the second DU.

The detected pulse ideally resembled a Dirac delta function (Fig. 11, C_{pulse}), omitting the modeling of the input signal C_{pulse}. In practice, tests revealed that the input signal was of an insignificant length of time compared to the duration of the output signal $C_{response}$ (depicted in Fig. 11), reasonably leading to the assumption of an ideal dirac delta pulse used as input function for modeling the RTDs.

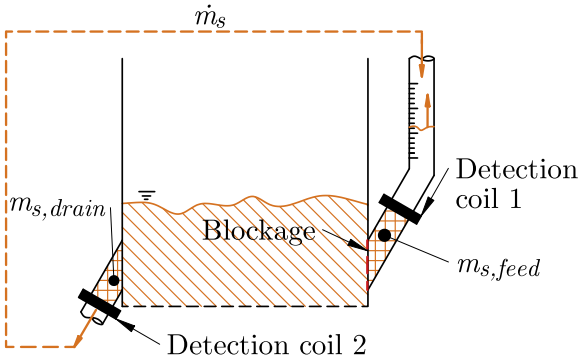

Fig. 9. Solids mass distribution (checkered = solids feed and drain - PFR, hachured = fluidized bed - CSTR), removable blockage for measuring the solids circulation rate.

2.2.5. Analyzing the recorded data

The data obtained with the RTD measurement system was recorded every ≈0.035 s and used for subsequent analysis, i.e. the determination of *E*-curves as a function of the SCR $\dot{m}_s$ and the superficial gas velocity *U*.

For signal processing, the continuous response signal $C_{response}$ recorded at the particle drain was truncated based on the acquired pulse input C_{pulse}. Thereby, the peak of the input signal determines the beginning of the measurement, referred to as tau_0, where $t = 0$. Although the DUs were kept at constant temperature, the DC-signal may have been subject to a slight drift considering the relatively long measuring time and the high signal amplification. To account for the temperature-based bias, 150 data points at the beginning, starting at tau_0, as well as at the end of the response signal, were averaged to level the $C_{response}$-curve zero. That is, both mean values were used for imprinting a straight line S_0 to be subtracted from $C_{response}$. The evaluation procedure is illustrated in Fig. 11.

For each combination of gas velocity *U* and solids circulation rate $\dot{m}_s$, measurements were repeated five times. The recorded data $C_{response}$ were synchronized in time, while tau_0 determines the beginning of each measurement. For each $C_{response}$-curve the exit age distribution *E* was calculated with the formula given in Eq. (5). The respective *E*-curves were averaged for further analysis.

$$E = \frac{C_{response}}{\int_{\tau_0}^{\infty} C_{response}\, dt} \tag{5}$$

The obtained exit age distributions *E* were modeled assuming a plug flow reactor (PFR) with axial dispersion (AD) and a CSTR in series (Fig. 10) according to Eq. (7), whereby an example is shown in Fig. 12a. Eq. (7) was obtained by the convolution of the exit age distribution function of a perfectly mixed CSTR, given in Eq. (1), and a PFR with imprinted AD. For small extents of dispersion, i.e. small vessel dispersion numbers $\mathbf{D}/(u \cdot L)$, the mathematical model interpreting a PFR with AD is given in Eq. (6). This approach was

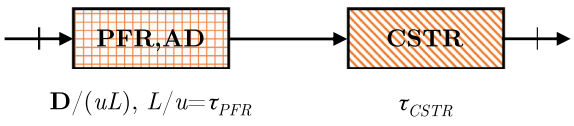

Fig. 10. Compartment flow model.

Please cite this article in press as: Hofer, G., et al. Particle mixing in bubbling fluidized bed reactors with continuous particle exchange. Chem. Eng. Sci. (2018), https://doi.org/10.1016/j.ces.2018.10.001

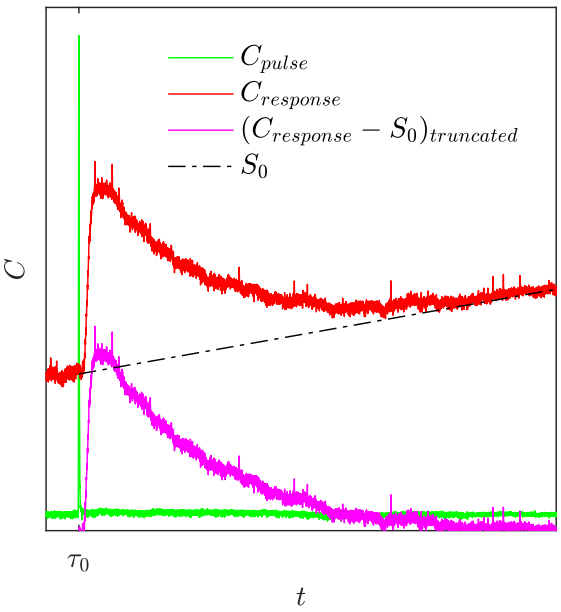

Fig. 11. RTD data preparation.

selected because of its physical plausibility considering the present experimental setup, i.e. a reaction zone resembling a single CSTR coupled with a particle in- and outlet similar to a PFR. With the detector coils arranged near the BFB in mind, the characteristic values coming from the dispersion model were mainly related to particle mixing processes in the BFB-zone.

Subsequently, the resulting E_{fit}-curves were used to assess characteristic data in view of the RTD and particle mixing, such as.

1. k_{max}, the maximum slope at the 'take-off' of the E_{fit}-curve,
2. τ_2, the breakthrough time at the occurrence of k_{max},
3. τ_1, the breakthrough time resulting from the straight line S_1, constructed considering k_{max}, intersecting the time axis (E_{fit}=0),
4. τ_3, the time span starting at tau_0 until the E-curve reaches its absolute maximum,
5. τ, the MRT calculated from the E-curve stemming from the $C_{response}$-signal,
6. τ_{fit}, the MRT stemming from the modeled E_{fit}-curve as well as
7. the vessel dispersion number $\mathbf{D}/(u \cdot L)$ and its individual components $\mathbf{D}$ and L/u=τ_{PFR}.

$$E_{PFR,AD} = \sqrt{\frac{u^3}{4 \cdot \pi \cdot \mathbf{D} \cdot L}} \cdot \exp\left[-\frac{L - u \cdot t}{4 \cdot \mathbf{D} \cdot L/u}\right] \tag{6}$$

$$\begin{aligned} E_{fit} = \; & E_{CSTR} * E_{PFR,AD} = \int_{\tau_0}^{\infty} E_{CSTR}(t\prime) \cdot E_{PFR,AD}(t - t')\, dt' \\ = \; & \frac{\sqrt{\mathbf{D}} \cdot \sqrt{L}}{2 \cdot \tau_{CSTR} \cdot u^{\frac{3}{2}}} \cdot \exp\left[\frac{\mathbf{D} \cdot L + \tau_{CSTR} \cdot u^2 \cdot (L - u \cdot t)}{\tau_{CSTR}^2 \cdot u^3}\right] \\ & \cdot \sqrt{\frac{u^3}{\mathbf{D} \cdot L}} \cdot \operatorname{erf}\left[\frac{2 \cdot \mathbf{D} \cdot L + \tau_{CSTR} \cdot u^2 \cdot (L + t' \cdot u - u \cdot t)}{2 \cdot \sqrt{\mathbf{D}} \cdot \sqrt{L} \cdot \tau_{CSTR} \cdot u^{\frac{3}{2}}}\right]_{\tau_0}^{\infty} \end{aligned} \tag{7}$$

$$\tau = \int_{\tau_0}^{\infty} t \cdot E\, dt \tag{8}$$

As for Item 6, it must be noted that the fit-function did not meet the criterion $E_{fit} = 0$ at the time of ending the experiment, which specifically held true for the low SCR of $\dot{m}_s = 88$ kg h^{-1}. Therefore, a termination criterion for calculating τ_{fit} was defined. By calculating the cumulative exit age distribution function F (Eq. (9)) based on the E_{fit}-curve and normalizing it to one in view of the time at the completion of the experiment, the required time $t_{0.632}$, that is when 63.2% of the tracer are recovered and $F = 0.632$ applies, was determined. In conclusion, τ_{fit} was calculated with Eq. (8) and the defined interval $[tau_0, 5 \cdot t_{0.632}]$.

On the one hand, results will be discussed based on the comparison of the calculated MRT τ_{fit} with the hydraulic residence time (HRT) τ_{hyd} (Eq. (10)). On the other hand, the E-curves were

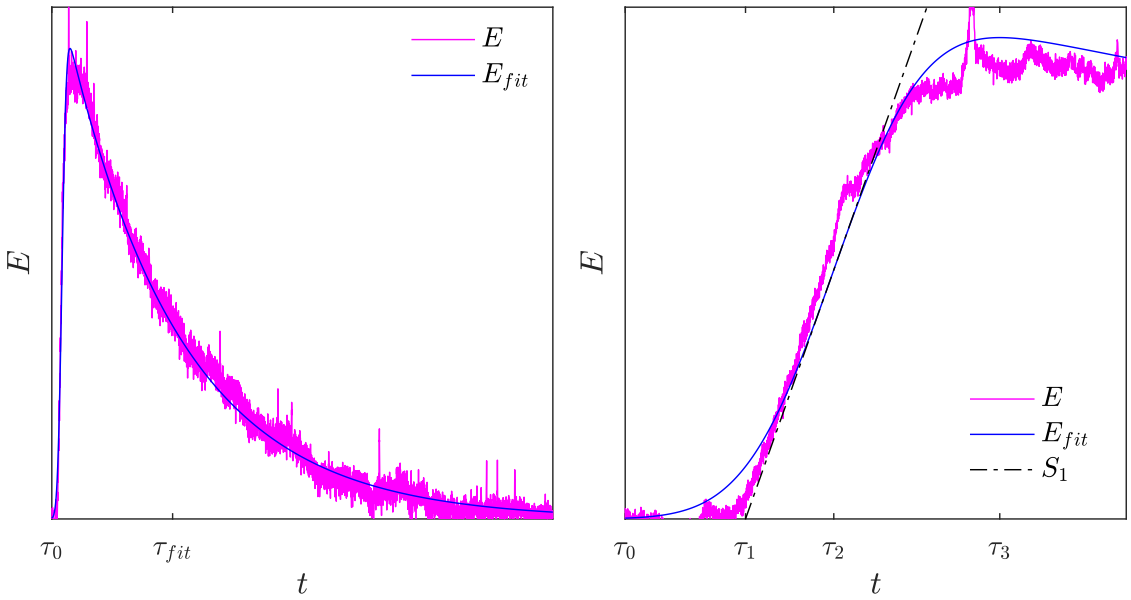

(a) Modeling the E-curve obtained from the $C_{response}$-signal.

(b) Determining RTD characteristic values.

Fig. 12. Mathematical fitting and analysis of the RTD data.

Please cite this article in press as: Hofer, G., et al. Particle mixing in bubbling fluidized bed reactors with continuous particle exchange. Chem. Eng. Sci. (2018), https://doi.org/10.1016/j.ces.2018.10.001

Table 2
Bulk material properties.

Bulk material		Glass beads	Flow tracer
d_{sv}	[µm]	130	72
ρ_p	[kg m^{-3}]	2450	7579
ρ_b	[kg m^{-3}]	1570	n/a
Ar	[1]	188	99
U_{mf}	[m s^{-1}]	0.017	0.016
μ/μ_0	[1]	≈1	1000…1800 (Carpenter Technology, 2018)

examined in view of the misbehaving characteristics of mixed flow reactors.

$$F = \int_{\tau_0}^{t} E\,dt \tag{9}$$

$$\tau_{hyd} = \frac{m_s}{\dot{m}_s} \tag{10}$$

2.3. Bulk materials

The experiments were performed with spherical glass beads with a Sauter mean diameter (SMD) of $d_{sv} = 130$ µm. Because of the large difference in their properties compared to other bulk materials, i.e. the magnetic permeability, steel particles were selected as the tracer used to measure particle RTDs. The material of the flow tracer was the ferritic stainless steel designated as 1.4742. The used bulk materials ought to achieve the best possible match in their fluid-dynamic properties, i.e. similarity in the minimum fluidization velocity U_{mf}. The properties of the used materials are given in Table 2. Both the glass beads and the steel particles are classified as Geldart Type B (Geldart, 1973).

The mass of glass beads contained in between the detection coils added up to 20.5 kg, assumed constant throughout the entire experimental campaign. To this, 0.2 kg were added in case of releasing the tracer to create the input-pulse. The bed height at minimum fluidization U_{mf} was 0.17 m.

The mass of glass beads contained in the feed-section $m_{s,feed}$, that is, in between detection coil 1 and the entrance to the fluidized bed, was 0.37 kg. The solids mass contained in the drain-section $m_{s,drain}$, i.e. in between the exit of the fluidized bed and detection coil 2, was 0.65 kg. Both values were used to calculate the plug flow HRT occurring in the particle feed and drain $\tau_{hyd} = (m_{s,feed} + m_{s,drain})/\dot{m}_s$.

2.4. Experimental plan

The RTD was measured for different superficial gas velocities and SCRs. The gas velocity U was varied in the discrete steps 0.08 m s^{-1}, U = 0.15 m s^{-1} up to U = 0.23 m s^{-1}, resembling the fluidization numbers U/U_{mf} 4.7, 8.8 and 13.5. For each of the three gas velocities the SCR $\dot{m}_s$ was set to 88 kg h^{-1}, 206 kg h^{-1} and 323 kg h^{-1}. Each measurement for the combination of the operational parameters U and $\dot{m}_s$ was repeated five times, enabling the statistical analysis of the recorded data.

In view of the low fluidization number the gas velocity was increased to U = 0.23 m s^{-1} right after completion of the experiment, causing enhanced particle mixing. This approach should reveal the possible formation of dead spaces.

3. Results and discussion

In the following, the mean residence times calculated from the experiments by applying Eq. (7) are discussed. At the same time, occurring deviations between τ_{fit} and τ_{hyd} are elaborated considering characteristic quantities such as k_{max} and the vessel dispersion number $\mathbf{D}/(u \cdot L)$ linking the results to particle mixing phenomena. In addition, the exit age distribution functions obtained during the experiments are examined in terms of possible reactor ills.

3.1. Low gas velocity

To start out with the lowest solids circulation rate of $\dot{m}_s$ = 88 kg h^{-1}, the calculated MRT τ_{fit} decreases as the circulation

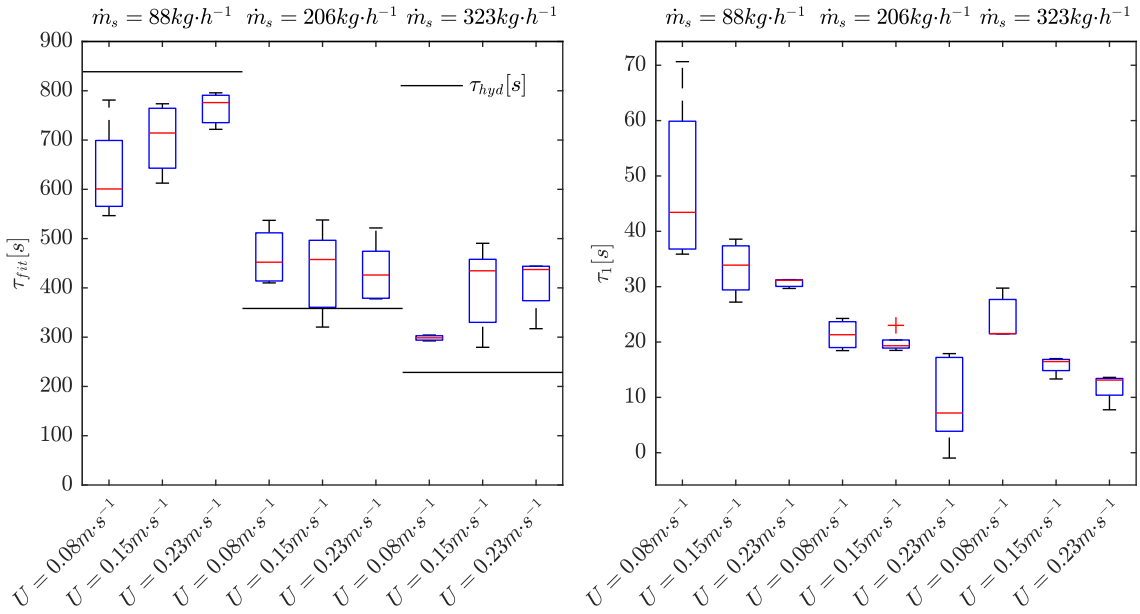

(a) τ_{fit} as a function of superficial gas velocity U and solids circulation rate $\dot{m}_s$.

(b) τ_1 as a function of superficial gas velocity U and solids circulation rate $\dot{m}_s$.

Fig. 13. τ_{fit} compared to $\tau_{hyd} = m_s/\dot{m}_s$ and τ_1.

Please cite this article in press as: Hofer, G., et al. Particle mixing in bubbling fluidized bed reactors with continuous particle exchange. Chem. Eng. Sci. (2018), https://doi.org/10.1016/j.ces.2018.10.001

rate increases, illustrated by the boxplot given in Fig. 13a. This circumstance already is indicated by Eq. (10). In specific view of the data obtained during the experiments with a SCR of $\dot{m}_s$ = 88 kg h^{-1}, the MRT τ_{fit} is observed to be lower than the expected value τ_{hyd}. The respective *E*-curve calculated from the $C_{response}$-signal as well as the E_{fit}-curve is shown in Fig. 16a for this operating point. A possible explanation for τ_{fit} being lower than τ_{hyd} may be the formation of dead spaces, i.e. stagnant zones, in which tracer particles are segregated. Thus, the total fluidized bed volume appears to be reduced by the volume of the dead spaces. Increasing the gas velocity after the experiment causes the stagnant particles to disperse, which is clearly indicated by the increasing signal at the particle drain indicating tracer detection. This circumstance is shown in Fig. 16a ($E_{U=0.23\ \mathrm{m\ s^{-1}}}$), confirming the reason given above. In addition, the exit age distribution function shows a tendency of sluggish slow turnover of the fluidized bulk at $t \approx 1000$ s, i.e. inadequate mixing, as depicted in Fig. 1.

In view of the mid-level SCR of $\dot{m}_s$ = 206 kg h^{-1}, τ_{fit} is slightly excessive compared to the expected value τ_{hyd}. The recorded exit age distribution function (*E*-curve) is shown in Fig. 16b. The *E*-curve for this operating point indicates short-circuiting by showing a relatively steep decrease after the exit age distribution function reaches its maximum as well as a characteristic bend at $t \approx 500$ s (refer to Fig. 1). However, the short-circuit flow stands in contrast to the slightly excessive MRT. Furthermore, tracer particles were detected after increasing the gas velocity (Fig. 16b, $E_{U=0.23\ \mathrm{m\ s^{-1}}}$), again indicating stagnant solids. This circumstance as well is contradictory to $\tau_{fit} > \tau_{hyd}$. One possibility is that tracer particles bypass the magnetic separation devices located at the downcomer, causing the tracer particles to travel a second loop. This explanation is supported by the observation that the effect is dramatically increased if only one magnetic separator is used.

At the highest SCR of $\dot{m}_s$ = 323 kg h^{-1}, the derived MRT τ_{fit} also lies slightly above the HRT τ_{hyd}. The formation of a short-circuit flow is clearly indicated by the obtained *E*-curve, given in Fig. 16c, showing an even more pronounced signal decrease after reaching the maximum. Again, a characteristic bend is observed at $t \approx 500$ *s*. With the increase of the gas velocity the formation of dead spaces has further reduced (Fig. 16c, $E_{U=0.23\ \mathrm{m\ s^{-1}}}$) and with short-circuiting in mind one should think that $\tau_{fit} < \tau_{hyd}$ holds ture. Again, the excessive MRT most likely stems from tracer particles bypassing the magnetic separation device.

Although the gas velocity was not changed in the experiments just described, a decrease in the formation of dead spaces was observed with the increase of the particle circulation rate, indicated by the cyan curves ($E_{U=0.23\ \mathrm{m\ s^{-1}}}$) shown in Fig. 16a, b and c. This circumstance means that the lateral particle movement also influences particle mixing and the reactor characteristics, i.e. the increase of the dispersion coefficient **D** (Fig. 15a). As the particle circulation rate increases, the probability of short-circuiting inherently increases, which is illustrated by the increase in the maximum slope k_{max} occurring at the steep increase ('take-off') of the *E*-curve (Fig. 14a. In addition, the decrease of the breakthrough time τ_1, shown in Fig. 13b, indicates that particles are transported more rapidly from the solids feed to the drain. Fig. 14b reveals that the change of the particle circulation rate appears not to influence the vessel dispersion number $\mathbf{D}/(u \cdot L)$. Merely examining the MRT of particles in the tubes of the particle feed and drain (PFR) reveals that $\tau_{pfr} = L/u$ decreases with an increase of the SCR. However, the difference between τ_{pfr} and τ_{hyd} of the PFR stays approximately the same for the superficial gas velocity of $U = 0.08\ \mathrm{m\ s^{-1}}$, indicating that the BFB as well is influenced by the characteristics of a plug flow reactor.

It is noted that the formation of dead-spaces and short circuit flows at a fluidization number of U/U_{mf} = 4.7 seems unexpected. This may be due to the specific design of gas distributor, whereby the pitch in between the sintered metal filters is quite large (refer to Fig. 2b).

3.2. Mid-level gas velocity

As observed for the low gas velocity, the calculated MRT decreases as the SCR increases. Starting at $\dot{m}_s$ = 88 kg h^{-1}, the

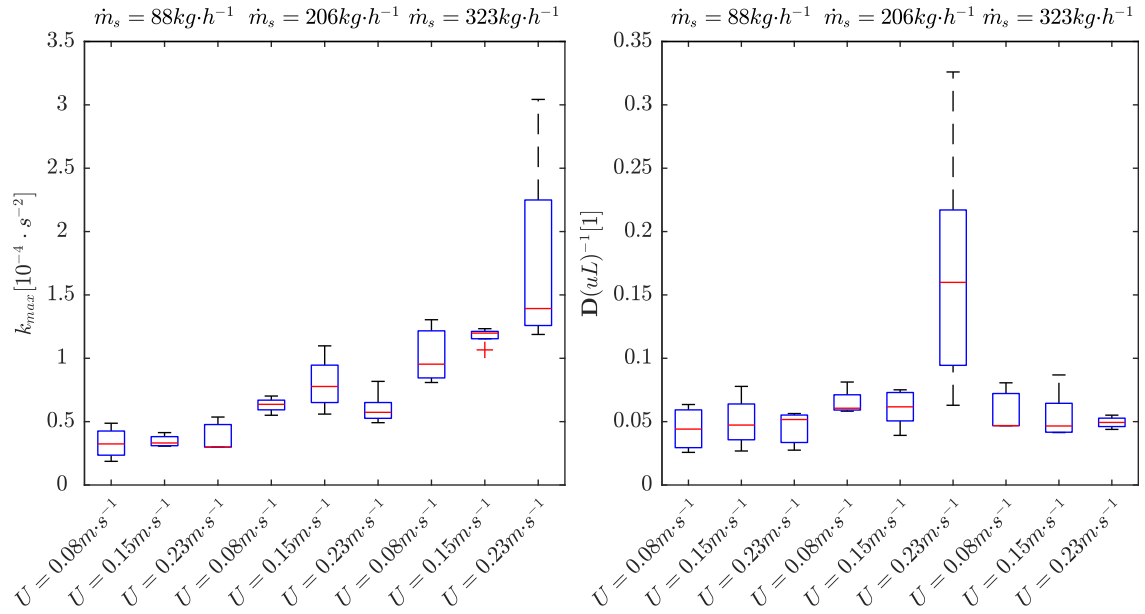

(a) k_{max} as a function of superficial gas velocity U and solids circulation rate $\dot{m}_s$.

(b) $\mathbf{D}/(u \cdot L)$ as a function of superficial gas velocity U and solids circulation rate $\dot{m}_s$.

Fig. 14. k_{max} and $\mathbf{D}/(u \cdot L)$.

Please cite this article in press as: Hofer, G., et al. Particle mixing in bubbling fluidized bed reactors with continuous particle exchange. Chem. Eng. Sci. (2018), https://doi.org/10.1016/j.ces.2018.10.001

observed MRT τ_{fit} is lower than the HRT τ_{hyd}, but above that observed at the low gas velocity. The exit age distribution, given in Fig. 16d, points to the absence of short-circuiting and dead spaces. This conclusively explains the increase in τ_{fit} compared to the values at low gas velocity $U = 0.08$ m s^{-1} (U/U_{mf} = 4.7). It is concluded that the slightly low MRT stems from the measurement time being too short, i.e. the E_{fit}-curve clearly not touching the x-axis.

Considering the mid-level SCR of $\dot{m}_s$ = 206 kg h^{-1}, τ_{fit} turns out to be slightly higher than τ_{hyd}. The exit age distribution is given by Fig. 16e. Increasing the gas velocity right after the actual experiment precludes stagnant fluid, since no significant amount of tracer material was detected at the particle drain indicated by the cyan signal data, also shown in Fig. 16e. The somewhat excessive MRT could thus be due to tracer particles bypassing the separation device, as already observed for the lower gas velocity $U = 0.08$ m s^{-1}. Belonging to the model of a PFR with AD, the vessel dispersion number does not appear to be subject to change compared to the other gas velocities as well as to the other SCRs.

At the highest SCR of $\dot{m}_s$ = 323 kg h^{-1}, the observed MRT τ_{fit} again is slightly higher than the HRT τ_{hyd}. As for the low gas velocity of $U = 0.08$ m s^{-1} (U/U_{mf} = 4.7) the reason for the observed behavior lies in the tracer bypassing the magnetic separator. The data is shown in 16f.

Increasing the SCR is accompanied by an increase in the maximum slope observed at the 'take-off' of the exit age distribution function E. Varying the SCR seems to have little influence on the vessel dispersion number $\mathbf{D}/(u \cdot L)$, since the increase of $\mathbf{D}$ is made up by the decrease of L/u. Thereby, it is evident that τ_{pfr} approaches τ_{hyd}, shown in Fig. 15b. This circumstance indicates an increase in particle mixing with the increase in gas velocity. With the MRT of the particles in the feed and drain tube being similar to the HRT of this equipment, the characteristics of the BFB is less pronounced by a PFR with AD compared to the lower gas velocity, i.e. the BFB almost behaves like an ideally mixed CSTR.

3.3. High gas velocity

With regards to the combination of the high gas velocity $U = 0.23$ m s^{-1} (U/U_{mf} = 13.5) and the low SCR $\dot{m}_s$ = 88 kg h^{-1} it is evident that $\tau_{fit} \approx \tau_{hyd}$, indicated in Fig. 13a. The MRT for the low SCR is highest compared to both lower gas velocities. The observation of the measured data indicates reasonably good flow (Fig. 1) and does not point the formation of dead spaces or short-circuit flow (Fig. 16g).

At the mid-level SCR of $\dot{m}_s$ = 206 kg h^{-1}, the experimentally determined MRT is slightly above the HRT τ_{hyd}. Again, this behavior is due to tracer particles bypassing the magnetic separator in the downcomer section of the CFM. The respective E-curve is shown in Fig. 16h, not indicating any short-circuit flows.

For the lower SCR of $\dot{m}_s$ = 206 kg h^{-1}, as well true for the lower gas velocities $U = 0.08$ m s^{-1} ($U/U_{mf} = 4.7$) and $U = 0.15$ m s^{-1} (U/U_{mf} = 8.8), the highest SCR $\dot{m}_s$ = 323 kg h^{-1} results the MRT being higher than the HRT. As discussed before, high SCRs cause tracer material bypassing the magnetic separator. The E-curves calculated from the data recorded during the experiments with high gas velocity and high SCR are shown in Fig. 16i, indicating reasonably good flow.

At the highest gas velocity, the HRTs in the particle feed and drain (plug flow) approaches the respective values τ_{pfr}, shown in Fig. 15b. The circumstance indicates that the particle mixing in the fluidized bed resembles an ideally mixed CSTR and is hardly overlayed by a plug flow. This is also underpinned by the data shown in Fig. 14, whereby the highest values for k_{max} is observed for the highest SCR, meaning that tracer intermixing into the bubbling fluidized bed happens adequately fast.

3.4. General aspects

The maximum slope k_{max}, occurring at the 'take-off' of the E-curve, increases with an increase in the SCR. The circumstance is shown in Fig. 14. It surprises that the gas velocity hardly

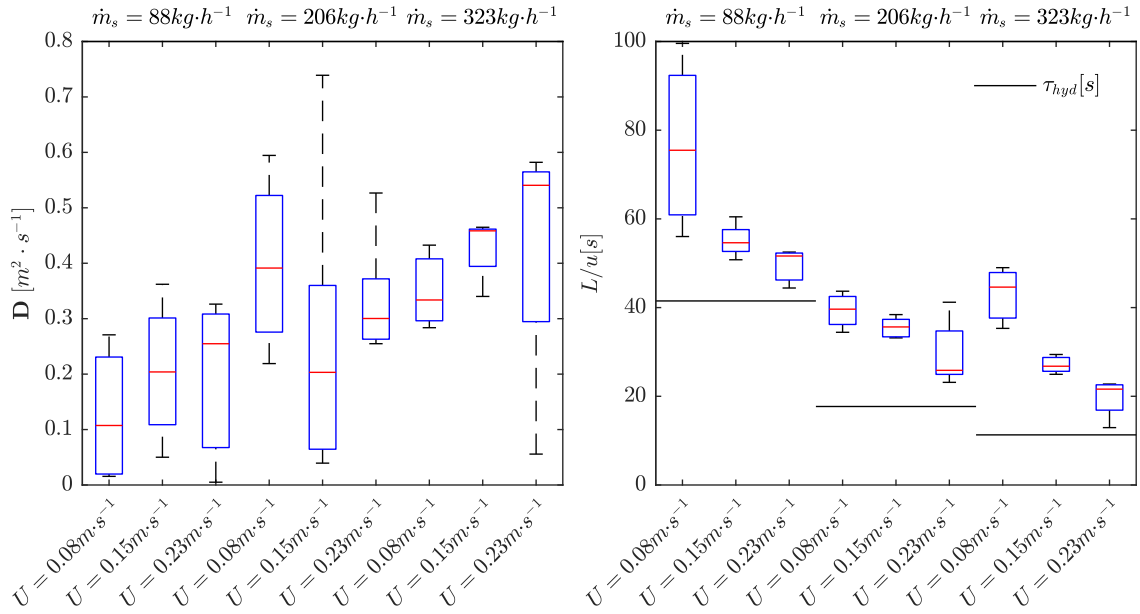

(a) $\mathbf{D}$ as a function of superficial gas velocity U and solids circulation rate $\dot{m}_s$. (b) L/u as a function of superficial gas velocity U and solids circulation rate $\dot{m}_s$.

Fig. 15. $\mathbf{D}$ and $\tau_{pfr} = L/u$ compared to $\tau_{hyd} = (m_{s,feed} + m_{s,drain})/\dot{m}_s$.

Please cite this article in press as: Hofer, G., et al. Particle mixing in bubbling fluidized bed reactors with continuous particle exchange. Chem. Eng. Sci. (2018), https://doi.org/10.1016/j.ces.2018.10.001

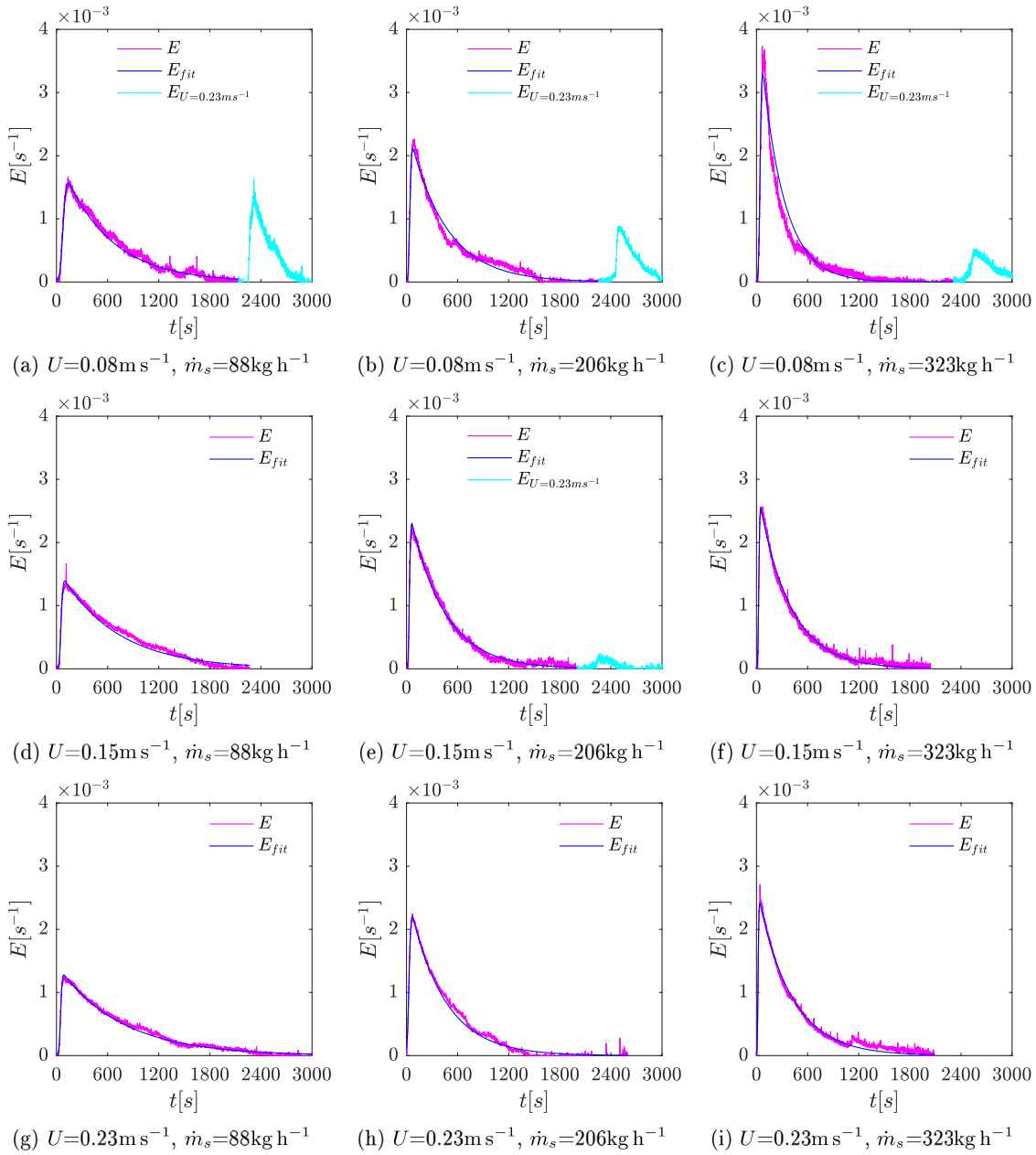

Fig. 16. *E*-curve vs. E_{fit}-curve for different superficial gas velocities U and solids circulation rates $\dot{m}_s$.

influences k_{max} for the SCRs $\dot{m}_s$ = 88 kg h^{-1} and $\dot{m}_s$ = 206 kg h^{-1}. At the largest SCR of $\dot{m}_s$ = 323 kg h^{-1} k_{max} increases with an increase of the gas velocity U. This behavior may be explained by improved mixing characteristics and the decrease in the formation of dead spaces and/or short-circuiting. Obviously, the increase in gas velocity leads to greater effects at larger SCRs.

The vessel dispersion number $\mathbf{D}/(u \cdot L)$ seems to be similar for all experiments, except for the tests at a gas velocity of U = 0.23 m s^{-1} (U/U_{mf} = 13.5) and a SCR of $\dot{m}_s$ = 206 kg h^{-1}. These data seem to represent an outlier. Merely considering the fraction of L/u, representing the MRT of a PFR with AD, indicates a more or less permanent decrease of τ_{pfr} with the increase in gas velocity as well as the SCR. Thus, the system tends to behave closer to an ideally mixed CSTR with an increase of the gas velocity and the SCR. This means that dispersion is more pronounced either at higher gas velocities or at higher SCRs.

The time span between the injection of the tracer until the tracer is initially detected at the particle drain, referred to as τ_1, decreases with increasing gas velocity U as well as the SCR $\dot{m}_s$. The data is illustrated in Fig. 13b. The same conclusions apply to both other characteristic values τ_2, the time span between the tracer injection and the occurrence of k_{max}, and τ_3, the time span between the tracer injection and the occurrence of the absolute maximum of the exit age distribution function (*E*-curve).

4. Conclusion

Particle mixing in bubbling beds with net cross-flow of gas and solids was investigated in a cold flow model by means of tracer experiments based on inductive measurements.

Please cite this article in press as: Hofer, G., et al. Particle mixing in bubbling fluidized bed reactors with continuous particle exchange. Chem. Eng. Sci. (2018), https://doi.org/10.1016/j.ces.2018.10.001

It was found that the experimental mean residence time follows the hydraulic residence time and that a four-parameter model consisting of a plug flow reactor with imprinted axial dispersion and a continuous stirred tank reactor in series allowed for satisfactory fits with the CSTR part clearly dominating the response. However, the mean residence times stemming from the experiments more or less diverge from the expected values depending on the operational parameters superficial gas velocity and solids circulation rate.

As for the low solids circulation rate of 88 kg h^{-1}, the experimentally obtained mean residence time more and more resembles the hydraulic residence time with an increase in gas velocity. The observed formation of dead spaces, declining with the increase of the gas velocity, explains the circumstance. Albeit U/U_{mf} = 4.7 applies for the low gas velocity of 0.08 m s^{-1}, consistent particle mixing seems to be hindered. A non-optimal gas distribution seems to be a possible reason for this and confirms the formation of short-circuit flows with the increase in the solids circulation rate, characterized with the sharp early peak observed at the *E*-curve.

At both higher solids circulation rates (206 and 323 kg h^{-1}) the experimentally obtained mean residence time excesses the hydraulic residence time. Thereby, the reason lies in the tracer bypassing separation by means of the magnetic shells mounted on the downcomer. Nevertheless, neither dead spaces nor short-circuit flows were observed at the higher gas velocities of 0.15 m s^{-1} ($U/U_{mf} = 8.8$) and 0.23 m s^{-1} ($U/U_{mf} = 13.5$) indicating reasonably good flow.

After improving tracer separation, further experimental work is going to be performed to investigate solids residence time distributions and particle mixing under the influence of bubbling bed immersed heat exchangers, i.e. tube bundles. Based on the knowledge gained from wall-to-bed heat transfer characteristics, it is assumed that the immersed tubes affect the shape of the *E*-curves towards a more pronounced plug flow reactor with imprinted axial dispersion.

Acknowledgement

The authors gratefully acknowledge the support by the Institute of Sanitary Engineering and Water Pollution Control (SIG), in particular the head of the institute Thomas Ertl for providing the lab facilities and Friedrich Kropitz for technical support.

References

AnalogDevices, 2015. Balanced Modulator/Demodulator AD630, Rev. G.
Avidan, Amos, Yerushalmi, Joseph, 1985. Solids mixing in an expanded top fluid bed. AIChE J. 31 (5), 835–841.
Bachmann, Philipp, Tsotsas, Evangelos, 2015. Analysis of residence time distribution data in horizontal fluidized beds. Proc. Eng. 102, 790–798.
Bachmann, P., Bück, A., Tsotsas, E., 2016. Investigation of the residence time behavior of particulate products and correlation for the bodenstein number in horizontal fluidized beds. Powder Technol. 301, 1067–1076.
Bachmann, P., Bück, A., Tsotsas, E., 2017. Experimental investigation and correlation of the bodenstein number in horizontal fluidized beds with internal baffles. Powder Technol. 308, 378–387.
Bellgardt, D., Werther, J., 1986. A novel method for the investigation of particle mixing in gas-solid systems. Powder Technol. 48 (2), 173–180.
Bruce Nauman, E., 2008. Residence time theory. Ind. Eng. Chem. Res. 47 (10), 3752–3766.
Carpenter Technology, 2018. Magnetic Properties of Stainless Steels. <https://www.cartech.com/en/alloy-techzone/technical-information/technical-articles/magnetic-properties-of-stainless-steels>.
Chen, Kaicheng, Bachmann, Philipp, Bück, Andreas, Jacob, Michael, Tsotsas, Evangelos, 2017. Experimental study and modeling of particle drying in a continuously-operated horizontal fluidized bed. Particuology 34, 134–146.
Fitzgerald, T., Catipovic, N., Jovanovic, G., 1977. Solids tracer studies in a tube-filled fluidized bed. In: Bliss, C., Williams, B.M. (Eds.), Circulating Fluidized Bed Combustion, vol. V, pp. 135–152.
Gao, Yijie, Muzzio, Fernando J., Ierapetritou, Marianthi G., 2012. A review of the residence time distribution (RTD) applications in solid unit operations. Powder Technol. 228, 416–423.
Geldart, D., 1973. Types of gas fluidization. Powder Technol. 7 (5), 285–292.
Guío-Pérez, Diana Carolina, Pröll, Tobias, Hofbauer, Hermann, 2013. Measurement of ferromagnetic particle concentration for characterization of fluidized bed fluid-dynamics. Powder Technol. 239, 147–154.
Guío-Pérez, Diana Carolina, Pröll, Tobias, Hofbauer, Hermann, 2013. Solids residence time distribution in the secondary reactor of a dual circulating fluidized bed system. Chem. Eng. Sci. 104, 269–284.
Guío-Pérez, Diana Carolina, Pröll, Tobias, Wassermann, Johann, Hofbauer, Hermann, 2013. Design of an inductance measurement system for determination of particle residence time in a dual circulating fluidized bed cold flow model. Ind. Eng. Chem. Res. 52 (31), 10732–10740.
Harris, A.T., Davidson, J.F., Thorpe, R.B., 2003. Particle residence time distributions in circulating fluidised beds. Chem. Eng. Sci. 58 (11), 2181–2202.
Kong, Weibin, Wang, Bin, Baeyens, Jan, Li, Shuo, Ke, Hui, Tan, Tianwei, Zhang, Huili, 2018. Solids mixing in a shallow cross-flow bubbling fluidized bed. Chem. Eng. Sci. 187, 213–222.
Kunii, D., Levenspiel, Octave, 1991. Fluidization Engineering. Butterworth Heinemann.
Levenspiel, Octave, 1998. Chemical Reaction Engineering, PAPERBACKSHOP UK IMPORT.
Nilsson, Lars, Wimmerstedt, Roland, 1988. Residence time distribution and particle dispersion in a longitudinal-flow fluidized bed. Chem. Eng. Sci. 43 (5), 1153–1160.
Pröll, Tobias, Schöny, Gerhard, Sprachmann, Gerald, Hofbauer, Hermann, 2016. Introduction and evaluation of a double loop staged fluidized bed system for post-combustion CO_2 capture using solid sorbents in a continuous temperature swing adsorption process. Chem. Eng. Sci. 141, 166–174.
Scott Fogler, H., 2015. Elements of Chemical Reaction Engineering, fouth ed. Pl.
Sette, Erik, Pallarès, David, Johnsson, Filip, 2014. Experimental evaluation of lateral mixing of bulk solids in a fluid-dynamically down-scaled bubbling fluidized bed. Powder Technol. 263, 74–80.
Sette, Erik, Pallarès, David, Johnsson, Filip, Ahrentorp, Fredrik, Ericsson, Anders, Johansson, Christer, 2015. Magnetic tracer-particle tracking in a fluid dynamically down-scaled bubbling fluidized bed. Fuel Process. Technol. 138, 368–377.
Sydenham, Peter H., Thorn, Richard (Eds.), 2005. Handbook of Measuring System Design. John Wiley & Sons, Ltd.
Yagi, Sakae, Kunii, Daizo, 1961. Fluidized-solids reactors with continuous solids feed—i. Chem. Eng. Sci. 16 (3–4), 364–371.

Please cite this article in press as: Hofer, G., et al. Particle mixing in bubbling fluidized bed reactors with continuous particle exchange. Chem. Eng. Sci. (2018), https://doi.org/10.1016/j.ces.2018.10.001

Appendix B

Process flow diagrams

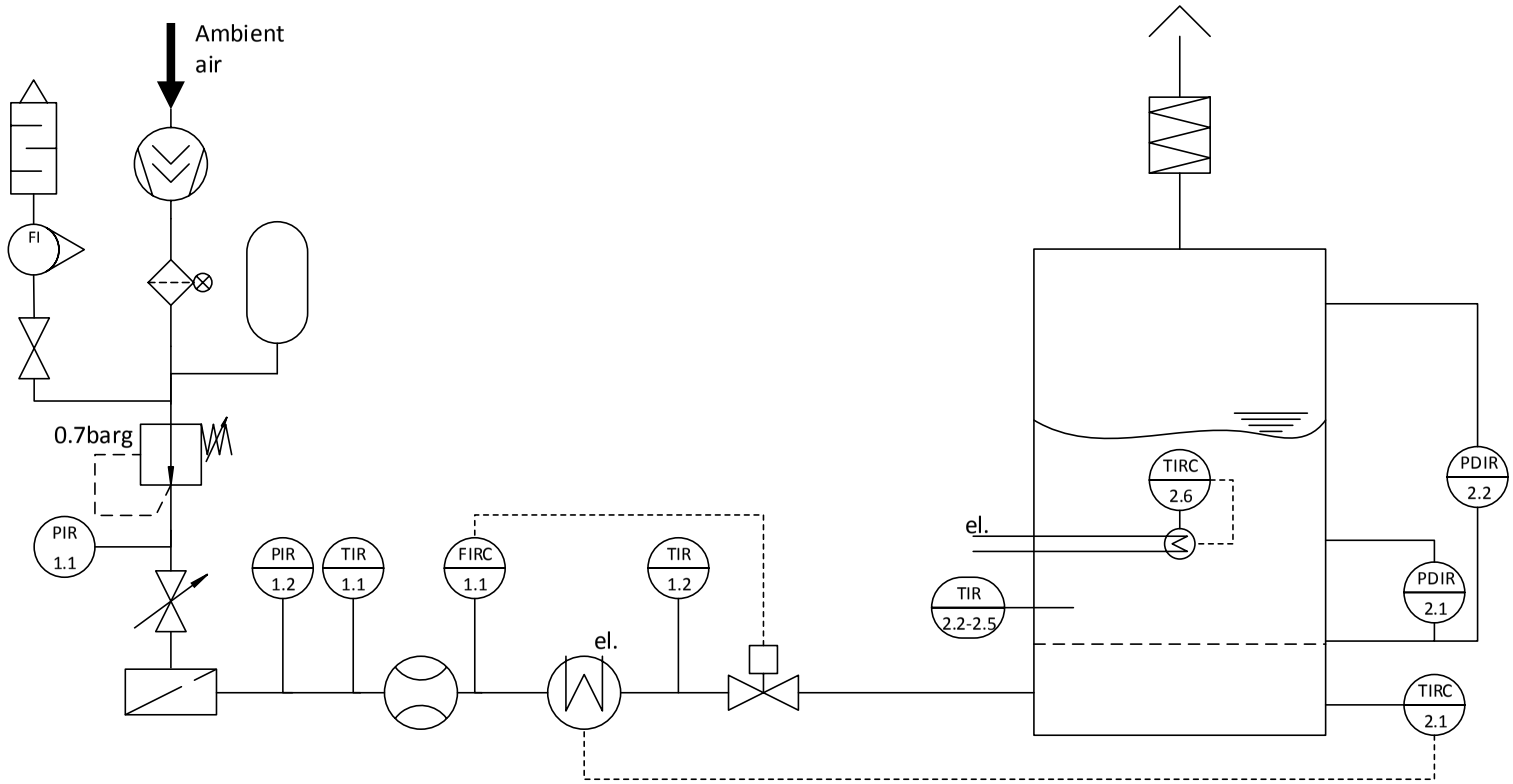

Figure B.1: CFM Stage I process flow diagram.

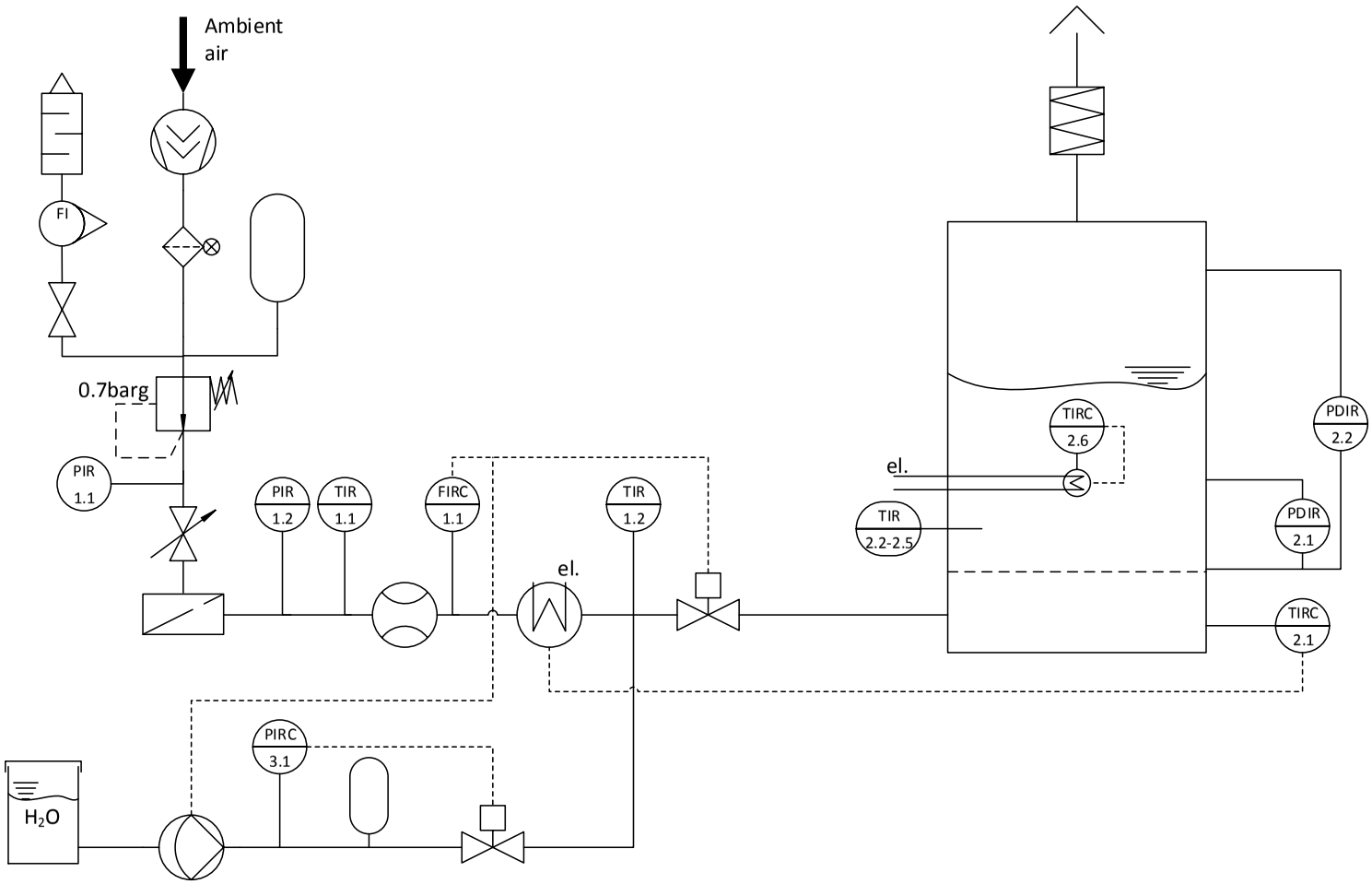

Figure B.2: CFM Stage II process flow diagram.

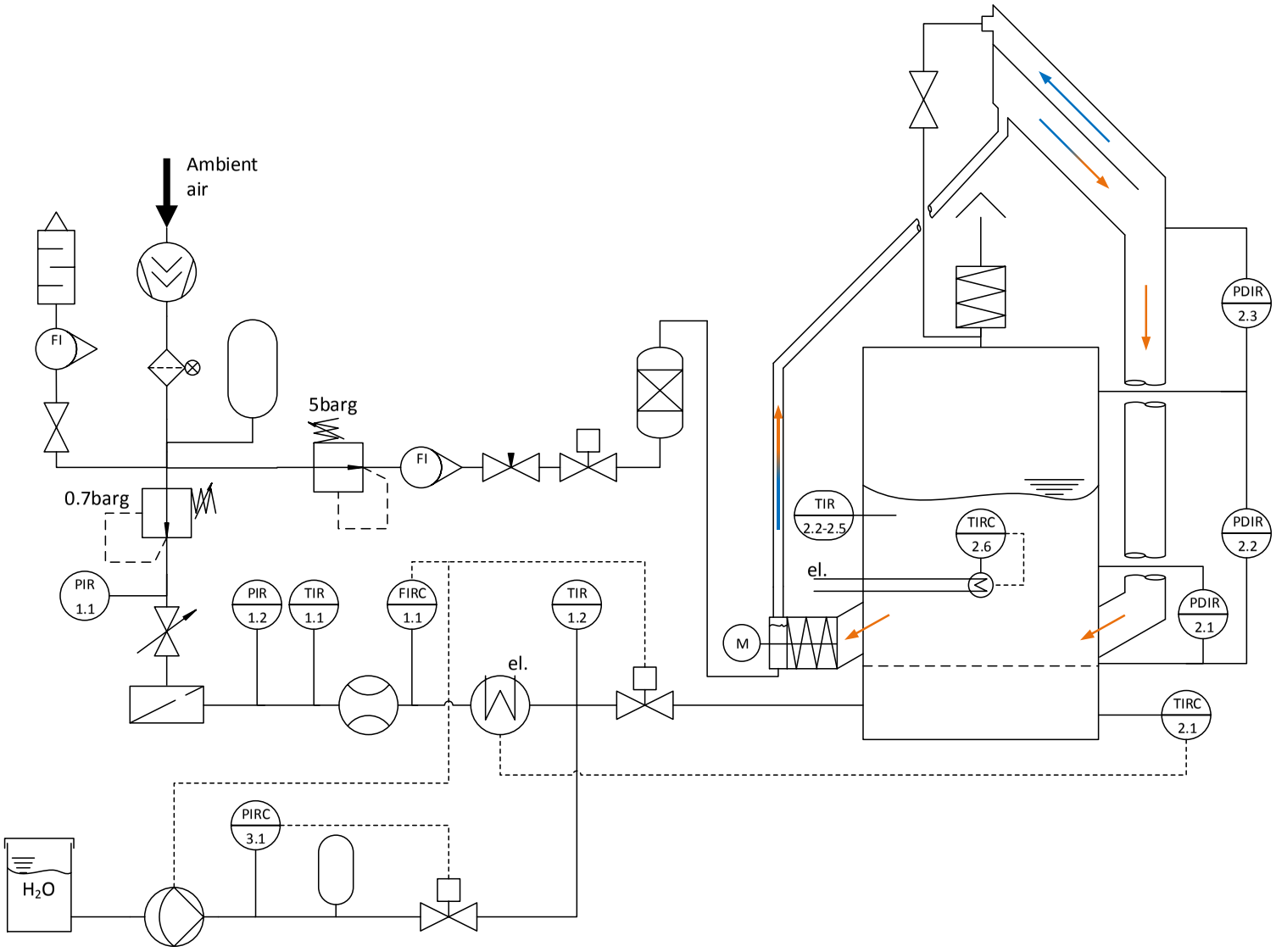

Figure B.3: CFM Stage III process flow diagram (blue=gas, orange=solids).

Appendix C

Particle size distribution analyses

MASTERSIZER 2000

Analyse Report

Probenname:	Glasperlen used	**SOP Name:**	Glasperlen Microrinne	**Gemessen:**	Tuesday, February 23, 2016 10:39:35 AM
Probenherkunft:	Factory	**Operator:**	tlaminger	**Berechnet:**	Tuesday, February 23, 2016 10:39:36 AM
Probenreferenz:				**Datenursprung:**	Gemittelt

Probenmaterial:	Glass beads (typical)		**Dispergiermodul:**	Scirocco 2000 (B)	**Abschattung:**	0.58	%
Partikel RI:	1.520	**Absorption:** 0	**Analysemodell:**	Monomodale Verteilung (fein)			
Dispergierfluid:			**Meßbereich:**	0.020 to 2000.000 um	**Fit(gewichtet):**	0.704	%
Fluid RI:	1.000		**Emulation:**	Aus			

Konzentration:	0.0025	%Vol	**Vol. Mittelwert D[4,3]:**	145.035 um	**Spezifische Oberfläche:**	0.0188	m²/g
Breite :	0.716		**Gleichförmigkeit:**	0.226	**D[3,2]:**	130.488	um
Verteilungsart:	Volumen						

d(0.1): 97.556 um **d(0.5): 141.952** um d(0.9): 199.220 um

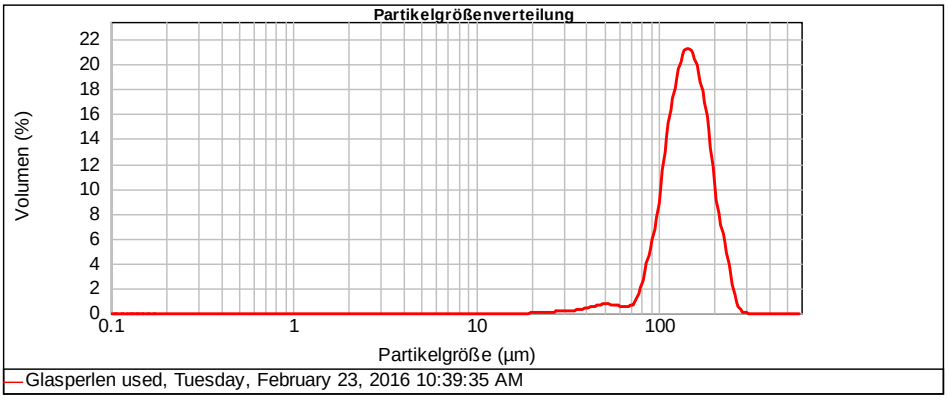

Größen-	Häufigkeit (%)	Größen-	Häufigkeit (%)	Größen-	Häufigkeit (%)	Größen-	Häufigkeit (%)	Größen-	Häufigkeit (%)	Größen-	Häufigkeit (%)
0.020	0.00	0.142	0.00	1.002	0.00	7.096	0.00	50.238	0.54	355.656	0.00
0.022	0.00	0.159	0.00	1.125	0.00	7.962	0.00	56.368	0.46	399.052	0.00
0.025	0.00	0.178	0.00	1.262	0.00	8.934	0.00	63.246	0.40	447.744	0.00
0.028	0.00	0.200	0.00	1.416	0.00	10.024	0.00	70.963	0.79	502.377	0.00
0.032	0.00	0.224	0.00	1.589	0.00	11.247	0.00	79.621	2.80	563.677	0.00
0.036	0.00	0.252	0.00	1.783	0.00	12.619	0.00	89.337	4.94	632.456	0.00
0.040	0.00	0.283	0.00	2.000	0.00	14.159	0.00	100.237	9.44	709.627	0.00
0.045	0.00	0.317	0.00	2.244	0.00	15.887	0.00	112.468	13.16	796.214	0.00
0.050	0.00	0.356	0.00	2.518	0.00	17.825	0.00	126.191	15.57	893.367	0.00
0.056	0.00	0.399	0.00	2.825	0.00	20.000	0.00	141.589	15.91	1002.374	0.00
0.063	0.00	0.448	0.00	3.170	0.00	22.440	0.02	158.866	14.09	1124.683	0.00
0.071	0.00	0.502	0.00	3.557	0.00	25.179	0.07	178.250	10.65	1261.915	0.00
0.080	0.00	0.564	0.00	3.991	0.00	28.251	0.08	200.000	5.86	1415.892	0.00
0.089	0.00	0.632	0.00	4.477	0.00	31.698	0.11	224.404	3.29	1588.656	0.00
0.100	0.00	0.710	0.00	5.024	0.00	35.566	0.16	251.785	0.57	1782.502	0.00
0.112	0.00	0.796	0.00	5.637	0.00	39.905	0.24	282.508	0.00	2000.000	0.00
0.126	0.00	0.893	0.00	6.325	0.00	44.774	0.37	316.979	0.00		
0.142	0.00	1.002	0.00	7.096	0.00	50.238	0.51	355.656	0.00		

Kommentar: *Mittelwert*

Malvern Instruments Ltd.
Malvern, UK
Tel.: +44 (0) 1684-892456; Fax: +44 (0) 1684-892789

Mastersizer 2000 Version 5.12G
S/N: MAL1034369

Dateiname: knorr bremse.mea
Messdatensatz-Nr.: 639
23 Feb 2016 10:45:27 AM

Figure C.1: PSD bulk material A.

MASTERSIZER 2000

Analyse Report

Probenname:	Glasperlen 0h	**SOP Name:**	Glasperlen Microrinne	**Gemessen:**	Tuesday, February 23, 2016 10:47:24 AM
Probenherkunft:	Factory	**Operator:**	tlaminger	**Berechnet:**	Tuesday, February 23, 2016 10:47:25 AM
Probenreferenz:				**Datenursprung:**	Gemittelt

Probenmaterial:	Glass beads (typical)		**Dispergiermodul:**	Scirocco 2000 (B)	**Abschattung:**	0.79	%
Partikel RI:	1.520	**Absorption:** 0	**Analysemodell:**	Monomodale Verteilung (fein)			
Dispergierfluid:			**Meßbereich:**	0.020 to 2000.000 um	**Fit(gewichtet):**	1.219	%
Fluid RI:	1.000		**Emulation:**	Aus			

Konzentration:	0.0054	%Vol	**Vol. Mittelwert D[4,3]:**	219.602	um	**Spezifische Oberfläche:**	0.0123 m²/g
Breite :	0.691		**Gleichförmigkeit:**	0.217		**D[3,2]:**	199.050 um
Verteilungsart:	Volumen						

d(0.1): 144.726 um **d(0.5): 218.930** um d(0.9): 296.108 um

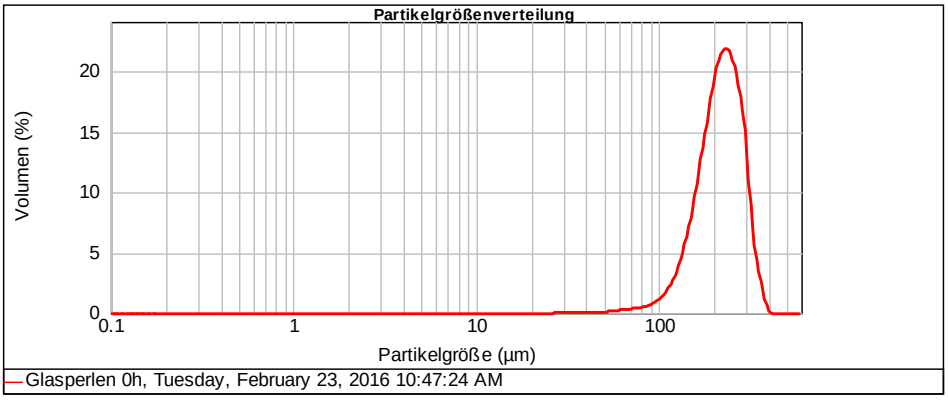

Größen-	Häufigkeit (%)	Größen-	Häufigkeit (%)	Größen-	Häufigkeit (%)	Größen-	Häufigkeit (%)	Größen-	Häufigkeit (%)	Größen-	Häufigkeit (%)
0.020	0.00	0.142	0.00	1.002	0.00	7.096	0.00	50.238	0.10	355.656	0.86
0.022	0.00	0.159	0.00	1.125	0.00	7.962	0.00	56.368	0.16	399.052	0.00
0.025	0.00	0.178	0.00	1.262	0.00	8.934	0.00	63.246	0.23	447.744	0.00
0.028	0.00	0.200	0.00	1.416	0.00	10.024	0.00	70.963	0.31	502.377	0.00
0.032	0.00	0.224	0.00	1.589	0.00	11.247	0.00	79.621	0.42	563.677	0.00
0.036	0.00	0.252	0.00	1.783	0.00	12.619	0.00	89.337	0.65	632.456	0.00
0.040	0.00	0.283	0.00	2.000	0.00	14.159	0.00	100.237	1.14	709.627	0.00
0.045	0.00	0.317	0.00	2.244	0.00	15.887	0.00	112.468	2.07	796.214	0.00
0.050	0.00	0.356	0.00	2.518	0.00	17.825	0.00	126.191	3.66	893.367	0.00
0.056	0.00	0.399	0.00	2.825	0.00	20.000	0.00	141.589	6.18	1002.374	0.00
0.063	0.00	0.448	0.00	3.170	0.00	22.440	0.00	158.866	9.44	1124.683	0.00
0.071	0.00	0.502	0.00	3.557	0.00	25.179	0.00	178.250	13.02	1261.915	0.00
0.080	0.00	0.564	0.00	3.991	0.00	28.251	0.03	200.000	15.86	1415.892	0.00
0.089	0.00	0.632	0.00	4.477	0.00	31.698	0.07	224.404	16.50	1588.656	0.00
0.100	0.00	0.710	0.00	5.024	0.00	35.566	0.08	251.785	14.82	1782.502	0.00
0.112	0.00	0.796	0.00	5.637	0.00	39.905	0.07	282.508	10.58	2000.000	
0.126	0.00	0.893	0.00	6.325	0.00	44.774	0.06	316.979	3.68		
0.142	0.00	1.002	0.00	7.096	0.00	50.238		355.656			

Kommentar: *Mittelwert*

Malvern Instruments Ltd.
Malvern, UK
Tel.: +44 (0) 1684-892456; Fax: +44 (0) 1684-892789

Mastersizer 2000 Version 5.12G
S/N: MAL1034369

Dateiname: knorr bremse.mea
Messdatensatz-Nr.: 648
23 Feb 2016 10:50:54 AM

Figure C.2: PSD bulk material B.

MASTERSIZER 2000

Analyse Report

Probenname:	Lewatit VP OC 1065 as	**SOP Name:**	PS_trocken2	**Gemessen:**	Wednesday, May 04,
Probenherkunft:	Factory	**Operator:**	tl	**Berechnet:**	Wednesday, May 04,
Probenreferenz:				**Datenursprung:**	Gemittelt

Probenmaterial:	Polystyrene latex		**Dispergiermodul:**	Scirocco 2000 (B)	**Abschattung:**	2.45	%
Partikel RI:	1.590	**Absorption:** 0	**Analysemodell:**	Universal			
Dispergierfluid:			**Meßbereich:**	0.020 to 2000.000 um	**Fit(gewichtet):**	1.988	%
Fluid RI:	1.000		**Emulation:**	Aus			

Konzentration:	0.0566	%Vol	**Vol. Mittelwert D[4,3]:**	730.451	um	**Spezifische Oberfläche:**	0.00845 m²/g
Breite :	0.738		**Gleichförmigkeit:**	0.235		**D[3,2]:**	676.527 um
Verteilungsart:	Volumen						

d(0.1): 493.802 um **d(0.5): 695.574** um d(0.9): 1006.960 um

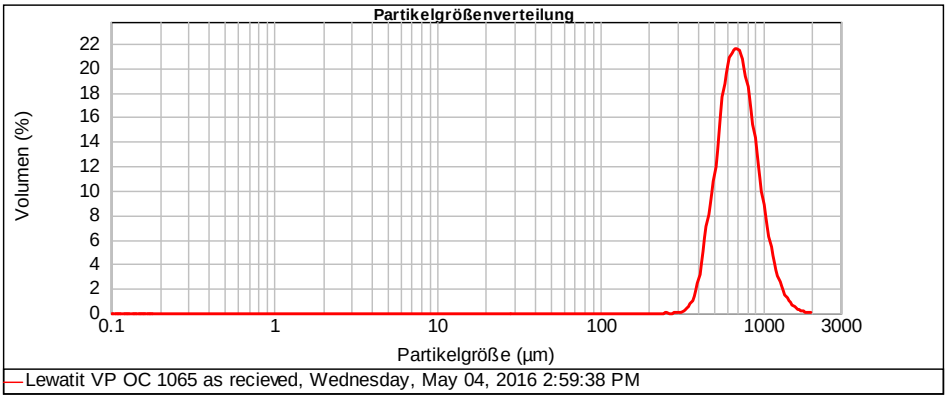

Größen-	Häufigkeit (%)	Größen-	Häufigkeit (%)	Größen-	Häufigkeit (%)	Größen-	Häufigkeit (%)	Größen-	Häufigkeit (%)	Größen-	Häufigkeit (%)
0.020	0.00	0.142	0.00	1.002	0.00	7.096	0.00	50.238	0.00	355.656	0.94
0.022	0.00	0.159	0.00	1.125	0.00	7.962	0.00	56.368	0.00	399.052	3.28
0.025	0.00	0.178	0.00	1.262	0.00	8.934	0.00	63.246	0.00	447.744	6.73
0.028	0.00	0.200	0.00	1.416	0.00	10.024	0.00	70.963	0.00	502.377	10.53
0.032	0.00	0.224	0.00	1.589	0.00	11.247	0.00	79.621	0.00	563.677	14.89
0.036	0.00	0.252	0.00	1.783	0.00	12.619	0.00	89.337	0.00	632.456	16.29
0.040	0.00	0.283	0.00	2.000	0.00	14.159	0.00	100.237	0.00	709.627	15.53
0.045	0.00	0.317	0.00	2.244	0.00	15.887	0.00	112.468	0.00	796.214	12.59
0.050	0.00	0.356	0.00	2.518	0.00	17.825	0.00	126.191	0.00	893.367	8.76
0.056	0.00	0.399	0.00	2.825	0.00	20.000	0.00	141.589	0.00	1002.374	5.34
0.063	0.00	0.448	0.00	3.170	0.00	22.440	0.00	158.866	0.00	1124.683	2.83
0.071	0.00	0.502	0.00	3.557	0.00	25.179	0.00	178.250	0.00	1261.915	1.33
0.080	0.00	0.564	0.00	3.991	0.00	28.251	0.00	200.000	0.00	1415.892	0.56
0.089	0.00	0.632	0.00	4.477	0.00	31.698	0.00	224.404	0.00	1588.656	0.17
0.100	0.00	0.710	0.00	5.024	0.00	35.566	0.00	251.785	0.00	1782.502	0.05
0.112	0.00	0.796	0.00	5.637	0.00	39.905	0.00	282.508	0.00	2000.000	
0.126	0.00	0.893	0.00	6.325	0.00	44.774	0.00	316.979	-0.00		
0.142	0.00	1.002	0.00	7.096	0.00	50.238	0.00	355.656	0.19		

Kommentar: *Mittelwert*

Malvern Instruments Ltd.
Malvern, UK
Tel.: +44 (0) 1684-892456; Fax: +44 (0) 1684-892789

Mastersizer 2000 Version 5.12G
S/N: MAL1034369

Dateiname: knorr bremse.mea
Messdatensatz-Nr.: 855
04 May 2016 3:20:52 PM

Figure C.3: PSD bulk material C.